Polyurethane-based Scaffolds
for
Bone Tissue Engineering

The Role of Hydroxyapatite Particles, Solvent Combinations, Electrospun Fibre Orientations, *In Vivo* & *In Vitro* Characterisation, and Particulate Leached Foams for creating 3-D Bone Models.

Gifty A. J. Tetteh

A thesis submitted in partial fulfilment of the requirements

for the degree of Doctor of Philosophy

Department of Material Science & Engineering

University of Sheffield

United Kingdom

September, 2016.

This page was intentionally left blank.

Awards and Conferences

Awards & Prizes

- Learned Society Travel Grant, University of Sheffield   **Aug, 2015**
- European Society of Biomechanics Travel Award   **July, 2015**
- Learned Society Travel Grant, University of Sheffield   **Mar, 2015**
- Best Biomechanics Paper, MECbioeng14, Imperial College   **Sept, 2014**
- Kroto Family Science Education Prize (Joint Winner)   **July, 2014**
- Best Poster Award, 10th Bose User Group Meeting   **June, 2014**
- Best Biomaterials & Tissue Engineering Poster Award   **May, 2014**
- Santander Research Mobility Award   **Nov, 2013**
- Learned Society Travel Grant, University of Sheffield   **Oct, 2013**
- Ghana Education Trust Fund Scholarship for PhD   **Mar, 2012**

Publications

Journal Papers

1. **G.Tetteh**, A.S.Khan, R.M.Delaine-Smith, G.C.Reilly & I.U.Rehman,"Electrospun polyurethane / hydroxyapatite bioactive scaffolds for bone tissue engineering: The role of solvent and hydroxyapatite particles". Journal of the Mechanical Behavior of Biomedical Materials. (2014) Vol. 39, pp. 95–110

Conference Proceedings

2. **G. Tetteh**, R.Delaine-Smith, N.H. Green, G.C.Reilly, July (2016), "Collagen and Mineral Deposition by MLO-A5 Late-Stage Osteoblasts, is Guided by the Fibre Alignment of Electrospun Scaffolds", Proc. of the 22nd Congress of the European Society of Biomechanics, Lyon, France.

3. **G. Tetteh**, M. Pogorielov, I.U. Rehman, G.C. Reilly, May (2016), "A 3-dimensional biomimetic *in vitro* bone model for testing small orthopaedic implants", Proc. of the 10th World Biomaterials Congress, Montreal, Canada.

4. **G. Tetteh**, I.U. Rehman, G.C. Reilly, August (2015), "*in vivo* and *in vitro* Characterization of Porous Polyurethane-Hydroxyapatite Scaffolds as A Bone Substitute," Proc. of the European Society for Biomaterials Conference, Krakow, Poland.

5. **G. Tetteh**, S. Puwanan, I.U. Rehman, G.C. Reilly, July (2015), "A Tissue Engineered Bone Membrane for Cleft Palate Repair", Proc. of the 21st Congress of the European Society of Biomechanics, Prague, Czech Republic.

6. **G. Tetteh**, M. Pogorielov, I.U. Rehman, G.C. Reilly, June (2015), "Developing Mechanically-Optimized & Highly Porous Polyurethane-Hydroxyapatite Constructs for Bone Tissue Engineering", Proc. of the 14th Annual Conference of the UK Society for Biomaterials, Belfast, Northern Ireland.

7. **G. Tetteh**, I.U. Rehman, G.C. Reilly, March (2015), "Using Tissue Engineering to develop an *in vitro* 3D Bone Model," Proc. of the Orthopedic Research Society Conference, Las Vegas, USA.

8. **G. Tetteh**, I.U. Rehman, G.C. Reilly, Sept (2014), "Engineering an *in vitro* 3D Bone Model for Implant Testing," Proc. of the Medical Engineering Centre's Annual Meeting and Bioengineering 14, London, UK.

9. **G. Tetteh**, I.U. Rehman, G.C. Reilly, August (2014), "Using Bioactive Scaffolds to synthesize an *in vitro* 3D Bone Model for Implant Testing," Proc. of the European Society for Biomaterials Conference, Liverpool, UK.

10. **G. Tetteh**, I.U. Rehman, G.C. Reilly, July (2014), "Particulate Leached Scaffolds for an *in vitro* 3D Bone Model for Implant Testing," Proc. of the 7th World Congress of Biomechanics, Boston, USA.

11. **G. Tetteh**, I.U. Rehman, G.C. Reilly, July (2014), "Bioactive Scaffolds as Bone Templates for *in vitro* Testing," European Cells and Materials Vol. 28. Suppl. 4, pp. 47.

12. **G. Tetteh**, I.U. Rehman, G.C. Reilly, May (2014), "Using composite scaffolds to engineer bone templates for *in vitro* testing," Proc. of the 2014 Bone Research Society Conference, Sheffield, UK.

13. **G. Tetteh**, I.U. Rehman, G.C. Reilly, December (2013) "A polyurethane-hydroxyapatite composite scaffold as a template for an *in vitro* bone model," Proc. of the ICMOBT 2013, Stiges, Spain.

14. **G. Tetteh**, I.U. Rehman, G.C. Reilly, "Polyurethane-Hydroxyapatite composite scaffolds for *in vitro* bone tissue engineering," European Cells and Materials Vol. 26. Suppl. 7, 2013 (page 38)

Conference Presentations

Oral Presentations

- 22nd Congress of the European Society of Biomechanics, Lyon, France.

- European Society for Biomaterials Conference, Krakow, Poland.

- 21st Congress of the European Society of Biomechanics, Prague, Czech Republic.

- 14th Annual Conference of the UK Society for Biomaterials, Belfast, Northern Ireland.

- Medical Engineering Centre's Annual Meeting and Bioengineering 14, London, UK.

- 2013 Tissue and Cell Engineering Society Conference, Cardiff, UK

Poster Presentations

- 10th World Biomaterials Congress, Montreal, Canada.

- Orthopedic Research Society Conference, Las Vegas, USA.

- European Society for Biomaterials Conference, Liverpool, UK.

- 7th World Congress of Biomechanics, Boston, USA.

- 2014 Tissue and Cell Engineering Society Conference, Newcastle, UK

- 10th Bose User Group Meeting

- 2nd Year Postgraduate Research Day

- 2014 Bone Research Society Conference, Sheffield, UK.

- ICMOBT 2013, Stiges, Spain.

- 7th MSC Meeting, 2013, Birmingham, UK.

This page was intentionally left blank.

Dedication

to Akwesi & Kwame....

I could not have done this without you two!

This page was intentionally left blank.

Acknowledgements

This page was intentionally left blank.

Thesis Summary

While small bone defects heal spontaneously, critical size defects may exceed the body's regenerative capabilities, and require the use of bone substitutes and implants. To date, *in vitro* and *in vivo* testing of implants remains the gold standard for rigorous mechanical stability and biological safety checks. Current 2D *in vitro* testing is limited by a lack of dynamic environment and an inability to investigate mechanical strength of the attachment between the bone-matrix and implant surface. 3D *in vivo* tests are also limited by differences in the behaviour and structure of human and animal cells, high costs and difficulty of replicating human ageing effects. The aim of this thesis is to develop biocompatible and osteoconductive polyurethane-based scaffolds with optimal mechanical and biological properties that can be used as 3D *in vitro* bone models for bone regeneration and implant testing.

17 Plain-PU and PU-HA scaffolds were fabricated from three different medical grade polyether-urethanes, namely, Z1A1, Z3A1 and Z9A1. The polymer's ability to dissolve in graded concentrations of DMF/THF solvents was assessed as part of this study. Composite scaffolds containing nano or micro HA particles were fabricated in a ratio of 3 PU: 1 HA by doping PU solutions with HA particles. Electrospinning, freeze drying, freeze extraction and particulate leaching were the main fabrication techniques explored for creating scaffolds. Electrospun scaffolds with non-aligned fibres were spun at 300 rpm whilst those with aligned fibres were spun at 1300 rpm. Particulate leaching using NaCl particles optimized 3 novel fabrication protocols namely, the layer-by-layer, homogenized or physical-mixing techniques for creating highly porous PU-based constructs.

Investigation of non-aligned electrospun scaffolds showed that the choice of solvents, on their own or in combination, strongly influences the final properties of solution, hence the fibre morphology of scaffolds. Reducing the amount of DMF contained in the solution, increased fibre diameter, eliminated beads in fibres and led to scaffolds with a more uniform morphology. Moreover, reducing the DMF solvent content led to lower tensile properties of electrospun scaffolds, whilst incorporation of nano and micro HA particles reinforced the mechanical properties of both aligned and non-aligned electrospun composites. RAMAN and FTIR spectroscopy confirmed the presence of HA in all composites. Xylenol orange staining showed that composite mHA scaffolds supported a higher percentage of mineral area coverage compared to plain-PU scaffolds.

SHG imaging identified that collagen deposition appeared to be guided by the alignment of the scaffold fibres in the matrix deposited near to the fibres, but changed orientation with an increase in distance from the originally deposited layers.

Layer-by-Layer particulate leached scaffolds made from all the three types of PU had a highly porous 3D structure. 3:1 PU:nano-HA composites had the highest Young's Modulus and yield strength in the Layer-by-Layer group and there was no significant difference between the mechanical properties of 3:1 micro-HA composites and 2:1 micro-HA composites. A novel physical mixing fabrication protocol shortened fabrication time by about 90% and was used to mass produce particulate leached scaffolds in a shorter period of time. Physically mixed particulate leached scaffolds had an interesting and contrasting mechanical profile compared to previously fabricated scaffolds. Physically mixed PU scaffolds without HA had the highest mechanical properties in this group and the inclusion of neither nano, micro nor combined micro and nano-HA particles enhanced their mechanical properties. Similar to the Layer-by-Layer particulate leached scaffolds, the inclusion of HA particles in physically mixed PU-only scaffolds did not support a higher cell viability. Osteoid bone formation was present in only nHA composites by D7 of the *in vivo* studies, but present in all scaffolds after D45. Collagenous matrix deposition increased over the 56 day period in all scaffold types, however, this increase was more pronounced in PU-only scaffolds. Finally, mimicking push-out and pull-out tests by inserting titanium screws into particulate leached scaffolds, showed that inserting the screws during cell seeding is a better method than inserting them after a D28 culture period. PU-based scaffolds that serve as a novel biomimetic *in vitro* 3D bone model for testing of small orthopaedic implants have been developed.

Table of Contents

This page was intentionally left blank.

List of Figures

List of Tables

Abbreviations

α	Alpha
β	Beta
βGP	Beta-Glycerolphosphate
μg	Microgram
μl	Microliter
μM	Micromolar
μm^2	Square Micrometre
%	Percentage
%BV	Percentage Bone Volume
2D	Two Dimensional
3D	Three Dimensional
AA_2P	Ascorbic Acid-2-Phosphate
AR	Alizarin Red S
ANOVA	Analysis of Variance
ATR-FTIR	Attenuated Total Reflectance Sampling FTIR
BMP-2	Bone Morphogenic Protein-2

BSA   Bovine Serum Albumin

Ca^2+ Calcium

Ca/P   Ratio of Calcium Phosphate

CD   Cluster of Differentiation

cHA   Combined mHA & nHA in the ratio of 0.5:0.5

CLSM   Confocal Laser Scanning Microscopy

cm   Centimetre

cm^2 Square Centimetre

cm^3 Cubed Centimetre

CO_2 Carbon Dioxide

CTan   CT Analyse Software

CTvol   CT Volume Software

DAPI   4',6 Diamidino-2-Phenylindole

Dex   Dexamethasone

dH_2O Deionised Water

DMF   Dimethylformamide

DMEM   Dulbecco's Modified Eagle's Medium

DMSO   Dimethyl Sulfoxide

DNA   Deoxyribonucleic Acid

ECM	Extracellular Matrix
EDTA	Ethylene Diamine Tetraacetic Acid
F	Fungizone
FCS	Foetal Calf Serum
FITC	Fluorescein Isothiocyanate
FTIR	Fourier Transform Infra-red Spectroscopy
g	Gram
GSI	Grey Scale Index
h	Hour
Hz	Hertz
HA	Hydroxyapatite
hBMSCs	Human Mesenchymal Stem Cells Derived from Bone Marrow
HCL	Hydrochloric Acid
HDFs	Human Dermal Fibroblasts
hESMPs	Human Embryonic Stem Cell Mesenchymal Progenitor Cells
HMDS	Hexamethyldisilazane
H-PL	Homogenized Particulate Leached Scaffolds
l	Litre
LbL-PL	Layer by Layer Particulate Leached Scaffolds
M	Molar

MEM	Minimum Essential Medium
mg	Milligram
MG-63	Human Osteosarcoma Cells
mHA	Micro-Hydroxyapatite Particle
Micro-CT	Micro Computed Tomography
min	Minute
ml	Millilitre
MLO-A5	Murine Lone Bone Osteocyte - A5
mm	Millimetre
mM	Millimolar
MPa	Megapascal
MSCs	Mesenchymal Stem Cells
MTT	(3-(4,5-Dimethylthiazol-2-yl)-2,5-diphenyltetrazolium bromide)
n	Number
NaOH	Sodium Hydroxide
nHA	Nano-Hydroxyapatite Particle
nm	Nanometre
nM	Nanomolar
nmol	Nanomole

NO	Nitrogen Oxide
O_2	Oxygen
OCN	Osteocalcin
OD	Optical Density
P/S	Penicillin/Streptomycin
Pa	Pascal
PAS-FTIR	PhotoAcoustic Sampling Fourier Transform Infrared Spectroscopy
PBS	Phosphate-Buffer Saline
PCL	PolyCaproLactone
pH	Potential of Hydrogen
PL	Particulate Leaching or Particulate Leached Scaffolds
PM-PL	Physically Mixed Particulate Leached Scaffolds
PU, PU-only & Plain-PU	Polyurethane Polymer or Scaffold
PU:cHA	PU: mHA: nHA in the ratio of 3:0.5:0.5
ROI	Region of Interest
RUNX-2	Runt-related Transcription Factor 2
SD	Standard Deviation
SE	Standard Error of the Mean
SEM	Scanning Electron Microscope
SHG	Second Harmonic Generation

SHGM	Second Harmonic Generation Microscopy
SM Medium	Supplemented Medium consists of AA, β-GP in the basic culture
SM+Dex	Supplemented Medium with 100nM of Dex
SR	Sirius Red
t	Time
TE	Tissue Engineering
Tecoflex	Polyurethane Elastomer
TGF-β1	Transforming Growth Factor Beta-1
THF	Tetrahydrofuran
TRITC	Tetramethyl Rhodamine Isothiocyanate
v/v%	Percentage by Volume
wt%	Percentage by Weight
XO	Xylenol Orange
XPS	X-ray Photoelectron Spectroscopy
XRD	X-ray Diffraction
Z1	Z1A1 Polyurethane Pellets from Biomer, UK
Z3	Z3A1 Polyurethane Pellets from Biomer, UK
Z9	Z9A1 Polyurethane Pellets from Biomer, UK
Z**n**A1 PU	Z(**n**=1/3/9) Polyurethane Pellets from Biomer, UK

Nomenclature

Name	PU wt%	mHA wt%	nHA wt%	Ratio of DMF(v%)	Ratio of THF(v%)
Electrospun scaffolds used for biological characterization					
Z9 & Z3 Solvent Group					
Z9-100	27	0	0	100	0
Z9-70	27	0	0	70	30
Z9-50	27	0	0	50	50
Z3-100	15	0	0	100	0
Z3-70	15	0	0	70	30
Z3-50	15	0	0	50	50
Z9 & Z3 Random Composite Grp					
Z9-PU	25	0	0	70	30
Z9-mHA	25	5	0	70	30
Z9-nHA	25	0	5	70	30
Z3-PU	15	0	0	70	30
Z3-mHA	15	5	0	70	30
Z3-nHA	15	0	5	70	30
Z3 Aligned Composite Group					
A_Z3-PU	15	0	0	70	30
A_Z3-mHA	15	5	0	70	30
A_Z3-nHA	15	0	5	70	30
Particulate leached scaffolds used for biological characterization					
Z3 Layer-by-Layer PL Group					
LbL-Plain PU	15	0	0	70	30
LbL-PU+mHA(3:1)	15	5	0	70	30
LbL-PU+mHA(2:1)	15	7.5	0	70	30
LbL-PU+nHA(3:1)	15	0	5	70	30
Z3 Homogenized PL Group					
H-PU+mHA(3:1)	15	5	0	70	30
H-PU+nHA(3:1)	15	0	5	70	30
H-PU+cHA(3:0.5:0.5)	15	2.5	2.5	70	30
Z3 Physically Mixed PL Group					
PM-Plain PU	15	0	0	70	30
PM-PU+mHA(3:1)	15	5	0	70	30
PM-PU+nHA(3:1)	15	0	5	70	30
PM-PU+cHA(3:0.5:0.5)	15	2.5	2.5	70	30

This page was intentionally left blank.

Chapter 1

INTRODUCTION

Musculoskeletal defects affect millions of people worldwide, resulting in pain and loss of personal and economic independence. In 2010, musculoskeletal disorders were reported by The Health and Safety Executive as the most common type of work related illness (Health and Safety, 2011) and as the second greatest cause of disability worldwide by a comprehensive study in 2012 (Vos et al., 2012).

Although bone has an ability to heal with practically no scarring, large bone defects could disrupt the repair and healing process and lead to delayed union, malunions or a non-union (Petite et al., 2000). While small bone defects heal spontaneously, critical size defects resulting from trauma, congenital birth defects, age-related osteopathologies, sport injuries, cancer and tumour resection may exceed the body's regenerative capabilities. Such defects usually require surgical intervention involving the use of bone-graft substitutes and implants, in isolation or combination to restore or replace the damaged bone.

Additionally, one of the most common causes of pain and disability in middle-aged and older people is the degeneration of the articular cartilage. This is often associated with a clinical syndrome of osteoarthritis and require the use of joint replacement implants. The strong correlation between increasing age and the prevalence of osteoarthritis, and recent evidence of important age-related changes in the function of chondrocytes, suggest that age-related changes in articular cartilage can contribute to the development and

progression of osteoarthritis (Buckwalter and Mankin, 1997).

Artificial implants and bone-graft substitutes ranging from autografts, allografts, xenografts and tissue engineered remedies provide an excellent solution to such defects with a reported 4 million operations involving bone substitutes performed around the world annually (Brydone et al., 2010). This figure is expected to increase with the ageing world population and increase in the number of implant surgeries that undergo revision, as the percentage of persons over the age of 50 years affected with bone diseases is reported to double by 2020 (BJD, 2013).

To date, autografts (tissue grafted from a donor site to host site of the same patient) is still considered the gold standard for replacing damaged bone as it provides the three core elements of osteoinduction, osteoconduction and osteogenesis, needed for bone growth. It is however limited by availability and donor site morbidity associated with bone harvesting, which could lead to chronic pain, nerve injury, cosmetic defects, infections and possible fractures. The use of allografts (transplanted tissue from another human donor/cadaver) and xenografts (tissue transplanted from other species/animals) addresses issues of availability, but is also challenged with infectious disease transmission, undesirable immune rejection response and reduced mechanical and osteogenic properties associated with the sterilization, storage and processing techniques of the donor bone.

From the above mentioned limitations associated with the use of autografts, allografts and xenografts, there is subsequently a major clinical need for artificial bone substitutes in the fields of orthopaedic, spinal, dental, cranial, and maxillofacial surgery. This is associated with a heightened demand for advancement into tissue engineered regenerative alternatives, bone substitutes, bone implant design as well as improvements in surgical techniques associated with the treatment of bone pathologies.

1.1 Tissue Engineering

With the loss or failure of an organ or tissue being one of the most frequent, devastating, and costly problems in human health care, tissue engineering presents a practical solution

by applying the principles of biology and engineering to the development of functional substitutes for damaged tissue (Langer and Vacanti, 1993). Additionally, bone tissue engineering aims at improving musculoskeletal health and augmenting the quality of human life by providing a living bone graft substitute to fill and aid in the repair of bone defects. An ideal bone graft substitute should be osteoconductive and preferably osteoinductive, biocompatible, show minimal fibrotic reaction upon implantation and support new bone formation.

1.2 Artificial Bone Substitutes

As at 2013, 59 bone graft substitutes marketed by 17 companies were commercially available for implantation in the United Kingdom (Kurien et al., 2013). Bone substitutes range from Demineralized Bone Matrix (DBM), Calcium phospates and Hydroxyapatite, Calcium sulphates, Polymer-based constructs, bioactive glasses and bioactive composites. Such substitutes can be implanted with or without pre-incorporated growth factors and/or pre-seeded with osteogenic cells. They are ideally osteoconductive and act as a temporary or permanent support during bone healing and ingrowth, with demineralized bone matrices in particular, presenting with some additional osteoinductivity.

DBM, produced through the decalcification of cortical bone is composed of collagen, non-collagenous proteins and glycoproteins. It has limited porosity and mechanical strength, and hence used as bone graft packaging in spinal and trauma surgery (Wang et al., 2007). Additionally, calcium phosphates cements consists of a combination of tricalcium phosphate, calcium carbonate and monocalcium phosphate. These present with high compressive strength but low tensile strength and brittle properties, and are usually degraded by osteoclastic activity within two years. Alternatively, osteoconductive calcium sulphate substitutes are usually resorbed within two or three months, hence not suitable for long-term structural support. Moreover, bone substitutes made from sintered HA resists degradation and can remain in bone for more than ten years (Bohner, 2001).

Futhermore, bioactive glass products composed of silicate, calcium and phosphorus,

can be both osteoinductive and osteoconductive (Pereira et al., 2005). By varying the proportions of silicon oxide, silicon dioxide and calcium oxide, different bioactive glass products, with varying solubility, can be manufactured. Upon implantation, a strong bond is created between bone and the bioactive glass without an intervening connective tissue interface, which gives it good apposition to bone. Alone, synthetic ceramics posse no osteogenic or osteoinductive properties, and demonstrate minimal immediate structural support. However, when attached to healthy bone, osteoid is produced directly onto the surfaces of the ceramic (Giannoudis et al., 2005).

Collagen and other polymer-based substitutes serve as an excellent carrier for growth and bone differentiation factors, although they provide minimal structural support as a bone graft substitute, hence limiting their clinical use. Such substitutes can however, be combined with other osteoconductive materials, such as hydroxyapatite or tricalcium phosphate, as well as osteoinductive bone marrow aspirate to create bioactive composites (Nandi et al., 2010). Composite substitutes range from stable to degradable, and most of those used in tissue engineering/regenerative medicine are biodegradable polymers reinforced with ceramic particles.

Bonfield first proposed the concept of polymer–ceramic combination materials in 1988, as an alternative for bone replacement. Mimicking the ductile and brittle properties of the collagen and mineral components of bone, respectively, it was later commercialised with the trade name, HAPEX^{TM} (Bonfield, 1988a,b). Mechanically, polymers such as polyurethane (PU) are noted for their extensive deformation and high toughness whilst ceramics, such as hydroxyapatites (HA), are noted for their high compressive strength but brittle failure (Tetteh et al., 2014).

Consequently, developing highly porous synthetic PU-HA composite bone-graft substitutes with biocompatible, osteoconductive, optimal mechanical properties and beneficial bioactivity, could enhance bone remodelling and growth, and ultimately provide a better alternative to autografts and allografts, as they could potentially eliminate donor-site morbidity and reduce immune response.

1.3   Bone Implants

Although successful advancements have been achieved in the development of bone substitutes and tissue engineered constructs, the reconstruction of extremely large bony defects created during trauma or revision surgery cannot be reconstructed using bone graft substitute alone, without additional structural support and hence, are major concern for orthopaedic surgeons.

Often whole joints fail due to weak bone (osteoporosis) or damaged cartilage (osteoarthritis); and as such, artificial joint replacement implants made of different materials are used in replacing the damaged joint. For example, in the USA alone there are an estimated, 280,000 hip fractures, 700,000 vertebral, and 250,000 wrist fractures each year at a cost of $10 billion indicating a strong need for artificial implants (Hollinger et al., 2000). Moreover, back pain requiring reconstructive surgery, is a crippling condition for individuals and society alike, and was reported as the second most common cause for sick leave in 2005–6 by The UK Health and Safety Executive (Health and Safety, 2006). Additionally, data from 1998 estimated that the direct cost of back pain to the UK is £1.6 billion with indirect costs at £10 million (Maniadakis and Gray, 2000). Surgical intervention combining the efforts of both bone graft substitutes and implants is an effective remedy for disabling back pain due to degenerative disease (Hsu and Wang, 2008).

Several artificial implant materials made from metals, ceramics, polymers and their composites have been utilised in the restoration of large bone defects. Three different conceptual generations of orthopaedic biomaterials made from bioinert materials, bioactive and biodegradable materials and tissue engineered constructs have been developed over the last 65 years (Navarro et al., 2008). However, bioinert metallic implants remain a popular biomaterial choice for artificial bone substitution as a result of the reproducibility, availability and reliability associated with its use.

Compiled statistics from the National Joint Registry (NJR) as shown in Figure 1.1

reveal that 168,794 hip and knee reconstructive surgeries involving the use of one or more implant material were performed for 2010. This shows an appreciable increase when compared to the 125,549 procedures carried out in 2005, with an equivalent increase in the number of revision surgeries from 9,037 to 14,170 respectively. Additionally, the total number of UK National Health Service (NHS), funded procedures also increased from 67% to 86% for hip procedures and from 72% to 89% for knee procedures for those years. Moreover, the year 2012 recorded the highest number of total hip and knee procedures at 184,917, which decreased to 171,499 in 2013 with a corresponding decrease in the number of revision surgeries from 17,151 to 15,502, respectively (NJR, 2014). Implant loosening, dislocation, implant failure and implant fracture were listed as some of the reasons for the 15,226 revision surgeries performed in 2011 as reported by the NJR (NJR, 2012).
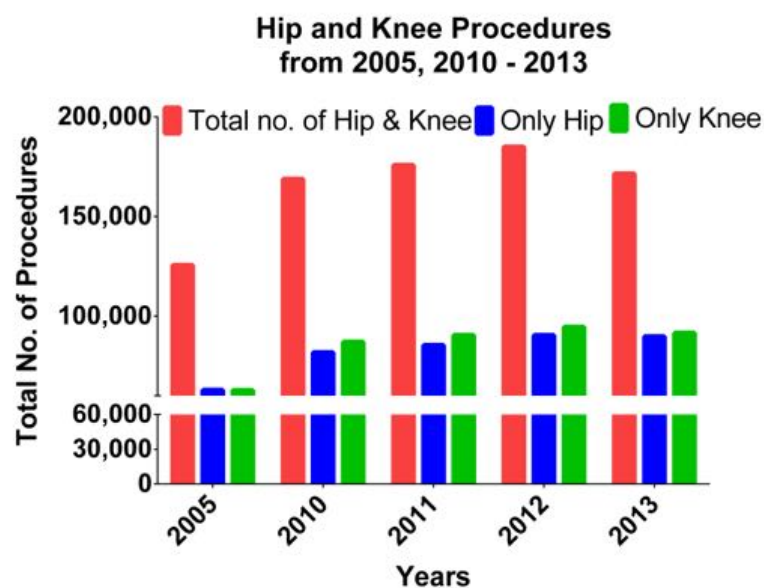
Figure 1.1: Total Number of Hip and Knee Procedures performed in the UK from 2005, 2010-2013, compiled from the 2014 National Joint Registry Annual Report

1.4 Implant Limitations

The production of wear debris leading to osteolysis, infection, initial poor bone on-growth onto the implants and the maintenance of a stable blood supply are major limitations of using metallic implants which prevents long-term improvements in the quality of life.

Implant loosening is also a major problem associated with the use of bioinert metallic implants. This results from the biomechanical mismatch of elastic moduli between the metallic implant and surrounding bone leading to poor osseointegration and ultimately, stress shielding. It is therefore predicted that understanding osseointegration between metallic implants and tissue engineered bone as part of implant testing, could enhance the development and design of cutting edge orthopaedic and dental implants with improved performance and survivability, and ultimately eliminate implant loosening.

1.5   Implant Testing

Similar to all other biomaterials, orthopaedic implants go through a series of rigorous physical, chemical, mechanical and biological testing mechanisms to ensure their quality and safety for human use. To date, *in vitro* and *in vivo* testing of implants remains the gold standard for rigorous biocompatibility, mechanical stability and biological safety checks of orthopaedic biomaterials. With a reported $16 billion yearly expenditure on animal testing in the United States (PETA, 2015) and an equivalent estimate for the United Kingdom, the exact cost of testing largely depends on factors such as the duration of the test, and the type and number of animals involved, which in turn depends on the type and size of the implant being tested. ISO 10993 lists a series of standards used to biologically evaluate medical devices; with ISO 10993-5 and ISO 10993-6 describing tests for *in vitro* cytotoxicity and *in vivo* implantation studies, respectively (F.D.A., 2013).

Current basic 2-dimensional *in vitro* testing of implant materials using cell culture is limited by a lack of dynamic environment and an inability to investigate the mechanical strength of the attachment between the bone matrix and implant surface. Alternatively, 3-dimensional *in vivo* tests to examine osseointegration consist of embedding sections of implant and control samples into holes, cut or drilled in animal's bone for a period of time. At the end of the study, the animal is sacrificed and the area of implantation is examined meticulously for local and systemic adverse effects, and possible osseointegration. The costly nature of these long term tests, the differences behaviour and structure in human

and animal cells as well as the difficulty of replicating the effects of human aging are key setbacks to this model. In addition, current EU legislation 2010/63/EU that took effect on 1st January, 2013, further restricts the use of animals for scientific testing by strictly enforcing the three R's of animal testing namely Reduction, Replacement and Refinement (European-Commission, 2013).

Animals such as rats, mice, rabbits and other rodents are regularly used to test new orthopaedic implants and also in regulatory and safety experiments used to certify medical devices. Statistics from the UK Home Office reveal that 82% of the total 4.12 million animals used for scientific procedures in 2013 were rodents, with mice accounting for 3.08 million of the total number. Mice were also utilized in 43,529 out of the 56,349 musculoskeletal procedures performed. Additionally, a further 940 and 470 mice were used in medical device safety and biocompatibility tests, respectively (Home-Office, 2014).

There is clearly a demand to validate new implant designs with *in vivo* experiments as current *in vitro* tests fail to provide a 3-Dimensional dynamic environment. Although there has been shown to be differences in the structure, genetic composition and cell behaviour between animals and humans, some animal experiments have made significant contribution to orthopaedic science (Pearce et al., 2007). Large animals such as dogs and sheep will still be needed to test large and complex implant designs like the total hip and knee replacement designs. Creating a dynamic tissue engineered *in vitro* bone model could be greatly beneficial in addressing the aforementioned limitations, associated with the current *in vitro* and *in vivo* implant testing.

Such a construct could be used for biocompatibility tests of small orthopaedic implant devices e.g. screws, pins and plates. It could also be used to investigate different implant surface modifications, experiment physical phenomena such as bioactivity and corrosion, gain appreciable insight into osseointegration and understand how bone grows around orthopaedic implants. This would provide *in vitro* 3D data and eventually reduce the number of *in vivo* experiments carried out to investigate scientific hypotheses like osseointegration, push out and pull out tests amongst others, and in turn contribute to

reducing the total number of animals used for scientific procedures.

1.6 *In vitro* Bone Model

Advances in tissue engineering have aided the development of several *in vitro* models for skin (Harrison et al., 2006), kidney (Subramanian et al., 2010), lung (Mondrinos et al., 2007), nerve (Gingras et al., 2003), cartilage (Risbud and Sittinger, 2002; Martin et al., 2007) and cornea (Suuronen et al., 2004) tissues. Such advances, particularly in skin regeneration, have improved the wound healing process, provided a deeper understanding of skin disorders and led to the engineering of skin models such as Epiderm and Episkin. These animal testing alternative skin models have been instrumental in testing cosmetic pharmaceutical and chemical compounds in the many thousands of human skin products (MacNeil, 2007).

Although substantial progress has been made in the development of *in vitro* bone tissue engineering constructs for regenerative purposes (Shea et al., 2000; Petite et al., 2000; Meinel et al., 2004), limited progress has been achieved in developing an ideal 3-D bone model to understand disease progression associated with bone pathologies such as osteoporosis, infection control, and osseointegration with extensive understanding of the bone-implant interface, and finally, as an animal alternative *in vitro* model for implant testing.

1.7 Aim and Objectives

The overall aim of the PhD was devised from the aforementioned limitations associated with the use of artificial bone substitutes, bone implants and challenges associated with current *in vitro* and *in vivo* implant testing. The aim was to develop a highly porous, mechanically durable and biocompatible tissue engineered bone, that could have clinical applications and serve as a biomimetic construct for implant testing.

The final hypothesis of this thesis is that tissue engineered bone grown in a 3-D

composite scaffold can be used as an *in vitro* test system to examine bone matrix growth around orthopaedic implant materials.

Short term objectives included:

1. Optimize various scaffold fabrication techniques and develop protocols for manufacturing PU and PU-HA composite scaffolds

2. Undertake in-depth analysis into the effect of micro and nano-sized HA particles on scaffold fabrication and bone regeneration

3. Optimize cell culture conditions for human mesenchymal progenitor hESMP's and matured animal osteoblastic MLO-A5 cells to produce a bone-like matrix

4. Characterize the deposited bone-like matrix

5. Investigate osseointegration between the developed bone-like matrix and small orthopaedic metallic screws

1.8   Thesis Outline & Chapter Summary

The first chapter of this thesis gives a general overview and background of the project, whilst the second chapter focusses on a coherent review of current and relevant literature pertaining to the entire project. A detailed description of the various materials and methods used in attaining the results presented in the subsequent chapters is in Chapter 3.

Chapter 4 is the first results chapter and focusses on identifying polyurethane solutions with ideal concentrations and solvent properties that can successfully be electrospun at room temperature to attain consistent non-aligned/random fibre mats without beads and irregularities. It was also to examine the effect of incorporating HA particles into these random scaffolds. The hypothesis was that HA would reinforce the mechanical properties of polymers and improve the bioactive properties compared to polymer-only scaffolds. The overall aim of Chapter 4 was to create a range of non-aligned scaffolds, with appropriate tensile mechanical properties that support bone cell and matrix growth.

The primary goal of Chapter 5 was to develop polyurethane-based scaffolds with aligned fibres that promote osteoid matrix production and guide collagen deposition. PU solutions that had already been optimized for electrospinning random fibrous mats were used for this study. The hypothesis was that increasing the speed of the rotating drum would create scaffolds with aligned fibres that have better mechanical properties which resemble the tensile properties of the collagenous fibres in bone. The overall aim of Chapter 5 was to determine whether the fibrous structure would guide MLO-A5 cell migration and subsequent orientation of deposited matrix. Second Harmonic Generation Imaging was used to investigate how the orientation and directionality of collagen changed with increasing depth.

The overall aim of Chapter 6, which is the final results and discussion chapter of this thesis, was to develop and test a 3D *in vitro* bone model for implant testing. Firstly, it was to explore a series of 3D fabrication techniques, and identify the best technique for creating thick scaffolds with uniform pores and consistent pore interconnectivity. It was also to fully characterize the fabricated scaffolds *in vitro* and assess their suitability for use in developing the *in vitro* model by undertaking in-depth physical, mechanical and biological characterisation.

The final chapter of this thesis (Chapter 7), summarises the key findings of this PhD project, and discusses possible follow up experiments that evolved from this project but could not be undertaken due to time constraints and circumstances beyond my control. These experiments can serve as PhD topics as well as final year undergraduate and MSc student projects.

This page was intentionally left blank.

Chapter 2

LITERATURE REVIEW

2.1 Introduction

In my bid to understand how bone grows around biomaterials, a detailed and coherent review of current and relevant literature pertaining to the entire project, has been compiled in this chapter. This review encompasses the anatomy and physiology of bone, generations of bone substitutes and implant materials. Scaffolding materials used in bone tissue engineering and composite design, tissue culture and mechanical conditioning as well as quantification methods used to analyse formed bone tissue are also discussed. Finally, experimental procedures similar to tests carried out for *in vitro* and *in vivo* testing of bone implants are also reviewed in this chapter.

2.2 Overview of Bone

Bone is a composite material made up of cells, mineral, bone matrix, and water (Boskey, 2005). It is a vital, dynamic and hard connective tissue with an ability to repair and regenerate. Bone functions to provide mechanical integrity for locomotion and serves as a primary site for haemopoiesis. Additionally, the interconnection of bone to form the skeleton serves as structural framework for the body and provides protection to vital organs (Boskey, 2001). Bone also serves as a mineral reservoir and is responsible for homeostasis of calcium and phosphate in the body (Ralston, 2009).

2.2.1   Anatomy of Bone

The two main structural types of bone found in human skeleton are cortical and trabecular bone. These are further classified according to shape into long, round, irregular and flat bones (Moore and Dalley, 1999) and located in either the axial (e.g. Pelvis, Vertebrae, skull) or appendicular (e.g. Femur, Humerus, Tibia) parts of the skeleton. Both cortical and trabecular bones are anatomically organized from woven and lamellar bone tissue. Woven bone is classified as immature bone and mostly found in embryos and certain metaphyseal regions of the growing skeleton. As compared to lamellar bone, woven bone has a more cells per unit volume, an uneven orientation of the collagen fibres, and randomly arranged mineral content and cells. Remodelling of woven bone creates lamellar bone. This begins at one month after birth, and by the age of four most of the bone in the body will have become lamellar. The regular arrangement of collagen fibres in lamellar bone makes it highly organized and anisotropic as compared to the isotropic nature of woven bone (Feldman et al., 2007).

2.2.1.1   Cortical Bone

Cortical bone also known as compact bone represents about 80% of skeletal bone mass Ralston (2009). It is mainly found in the shafts of long bones and is formed from haversian systems, which consist of concentric lamellar of bone tissue, surrounding a central canal of blood vessels. Cortical bone is dense in structure with an average porosity of about 5-30% and has a low surface area that forms an envelope around the marrow cavity. With a stiffness range of about 4-27 GPa, cortical bone is able to withstand higher stresses (amount of load) compared to trabeculae bone (Carter and Spengler, 1978).

2.2.1.2   Trabecular bone

Trabecular bone also known as spongy or cancellous bone is mostly found in flat bones and the ends of long bones and vertebrae. Having a higher surface area and an average porosity of about 30-90% of volume, spongy bone has a lower density than cortical bone. Trabecular bone is rapidly remodelled and made up of an interconnected meshwork of

bony trabeculae, separated with bone marrow filled spaces. In addition, trabecular bone has a stiffness of about 0.1-3 GPa and is able to withstand higher strain (amount of deformation) levels as opposed to cortical bone (Ralston, 2009).

2.2.2 Composition of Bone

Both cortical and trabecular bone consist of bone matrix made by bone cells. This matrix is further classified into two main components, a protein rich organic matrix and mineral rich inorganic constituent.

2.2.2.1 Organic Matrix

The organic component of bone is noted to be predominantly collagen Type 1, which has been found to account for about 30% of bone dry weight (Hollinger, 2005). As shown in Figure 2.1 on page 16, collagen Type 1 is a fibrillar heteropolymer protein composed of two identical collagen α-1 peptide chain and one distinct α-2 chain, wound together to form a triple helix structure. It has a primary structure of $(Gly-X-Y)_n$, where X and Y are frequently proline and hydroxyproline, with possible post translation modification to contain hydroxyproline, hydroxylysine and glycoslyated hydroxylysine (Burgeson and Nimni, 1992; Ralston, 2009). Individual collagen molecules are linked together by specialized covalent bonds called pyridinium cross-links to form a self assembly of staggered configuration of collagen fibrils, known to provide tensile strength to bone and a framework for mineral deposition (Knott and Bailey, 1998).

Bone matrix also contains varying amounts of other types of collagen such as Collagen Type III and V, and non-collagenous proteins, namely osteopontin, osteocalcin, proteoglycans, bone sialoprotein and other phosphoproteins and proteolipids (Bonucci, 2000). Most of these bone matrix proteins contain arginine-glycine-aspartic acid (RGD) sequences, characteristics of cell binding proteins which are recognized by a group of cell membrane proteins known as integrins. These function to aid in the attachment of bone cells to extracellular matrix, calcium and mineral-binding, and the regulation of cellular activity during bone remodelling. Anchorage of cells to extracellular matrix

2.2. OVERVIEW OF BONE
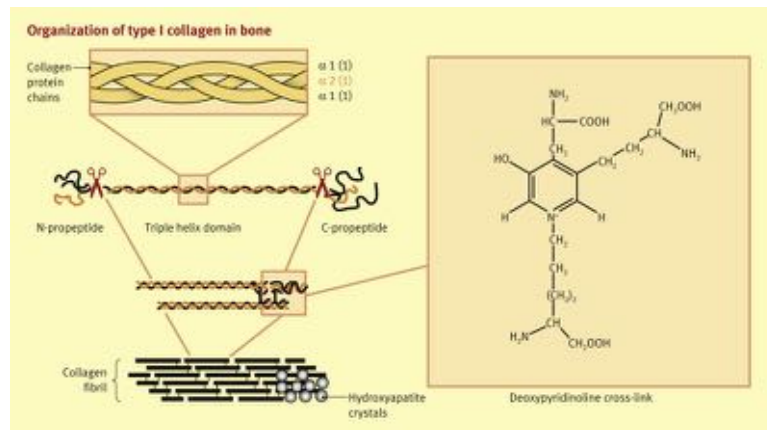
Figure 2.1: Organisation of Collagen Type 1 - Reprinted from (Ralston, 2009) with kind permission from Elsevier

enables cells to express their phenotype and conduct activities that characterize their functions (Ruoslahti, 1991).

Growth factors and cytokines such as transforming growth factor beta (TGF-β), insulin-like growth factor (IGF), osteoprotegerin (OPG), interlukins, tumour necrosis factors (TNFs) and bone morphogenetic proteins (BMPs 2-10) are also present in very small quantities in bone matrix. These proteins function in regulating bone differentiation, activation, growth and overall turnover, with a likely function of serving as a coupling factor for the processes of bone remodelling (Feldman et al., 2007).

2.2.2.2 Bone Mineral

Bone mineralization entails the deposition of bone mineral, mainly in a form of carbonated hydroxyapatite crystals, $[Ca_{10}(PO_4)_6(OH_2)]$ on collagen fibres shown in Figure 2.2 on page 17, to reinforce bone matrix and provide structural integrity (Bonfield, 1971; Rehman and Bonfield, 1997). By weight, approximately 70% of bone tissue is mineral, with an estimated 95% of the mineral phase composed of a crystalline hydroxyapatite and impurities account for the remaining 5% (Feldman et al., 2007). Bone mineralization comprises of complex processes involving physiochemical activities, cells, and extracellular organic matrix. Mineralization complements the tensile strength and elasticity derived from collagen by conferring mechanical rigidity to bone.
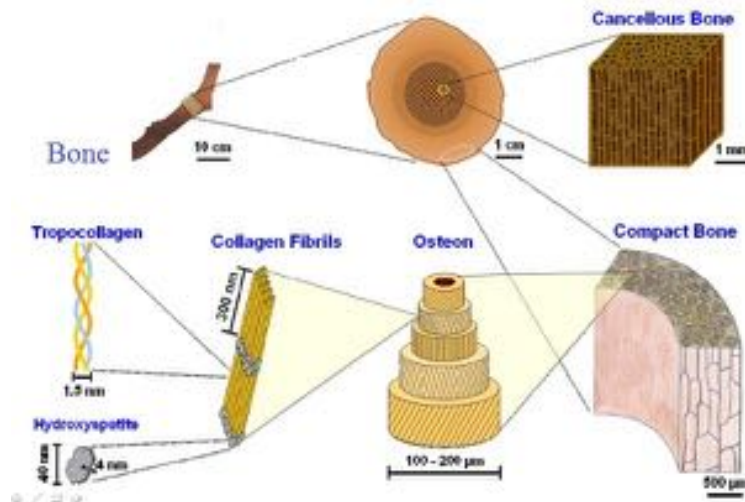
Figure 2.2: Organisation of Bone - Reprinted from (Chen et al., 2009) with kind permission from Elsevier

2.2.3 Bone Formation

Intramembraneous ossifications and endochondral ossification are the two main processes by which bone formation occurs. Depending on the type of bone being formed, one of these processes occurs, with variations occurring in the differentiation stages of bone for each type of bone (Holtrop, 1967). Bone formation succeeds bone resorption from childhood; it begins with the attraction of osteoblast precursors to the site that previously underwent resorption. These osteoblastic precursors derived from mesenchymal progenitor cells in the bone marrow stroma differentiate into mature osteoblasts which are able to bind to several osteoblast specific proteins such as osteocalcin, alkaline phosphatase, and collagen type 1. Bone formation is also thought to be enhanced by the action of bone morphogenic proteins which are known to encourage the proliferation and differentiation of osteoblastic progenitors into mature osteoblasts (Ralston, 2009).

2.2.3.1 Intramembraneous Ossification

Intramembraneous ossification involves the differentiation of primitive mesenchymal fibroblasts into bone cells, leading to the formation of flat bones such as the mandible and the maxilla.

2.2.3.2 Endochondral Ossification

Longer bones of the limbs, ribs and vertebrae are formed by endochondral ossification, which begins within cartilaginous modelling. This type of bone formation involves the replacement of cartilage with bone, and results from an invasion of osteoprogenitor cells contained in vascular tissue.

2.2.4 Bone Remodelling

Bone is metabolically active throughout life. After bone skeletal growth is complete, remodelling of both cortical and trabecular bone continues throughout one's life and requires the co-ordinated actions of osteoclasts and osteoblasts (Compston and of London, 1996). Bone remodelling as shown in Figure 2.3 on page 19, involves the repair and renewal of complex and dynamic bone tissue. Bone remodelling involves three kinds of cell behavioural activities. An initial stimulus causes the activation of mesenchymal cells to begin producing batches of new osteoclasts (from hematopoietic) and osteoblasts daughter cells. A batch of the osteoclasts resorb the existing bone and disappear afterwards. New osteoblasts then appear to form new bone, replacing what had been previously removed. Finally, this new bone remains in situ as "mature" bone for a period of time depending on the remodelling rate (Frost, 1966). Remodelling is a balanced response of mineral resorption of osteoclasts and bone deposition by osteoblasts and is consistent with mechanical and molecular influences governed by metabolic factors (Lee and Taylor, 1999; Burr and Martin, 2005). Most bone pathologies are said to result from abnormalities in bone remodelling which compromise the architecture, structure and mechanical strength of bone. This leads to clinical symptoms such as pain, fracture, deformity and abnormalities of calcium and phosphate homeostasis. It has been estimated that approximately 10% of the adult skeleton is being remodelled at any one time (Ralston, 2009).

It is postulated that bone possesses mechano-sensor cells in the form of osteocytes which detect changes in mechanical stimulus by comparing current mechanical strain

to physiologically desirable values, and engaging the action of corrective biological processes upon variation. Extensive work carried out on simulations of bone adaptation to mechanical stimulus, assumes that remodelling to remove bone occurs when the mechanical stimulus is low, whilst bone formation occurs to add bone when the mechanical stimulus is high (Doll and Koch, 2004; Hollinger, 2005).
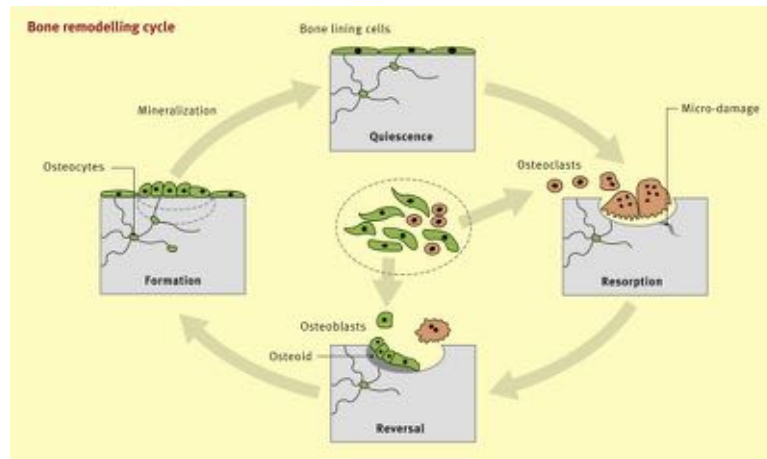
Figure 2.3: Bone Remodelling Cycle - Reprinted from (Ralston, 2009) with kind permission from Elsevier

2.2.5 Mechanical Properties of Bone

As bone functions to provide mechanical integrity for locomotion and structural rigidity to the body, the mechanical properties of bone is of great importance. Bone is an elastic, anisotropic, heterogeneous and composite material, hence the determinants of the mechanical properties of bone largely depend on density, porosity, macroscopic to sub nanoscopic architecture of bone structure, the orientation of testing, magnitude to load, the physical shape and state of the sample, amongst others (An and Draughn, 2000; Rho et al., 1998). The mechanical properties of natural bone change with their biological location since the crystallinity, porosity and composition of bone adjust to the biological and biomechanical environment.

The high tensile strength and fracture toughness of bone is attributed to the tough and flexible collagen fibres reinforced with hydroxyapatite crystals (Rezwan et al., 2006).

However, the magnitude of strength of cortical bone depends mostly on the type of mechanical testing and bone density whilst that of trabeculae bone depends greatly on shape and density in estimating mechanical properties. Table 2.1 outlines some data sets ranges (Means±SD), all at the tissue level, of various mechanical tests for human and bovine femur and tibia compiled by An and Draughn (An and Draughn, 2000).

Table 2.1: Mechanical Properties of Cortical Bone - Reprinted from (An and Draughn, 2000) with kind permission from CRC PRESS LLC

| Mechanical Test | Compact Bone | |
	Strength (MPa)	Stiffness (GPa)
Compression	133-295 (200±36)	14.7-34.3 (23±4.8)
Tension	66-188 (141±28)	7.1-30.4 (19.6±6.2)
Torsion	53-76 (65±9)	3.1-3.7 (3.3±0.1)

Although some work has been reported in the literature on the mechanical properties of cancellous bone, very little data is present on the different mechanical testing methods because of the difficulties associated with cutting samples. However, cancellous bone is generally known to have strength and stiffness values of 1.5-38 MPa and 0.1-3 GPa in compression, respectively. In addition, the work of Kaplan et al. established a relation that depicts that the strength of trabecular bone in tension is about 60% its strength in compression (Kaplan et al., 1985). Keaveny et al. also established that the elastic modulus of cancellous bone in tension is about 70% of its value in compression (Keaveny et al., 1994).

2.2.6 Pathologies of Bone

Although coupled, the cellular link between bone formation and bone resorption is not entirely understood, it is known that consequences of accentuating either component of bone remodelling, leads to bone diseases such as osteoporosis, osteoarthritis (Feldman et al., 2007) and Paget's disease. These pathologies and other causes of frequent bone loss including tumour resection, high energy trauma, infection and congenital defects like cleft palate, necessitate orthopaedic treatments (Gogolewski, 2001).

2.2.6.1   Osteoarthritis

Osteoarthritis is a pathology of the joint which leads to degeneration of bone and cartilage (Gelber et al., 2000). Accounting for about a million yearly hospital visits, osteoarthritis is considered the most common type of arthritis in the United Kingdom, with joints in the hip, knee and spine being the most affected (NHS, 2012). Key risk factors of osteoarthritis include obesity, female sex, age, history of joint injury, joint geometry, force distribution across a joint, exposure to heavy mechanical loads and certain sporting activities (Croft et al., 1992; Vingård et al., 1993).

Knee and hip anatomical abnormalities including acetabular dysplasia, femoroacetabular impingement, wide femoral neck, and changes to the global shape of hip and tibiofemoral joint account for architectural changes predating the radiographic appearance of osteoarthritis (Arokoski et al., 2002; Bredbenner et al., 2010; Ganz et al., 2003; Gregory et al., 2007; Harris, 1986). Variation in bone metabolism and distribution of biomechanical forces that result in changes to bone across a joint are considered the two main hypotheses of how bony changes may lead to cartilage joint deterioration. Additionally, pain associated with osteoarthritis is believed to stem from structural changes in the bony cortex and edema-related bone marrow lesions which are also highlighted to play a potential etiologic role in the development of knee osteoarthritis. Increasing evidence linked with radiographical studies, suggest that bone and cartilage pathology are linked to osteoarthritis (Baker-LePain and Lane, 2012; Radin and Rose, 1986).

2.2.6.2   Osteoporosis

Osteoporosis is an abnormality of bone which arises when the amount of bone resorbed with age exceeds the quantity of bone formed during skeletal growth and bone remodelling. This leads to a decrease in total bone density and micro-architectural deterioration of bone tissue, and results in porous and fragile bones with impaired skeletal strength and a consequent increased susceptibility to fractures (CDC, 1991).

2.2. OVERVIEW OF BONE

Such fractures mostly affect the femoral neck, vertebral bodies and wrist and result in pain, disability, premature death and a huge financial cost to health services. An annual expenditure of about £742 million was reported by the 1994 Advisory Group on osteoporosis (Compston and of London, 1996; Barlow, 1994).

The risk of osteoporosis increases with age and has been found to be more common in women than in men, with variation occurring amongst countries (Kanis et al., 1994). Those at the greatest risk for osteoporosis are white and Asian women, who are thin or petite and with a family history of the disease (CDC, 1991). Other risk factors associated with the pathogenesis of osteoporosis, include lack of sufficient calcium and vitamin D intake, age, genetic factors, heavy alcohol consumption, smoking and oestrogen deficiency associated with postmenopausal osteoporosis (Albright F, 1941; Laszlo, 2004).

The work of Kanis et al utilized the World Health Organization (WHO) criteria for diagnosing osteoporosis. This is based on a bone mineral density value higher than a 2.5 Standard Deviations below a young healthy adult mean value (Kanis et al., 1994). However, the work of Lewieski suggests a combined use of clinical risk factors for fracture and bone mineral density testing, as a better diagnostic tool for osteoporosis. Although, unlikely to fully restore the quality and strength of osteoporotic bone to normal, certain lifestyle changes involving physical activity and nutrition rich in calcium and Vitamin D can help. Pharmacological therapy using drugs and hormonal treatment involving Raloxifene, Biphosphonates and oestrogen can also be used to bind to calcium and moderate bone resorption (Lewiecki and Silverman, 2006).

2.2.6.3 Paget's Disease

Paget's disease is an abnormality of localized bone remodelling, which result in large size bones with diminished quality that are less compact and more vascular, as well as an irregular and weakened structure (Pfeifer and Pollahne, 2011). With variation occurring amongst patients around the world, the highest rate of Paget's disease is recorded in the United Kingdom (NHS, 2012). Statistics show that, Paget's disease is the second most common bone disease after osteoporosis in the United Kingdom, and is known to affect

8% of men and 5% of women by the age of 80 years (Wilkinson, 2012).

Although the exact cause of the disease is not known, it is often associated with genetic factors linked to inheritance, environmental factors including viral exposure and lifestyle factors such as malnutrition. Only a small fraction of patients (about 5%) suffering from Paget's disease show clinical symptoms. These symptoms usually include intense pain, a variety of neurologic complications, fracture, deformity and weakness in the localized regions of bones of the spine, skull, pelvis and femur (Scharla, 2011). Diagnosis of Paget's disease involves the use of alkaline phosphate activity blood tests, X-Ray examinations and an isotope bone scan to determine the extent and activity of the disease (Colina et al., 2008). To date, there is no known cure of the disease, however, treatment options include the use of bisphophonate and calcitonin drugs to lessen pain and normalise bone turn over, and surgery to correct deformities resulting from the disease (Seitz et al., 2008).

2.3   Orthopaedic Biomaterials

While small bone defects heal spontaneously, critical size defects resulting from osteopathologies such as Osteoporosis, Osteoarthritis and Paget's disease, as well as from trauma, congenital birth defects and tumour resection may exceed the body's regenerative capabilities. Such defects usually require surgical intervention involving the use of bone-graft substitutes and implants, in isolation or combination to restore or replace the damaged bone.

Orthopaedic biomaterials are designed to perform certain biological functions permanently or temporarily, by replacing or substituting diseased bone, cartilage, tendons and ligament tissues (Navarro et al., 2008). They are used in addressing osseous defects and bone loss resulting from bone damage. Approximately 2.2 million bone-graft procedures are performed each year worldwide to repair bone defects in orthopaedics, oral and maxillofacial surgery, with a yearly estimated costs of $2.5 billion (Kolk et al., 2012; Van Heest and Swiontkowski, 1999).

Bone repair materials include autografts, allograft, xenografts and a generational

evolution of synthetic orthopaedic implants. Others include alternative treatment modalities involving the use of gene therapy, bone marrow aspirates, and growth factors among others. Each of these grafts present its own merits and demerits. The ideal bone replacement is expected to be biocompatible, bioresorbable, osteoconductive, osteoinductive, structurally similar to bone, easy to use, sterilizable and cost-effective, with resorbable polymeric scaffolds considered as promising candidates for cancellous bone replacements in small non-load bearing defects (Gogolewski, 2001; Gunatillake et al., 2003).

2.3.1 Autografts

Bone grafting using autologous cancellous or cortical bone with varying amounts of osteogenic stem cells is a common surgical procedure and considered the gold standard in repairing bone defects. The procedure involves harvesting bone from one part of the body usually the iliac crest, for use in healing critical-size segmental long bone and maxillofacial skeleton defects of the same patient. This procedure raises minimal ethical and immunological concerns, but is however limited by availability, harvesting time, trauma associated with bone harvesting. Such turnover results in donor site morbidity, and could possibly lead to further complications including a tendency towards resorption and compromise in biomechanical properties of the bone (Banwart et al., 1995; Gorna and Gogolewski, 2003; Goulet et al., 1997; Hench, 1998). Other contraindications include elderly or paediatric patients and patients with malignant disease.

2.3.2 Allografts and Xenografts

The use of allografts in treating bone defects involves the transfer of bone tissue from another human donor mostly from a cadaver into a host patient. Xenotransplantation entails the use of chemically treated substitutes, xenografts, from non-human species in treating human bone defects (WHO, 2005). These procedures present a partial solution to the donor site morbidity limitation faced by the use of autografts and reduce surgical time. They are however challenged with concerns of disease transfer, immune rejection, yielding

variable clinical results and ethical and religious concerns amongst others (Bostrom and Mikos, 1997; Hench, 1998). Additionally, preservation and sterilization techniques have been shown to compromise the biomechanical and biological properties of these substitutes, presenting a further limitations to the use of allografts and xenografts for bone repair (Pelker et al., 1983).

2.3.3 Artificial Bone Substitutes

Over the last 60 years, the field of orthopaedics has observed an evolution of three different generations of synthetic biomaterials. These conceptual evolutions are clearly distinguishable by the properties and requirements of each generation; with first generation implants focussing on bioinert materials, second generation implants highlight bioactive and biodegradable properties, whilst third generation implants are designed to stimulate specific cellular responses (Navarro et al., 2008).

2.3.3.1 First Generation Implants

These were among the first set of metallic, ceramic, polymeric and composite implants to be used for orthopaedic applications. They were mostly based on the industrial applications of materials used in aerospace, mechanical and chemical industries. Biocompatible materials with properties such as minimum toxic response, nearly inert chemical properties, high corrosion resistance and desirable mechanical properties that attach by morphological fixation were utilised in treating orthopaedic defects. With the main aim to replace structure and possibly reduce immune response and foreign body rejection to the barest minimum (Hench, 1980).

Stress shielding, inability to remodel with time, generation of wear particles and the formation of fibrous capsules around implants are major limitations associated with the use of first generation implants. With an order of magnitude higher in stiffness than that of cortical bone ($\backsim$20 GPa), correction of orthopaedic defects with e.g. stainless steel implants, causes load sharing between implant and host bone, with an insignificant amount of the load borne by the bone. Since bone is a dynamic organ that is constantly

being remodelled, the reduction in mechanical stimuli presented by stress shielding induces bone resorption and ultimately leads to implant loosening and failure (Bonfield, 1988b; Huiskes et al., 1992).

Additionally, as no implant is completely inert, tissue response to a biologically inactive implant is the formation of a non-adherent fibrous capsule. The thickness of the fibrous layer depends on many factors, such as the conditions of the implant, the conditions of the host tissue, the conditions of motion and fit at the interface and the mechanical load applied. Furthermore, first generation implants attach by morphological fixation, hence their interface is not chemically or biologically bonded, and as such relative movement called micro-motion can occur. This movement could result in the generation of wear particles from the implant which could cause osteolysis and aseptic loosening of the implant, in addition to the progressive development of a non-adherent fibrous capsule (Cao and Hench, 1996).

2.3.3.1.1   First Generation Metals

Fracture plates, pins, dentures, screws and hip nails made from stainless steel, cobalt-chrome alloys, titanium metal and shape memory titanium alloys have been used as metallic implants since the 1940's. This was largely due to their relatively low cost, availability and low processing requirements, with the first successful total hip prosthesis reported by Charnley in the late 1950's (Charnley, 1960).

2.3.3.1.2   First Generation Ceramics

Other non-metallic first generational implants including Alumina and Zirconia ceramics, have also been used in varying combinations as femoral heads and acetabular cups, with the first successful femoral head alumina replacement in 1972 by Boutin (Boutin, 1972). These ceramics present with advantages of good biocompatibility, desirable mechanical properties, excellent wear rates and corrosion resistance.

2.3.3.1.3   First Generation Polymers

Examples of first generation polymeric materials include polyurethane, polypropylene,

polymethylmethacrylate (PMMA) and silicon rubber. PMMA has been utilised as space fillers and bone cement for centuries in the field of orthopaedics as it provides anchorage and excellent primary fixation to prosthesis. It also possess high impact strength, excellent toughness and low friction, ease of fabrication, biocompatibility and biostability (Navarro et al., 2008).

2.3.3.2   Second Generation Implants

Second generation implant materials came into focus after the concept of bioactive materials was discovered in 1969 (Hench et al., 1971). Bioactivity, a major characteristic of second generation implants refers to any interaction or effect that materials exert on cells, with the aim of guiding or activating them to specific responses and behaviours. It describes an implant's ability to interact with the biological environment, and to enhance biological response and tissue bonding with the ability of bioresorbable materials' to undergo progressive degradation while new tissue regenerates and heals (Navarro et al., 2008).

Osteoproductive bioactivity and osteoconductive bioactivity are the two main types of bioactivities, which result from the different rates and mechanisms of implant-tissue interactions (Cao and Hench, 1996). Periodontal implants, intervertebral spacers, artificial vertebrae, iliac spacers and alveolar ridge maintenance implants are some examples of clinically used second generation implants made from ceramics, metals, polymers and composites.

2.3.3.2.1   Second Generation Metals

Although second generation metallic implants are not naturally bioactive; surface coatings and chemical modification of the implant surface are two methods used to attain bioactive metal products. Plasma spraying is an example of surface coating, although this has been shown to result in long term weak substrate bonds and reduced interfacial strength (Herøet al., 1994; Klein et al., 1994). Chemical modification of the implant surface involves thermochemical treatments that aim at promoting the deposition of a bioactive

ceramic *in vivo* or the induction of proteins and cell adhesion and other tissue and material (Kokubo et al., 1996; Navarro et al., 2008).

2.3.3.2.2 Second Generation Ceramics

As defined by Hench, bioactivity is a time-dependent kinetic surface modification that occurs upon implantation; it's the ability of an implant surface to form a biologically active hydroxy carbonate apatite layer which provides the bonding interface with host tissues. Bioactive ceramics include bioactive glasses, bioactive glass-ceramics, bioactive calcium phosphate ceramics and bioactive composites and coatings. These have chemical and structural similarities with the bone mineral phase and as such bond to living tissues through bioactive fixation (Hench, 1991). The most common types of second generation ceramics whose chemical and physical properties are largely dependent on its synthesis process are particles of Hydroxyapatite (HA-$Ca_{10}(PO_4)_6OH_2$), β-Tricalcium Phosphate (β–TCP–$Ca_3(PO_4)_2$, their derivatives and combinations (El-Ghannam, 2005).

2.3.3.2.3 Second Generation Polymers

Biodegradable polymers of synthetic and natural origin such as collagen, chitosan, polyurethane, poly (α-hydroxy acids) such as polylactic acid (PLA), polyglycolic acid (PGA) and their copolymers; polycaprolactone (PCL), tyrosine-derived polycarbonates and polyhyrdoxybutarate to list but a few, have been used in bone repair applications for more than thirty years. They have been shown to be biocompatible and non-toxic whilst providing an advantage of eliminating the need for revision surgery, as they degrade by a controlled chemical breakdown with the resorption of polymer chains (Andriano et al., 1999; Hollinger, 1983; Muggli et al., 1998; Ulery et al., 2011).

These second generation polymeric materials have been used to repair fractures of the femur and humerus, and as screws, rods, fixation devices, pins and plates bone substitutes (Ciccone et al., 2001; Mayer and Hollinger, 1995; Rokkanen et al., 2000). They present with advantages of biocompatibility, ability to tailor mechanical properties and degradation kinetics to suit the application, reduced stress shielding and need for revision surgery, ability to be fabricated into various shapes with desirable pore structures as well

as enhanced radiolucency, since it does not interfere with clinical imaging techniques like Magnetic Resonance Imaging (MRI) (Gunatillake et al., 2003). They are however challenged with the difficulty of tailoring degradation profiles to allow gradual load transfer to healing tissue, possessing adequate mechanical properties, osteolysis and synovitis (Lokesh and Dhillon, 2006).

2.3.3.3 Third Generation Substitutes

With a survivability half life of 15 years for bioinert materials, regeneration of bone tissue instead of replacement is considered the best approach in addressing osseous defects (Hench, 1998). Whereas second-generation biomaterials were designed to be either resorbable or bioactive, third generation implants combine these two properties, with the aim of developing materials that posses an ability to stimulate specific cellular responses at the molecular level, such that once implanted, it will aid the body to heal itself (Hench and Polak, 2002). Such implants are fabricated from polymers of natural and synthetic origin, (Armentano et al., 2010) decalcified or demineralised bone matrix, (Russell and Block, 1999) and polymer-ceramic bioactive composites have been uses successfully in various orthopaedic and dental clinical trial applications (Navarro et al., 2005; Rezwan et al., 2006).

2.3.3.4 Commercially Available Bone Substitutes

Some commercially available bone substitutes include hydroxyapatite and carbonated hydroxyapatite based porous scaffolds, marketed under the trade names ProOsteon and ProOsteon500R from Interpore. These support bone in-growth and have been used in the treatment of metaphyseal fractures. In the United Kingdom ReproBone from Ceramisys comes in the form of blocks, granules, wedges and discs, made from 60% restorable HA and 40% α-TCP. Osteoglass from US Biomaterials is a bioactive glass substitute that is claimed to bind to collagen and promote bone formation, it has been used in the treatment of periodontal and facial bone defects (Gogolewski, 2001).

Other ceramic composites composed of tricalcium phosphate and hydroxyapatite

which comes in a paste, puty, porous granule formats, that undergo endothermic hardening are used as bone void fillers. These include Norian's Skeletal Repair System, α-BSM from ETEX Corporation, Bi-Ostetic from Berkeley and Collagraft from Zimmer. These collagen and ceramic bone substitutes are advantageous in enhancing stability of fixations and facilitating healing whist providing protection against the infiltration of soft tissues; however, they present with disadvantages of stress concentration and could impede vascularisation (Gogolewski, 2001).

2.3.4 Implant Testing

Like all other developed products, orthopaedic implant materials are examined with a series of standardized testing procedures before they are commercialized. Bone functions as a major load bearing component of the body, hence implant materials and bone graft substitutes are tested mechanically to access their ability to support the body in performing everyday activities and also tested biologically to examine their biocompatible nature.

2.3.4.1 Mechanical Testing

Several different mechanical tests are available for medical implant testing, however, depending on the final application of the implant, a particular compression, fatigue or tensile test that conforms to ISO and ASTM standards is used to estimate ultimate strength, stiffness, toughness and behaviour at failure. The table 2.2 on Page 30 lists some of the common ISO and ASTM standards applied to implant testing (DDL, 2013).

Table 2.2: Mechanical Tests applied to Medical Implants

Standard	Test
ASTMF1541	Compression Test for External Skeletal Fixation Devices
ASTMF384	Test Methods for Metallic Angled Orthopaedic Fracture Fixation Devices
ASTMF2118	Fatigue Testing of Acrylic Bone Cement Materials
ASTMF382	Fatigue - Four Point Bend Testing - Metallic Bone Plates
ASTMF897	Fretting Fatigue Test of Osteosynthesis Plates and Screws
ISO12189	Fatigue Testing of Spinal Implant Assemblies
ISO14801	Dynamic Fatigue Testing of Dental Implants
ISO14879	Fatigue Testing of Knee-Joint Prostheses

2.3.4.2 Biological Testing

The cost of biological testing for medical implants ranges from several pounds to hundreds of thousands of pounds. This largely depends on factors such as the duration of the test, and the type and number of animals involved. Which also in turn depends on the type and size of the implant being tested (Leventon, 2008). The duration of testing can vary from two weeks to several years. ISO 10993 lists a series of standards used to biologically evaluate medical devices; with ISO 10993-5 and ISO 10993-6 describing tests used for *in vitro* cytotoxicity and *in vivo* implantation studies respectively (F.D.A., 2013).

2.3.4.2.1 *In Vitro* Testing

Cytotoxicity and pyrogenicity are types of *in vitro* studies carried out to access an implant's biocompatibility status prior to commercialization. For cytocompatibility studies, osteoblasts or their precursors are seeded onto the surface of an implant and cultured for a period of time under physiological conditions of temperature, culture medium and humidity. After an appropraite time point, standardized laboratory assays such as MTT, total DNA, Alizarin Red and Sirus Red are used to examine cell viability, proliferation and early expression of bone mineral. This kind of biological testing is however limited by a lack of dynamic environment and an inability to investigate mechanical strength of attachment between matrix and implant surface (F.D.A., 2013; Leventon, 2008).

2.3.4.2.2 *In Vivo* Testing

Current *in vivo* testing of implants consists of an initial surgical implantation of a test sample of the implant into a healthy animal for a period of time. A time point of four weeks is usually used to investigate early stage reaction, whilst three to six months and sometimes a year are used for longer term reaction studies. Animals usually used for such investigations include mice, rats, rabbits, guinea pigs, dogs and sheep depending on the size and application of the implant (Pearce et al., 2007; Martini et al., 2001). At the end of the study, the animal is sacrificed and the area of implantation is examined

meticulously for local effects such as cell attachment, tissue formation, and if possible indications of any adverse systemic effects including foreign body response and tissue necrosis amongst others (Wallin, 1998).

As well as being a costly procedure, this type of biological testing is also limited by the difference in structure and cell behaviour of animal and human bone. Therefore creating a dynamic tissue engineered *in vitro* bone model could be greatly beneficial in addressing the aforementioned limitations, associated with both the current *in vitro* and *in vivo* implant testing.

2.4 Bone Tissue Engineering

Bone tissue engineering is the use of materials to either induce formation of bone from surrounding tissue or as a carrier/template for implanted bone cells and agents. Bone regeneration requires four components: a morphogenetic signal, responsive host cells that respond to the signal, a suitable single carrier to serve as scaffolding for the growth of responsive host cells and a viable and well vascularised host bed (Burg et al., 2000; Croteau et al., 1999). Osteoconduction and osteoinduction are also important properties in bone tissue engineering. Osteoconduction is the ability of a material to support cell ingrowth to form bone whilst osteoinduction is the ability to cause pluripotent cells from a nonosseous environment to differentiate into osteoblasts leading to bone formation (Urist et al., 1967).

2.4.1 Scaffolds

The era of third generational orthopaedic implants coincided with the emergence of scaffolds for tissue engineering; these scaffolds provide biological functions and a three dimensional porous structure. Scaffolds were initially selected for structural restoration based on their biomechanical properties, scaffolds were later engineered to be bioactive or bioresorbable to enhance tissue growth, currently, scaffolds are designed to induce bone formation (Bose et al., 2012).

An ideal scaffold should posses a suitable surface chemistry that supports cell attachment, proliferation, migration and growth as its biological functionality. Additionally, it should provide structural functions of serving as a biocompatible template for osteoprogenitor cell ingrowth and aid differentiation of mesenchymal stem cells into osteoblasts, as well as the production, organization and maintenance of extracellular matrix (Armentano et al., 2010; Gogolewski and Gorna, 2007; Gorna and Gogolewski, 2003).

In addition to being biocompatible, scaffolds are required to be composed of highly interconnected macro and microporous networks. Furthermore, they should degrade to non-toxic products in a timely manner as tissue regeneration occurs, and have appropriate mechanical properties and structural integrity as degradation occurs (Boccaccini et al., 2008; Hutmacher, 2000). They should also be sterilizable without loss of properties and possibly be radiolucent to facilitate subsequent radiographic imaging after implantation (Gogolewski, 2001).

2.4.1.1 Composite Scaffolds

Composite bone substitutes are mostly biodegradable polymers reinforced with ceramic particles. These substitutes came into focus after Bonfield et al proposed the concept of polymer-ceramic combination in mimicking the ductile and brittle properties of the collagen and mineral components of bone, respectively (Bonfield, 1988a,b).

Mechanically, polymers such as polyurethane and polycaprolactone are noted for their extensive deformation and high toughness whilst ceramics are noted for their high compressive strength but brittle nature. Hydroxyapatite (HA) has been extensively investigated due to its excellent bioactivity, osteoconductivity and its similarity to the main mineral component of bone. However, its poor tensile strength and fatigue failure limits its applicability to low or non-load-bearing sites (Li et al., 2005). Polyurethane (PU) presents with desirable properties of greater elasticity, viscoelastic behaviour and higher mechanical strength associated with its versatile chemistry (Boissard et al., 2009). Although PU is a promising material for scaffold fabrication, the lack of bone-bonding

2.4. BONE TISSUE ENGINEERING

bioactivity limits its use in bone.

Combining polymer with hydroxyapatite has been shown by many researchers to improve the mechanical properties of the resulting composite as long as a strong interfacial bond strength is established between the ceramic phase and the polymer matrix (Attawia et al., 1995; Boccaccini and Maquet, 2003; Bonzani et al., 2007). Yoshii et al developed a polyurethane-calcium phosphate composite containing 70 and 79% of both HA and TCP scaffolds. They reported compressive modulus and strength values ranging from 2.5-3.6 GPa and 59.6-87.0 MPa, respectively for all scaffolds, although composites with HA recorded higher compressive modulus and strength (Yoshii et al., 2012).

Biologically, the bioactive and osteoconductive nature of HA makes their use in composite scaffolds for bone tissue engineering an ideal biocompatible choice. This is largely due to HA possessing a calcium/phosphate ratio of 1.50 -1.67 which is within the range known to promote bone regeneration in several clinical applications (Armentano et al., 2010). The degree of bioactivity is however dependent on the volume fraction, size, shape, surface functionality and arrangement of inclusions of the calcium phosphate granules (Maquet et al., 2004).

Inclusion of calcium phosphate in polymeric scaffold fabrication has also been shown to modify surface and bulk properties of resulting composites by increasing the hydrophobic polymer matrix and thus altering the degradation kinetics of the scaffold. Additionally, composites have been shown to present with an advantage of reducing undesirable acidic degradation effects, associated with the use of plain polymeric materials (Boccaccini and Maquet, 2003; Rezwan et al., 2006).

2.4.1.2 Nano-Composite Scaffolds

Nanotechnology enables the development of new systems that mimic the complex and hierarchical structure of native tissue, hence it is believed that a combination of biology and nanotechnology can revolutionize tissue engineering and medicine (Gleiter, 2000). Polymer nanocomposites are the result of combining polymers and inorganic/organic

fillers at the nanometer scale (Gorrasi et al., 2008). Interaction at this level is considered to possess advantageous mechanical and functional properties as opposed to those of microcomposites. Upon overcoming processing and dispersion challenges, nanocomposites often show an excellent balance between strength and toughness as well as improved characteristics compared to their individual components (Imam Khasim et al., 2010; Tjong, 2006).

2.5   Polyurethanes

Several polymers of both natural and synthetic origin can be used for bone tissue engineering; however polyurethanes are of particular interest due to the flexibility associated with their versatile chemistry (Guelcher, 2008). This makes it possible to customise scaffolds in order to attain desirable chemical, physical and mechanical properties such as durability, elasticity and fatigue resistance by altering the choice and quantity of starting materials (Zdrahala and Zdrahala, 1999). Thus, polyurethanes can be synthesised as rigid or elastomeric, hydrophobic, hydrophilic or amphiphilic depending on the type of hard and soft segment used, with an added functionality of incorporating biologically active moieties into the backbone chain or as side pending chains to enhance polymer-cell interaction, growth and proliferation (Gogolewski and Gorna, 2007; Gorna and Gogolewski, 2003; Gorna K., 2006).

2.5.0.3   Polyurethane Scaffolds

Biocompatible and biodegradable polyurethanes have been investigated as scaffolds for tissue engineering applications for almost thirty years (Guelcher et al., 2004), and also as heart valves, stents, intra-aortic balloons, pacemaker lead insulators amongst others (Grad et al., 2003). Microphase separation between the hard and soft segment enables polyurethane scaffolds to excellently handle physical stresses and possess desirable mechanical properties, useful for bone tissue engineering (Wen et al., 1997). The use of elastomeric scaffolds as alternatives to bone grafts prevents the generation of shear

forces at the interface between native bone and the bone substitute. Thus enabling intimate contact with bone and enhancing the proliferation of osteogenic cells and bone regeneration (Gorna and Gogolewski, 2003).

2.5.1 Synthesis Materials

Thermoplastic polyurethane elastomers are a class of linear segmented copolymers characterized by the presence of the urethane functional group. They are prepared from three components, namely a diisocyanate, a macrodiol (or polyol) and a chain extender (Wirpsza, 1993). The diisocyanates and chain extender are normally referred to as the hard segment which imparts cohesive strength and stiffness whilst macrodiols which could be polyether, polyester, polycarobonate, polydimethylsiloxane or polybutadiene based, are referred to as the soft segment which imparts softness and extensibility (Zdrahala and Zdrahala, 1999).

2.5.1.1 Toxicity of Hard segments

Although a vast number of combinations of diisocyanates, macrodiols and chain extenders are available, only a few are utilised for biomedical applications due to the cytotoxic nature of some combinations (Gunatillake et al., 2003). To avoid using toxic diamine decomposition products from aromatic diisocyanates, (Szycher, 1988) aliphatic diisocyanates such as methyl 2, 6-diisocyanatohexanoate (lysine methyl ester diisocyanates, LDI) and dicycohexylmethane diisocyanate (H_{12}MDI) have been used to synthesis biodegradable polyurethanes (Ciardelli et al., 2006; Guelcher et al., 2004).

In addition, 1, 4-diisocyantabutane (BDI) has also been suggested to be used in place of methlylene disdiphenylisocyanate (MDI), which has been suggested to degrade into carcinogenic and mutagenic compounds (Spaans et al., 1998; Szycher, 1988). However, it is worthy to note that, aromatic diisocyanates such as MDI and TDI are known to exhibit microphase separated morphologies, ordered high structural domains and useful mechanical properties (Kavlock et al., 2007).

2.5.1.2 Synthesis Methods

Polyurethanes are usually synthesised by one or two-step batch procedures or by semi-continuous processes such as reactive extrusion (Wirpsza, 1993). The one-step synthesis method consist of a reaction of the hard and soft segments usually in the presence of a catalyst and sometimes water. Water reacts with the diisocyanate to form carbon dioxide, a biocompatible foaming agent, useful in creating porous structures (Guelcher et al., 2004).

On the other hand, the two-step synthesis method (Figure 2.4 on page 37)) involves end-capping the macrodiol with diisocyanate and subsequently chain extending the resulting polymer with a low molecular weight diol or diamine (for polyurethane-urea). This has been shown to offer good control of polymer architecture as compared to the one-step synthesis method (Lyman, 1960). A summary of the synthesis route of polyurethane and polyurethane-urea is shown in the figure 2.4 below (Gunatillake et al., 2003).
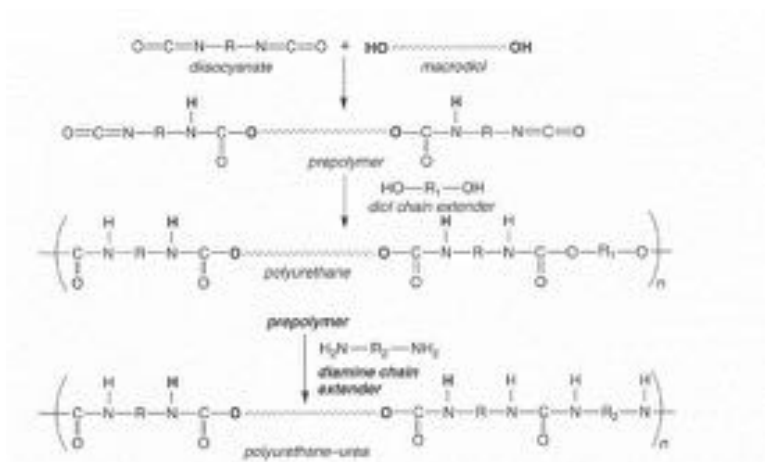
Figure 2.4: Synthesis of Polyurethane and Polyurethane-Urea- Reproduced from (Gunatillake et al., 2003), with kind permission from CSIRO Publishing

2.5.1.3 Synthesis Modifications

Kavlock et al synthesized segmented polyesterurethane urea elastomers using 1, 4-diisocyan-tabutane (BDI), poly (ε-caprolactone) (PCL) macrodiol as soft segment

and tyramine-1, 4-diisocyan-atobutane-tyramine as chain extender. They reported that increasing PCL macrodiol molecular weight at 37°C increased melting temperature and storage modulus from 21 to 61°C and 52 to 278 MPa, respectively. Their study indicated that the crystallinity of PCL macrodiol and soft segments, contributes significantly to the mechanical properties of polyurethanes (Kavlock et al., 2007). It has also been reported that, thermal and mechanical properties of polyurethanes are strongly dependent on the polyol chain length and the hard-segment content. Although the use of different chain extenders does not have a measureable effect on the mechanical and thermal properties of polyurethanes, for polyurethanes with the same hard–segment content, it has been shown that there is no effect of the material molecular weight on thermal properties (Gorna et al., 2002).

2.5.1.4 Catalysts

Catalysts are used in accelerating the rate of reactions. Several catalysts have been utilised in different polyurethane synthesises routes. Gorna et al, studied the effect of six different catalysts on the molecular characteristics, thermal and mechanical properties of polyurethane. The biocompatible catalysts used were zinc octoate (Zn), ferric acetyl acetoanate (Fe), manganese 2-ethyl hexamanoate (Mn), stannous octoate (Sn), dibutyltin dilaurate (DBDL) and magnesium methoxide (Mg). They reported their findings based on the significant effect of a catalyst on the rate of polymerization, Fe was the most effective catalyst although it was difficult to control reaction temperature when used, whilst Mg was the least effective. In addition, Sn and Mn were less effective than DBDL and Zn with respect to the thermal and mechanical properties attained (Gorna et al., 2002).

2.5.1.5 Synthesis of Biodegradable Polyurethanes Foams

Gorna and Gogolewski synthesized biodegradable polyurethane foams with varying hydrophobic and hydrophilic components, using hexamethylene diisocyanates, poly (ethylene oxide) diol, polycaprolactone diol, amine-based and sucrose based polyol. They

used water as a change extender and forming agent, citric acid as a calcium complexing agent, lecithin and solutions of vitamin D_3 as surfactants and inorganic fillers such as hydroxyapatite, glycerol phosphate calcium salt and calcium carbonate (Gorna and Gogolewski, 2003).

It is worthy to note that the use of lecithin as a surfactant enhanced the miscibility of reactants with water. This consequently led to foams with finer and more regular pore structure. The incorporation of lecithin, citric acid and vitamin D_3 however, reduced the mechanical properties whilst the presence of inorganic fillers increased the compressive strength and modulus. In addition, the hydrophilicity of foams decreased with the presence and amount of inorganic fillers and subsequently the rate of degradation whilst the inclusion of citric acid accelerated degradation (Gorna and Gogolewski, 2003).

Furthermore, ascorbic acid (AA) has been shown to be necessary for the production of collagen matrix and expression of osteoblast markers such as ALP and osteocalcin. Zhang et al synthesized a novel biodegradable polyurethane-ascorbic acid scaffold by copolymerizing ascorbic acid with glycerol and lysine diisocyanate, LDI. They reported that polyurethane scaffolds containing AA stimulated bone cell proliferation, type I collagen and ALP synthesis. The scaffolds degraded by hydrolysis into biocompatible substances at 37°C, with no change of the pH of the degradation solution (Zhang et al., 2000, 2003). A summary of different synthesis routes used in producing biodegradable polyurethanes has been compiled from literature and tabulated in the appendix of this thesis.

2.5.1.6 Synthesis of Biodegradable Injectable Polyurethanes

Minimally invasive polyurethane-based injectables which polymerise in-situ at biological temperatures, have attracted attention since Bonzani et al developed a novel material by reacting two pentaerythritol-based prepolymers. They characterized the materials mechanical and surface properties, and undertook cytocompatibility studies using primary osteoblasts. They reported of findings which indicated potential use of such injectables for a range of orthopaedic applications (Bonzani et al., 2007).

In a similar manner, Adhikari et al developed a series of cross linked injectable polyurethanes using a two part pre-polymer system. They combined lactic acid and glycolic acid based polyester star polyols, pentaerythritol and ethyl lysine diisocyante (ELDI). They reported of high compressive strength (100-190 MPa) and modulus (1.6-2.3 GPa) which were higher than that of cancellous bone, and significantly stronger than most acrylic bone cements (Adhikari et al., 2008).

2.5.2 Degradation of Scaffolds

The degradation of a scaffold relates to a loss in material mass and or functionality of the scaffold over a period of time, either *in vitro* or *in vivo*. The gold standard of biodegradable polymer scaffolds is the ability to match the rate of degradation to the rate of regeneration of new tissue. Since bone is able to remodel *in vivo* under physiological loading (Hillsley and Frangos, 1994) it is a requirement that the degradation and resorption kinetics be controlled effectively. This allows the bioresorbable scaffold to retain its physical properties for at least 6 months (4 months for cell culture and 2 months in situ) with complete metabolization from the body occurring after 12-18 months (Hutmacher, 2000). However, previous work by Hill et al reported of more than 50% polyurethane scaffold resorption after 5 weeks of *in vivo* studies with male mice (Hill et al., 2007).

2.5.2.1 Types of Polyurethane Degradation

Polyurethane scaffolds made from aromatic diisocyanates with polyether soft segments undergo oxidative degradation. Those synthesized from aliphatic diisocyanates with polyester soft segments undergo hydrolytic degradation, however, both types of scaffolds are known to be susceptible to enzymatic degradation (Griesser, 1991). Several researchers have also reported that polyurethanes based on aromatic diisocyanates are more biostable than their aliphatic counterparts. This has been attributed predominately to their ability to form hard segment crystalline orders resulting from molecular symmetry and strong intermolecular π-electron interactions (Gunatillake et al., 2003).

2.5.2.1.1   Hydrolytic and Oxidative Degradation

Hydrolytic degradation of polyesterurethanes occurs in aqueous media and mainly proceeds with the scission of carboxylic ester, urethane or urea linkages in the main chain into shorter hydroxyl and carboxyl chains (Guelcher, 2008). Generally, polyetherurethanes degrade under oxidative conditions, for example in hydrogen peroxide or from a build-up of peroxides excreted from macrophages in a biological environment (Ratner et al., 1988). These types of polyetherurethanes are resistant to hydrolytic degradation conditions since the polyether segment is thought to be the structural element that is most susceptible to oxidative degradation and highly resistant to hydrolysis (Marchant et al., 1987).

Previous studies have shown that under increased temperatures, acidic or alkaline environments, polyether based polyurethanes are also susceptible to hydrolytic degradation. One of these studies carried out over a six month period showed that, at an increased temperature of 100°C polyetherurethanes were susceptible to hydrolytic degradation whereas no evidence of degradation was found when samples were aged at 37°C (Coury et al., 1988).

2.5.2.1.2   Enzymatic Degradation

Hydrolytic and oxidative enzymes such as papain, urease, leucine amino-peptidase, esterase, trypsin and trypsin derivatives have been shown to cause enzymatic degradation on both polyether and polyester based polyurethanes. It has been proposed that different papain enzymes hydrolyses urethane and urea linkages whilst urease enzymes attack only urea linkages. There is also evidence from literature supporting the hypothesis that, enzymatic attack by living cells plays an important role in the *in vivo* degradation of polyurethanes (Griesser, 1991; Marchant et al., 1984).

2.5.2.2   Factors that affect Polyurethane Degradation

The degradation rate of polyurethanes depends on the chemical composition and structure, crystallinity, molecular weight, presence of additives, scaffold size and geometry

and porosity. It also depends on processing history, applied stresses and the level of hydrophilicity and hydrophobicity of the starting material (Gorna and Gogolewski, 2003; Heidemann et al., 2001). Additionally, it has also been reported in the literature that, the incorporation of inorganic fillers and high levels of the hydrophobic content in the synthesis of polyurethane scaffolds extends the degradation time of such scaffolds, whilst the incorporation of additives such as citric acid accelerates the rate of degradation (Dunn et al., 2001; Gorna and Gogolewski, 2003).

The rate of degradation is further auto-catalysed by the acidic nature of the carboxyl group, which accelerates additional hydrolysis (Schollen.Cs and Stewart, 1973). Degrading at a rate of 8.3×10^{-9} s^{-1} (Chapman, 1989), the degradation of polyurethane scaffolds was initiated by an increase in irregularities in the scaffold wall, formation of cracks in the walls separating the pores, and the fragmentation of the material coupled with a complete loss of shape in the final stage of degradation (Gorna and Gogolewski, 2003).

2.5.2.3 Experimental Degradation Studies

Wet and dry degradation studies can be used to access the degradation rate of a polymer and composite *in vitro* (Marra et al., 1999). An extensive wet degradation study involves testing cylindrical plugs of polyurethane scaffolds in glass ampoules filled with phosphate buffered solution at a pH of 7.4±0.2 and at a temperature of 37±0.1°C, at an eight week time point over a one year period. The amount of water absorbed, the mass of water trapped within the pores of the polymer, loss of polymer mass, and solution pH were investigated as part of this study (Adhikari et al., 2008). Also at each time point, polymers were removed from the buffered solution after wet degradation tests, rinsed three times with distilled water and dried to constant weight in vaccum of about 3×10 s^{-1} at 60°C for dry degradation studies (Gorna and Gogolewski, 2003).

Determining amine concentration with the Ninhydrin assay as part of wet degradation studies is a useful technique for examining the degradation of urethane and urea linkages under test conditions for polyurethane scaffolds. Data from this assay has been shown

by Adhikari et al to correlate with mass loss (Adhikari et al., 2008).

In vivo and *in vitro* studies carried out on the degradation of polyurethane from literature reports satisfactory results on the biocompatibility of degradable polyurethanes, although the effect of degradation products and how they are removed from the body is still not properly understood (Gunatillake et al., 2003). Gunatillake et al. (2003) used Attenuated Total Reflectance–Fourier Transform Infrared Spectroscopy (ATR-FTIR) to quantify biodegradation of polyurethanes and scanning electron microscopy (SEM) to qualitatively describe cellular response and biodegradation.

2.6 Calcium Phosphates

Calcium phosphates are noted for their excellent biocompatibility due to the close resemblance they have with the chemical and crystal structure of bone (Jarcho et al., 1977). Although HA possesses very good bioactive properties, TCP's advantageous ability to be completely resolved after implantation as opposed to crystalline HA, stems from the chemical stability of HA which reduces its solubility rate (Takahashi et al., 2005). The degradation rate of calcium phosphates is highly dependent on crystallinity and the order of degradation. This has been established as amorphous HA > α-TCP > β-TCP > crystalline HA, with crystalline HA exhibiting the slowest degradation and amorphous HA possessing the highest degradation potential (Oonishi et al., 1995).

2.6.1 Choice of Calcium Phosphate: Hydroxyapatite

Hydroxyapatite crystals are the main component of bone mineral (Clarke et al., 2008). By weight, approximately 70% of bone tissue is mineral, with an estimated 95% of the mineral phase composed of a specific carbonated crystalline hydroxyapatite and impurities account for the remaining 5% (Feldman et al., 2007). Like other calcium phosphates, HA presents with other desirable properties such as osteoconductivity and bioactivity, making their use advantageous in eliminating implant loosening, although they are noted for being brittle and difficult to process into complex shapes (Hollinger

2.6. CALCIUM PHOSPHATES

et al., 1996). Additionally, HA's injectability and low setting temperature also make it an ideal carrier of growth factors, facilitating delivery to bone tissue engineering (Ginebra et al., 2006). Silicon has been found to play a key role in bone mineralization and remodelling, skeletal development and gene activation, and as such replacing the calcium content of HA with silicon has been shown to remarkably enhance bone growth *in vivo* (Rezwan et al., 2006; Porter et al., 2004; Thian et al., 2006). Histomorphometry results of a comparative study on the *in vivo* behaviour of HA and silicon substituted HA granules (SiHA) by Patel et al revealed a (37.5%±5.9) bone ingrowth for SiHA which was significantly greater than that of the pure phase calcium based HA at (22.0%±7.3) (Patel et al., 2002).

2.6.1.1 Hydroxyapatite Synthesis

Hydroxyapatite synthesis usually consists of mixing stoichiometric quantities (Ca/P=1.67) of calcium nitrate tetrahydrate $[Ca(NO_3)_2.4H_2O]$ and diammonium hydrogen phosphate $[(NH_42HPO_4]$ precursor solutions. Prior to mixing, and depending on the synthesis method used, the pH values of the precursor solutions are usually adjusted between 8.5 to values above 10 using ammonium hydroxyl solution (NH_4OH) (Martinez-Valencia et al., 2011).

In recent times, several synthesis processes have been developed to produce nano-sized HA powder. Sol-gel syntheses (Anee et al., 2003; Khan et al., 2008), wet precipitation method (Sarig and Kahana, 2002), hydrothermal synthesis and ultrasound precipitation (Martinez-Valencia et al., 2011; Chaudhry et al., 2006), microwave synthesis (Kalita and Verma, 2010), solid state reactions (Rao et al., 1997), and micro emulsion technique (Lim et al., 1997) are some of the methods that have been used to synthesize hydroxyapatite (Kalita and Verma, 2010). In synthesizing HA, some researchers have capitalized on the advantages of additives such as zinc, silicon, citric and fluoride to syntheses HA composites, with these additives to preferentially suit dental and orthopaedic applications (Asefnejad et al., 2011; Patel et al., 2002).

Martinez-Valencia et al synthesized HA by hydrothermal and ultrasound precipitation

methods and compared the time of synthesis, particle size and surface area of the resulting nano-HA structures. From their results, nano-HA synthesised by the shorter ultrasound assisted co-precipitation method proved to have smaller particle size of about 20-40 nm and a high surface area value of about 97.9 m^2g^{-1}. This implies a better interface that may promote better interaction between the HA-polymer matrix (Martinez-Valencia et al., 2011).

On the other hand, microwave synthesis of hydroxyapatite offers several advantages including rapid heating, easy reproducibility, shorter synthesis time, narrow particle range distribution, high yield and purity and efficient energy transformation. This can possibly be attributed to the fact that microwave heating is different from conventional heating, in that, heat is generated internally within the material instead of originating from an external heating source and subsequent radiative transfer (Kalita and Verma, 2010).

2.6.2 Polyurethane-Nano Hydroxyapatite Composites

When incorporating nano-HA granules into polyurethane composites, the interface adhesion between the resulting polymer matrix and nanoparticles is of great importance to the mechanical properties of the composites. The mechanical properties of such composites are in turn controlled by several microstructural parameters including synthesis and processing methods, properties of the matrix, properties and distribution of the fillers as well as the nature of interfacial bonding (Armentano et al., 2010). Some researchers have investigated the incorporation of nHA and other nanoparticles in polyurethane composites for bone tissue engineering applications using ultrasound cavitations (Mahfuz et al., 2004; Schreader et al., 2013), hot isostatic pressing (Zhao et al., 2006), in-situ polymerization, electrospraying (Khan et al., 2008) and one step solution poly-condensation (Boissard et al., 2009). Additionally, initial calcium absorption to nanoceramic surfaces has also been shown to be enhanced by the binding of vitronectin that subsequently promotes osteoblast adhesion (Webster et al., 2001).

2.7 Chemical Characterization

Small angle X-ray scattering (SAXS), wide angle X-ray diffraction (WAXD), differential scanning calorimertry (DSC), dynamic mechanical thermal analysis and various forms of microscopy, are techniques used in probing the morphology, composition, thermal and mechanical properties of polyurethane, hydroxyapatite and their composites (Gunatillake et al., 2003; Hing et al., 1999). With the chemical structure of polyurethanes usually characterized with nuclear magnetic resonance (NMR) and Infrared (IR) spectroscopy (Kavlock et al., 2007; Zhang et al., 2003).

2.7.1 Fourier Transform Infra-red Spectroscopy (FTIR)

Fourier transform infra-red spectroscopy (FTIR) is a widely used analytical technique that is routinely applied to the characterization of biomaterials. An infra-red spectrum represents the chemical finger print of a sample, with absorption peaks which correspond to the frequencies of vibrations of the bonds between the atoms that make up the material (TNC, 2001). Diffuse reflectance (DRIFT), attenuated total reflectance (ATR) and photo acoustic sampling (PAS) are various sampling techniques used in FTIR spectroscopy. PAS is however considered the best technique for imaging biomaterials as it addresses limitations of surface requirements and optical density associated with the use of DRIFT and ATR (Rehman and Bonfield, 1997). As shown in table 2.3 on Page 47, Khan et al. (2008) compiled a collection of bands assigned to polyurethanes using FTIR spectroscopy in their design of a novel bioactive polyurethane-hydroxyapatite composite for dental restoration applications.

2.8 Scaffold Fabrication

Electrospinning, thermally induced phase separation, solvent casting and particulate leaching, gas forming, solid free-form fabrication, microsphere sintering and freeze drying are various methods of used in scaffold fabrication (Armentano et al., 2010; Hutmacher,

Table 2.3: Bands assigned to FTIR spectroscopy of PU - Reprinted from (Khan et al., 2008) with kind permission from Elsevier

Wavenumber (cm $^{-1}$)	Assigned
3310	Strong vs. (N——H) bonded N——H
2930	Strong vs. (CH$_2$)
2860	Strong vs. (CH$_2$)
1730	Very strong free (C══O)
1702	Very strong bonded (C══O)
1600	Strong vs. (C══C)
1530	Very strong δ (N——H) + v (C——N)
1410	Strong vs. (C–C) in benzene ring
1310	Strong δ (N——H) + v(C——N) β(C——H)
1230	Strong δ (N——H) + v(C——N)
1110	Very strong vs. (CH$_2$–O–CH$_2$) of aliphatic ether
1020	Weak β (C——H) in benzene ring
818	Weak γ (C——H) in benzene ring

2000). As shown in table 2.4 on Page 48, each of these methods presents with its own advantages and disadvantages (Rezwan et al., 2006).

2.8.1   Electrospinning

Electrospinning is an efficient, simple and relatively easy polymer fabrication technique. It produces nano and micro polymer fibres, with the advantage of being performed from polymers in solution or melt states. Such thin fibres provide unexpectedly high surface area to volume ratios, high porosity, flexibility in surface functionalities, superior mechanical performance and membrane technology (Demir et al., 2002).

In the field of biomaterials and tissue engineering, electrospinning has been utilised in producing ideal scaffolds that mimic the morphological characteristics and biological function of the natural extracellular matrix. Electrospun scaffolds provide an optimal template for cell attachment, proliferation and growth (Carlberg et al., 2009; Huang et al., 2003). Several different polymers such as polyurethanes, poly(ε-caprolactone), poly(lactic acid), poly (glycolic acid) and their co-polymers have been successfully span for musculoskeletal, nerve, skin, vascular and drug delivery applications (Bashur et al., 2009; Clarke et al., 2008; Nirmala et al., 2011).

2.8. SCAFFOLD FABRICATION

Table 2.4: Advantages and Disadvantages of Fabrication routes for 3D composite scaffolds - Reprinted from (Rezwan et al., 2006) with kind permission from Elsevier

Fabrication Method	Advantages	Disadvantages
Electrospinning	Relatively easy technique High surface area to volume ratio High porosity (80%) Nanometre fibre diameter resembles the body's natural extracellular matrix	Longer processing time Low scaffold thickness Use of organic solvents
Thermally Induced Phase Separation (TIPS)	High volume of interconnected pore structures High porosity (95%) Anisotropic and tubular pores possible Control of structure and pore size by varying preparation conditions Ability to produce thick constructs	Shrinkage issues Use of organic solvents Small scale production
Solvent Casting / Particle Leaching	Controlled porosity (20-50%) Controlled interconnectivity (if particles are sintered) Control of structure and pore size by varying preparation conditions Ability to produce thick constructs	Structures generally isotropic Use of organic solvents Residual particles in polymer matrix Limitation to thin constructs Solvent evaporation could prolong the process
Solid free-form	Porous structure can be tailored to host tissue Protein and cell encapsulation possible Good interface with medical imaging	Resolution needs to be improved to the micro-scale Some methods use organic solvents
Microsphere sintering	Graded porous structures possible Controlled pore size Can be fabricated into complex shapes	Limited pore interconnectivity Use of organic solvents

2.8.1.1 The Experimental Set-Up

The electrospinning process combines a high voltage supplier, a set of capillary tubes with small needles, and a grounded metallic collecting plate covered with foil, as shown in Figure 2.5 on page 49. Electrically charged polymer jets emitted from capillary tubes are deposited on the rotating metallic collector during the electrospinning process. The foil containing deposited jets is removed from the collector and dried at about 60 °C under vacuum to remove all remaining solvent (Khil et al., 2003).

2.8.1.2 Factors that affect the properties of electrospun fibres

Variables that influence the nature and geometry of fibres produced by electrospinning include solution properties such as viscosity, elasticity, conductivity and surface tension. Additionally, ambient parameters such as solution temperature, humidity, and air velocity in the electrospinning chamber and governing variables such as hydrostatic pressure in the capillary tube, electric potential at the capillary tip, and the distance between the tip and the collecting screen are also said to influence fibre morphology (Doshi and Reneker,

Figure 2.5: The Electrospinning Set-Up in our Lab (used in this thesis)

1995; Raghavan et al., 2012). A change in the diameter observed between the ejected and deposited polymer jets, is said to be caused by continuous stretching and solvent evaporation as the jets travel from the tube onto the collector (Deitzel et al., 2001).

The work of Demir et al reported that, the morphology of polyurethane electrospun fibres is strongly correlated with viscosity, concentration and temperature. As concentration, or equivalently, the viscosity increases, higher electrical forces are required to overcome both the surface tension and viscoelastic forces responsible for stretching the fibre (Demir et al., 2002; Reneker and Chun, 1996). Demir et al went further to report of a mathematical relationship between flow rate, voltage, average fibre diameter (AFD) and concentration as

Flow rate $\smile$ (Voltage)^3 AFD$\smile$ (Concentration)^3

In their study, the morphology of polyurethane fibres varied between curly, wavy, and straight structures, with defective bead formation being present in thinner fibres fabricated from solutions with lower viscosities and higher surface tensions. The occurrence of bead formation stems mainly from the high electrical field applied to the system at a fixed power source and collector distance. With decreasing concentration and viscosity leading to a significant decrease in the fibre surface area to volume ratio. Temperature of the polymer solution has also been stated as a key parameter that affects fiber morphology and spinnability. Thus it is possible to improve fiber morphology and

attain more uniform fibres by increasing the solution temperature (Demir et al., 2002).

2.8.1.3 Characterization of Electrospun Fibres

Different characterization techniques have been used to examine electrospun fibres. Such fibres fabricated from both plain polyurethanes and composites which are reinforced with nanohydroxyapatite, calcium chloride, copper, and other materials. Such scaffolds have been used in orthopaedic applications, restorative dentistry, wound healing, anterior cruciate ligament tissue replacements, anti-microbial studies, amongst others (Bashur et al., 2009; Khan et al., 2008; Khil et al., 2003; Nirmala et al., 2011; Sheikh et al., 2011).

2.8.1.3.1 Physical & Chemical Characterization

Characterization of electrospun fibres to investigate geometric properties such as fibre diameter, orientation and morphology can be carried out with the Atomic Force Microscope, Scanning Electron Microscope, Transmission Electron Microscope, Energy Dispersive X-ray Spectroscopy and the Field Emission Scanning Microscope (Nirmala et al., 2011). These types of equipment have been used in combination with image processing software like ImageJ from the NIH, to characterize fibre diameters ranging from a few nanometres to several microns (Reneker and Chun, 1996). Chemical characterization using Fourier Transform Infra-Red (FTIR) and Nuclear Magnetic Resonance (NMR) also facilitates the analysis of molecular structure of electrospun fibres.

2.8.1.3.2 Mechanical Characterisation

The work of Pedicini and Farris, characterised the mechanical structure of an electrospun fibres as well as its bulk material polyurethane using uniaxial tensile tests. They reported characteristic differences in the stress-strain responses of the materials and attributed this to fibre orientation and strain-induced orientation of the fibres (Pedicini and Farris, 2003). Furthermore, the work of Yaganegi et al, also showed that aligned scaffolds presented with tensile strength and modulus of 14 ± 1 MPa and 46 ± 3 MPa, respectively. These were much higher than that of random fibre scaffolds at 1.9 ± 0.4 MPa and $2.1\pm.2$ MPa, respectively (Yeganegi et al., 2010).

2.8.2 Phase Separation

Phase separation or inversion is a process of transforming a polymer in a controlled manner, from a liquid state to a solid state. Phase inversion can be initiated by solvent evaporation as in the case of solvent casting, thermal precipitation or precipitation with a non-solvent (Tsui and Gogolewski, 2009). Freeze drying, freeze gelation and freeze extraction are variations of thermal precipitation. Polymer solutions are initially frozen at very low temperature of about -20 °C to -210 °C and the solvent is sublimed in the case of freeze drying, or a gelation media is added to aid in gelling the polymer in the case of freeze gelation. For freeze gelated scaffolds a non-solvent is used to precipitate the polymer, removing the solvent and creating pore structures with a porosity of about 95% (De Mulder et al., 2013).

A comparative study carried out by Tsui and Gogolewski compared pore sizes of polyurethane membranes fabricated with different solvents using the phase inversion technique at 23 °C. They compared dimethylformamide (DMF), dimethylacetamide (DMAC) and dimethylsulfoxide (DMSO) as solvents, and deionised water and distilled water as non-solvents. They further investigated the effect of sedimentation time, polymer concentration, and thickness of cast samples on pore size and distribution. From their study, they reported that polymer solutions made from DMF with 5wt% polymer, with sedimentation time of 24-72 hours and a thickness of 1 mm had well defined pore structures and pore interconnectivity (Tsui and Gogolewski, 2009).

The work of Gorna and Gogolewski that also compared scaffold fabrication using DMF, DMSO, methyl-2-pyrrolidone (NMP), acetone (A), ethanol (EtOH), isopropanol (I) and tetrahydrofuran (THF). They reported that DMF is the best solvent for polyurethane scaffold preparation, as it produced scaffolds with open interconnected pores and higher water permeability (Gorna K., 2006).

2.8.3 Scaffold Porosity

Pore size and morphology, quantity and pore interconnectivity are of great importance to scaffolds fabricated with phase separation techniques. Such characteristics facilitate efficient cell seeding, growth and transfer of vital cell nutrients and metabolic waste. Good pore interconnectivity facilitates diffusion and promotes cells buried deep inside the scaffold to survive, although high scaffold porosity has also been reported to be detrimental to desirable mechanical properties (Bose et al., 2012; Heijkants et al., 2006).

An optimum pore size between 100 and 350 μm has been reported to be ideal for bone tissue engineering applications (Klawitter and Hulbert, 1971). This enables proper bone ingrowth, vascularisation and nutrient delivery as the average human osteon size is reported to be approximately 223 μm (Holmes, 1979). In addition, multi-scale porous scaffolds that combine micro and macro porosities are said to perform better than only macro porous scaffolds (Woodard et al., 2007).

2.8.3.1 Estimation of pore size and water uptake ability

The porosity of a scaffold can be determined with Equation 2.1 by measuring the dimensions and mass of the scaffold and using simple techniques of bulk density and upthrust to calculate porosity. Similarly, x-ray microtomography coupled with image analysis, impedance spectroscopy, micro-CT and mercury porosimetry are other reliable tools used in quantifying 3D pore structures, and characterizing pore interconnectivities of porous scaffolds (Rezwan et al., 2006). Heijkants et al calculated the porosity of a polyurethane scaffolds fabricated with the TIPS technique (Heijkants et al., 2006)

$$P(\%) = \left\{ 1 - \frac{m}{\rho \text{Polymer} \times v} \right\} \times 100\% \qquad (2.1)$$

Where

P is the porosity,

m is the mass of the scaffold,

ρPolymer is density of the polymer,

and V is the volume of the scaffold.

Similarly, the water absorption ability of functionalized polyurethane scaffolds (Cao et al., 2010) can also be calculated with Equation 2.2 as

$$P(\%) = \left\{ \frac{Wi - Wo}{Wo} \right\} \times 100\% \tag{2.2}$$

Where

Wo is the weight of scaffold after vacuum drying

Wi is the weight of the scaffold at a particular time point after being placed in distilled water.

2.8.4 Scaffold Modifications

The effect of chemical modifications to scaffolds such as hydrophilicity, crystallinity and surface charge to scaffolds, have been shown to affect cellular spreading and cause changes to phenotypic expression (Hollinger and Schmitz, 1997; Holy et al., 1999).

In addition, physical alterations arising from changes in pore shape, size and number, coupled with surface roughness have also been reported to have a great effect. Such effects affect cell attachment, proliferation and long-term survival of cells on scaffolds, as osteoblastic proliferation is said to be sensitive to surface topography (Burg et al., 2000; Kieswetter et al., 1996). Furthermore, high interatomic and intermolecular bonding has also been reported to be necessary in achieving significantly high scaffold strength (Hutmacher, 2000).

2.8.5 Incorporating Biomolecules

Scaffolds can also be used to deliver biomolecules that facilitate bone tissue engineering. Transforming growth factor-Beta (TGF-β) and bone morphogenetic proteins (BMP) have been shown to be integral in the regulation of bone formation and post-traumatic bone healing (Cao and Chen, 2005; Mauney et al., 2005).

The work of Wozney et al, demonstrated new bone formation with the addition of BMP in sufficient quantities (Wozney et al., 1990). Hence the inclusion of such biomolecules and many others growth factors such as fibroblast growth factor (FGF), vascular endothelial growth factor (VEGF) and insulin-like growth factors (IGF) in scaffold development have also been shown *in vivo* to enhance osteogenesis, bone tissue regeneration and extracellular matrix formation, by recruiting and differentiating osteoprogenitor cells into osteoblasts (Bose et al., 2012; Jansen et al., 2005; Linkhart et al., 1996).

However, the sensitivity of these biomolecules to high temperature ranges and aggressive chemical conditions makes their incorporation into scaffold fabrication is a skilful process. Surface functionalization has therefore been suggested as a possible mechanism of immobilizing proteins and growth factors on to scaffolds in the post-processing stage (Babensee et al., 2000; Rezwan et al., 2006).

2.9 *In vitro* Studies: Cell Types and Assays

Prior to *in vivo* testing of biomaterials and cell constructs, *in vitro* studies utilising cells of either human or animal origin are seeded onto scaffolds and cultured for a period of time under physiological conditions. Such cells could be of a primary source such as bone marrow stromal cells or of an established cell line extracted for experimental purposes. As part of *in vitro* testing, standardized cell assays such as MTT and Alamar blue cell viability assays, and immunochemistry studies are performed to investigate the material's biocompatibility status, thus predict its ability to perform as expected when implanted *in vivo*.

2.9.1 Bone Marrow Stromal Cells (BMSCS)

Bone marrow stromal cells (BMSCs) represent a particularly attractive osteogenic cell source. They have been reported to contain a phenotypically and functionally heterogeneous population of mesenchymal progenitors which contribute to the

physiological regeneration of bone, cartilage, muscle and other connective tissue (Mauney et al., 2005; Zanetta et al., 2009).

Kavlock et al cultured bone marrow stromal cells on rigid fibronectin coated polyurethane films under osteogenic conditions for up to 21 days and used cell density, alkaline phosphatase activity, osteopontin and osteocalcin expressions with western blot analysis to confirm that polyesterurethane urea scaffolds support osteoblastic differentiation to the same extent as PLGA scaffolds (Kavlock et al., 2007). Chorionic mesenchymal cells isolated from human term placenta which presents with advantages of availability, minimum invasive extraction procedures and low ethical concerns have also been shown to differentiate towards an osteoblastic phenotype when cultured on polyurethane formed scaffolds (Bertoldi et al., 2010).

2.9.2   Mesenchymal Progenitor Cells - hES-MP

Mesenchymal progenitor cells such as the human embryonic stem cell-derived mesenchymal progenitor cell line (hES-MP) have been shown to play a key role in bone regenerative medicine. As compared to BMSC's, the reduced risk of donor site morbidity and good availability for *in vitro* culture makes the use of these progenitor cells advantageous to bone tissue engineering. In the presence of osteogenic supplements, these hES-MP cells have been shown to differentiate towards osteogenic lineages *in vitro* (Delaine-Smith et al., 2012).

2.9.3   Human Osteoblast-like Cells

Primary human osteoblast-like cells have been used in bone tissue engineering since the early 1940's when the isolation, culture and characterisation of such cells on a large scale were established by Graham Russell's laboratory at the University of Sheffield (Helfrich and Ralston, 2003). Primary human osteoblasts isolated from trabecular bone at passage 2 have successfully been cultured on polyurethane scaffolds, with live and dead assay used to qualitatively access cell viability over a 7 day period and an MTS assay used to

metabolically quantify cellular activity (Bonzani et al., 2007)). Nirmala et al capitalized on calcium's ability to improve cell attachment and tissue morphology, and electrospun calcium chloride infused polyurethane fibres. They used a commercially available human osteoblast cell line CRL-11372 in conjunction with MTT assay and lactate dehydrogenase (LDH) activity to examine cytotoxicty in their electrospun scaffolds (Nirmala et al., 2011).

2.9.4 Cell Lines

Choosing between primary cells or cell lines is important for *in vitro* cell culture. As opposed to freshly isolated cells, cell lines present advantages of immediate availability of large number of cells, homogeneity of cell cultures and expected stability of the phenotype (Bakker and Klein-Nulend, 2012).

2.9.4.1 Osteosarcoma Cell Line – MG 63

Osteosarcoma cell lines have been widely used as an experimental model of osteoblasts in bone tissue engineering. They proliferate more rapidly than primary cells and are immortal, making them easy to work with. The MG-63 cell line is said to be the least differentiated when compared to other experimental model cell lines like SaOS-2 and TE85 (Dillon et al., 2012; Helfrich and Ralston, 2003). MG-63 human osteosarcoma cells have been used in combination with the live and dead assay to access the biocompatibility of polyurethane scaffolds *in vitro* (Guelcher et al., 2004). Gogolewski et al utilised human lung adenocarcinoma cell line A549, mouse fibroblast-like cell line L929 and human leukocytes, together with an MTT cytotoxicity assay and an *in vitro* evaluation of proinflammatory cytokines Interleukin-6 and Interleukin -8 to show that, isosorbide based polyurethane scaffolds are non-toxic (Gogolewski and Gorna, 2007).

2.9.4.2 Mouse Osteoblast-like Cells – MLOA-5

MLOA-5 cell line derived from transgenic mouse has characteristics of a post-osteoblast and pre-osteocyte cell. These include an ability to express high alkaline phosphatase, bone sialoprotein and osteocalcin, and rapid mineralization in sheets rather than in nodules.

Another key characteristic used to monitor the stability of cell phenotype in MLOA-5 cells, is its ability to form a honey-comb like mineralized matrix after 7-9 days in culture. These cells have been used to study the osteoblast to osteocyte differentiation, bone mineralization and the effects of mechanical loading on biomineralization (Rosser and Bonewald, 2012).

2.9.5   Bioreactors

Bioreactors are defined as devices in which biological and or biochemical processes develop under closely monitored and tightly controlled environmental and operating conditions of temperature, pH, pressure, nutrient supply, waste removal and mechanical stimulation (Martin et al., 2004).

Bioreactors have been used in recent times to successfully seed and culture cells on 3-D tissue engineered scaffolds *in vitro* by facilitating efficient mass transfer within the scaffold. A major advantage associated with the use of bioreactors as opposed to static culture is the possibility of using biomechanical cues to stimulate cell differentiation towards a particular phenotype (Sittichokechaiwut et al., 2010), and the opportunity of seeding cells at a higher density, uniformly and efficiently throughout large polyurethane scaffolds (Woźniak et al., 2010).

The spinner flask model (Vunjak-Novakovic et al., 1996), rotating wall vessels (Unsworth and Lelkes, 1998), flat membrane and hollow fiber models (Jasmund and Bader, 2002), and the flow perfusion model (Bancroft et al., 2003; Schliephake et al., 2009) are some examples of bioreactors.   These models were developed to apply dynamic compression, continuous and oscillatory fluid stresses to physiologically load and mechanically condition cells on scaffolds.

2.9.6   Mechanical Conditioning

Increasing evidence suggests that mechanical forces, which are known to be important modulators of cell physiology, could possibly improve or accelerate the rate of bone tissue

formation *in vitro* (Altman et al., 2002). Although various studies have demonstrated the validity of this principle, little is known about the specific details of the mechanical forces that should be applied to a particular tissue (Martin et al., 2004).

Sittichockechaiwut et al demonstrated that short periods of mechanical loading can accelerate matrix maturation in 3D scaffolds using rapidly mineralising MLOA-5 osteoblasts (Sittichockechaiwut et al., 2009). Additionally, Powell et al utilised mechanical conditioning to cause differentiation in human bioartificial muscles (HBAM), they reported that mechanical stimulation caused morphological changes in the HBAM which were representative of skeletal muscles (Powell et al., 2002). Delaine-Smith et al also applied fluid shear stimulus to human embryonic stem cell-derived mesenchymal progenitor cell line (hES-MP) and human dermofibroblasts and reported of enhanced osteogenic differentiation and matrix production (Delaine-Smith et al., 2012).

Liu et al studied the influence of perfusion and compression on the proliferation and differentiation of human bone marrow stromal cells seeded on polyurethane scaffolds. They reported that a perfusion rate of 10 ml/min and a mechanical stimulus of 10% cyclic compression at 0.5 Hz, carried out 4 times/day for 2 hours/time with a 4 hour rest period maintained viability, and promoted proliferation and differentiation towards a musculoskeletal lineage. They also reported of elevated tensile and equilibrium modulus after a two week culture period (Liu et al., 2012).

2.9.7 *In vivo* Studies

Several *in vivo* studies using plain polyurethane and polyurethane-hydroxyapatite composite scaffolds have confirmed bone formation and material resorption in different animal models. Hill et al reported of higher woven bone formation in PU-HA scaffolds as compared to plain PU scaffolds, in a study that seeded bovine osteoblasts at a concentration of 5×10^6 cells, per 10x2.5 mm scaffold with an average porosity of 90%. These scaffolds were implanted into 4-6 weeks old athymic mice for a 5 week period, after which the animals were sacrificed and extracted implants analysed for bone formation

with histology using Hematoxylin and Eosin staining (Hill et al., 2007).

Gorna and Gogolewski reported new cancellous bone formation in three dimensional porous polyurethane scaffolds implanted into the monocortical defects of the ilium of healthy sheep. In their study, cylindrical 6.5x30 mm^2 defects made in swiss mountain sheep were implanted with polyurethane plugs for a six month period after which the animals were euthanized. Giemsa and eosin staining with histology, and contact radiographic images confirmed regeneration of cancellous bone, which was argued to be denser than the structure of native bone (Gogolewski and Gorna, 2007).

Additionally, a study by de Mulder et al, utilised isotropic and anisotropic polyurethane scaffolds made with different fabrication techniques to investigate the effect of scaffold architecture on bone ingrowth speed and collagen orientation. They used subcutaneous rat pocket models over a 24 week period and reported full tissue ingrowth after 8 and 24 weeks for the isotropic and anisotropic scaffolds, respectively (De Mulder et al., 2013).

2.10   Estimation of Bone Matrix Deposition

Bone formation and mineral deposition in tissue engineered constructs are usually examined with histology, histomorphometry, micro-CT and also collagen and calcium deposition staining assays such as Sirus Red, Xylenol orange, Alizarin red amongst others.

2.10.1   Histology

Histology is the microscopic examination of biological cells and tissues that have been carefully prepared using a series of histological processes of fixation, processing, embedding, sectioning and staining. Different staining media are used to stain for different structures, with literature search revealing some common types of stains used for polyurethane based tissue engineered constructs during histology.

Haematoxylin and Eosin (H & E) stains have been utilised by several researchers to

examine bone formation, collagen orientation, cell differentiation and morphology, but mostly to investigate cell distribution and extracellular matrix formation with tissues and scaffolds. Hill et al used Haematoxylin and Eosin to stain 5 μm sections of plain polyurethane and polyurethane-hydroxyapatite scaffolds after a 5 week implantation period in athymic mice to study the extent of bone formation, (Hill et al., 2007) whilst de Mulder et al, used H & E stain after embedding polyurethane scaffolds in Polymethylmethacrylate (PMMA) constructs (De Mulder et al., 2013).

Gogolewski and Gorna however argue that, the use of a the LR White® as an embedding medium does not react with polyurethanes, or cause them to swell and consequently does not also modify the interface between bone and implant. They utilised Geimsa and eosin staining in evaluating bone formation in scaffolds that were previously implanted into the iliac crest of sheep (Gogolewski and Gorna, 2007), whilst Liu et al utilised Masson Goldner stains on 20 μm sectioned polyurethane scaffolds embedded in OCT compound media prior to cryo-sectioning (Liu et al., 2012).

2.10.2 Histomorphometry

Histomorphometry is a quantitative analysis of histological images. Petal et al used this technique to analyse a set of histological images stuck together to form a collage, in their work with HA granules that was implanted into the femoral condyle of female rabibits (Patel et al., 2002).

A 42 point Weibel grid in conjunction with a histological collage can be used to calculate the percentage of bone ingrowth per grid, AG_{BI} and an absolute percentage of bone ingrowth for the whole section, AS_{BI} using Equation 2.3 and 2.4 respectively (Weibel and Elias, 1967). In a similar manner, Merz grids (Figure 2.6 on Page 62) that have been previously used in a quantitative histological study of cancellous bone formation in cancellous bone by Merz and Schenk can also be used to calculate the percentage of bone coverage. Equations 2.5 and 2.6 represent percentage of bone coverage per grid, G_{BC} and the absolute percentage of bone coverage per section, S_{BC}, respectively when

using Merz grids (Merz and Schenk, 1970).

$$\text{AG}_{\text{BI}} = \left\{ \frac{\sum_{i=1}^{i=42} HBI_i}{42} \right\} \times 100\% \tag{2.3}$$

$$\text{AS}_{\text{BI}} = \left\{ \frac{\sum_{i=1}^{i=N_w} AGB_i}{N_w} \right\} \tag{2.4}$$

$$\text{G}_{\text{BC}} = \left\{ \frac{\sum_{i=1}^{i=x} HBC_i}{\sum_{i=1}^{i=y} HIS_i} \right\} \times 100\% \tag{2.5}$$

$$\text{S}_{\text{BC}} = \left\{ \frac{\sum_{i=1}^{i=N_w} GB_c}{N_m} \right\} \tag{2.6}$$

Where

AG_{BI} represents the percentage of bone ingrowth per Weibel grid

H_{BI} represents the a hit for bone ingrowth when a point fell over an area of bone

N_{w} represents the mean number of Weibel grids

AS_{BI} represents the absolute percentage of bone ingrowth for the whole section

H_{BC} represents a hit for bone coverage when a line intercepted a bone/implant interface

H_{IS} represents a hit for implant/trabecullar space when a line intercepted an implant/trabecular space interface

N_{M} represents the mean number of Merz grids

G_{BC} represents the percentage of bone coverage per grid

S_{BC} represents the absolute percentage of bone coverage per section

2.10.3   Mechanical Testing of the Bone-Implant Interface

Implant push out and pull out tests are two established assessment tools used in investigating the strength of a bone-implant interface. The final section of this report examines some of the factors that affect the strength of a bone-implant interface.
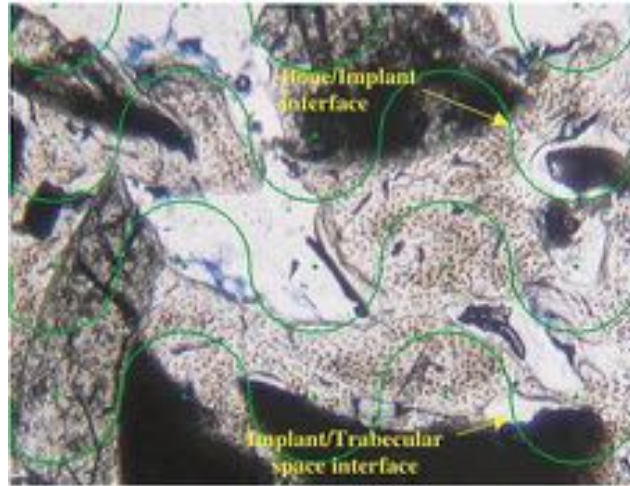
Figure 2.6: Histomorphometry Measurement of bone ingrowth with a Merz grid - Reprinted from (Merz and Schenk, 1970) with kind permission from Karger Publishers

2.10.3.1 Implant Pullout and Pushout Test

The shear strength of bone–implant interface of explanted *in vivo* samples are usually evaluated using pullout and pushout tests. This provides an opportunity to analyze the mechanical competence of a biological fixation for orthopaedic and dental implants. Such tests are commonly applied in testing the effect of implant materials, surface texture, porosity, cross-sectional geometry and surface composition resulting from bone ingrowth or bone apposition to the implant surface. In addition, these tests are usually used on cylindrical implants that have previously been implanted *in vivo* for a period of time (An and Draughn, 2000).

In a typical test, a load is applied to the implant via a device connected to the crosshead of the materials testing machine and a force-displacement curve is recorded until the test is terminated with failure of the bone-implant interface (Berzins and Summer, 2000). The ultimate shear strength of the interface is then calculated as:

$$\sigma = \left\{ \frac{Fmax}{\pi \times \mathrm{DL}} \right\} \tag{2.7}$$

Where

σ is the ultimate shear strength at the interface

D is the outer diameter of the cylindrical implant

L is the length of the cylindrical implant in contact with bone

2.10.3.2 Factors that affect the Strength of Bone-Implant Interface

Several factors affect the strength of an *in vivo* bone-implant interface. These include patient and medication factors, implant factors, local and *in vitro* factors, as well as surgical and hospital factors (An and Draughn, 2000). Patient factors such as age, lifestyle, inflammation and history of bone disease, medicational and local effect of systemic hormones and growth factors, non-steroidal anti-inflammatory drugs, and electromagnetic or electrical stimulations are said to also affect the strength of the bone-implant interface (McKoy et al., 2000).

Additionally, other implant factors including implant geometry, surface coatings and configurations, material properties of the implant, implant design and stress shielding, is also reported to influence the strength of the interface. Specimen preparation prior to surgery, surgical skills of surgeons and the nature of post-operative care given to patients after implant surgery are also reported to have an effect on the strength of the bone-implant interface (Brunski, 1992; McKoy et al., 2000).

2.11 Chapter Summary

Although various polymeric materials are available and have been investigated for tissue engineering, no single biodegradable polymer or composite has yet been able to meet all requirements for bioengineered scaffolds. Moreover, the challenge of seeding relatively thick scaffolds with cells and maintaining cell viability for prolonged periods also remains (Marra et al., 1999). Nanocomposites infused with HA particles and biodegradable polyurethane have attracted attention for their good osteoconductivity, osteoinductivity, biodegradability and mechanical strength (Armentano et al., 2010).

It is therefore believed that such composites could be used to circumvent the above

2.11. CHAPTER SUMMARY

mentioned limitations and act as ideal scaffold for bone tissue engineering. The scaffold developed as part of this project, was seeded with osteoblasts and mesenchymal progenitor cells, and used as an *in vitro* biomimetic model of bone. It was further used to examine bone growth, with an optimistic long-term goal of serving as a testing kit for orthopaedic implants and also as a bone-graft substitutes.

Chapter 3

MATERIALS AND METHODS

3.1 Introduction

This chapter outlines materials and methods used in attaining the results presented in the subsequent chapters of this thesis. Unless otherwise stated, all experimental procedures were carried out with facilities available in the S20 Biomaterials and Tissue Engineering Laboratory of the Kroto Research Institute, University of Sheffield, UK.

3.2 Polyurethane

Most common polymers such as polystyrene and polyethylene have fairly simple chemical structures as they are synthesized from one or two monomers. Polyurethanes on the other hand, have more complex chemical structures with a higher degree of freedom. This results from the fact that polyurethanes are synthesized from three starting monomers, namely a diisocyanate and a chain extender which forms the hard segment, and a macroglycol or polyol which forms the soft segment. Such features make it possible to synthesize a wide variety of polyurethane materials with unique compositions, and different physiochemical and mechanical properties.

Since its first synthesis by Otto Bayer and co-workers in 1937 (Ulrich, 1983), polyurethanes have been used extensively to develop a variety of products, such as

foams, paints, adhesives, protective casing, home furnishing etc. They have also been used in developing implantable medical devices and biomaterials for biomedical applications since 1958 (Pangman et al., 1958; Pangman, 1968). This is because of their desirable biocompatibility, excellent mechanical properties and long lasting durability. By capitalizing on PU's alternating chains of hard and soft segments with urethane links, one can select the right type and quantity of intermediates to develop polyurethanes with either rigid, flexible or thermoplastic elastomer structures.

3.2.1 Polyurethane (PU) Solutions

In creating any polymer solution, the interaction between polymer segments and solvent molecules is very important for successful dissolution, as the extension of high polymer molecules in solution is markedly influenced by the existence of this interaction (Kuwahara, 1963). It was therefore important to dissolve polyurethane pellets in an appropriate solvent, in order to attain a consistent and uniform solution.

After obtaining medical grade polyurethane pellets from Biomer Technology, UK, the ability of the pellets to dissolve completely in different solvents was examined. The solvents Dimethylformamide, Tetrahydrofuran, Dichloromethane, Xylene, Dioxane and Ethanol were tested in isolation and in combination at different concentrations to dissolve PU pellets. Simultaneously, various PU solute concentrations were also explored to identify the best solute-solvent combination for a timely, effective and consistent dissolution.

These solvents differ in chemical composition, polarity, viscosity, boiling point, solubility, evaporation rate, density and electrical conductivities, amongst others. Such key parameters affect polymer solubility, and the overall viscosity and surface tension of the final solution, which could in turn affect scaffold fabrication parameters, hence it is important to identify the best solvent combination.

3.2.2 PU and PU-HA Scaffold Materials

All the scaffolds fabricated as part of this study were polyurethane based. Three different aromatic medical grade polyether-urethanes obtained from Biomer Technology, UK, were used. The polymers, listed below, were composed of 4,4'-diphenylmethane diisocyanate, polyether diol, and 1,4 butane diol, and had different molecular weights. Mn and Mw are measured in g/mol.

1. Z1A1 (Mn-148,654 Mw-286,902, PD-1.93)

2. Z3A1 (Mn-143,566 Mw-272,857, PD-1.90)

3. Z9A1 (Mn-100,428 Mw-197,459, PD-1.97)

For scaffold fabrication, all concentrations of polyurethane pellets were dissolved in Dimethylformamide (DMF) and Tetrahydrofuran (THF) solvents, obtained from Sigma Aldrich, UK and Fisher Scientific, UK, respectively. Additionally, all fabricated composite scaffolds were prepared from PU solutions doped with either sintered micro HA (<5 μm) from Captal® S, Plasma Biotal, UK or nano-sized HA particles (<200 nm) from Sigma Aldrich, UK.

3.2.2.1 Optimizing Solution Concentration

Highly polar and organic solvents DMF and THF are popularly used in dissolving and synthesising polyurethane (Khil et al., 2003; Gorna K., 2006; Tsui and Gogolewski, 2009). They were also found to be the best amongst all the solvents tested for dissolving the PU pellets used in this study, and were therefore used in making all scaffold fabricating solutions.

For Z9A1, PU solutions with concentrations of 12-32 wt% in 100% DMF, 70/30 DMF/THF and 50/50 DMF/THF solvents were prepared, whilst solutions of 13-18 wt% in similar solvent combinations were made for Z3A1. For Z1A1, 10-20 wt% in 100% DMF, 70/30 DMF/THF, 50/50 DMF/THF and 100% THF solvents were prepared

3.2. POLYURETHANE

whilst 12-20 wt% of Tecoflex solutions in 100% DMF and 80/20 DMF/THF solvent combinations were also made.

These solutions are summarized in table 3.1 on page 68. In all preparations, solutions were stirred with magnetic beads on the UC151 ceramic plate stirrer for a period of 24 hours and a rotation speed of 500-600 rpm. However, extremely viscous solutions were stirred for 48-72 hours.

Table 3.1: Optimization of Solution Concentration

Type of PU	wt% Conc.	Solvent Combinations(v/v)
Z1A1	10-20	100% DMF, 70/30 DMF/THF, 50/50 DMF/THF & 100% THF
Z3A1	13-20	100% DMF, 70/30 DMF/THF & 50/50 DMF/THF
Z9A1	12-32	100% DMF, 70/30 DMF/THF & 50/50 DMF/THF
Tecoflex	12-20	100% DMF & 80/20 DMF/THF

3.2.2.2 Optimum Solution Concentration

With identical chemical composition but varying molecular weights, it was established as part of this study that each of the PU pellets from the **ZnA1** series (**n**=1/3/9), had ideal solute concentrations that produced a consistent and uniform dissolution in an appropriate solvent after 24 hours of mixing.

Z1A1 pellets dissolved best at a maximum concentration of 10 wt%, whilst Z3A1 was best at 15 wt%. Additionally, Z9A1 pellets dissolved best at a maximum concentration of 25 wt% for electrospinning and 20 wt% for particulate leaching and other fabrication techniques. The dissolution process is summarized in Figure 3.1 on page 69. It was also observed that, solutions made from solvents containing a higher amount of DMF, were more viscous than solutions made with a higher THF content at the same solute concentration. Thus, 15 wt% Z3A1 in 100% DMF, was more viscous than 15 wt% Z3A1 in 50/50 DMF/THF.
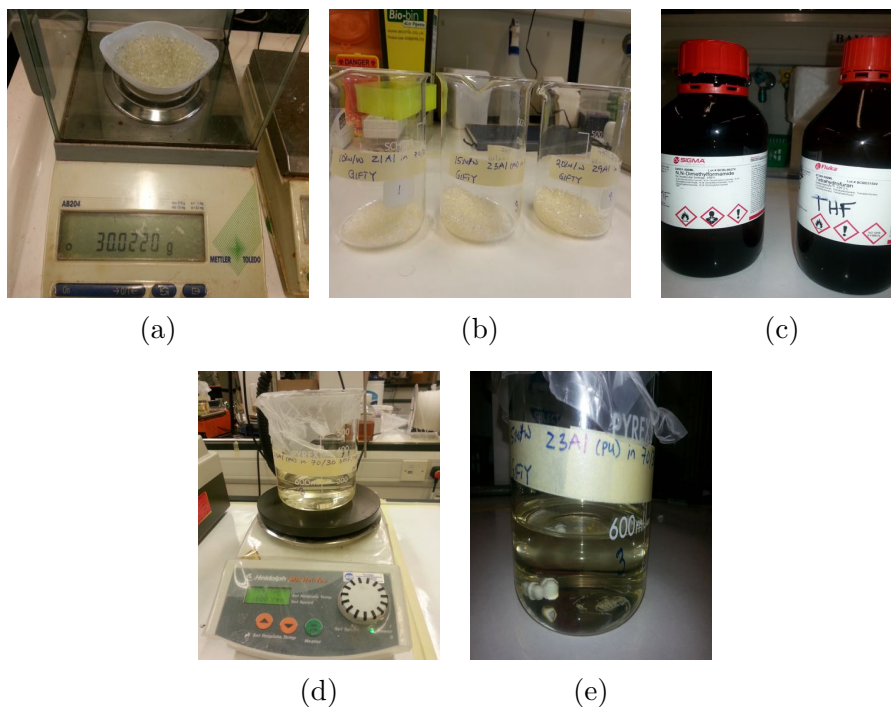
Figure 3.1: Dissolution of Z**n**A1 PU pellets (a) Z**n**A1 PU pellets being measured on a balance (b) Measured Z**n**A1 PU pellets in glass beakers (c) DMF and THF solvents (d) Z**n**A1 PU solution being stirred on a mixer (e) Z**n**A1 PU Solution

3.2.3 PU-HA Composite Solutions

For composite solutions, 15 wt% Z3A1 in 70/30 DMF/THF PU solutions were doped with either sintered micro HA ($<5 \mu$m, Captal® S, Plasma Biotal, UK) or nano-sized HA (<200 nm, Sigma Aldrich, UK) particles in a ratio of 3:1, PU: HA for most solutions. However, some composite solutions containing were made with combined nano and micro-HA particles in a ratio of 3:0.5:0.5, PU: mHA: nHA, were also prepared and simply denoted as PU:cHA.

For Z9A1 composites, 25 wt% Z9A1 in 70/30 DMF/THF was doped with either nano and micro-HA particles in a ratio of 5:1 PU: HA. Note that, the 25 wt% concentration of Z9A1 used for composite solutions is lower than the initial 27 wt% used in non-composite formulations. This is because the 27 wt% PU solutions were too viscous to enable adequate distribution of HA particles. In all preparations, doping with HA particles was performed by physical mixing on the UC151 ceramic plate stirrer, using magnetic beads at a rotation speed of 500 rpm for 24 hours at room temperature.

3.3 Scaffold Fabrication

A scaffold is a well-designed three-dimensional template used to guide tissue formation *in vitro* and/or *in vivo*. Scaffolds enhance cell attachment and distribution, promote cell ingrowth, support the synthesis and organization of extracellular matrix, transportation of other biological molecules, and ultimately, facilitate the replacement of damaged functional tissue and organs.

Ideally, a scaffold should posses a high surface area, inter-connected porosity and have an optimum pore size. Additionally, it should present with desirable mechanical properties and maintain structural tissue integrity during development and function. It should also be biocompatible and facilitate cell adhesion, migration and growth, and also promote differentiation.

Electrospinning, freeze drying, particulate leaching and freeze extraction were the main fabrication methods investigated as part of this project. PU-only and PU-HA composites solutions were used to engineer scaffolds aimed at enhancing bone regeneration and also for developing an *in vitro* bone model for implant testing.

3.3.1 Electrospinning Fabrication Technique

Electrospinning is a scaffold fabrication technique widely used for creating fibres with diameters in the nanoscale or microscale range. It is an advantageous fabrication method as it produces scaffolds with fibres that mimic the extracellular matrix structure. The extracellular matrix in the body is a complex three-dimensional network for cell growth, proliferation and differentiation, and consists of a cellular matrix of nanofibres with nanopores that create various local micro-environments (Zhang et al., 2005).

The electrospinning set-up comprises of a syringe pump (one or more), a high voltage source and either a static or rotating collector drum, as shown in Figure 3.2 on page 71. During operation, a high voltage (usually above 12 kV) is applied to the capillary tube filled with polymer solution and held at the tip of the capillary via surface tension.

Figure 3.2: The Electrospinning Set-Up

This is followed by a mutual charge repulsion caused by the application of an induced electrical field within the polymer solution, which directly opposes the surface tension of the polymer solution. As the intensity of the electrical field increases, the charge repulsion overcomes the surface tension to form a polymer jet. Finally, the ejected polymer jets repel each other as the solvent evaporates to form fibres, whilst travelling to the grounded collector (Lu et al., 2013).

3.3.1.1 Optimization of Electrospinning Parameters

Electrospun scaffolds with different fibre morphology and thickness can be produced by alternating intrinsic solution properties, e.g. viscosity, conductivity and surface tension. Additionally, operational conditions such as humidity, temperature, the hydrostatic pressure in the capillary tube, strength of the electrical field applied, and distance between the tip and collector can also affect the structure of fibres. These properties were investigated as part of this study to find the appropriate set of conditions needed to spin PU-only and PU-HA composite scaffolds.

The optimization process was carried out with either a single or combined set of syringes containing a PU-only solution. A high voltage of +15-21 kV was connected to the tip of 20 gauge luer stub adapter(s) to charge the polymer solution and cause jet formation at a flow rate of 3-5 ml/hr and a tip to collector distance of 15-25 cm. A mat of random polymeric jets was collected on an aluminium foil wrapped around a grounded

71

mandrel, rotating at the rate of 145-300 rpm. At the end of each process, the aluminium foil was removed and dried in a vacuum oven at a negative pressure of 1020 mBar for 12 hours to evaporate any remaining solvent.

3.3.1.2   Non-Aligned and Aligned Electrospinning Parameters

After optimizing parameters of solution concentration, tip to collector distance, high voltage, flow rate, number of needles, and speed of the rotating drum, a protocol was developed for creating electrospun PU-only and PU-HA composite scaffolds.

To create random electrospun scaffolds, either PU-only or PU-HA composite solutions were placed into four 5 ml syringes with 20 gauge luer stub adapters and spun at a voltage of + 16.5 kV, a flow rate of 3 ml/hr and a tip to collector distance of 20 cm, at room temperature. A mat of randomly orientated polymeric fibres was collected on a sheet of aluminium foil wrapped around a grounded metallic mandrel, rotating at 150 rpm for all non-aligned scaffolds with the exception of R_Z3-PU, R_Z3-mHA and R_Z3-nHA from the Z3A1 composite scaffold group, which were electrospun at a rotation speed of 300 rpm. After each electrospinning process, the aluminium foil was removed and the fibre mat was dried in a vacuum oven at a negative pressure of 1020 mBar for 12 hours to evaporate any remaining solvent.

To create aligned Z3A1 electrospun scaffolds, the above procedure was repeated with a modified speed of the rotating drum. Thus, for experiments in which aligned and non aligned Z3 scaffolds were directly compared, the speed was 300 rpm for non-aligned and 1300 for aligned fibre scaffolds. Solvent and electrospinning conditions used in creating scaffolds for biological characterization are discussed in Section **3.7.3.2** on page 94 of this chapter and summarized in table 3.2 on page 73.

3.3.2   Particulate Leaching Fabrication Technique

Particulate leaching is a relatively simple and common technique used to fabricate scaffolds for various tissue engineering applications. It consists of combining either salt or sugar particles of a particular size (as porogens) with polymer solution in a predefined

Table 3.2: Parameters used in preparing electrospun scaffolds for biological characterization

Name	PU wt%	HA wt%	Vol. ratio of DMF (%)	Vol. ratio of THF (%)	Spin Speed (rpm)
Z9-100	27	0	100	0	150
Z9-70	27	0	70	30	150
Z9-50	27	0	50	50	150
Z3-100	15	0	100	0	150
Z3-70	15	0	70	30	150
Z3-50	15	0	50	50	150
Z9-PU	25	0	70	30	150
Z9-mHA	25	5	70	30	150
Z9-nHA	25	5	70	30	150
R_Z3-PU	15	0	70	30	300
R_Z3-mHA	15	5	70	30	300
R_Z3-nHA	15	5	70	30	300
A_Z3-PU	15	0	70	30	1300
A_Z3-mHA	15	5	70	30	1300
A_Z3-nHA	15	5	70	30	1300

mold for a period of time to allow the solvent to evaporate. After the solvent has evaporated, the sugar or salt particles, which dissolve in water are leached away to obtain a porous three dimensional scaffold.

Particulate leaching is advantageous for creating thicker 3D scaffolds with particular pore sizes and improved pore interconnectivity, as the pore size can be controlled by the size of the porogen crystals and its porosity by altering the salt/polymer ratio.

3.3.2.1 Particulate Leaching with Sugar Particles

In making initial porous scaffolds by particulate leaching, samples were prepared using 1.4 g of granulated sugar particles with an estimated size of 200 μm as a porogen. The sugar particles were added to 15 wt% or 25 wt% Z9A1 solutions made from 100% DMF solvent, and stirred. The solutions were then poured into glass disks and the solvent was evaporated under vacuum for 24 hours. Enough distilled water was poured into the glass disk to cover the entire surface of the scaffold and for the sugar particles to leach out over

4 day period. The water was changed every 24 hours.

3.3.2.2 Particulate Leaching with Salt Particles

Due to the difficulty experienced with leaching sugar particles from scaffolds manufactured with the PL technique, two novel particulate leaching casting techniques were developed using salt particles with an estimated size of about 250 μm as a porogen. These included a layer-by-layer casting technique and a physical mixing technique.

3.3.2.2.1 Layer-by-Layer Particulate Leaching (LbL-PL)

The layer-by-layer casting technique as its name suggests, consisted of adding alternating layers of polymer and salt in a glass disk. In a fume cupboard, a 100 mm glass disk was first filled with 17.5 g of salt, before 12 ml of polymer or composite solution was evenly distributed onto the salt platform. Three more layers of 17.5 g of salt and 12 ml of solution were added in an alternating pattern before finally adding 10 g of salt onto the surface of the cast to prevent a thick non-porous polymer surface. This process is illustrated in Figure 3.3 on page 74.

(a)	(b)	(c)	(d)
(e)	(f)	(g)	(h)
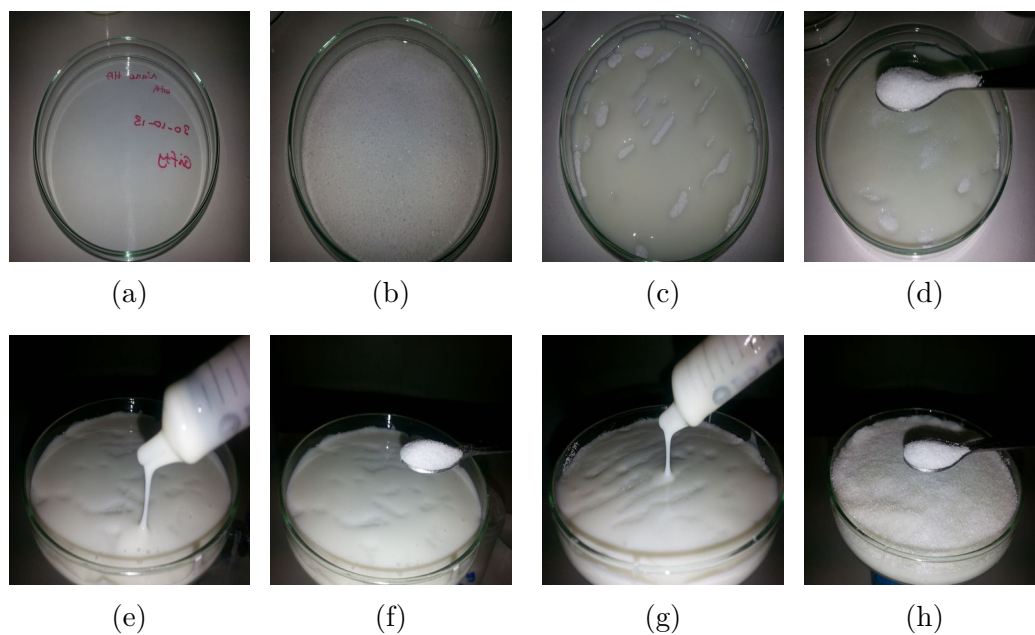
Figure 3.3: Layer-by-Layer Particulate Leaching Protocol (a) Empty Glass Disk (b) 1st Salt Layer (c) 1st Solution Layer (d) 2nd Salt Layer (e) 2nd Solution Layer (f) 3rd Salt Layer (g) 3rd Solution Layer (h) Final Salt Layer

The cast was then allowed to solidify for 4 days through solvent evaporation, before leaching the salt particles with 2000 ml of deionised water on a rotating spinner at a rate of 600 rpm for 4 days. The water was changed every 24 hours. Once all the salt had been removed, the porous construct was dried at room temperature in a fume cupboard for 2 days. The leaching out and drying process is shown in Figure 3.4 on page 75.

(a)   (b)
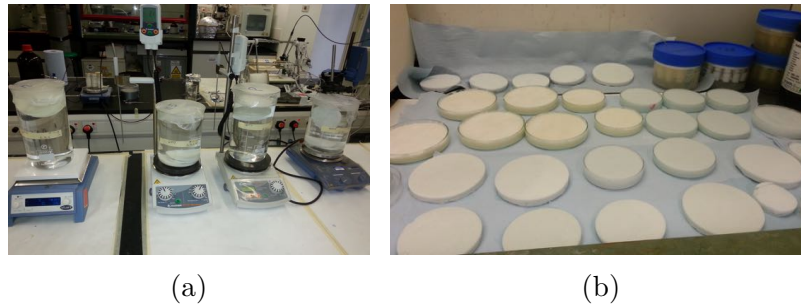
Figure 3.4: Leaching and drying stages of the PL technique (a) Leaching salt particles from solidified cast (b) Drying porous PL scaffolds in a fume cupboard

In developing a protocol for the layer-by-layer casting technique, all the three types of polyurethanes in the ZnA1 series were examined. The technique was used for creating PU-only scaffolds from 10 wt% Z1A1 solution, 15 wt% Z3A1 solutions and 20 wt% Z9A1 solutions made with 100% DMF solvent. However, to allow for consistency and uniformity in scaffold fabrication, PU-only particulate leached scaffolds used for biological characterization were made from Z3A1 solutions prepared with 70/30 DMF/THF solvent.

To create composite scaffolds, Z3A1 PU solutions were doped with either micro, nano or combined micro and nano-sized HA particles in the ratio of 3:1, PU:HA. Additionally, micro HA composites with higher amounts of HA in the ratio 2:1, PU:HA, were also created to access the effect of incorporating high HA quantities on scaffold fabrication.

Homogenized PL Scaffolds (H-PL)

Homogenization is the process of further reducing the size of a substance to extremely small particles and uniformly distributing it throughout a fluid. In order to produce composite scaffolds with improved mechanical properties, a homogenizer was used to carefully mix HA particles with the PU solution.

Combining polyurethane with hydroxyapatite has been reported in literature to

improve the mechanical properties of the resulting composite, as long as a strong interfacial bond strength is established between the ceramic phase and the polymer matrix (Attawia et al., 1995; Boccaccini and Maquet, 2003; Martinez-Valencia et al., 2011). It was therefore hypothesised that, mixing HA particles using a homogenizer could greatly improve the interfacial bond between the PU solution and the particles, as compared to, incorporating particles by just physical mixing with magnetic beads on ceramic plate stirrer.

The homogenizer was used to create composite PU-HA solutions with nano, micro and combined HA particles in a ratio of 3:1 for PU:mHA and PU:nHA composites, and 3:0.5:0.5 for PU:mHA:nHA (or simply as PU:cHA) for combined HA composites. Prior to scaffold fabrication,previously synthesized 15 wt% Z3A1 in 70/30 DMF/THF PU solutions were homogenized with the HA particles at 5000 rpm for 20 mins. H-PL composite scaffolds were then fabricated by the layer-by-layer method described in Section **3.3.2.2.1** on page 74.

3.3.2.2.2   Physical Mixing Particulate Leaching Technique(PM-PL)

The LbL-PL technique took an average of 50 mins to cast scaffold on a glass disk. Although this is an effective fabrication method for making thicker and highly porous 3D scaffolds, the length of time it took to reproduce a large number of glass disks was significantly long. Therefore, a more efficient mass production method for creating reproducible PL scaffolds in a shorter period of time was needed. A novel physical mixing particulate leaching protocol was therefore developed to address this limitation. The modified technique required as little as 5 mins to efficiently create a PM-PL scaffold, which was a tenth of the time needed to create a LbL-PL scaffold.

The process as shown in Figure 3.5 on page 77, consisted of adding 90 g of salt porogen into a 120 mm glass disk. 48 ml of polymer or composite solution was then added to the salt in the disk and rigorously stirred with a metallic spatula for 5 mins or until a homogeneous dispersion was attained. A further 12 ml of polymer or composite solution was then added to the dispersion and it was rigorously stirred again. Finally, the 10 g of

salt was used to cover the surface of the cast to prevent a non-porous surface. A total of 100 g of salt was mixed with 60 ml of solution in a 120 mm glass disk whilst 80 g was used with 48 ml of solution in a 100 ml glass disk. Solutions used for fabricating PM-PL scaffolds had the same composition to those used in making homogenized scaffolds.
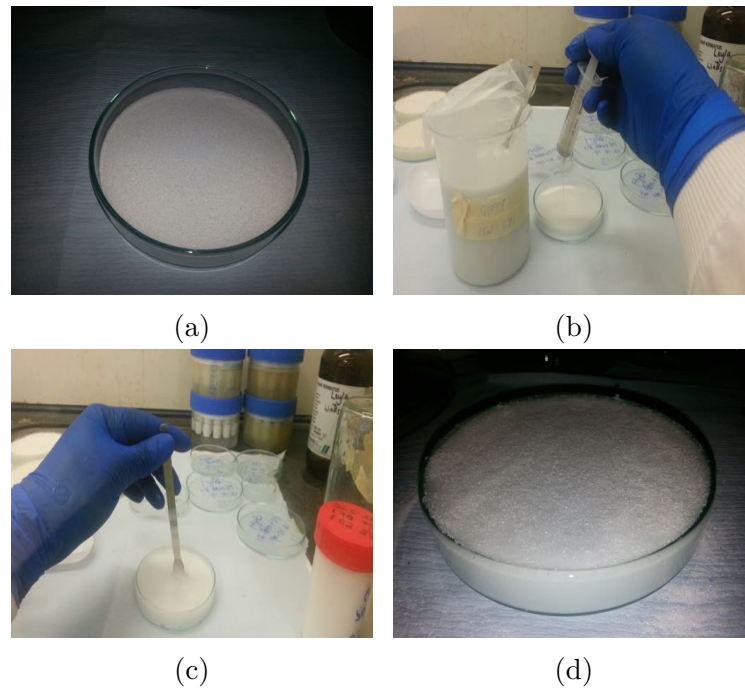
Figure 3.5: PM-PL technique (a) Salt porogen in glass disk (b) Adding polymer/composite solution (c) Physical stirring with spatula (d) Finished cast topped with salt

3.3.3 Freeze Drying Fabrication Technique

Freeze drying is a low-pressure, low-temperature, condensation process widely used for manufacturing pharmaceuticals, biotech products and emergency food supplies. The technique is also gradually becoming a popular fabricating method for creating porous scaffolds (Haugh et al., 2009; Lv and Feng, 2006), due to its versatile and simple approach to controlling pore structures. The ultimate goal of freeze drying is to create a stable material by removing solvent from solutions in a manner such that, the sensitive molecular structure of the active substances are least disturbed (Ganguly et al., 2012).

This is done by a three-stage process, which consists of unidirectional freezing of slurries, followed by the sublimation of crystals and subsequent sintering. This creates

a porous body with unidirectionally aligned channels, where pores are a replica of the solvent crystals. In effect, pore structures in freeze drying can be easily controlled with the amount of solid contents in slurry, freezing conditions and sintering temperatures (Jeon et al., 2015).

As part of this project, 8 solutions of either 15 wt% or 20 wt% of Z9A1 or Z3A1 PU solutions, made with either 70/30 DMF/THF or 50/50 DMF/THF, solvents were prepared as described in Section **3.2.2.2** on page 68. The solutions were poured into glass disks and lyophilized with a freeze dryer at Sheffield Hallam University.

For the freeze drying process, samples were initially frozen at a temperature of -99 °C and a pressure of 15 mBar for an hour, after which the pressure was reduced from 15 mBar to 10 mBar for 5 hours, and then for minute intervals at 6, 4, 5, 3 and 2 mbar to allow the solvent to sublimate. The pressure was further reduced to 1 mBar for an hour and then to 0 mBar for almost 21 hours by which time complete sublimation had occurred. Finally, the pressure was gradually increased from 0 to 10 mBar in the last 10 minutes to create rigid porous PU scaffolds. The entire process lasted about 28 hours.

3.3.4 Freeze Extraction Fabrication Technique

Phase separation is the process of transforming a polymer in a controlled manner, from a liquid state to a solid state. It can be initiated by solvent evaporation as in the case of solvent casting, thermal precipitation or by precipitation with a non-solvent (Tsui and Gogolewski, 2009). Similar to freeze drying, freeze extraction is a form of phase separation.

It involves a homogeneous multicomponent system which becomes thermodynamically unstable under certain conditions, and hence separates into more than one phase in order to lower the system's free energy. A polymer solution undergoing freeze extraction would separate into two phases, a polymer-rich phase and a polymer-lean phase. Upon removal of the solvent, the polymer-rich phase subsequently solidifies. Freeze extraction, which is a solid-liquid type of phase separation, can be achieved by lowering the temperature in a polymer solution to induce solvent crystallization. Upon removal of the solvent crystals

through solvent exchange and solid precipitation, the space originally taken by the solvent crystals becomes pores, creating a porous scaffold for tissue engineering (Ma, 2004).

The freeze extraction method was used in fabricating thicker scaffolds as part of this project. 20 wt% Z9A1, 15 wt% Z3A1 and 10 wt% Z1A1 solutions in 100% DMF solvent were prepared as described in Section **3.2.2.2** on page 68. The solutions were poured into individual glass disks and frozen at different temperatures of -196 °C, -80 °C, -20 °C and also at +20 °C (solvent casting) for 8 hours, to investigate the best temperature for creating highly interconnected porous PU scaffolds with uniform pore sizes. After 8 hours, 20 ml of distilled water was poured unto each polymer cast to cover the entire surface and precipitate the PU scaffolds at room temperature for 4 hours. The scaffolds were then removed from the glass molds and allowed to dry at room temperature for 24 hours.

3.4   Physical Characterization

This section of the chapter outlines various physical characterization techniques performed on fabricated scaffolds to examine detailed morphological features. It consists of scanning electron microscopy and micro-computed tomography investigations into surface features, internal structures, fibre diameter and orientation, pore size and pore interconnectivity, and overall porosity of fabrication scaffolds. The section also includes various physical processing techniques carried out as part of sample preparation prior to biological characterization.

3.4.1   Scanning Electron Microscopy (SEM)

The Philips XL-20 scanning electron microscope at the Department of Biomedical Science of the University of Sheffield was used to examine morphological and topographical details of fabricated scaffolds. Prior to imaging, cut and dried samples of scaffolds were mounted unto SEM studs and sputter-coated with gold powder. Coated scaffolds were imaged at an accelerating voltage of 20 kV. For electrospun mats, fibre diameter and

orientation, inter-particle distance and bead formation were investigated with SEM whilst pore diameter, surface roughness and porosity were investigated for scaffolds fabricated using the particulate leaching, freeze drying and freeze extraction techniques.

3.4.1.1   SEM of Electrospun Scaffolds

SEM was used to examine morphological and topographical details of the top and bottom surfaces of electrospun scaffolds. Prior to imaging, samples were mounted onto 12.5 mm aluminium stubs using double-sided carbon adhesive tabs (12 mm) or sticky tabs (Agar Scientific, UK), and sputter-coated with gold powder once. Coated scaffolds were imaged at a spot size of 3.0 and a magnification of 1250x.

Average fibre diameter and orientation, inter-particle distance and the size of formed beads were analyzed using ImageJ software version 1.48 and the results exported as Microsoft Excel files. The Excel results were then binned with MATLAB **R**2014**b** software to attain an average distribution of fibre diameters. The bulk porosity of electrospun fibres was also calculated as shown in Equation 3.1 below.

$$\text{Bulk Porosity} = \left\{ \frac{Density\ of\ Electrospun\ Scaffold}{Density\ of\ Plain\ Polyurethane} \right\} \times 100\% \qquad (3.1)$$

3.4.1.2   SEM of Particulate Leached, Freeze Dried & Extracted Scaffolds

SEM was used to examine pore diameter and shape, surface roughness, porosity, presence of HA and other impurities on the top of particulate leached, freeze dried and freeze extracted scaffolds. It was also used to image along the scaffold's cross-section to explore pore interconnectivity and potential non-porous regions.

Before imaging, samples were sectioned and mounted onto 25 mm aluminium stubs using Leit adhesive carbon tabs (25 mm) or silver paste (Agar Scientific, UK) to improve electrical conductivity and facilitate detailed imaging. Once securely mounted, the samples were sputter-coated with gold powder three times to create an ample conductive layer of metal on the sample. This suppressed surface charging, reduced thermal damage and improved the emission of secondary electron signal, allowing the scaffold to conduct

evenly and posses a homogeneous surface needed for topographical analysis and imaging (Leslie and Mitchell, 2007).

The surface of coated scaffolds were imaged at a spot size of 3.0 and at field of views with scale bars of 20 μm, 50 μm, 100 μm, 200 μm, 500 μm and 1 mm. The cross-section of coated samples was imaged at a scale bar of 2 mm.

3.4.1.3 SEM of Nano-HA, Micro-HA & Salt Particles

Sintered micro-HA from Captal® S Plasma Biotal, UK, nano-sized HA particles from Sigma Aldrich, UK, cooking salt and everyday value table salt from TESCO, UK used for particulate leaching, were also imaged with SEM to examine their respective particle sizes, surface area and the shape of the particles.

A spatula was used to scoop a miniature portion of each particle-type, which were placed onto a clean hard surface. 12.5 mm aluminium stubs covered with double-sided carbon adhesive tabs (12 mm) (Agar Scientific, UK), were dipped into the particles and gently tapped to ensure a uniform distribution. The particles were then sputter-coated with gold powder once and imaged at an accelerating voltage of 20 kV, a spot size of 3.0, and at field of views with scale bars of 2 μm, 5 μm, 10 μm, and 20 μm for nano-HA particles; 5 μm, 10 μm, and 20 μm for micro-HA particles and 200 μm, 500 μm, 1 mm, and 2 mm for the salt particles.

3.4.2 Micro-Computed Tomography Porosity Estimation

Micro-CT is a high resolution three dimensional imaging technique that utilizes x-rays to scan cross-sections of a physical object. After imaging, the scanned images can be used to recreate a virtual 3D model of the sample without destroying the original object. Its an advantageous imaging tool as it requires minimum sample preparation, is non-destructive and allows for detailed high resolution 3D imaging in a short period.

To determine pore interconnectivity and overall porosity of particulate leached scaffolds, the Skyscan 1172 micro-CT scanner in the Bone Analysis Laboratory, Mellanby Centre for Bone Research at the University of Sheffield Medical School was used to scan

fabricated scaffolds. Acquisition conditions of 44 kV, 226 uA, no filter, with an image pixel size of 9.08 μm, a rotation step of 0.7 $^{\text{o}}$, and an exposure time of 295 ms were used to scan the dried PL scaffolds after fabrication.

The NRecon$^{\textcircled{R}}$ software version: 1.6.9.4 from Skyscan, Belgium, and a GPUReconServer engine version: 1.6.9, were used to reconstruct the acquired image slices. Approximately, 537 slices of images were generated for each sample. Reconstructed images were processed with CTAn software version: 1.13.11.0+ from SkyScan, Belgium. Selected regions of interest (ROIs) were saved and loaded as new data sets. An appropriate threshold (PU:148-high & ~40-low, mHA and nHA: 255-high & ~148-low) was then applied to the ROI's for porosity estimation and standard 3D analysis, and a 3D model was also generated for each ROI. The standard 3D analysis included calculations of the volume of open pores, volume of closed pores, total percentage porosity and connectivity.

3.4.3 Laser Cutting of Scaffolds

The Epilog Mini 40 W laser cutter from Epiloglaser, USA in the Wolfson Biomaterials Laboratory (J9, Sir Robert Hadfield Building) of the Department of Materials Science was used to cut scaffolds into appropriate sizes prior to SEM and *in vitro* cell culture, *in vivo* experiments, and other physical, chemical and mechanical characterization studies. Prior to cell culture, electrospun scaffolds were cut with vector settings at a speed of 80% and a laser power of 6% into circular disks with a diameter of 1.6 cm.

Particulate leached scaffolds required repeated cutting due to their relatively high thickness of 5-10 mm. It was therefore necessary to reduce the speed and power settings when cutting PL scaffolds to prevent burning, especially along the edges.

PL scaffolds with and without HA particles were therefore cut with vector settings at a speed of 20% and a laser power of 4% into cylindrical tubes with an internal diameter of 0.5 cm and an external diameter of 1.5 cm. PU-only scaffolds were cut repeatedly for 8 times, whilst PU-mHA and PU-nHA scaffolds were cut for 10 times to ensure a complete top to bottom precision cut.

3.4.4   Cutting of Titanium Implants

Investigating bone matrix deposition onto commercially available small orthopaedic biomaterials was the final objective of this project. Two types of titanium orthopaedic screws from Smith and Nephew, UK were used for this study. Cortex and Osteopenia titanium alloy (Ti-6Al-4V) screws were cut into smaller 10 mm length dimensions prior to cell culture.

Marked samples were securely clamped and cut with the manual AbrasiMet 250 Chop-Cutter from Buehler, Germany, located in the micro-preparation laboratory on the I-Floor of the Sir Robert Hadfield Building. As shown in Figure 3.6 on page 83, the AbrasiMet 250 was equipped with a 254x1.5x32 mm 102507 P premium cut-off wheel blade used for cutting ductile materials such as Ti & Ti-alloys and Zi & Zr-alloys.

(a)   (b)   (c)

(d)   (e)   (f)
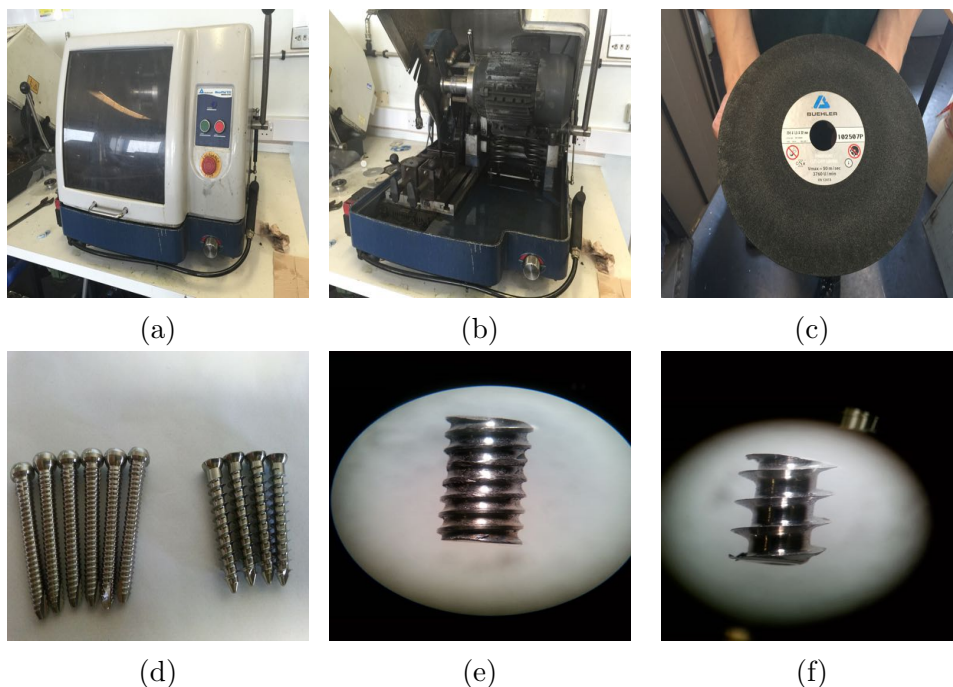
Figure 3.6: Cutting Titanium Screws (a) AbrasiMet 250 chop-cutter (b) Interior view of AbrasiMet 250 chop-cutter (c) 102507 P premium cut-off wheel (d) Cortex and Osteopenia screws prior to cutting (e) Cortex screws after cutting (f) Osteopenia screw after cutting

3.5 Chemical Characterization

Chemical-structural characterization of fabricated composites was carried out using Fourier Transform Infra-red spectroscopy (FTIR) and Raman spectroscopy in the Wolfson Biomaterials Laboratory and the S21 laboratory of the Kroto Research Institute, both at the University of Sheffield.

Spectroscopy is an analysis technique used to study the interaction of electromagnetic radiation with atoms and molecules. It operates on the principle of light scattering or absorption, which creates component energies upon interaction with matter.

All matter is made up of atoms and molecules in a stable or minimum energy state, E_0, which could be an electronic, vibrational or rotational state. With spectroscopy, a change in energy state occurs when electromagnetic radiation interacts with matter. This changes the stable state of the particles to an excited state, E^*, creating an energy difference, as shown in Equation 3.2 below. Spectroscopy is therefore an advantageous technique for analysing the chemical composition and molecular interaction of unknown materials and also useful for exploring the physical and chemical properties of materials (ur Rehman et al., 2012).

$$\text{Energy Difference} = E^* - E_0 \tag{3.2}$$

3.5.1 FTIR Spectroscopy

Fourier transform infra-red spectroscopy (FTIR) is a widely used analytical technique routinely applied to the characterization of biomaterials due to its ability to provide detailed information on the chemical composition of molecules.

An infrared spectrum generated with FTIR spectroscopy represents the chemical fingerprint of a sample, hence is useful for qualitative and quantitative analysis. It operates on the principle that chemical bonds or groups of bonds vibrate at characteristic frequencies, and that, molecules have specific vibrational modes that can be activated when hit by photons of a specific energy level (Dimitrova et al., 2009).

The Nicolet 8700 Fourier transform infra-red spectrometer (FTIR) from Thermo Fisher Scientific Inc., USA, equipped with either an Attenuated Total Reflectance (ATR) or a Photo-Acoustic (PAS) sampling cell, was used in this study. ATR sampling was used for initial characterization of random Z9A1 electrospun scaffolds whereas PAS sampling, which allows the analysis of samples without the need of sample preparation, was used for both random and aligned Z3A1 electrospun scaffolds and Z3A1 particulate leached samples.

For ATR sampling, a circular sample with a diameter of about 1 cm was placed in the sample chamber and the spectra measured at a resolution of 4 cm^{-1}, accumulating over a total of 230 scans. With PAS sampling, the PAS cell was purged with helium gas. All PAS spectra were recorded at 4 cm^{-1} resolution, accumulating over a total of 256 scans. Both ATR and PAS spectral data were acquired and processed using the OMNIC 7.4^{TM} software.

3.5.2 Raman Spectroscopy

Raman Spectroscopy is a vibrational spectroscopy technique used for analysing the chemical composition, molecular structure, and molecular interactions of non-biological samples, as well as cells and tissues. It is based on the scattering of monochromatic light or laser in the visible, near infra-red and near-ultraviolet region of the electromagnetic spectrum.

The Thermo-Electron Nicolet Raman spectrometer was used to analyse the chemical composition of fabricated electrospun and particulate leached scaffolds. It was also used to confirm the presence of hydroxyapatite in PL scaffolds before and after autoclaving.

All spectra were collected with the bench set-up described as follows. A 532 nm green laser with a power of 10 mW, a pinhole aperture of 50 μm, resolution of 6 cm^{-1}, an objective of 10x and a spot size of 2.1 μm was used to capture all data with a 10 s exposure over 3 sample accumulations. All spectral data were acquired and processed using the OMNIC 7.4^{TM} software.

3.6 Mechanical Characterization

Bone is a load bearing tissue that functions to provide structure and support to the body. Hence its mechanical features are of great importance to its ability to function effectively.

Although the mechanical properties of bone have been shown to vary at different structural levels, it is unclear whether this discrepancy is due to how bone is tested or the influence of its microstructure (Rho et al., 1998). For example, the Young's modulus of large cortical wet specimens has been shown to be tested in tension in the 14–20 GPa range (Reilly et al., 1974), whilst that of micro-machined cortical wet specimens tested in bending was 5.4 GPa (Choi et al., 1990).

As part of this study, the mechanical properties of fabricated scaffolds were analysed with the ElectroForce 3200 materials testing machine from Bose, USA. Fabricated scaffolds were cut with the Epilog laser as described in Section **3.4.3** on page 82 and measured with vernier callipers before mounting. Mounting was performed either between two tensile grips or compression plates to give a desired gauge length.

Deformation was measured by the movement of the cross-head, and load measured using a 22 N load cell for tensile tests and 450 N load cell for compression tests. The resulting load/deformation curves generated by the Wintest software$^{®}$ were easily converted to a stress-strain curves by dividing by the sample bulk cross-sectional area, as described in Section **3.6.1** and **3.6.2**, using measured parameters of thickness, width and gauge distance. Young's modulus was calculated as shown in Figure 3.7 on page 87, as a change in stress divided by change in strain in the linear portion of the curve, whilst yield was defined as the point at which the load deformation curve deviated from the straight line and yield strength as the stress at yield.

3.6.1 Tensile Mechanical Testing

Rectangular shaped electrospun scaffolds with average dimensions of about 5 mm x 20 mm were tested at a strain rate of 1 hz over a displacement of 6 mm for 100% strain deformation using the 22 N. Freeze dried scaffolds with similar dimensions was also tested
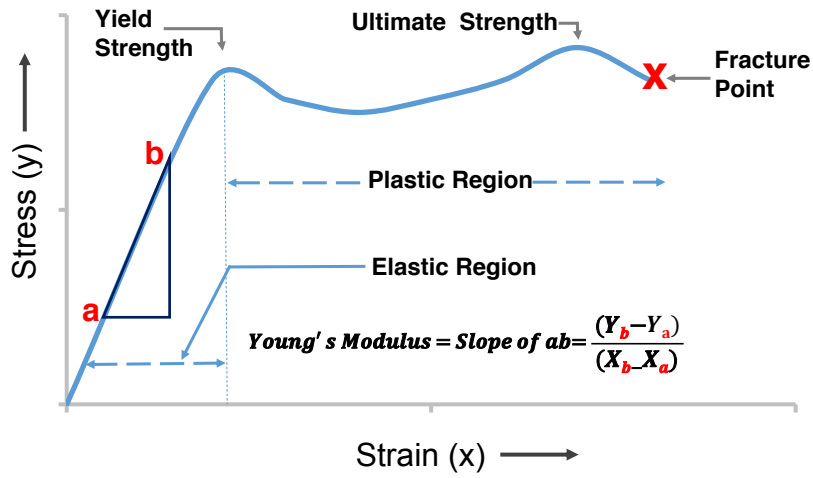
Figure 3.7: Typical stress-strain curve of a polymer

in tension using the 450 N load cell. Stress and strain in tension were calculated as shown in Equation 3.3 and 3.4 on page 87.

$$\text{Stress in Tension} = \left\{ \frac{Force}{Thickness\ of\ scaffold\ *\ Width\ of\ scaffold} \right\} \tag{3.3}$$

$$\text{Strain in Tension} = \left\{ \frac{Deformation}{Gauge\ Length\ (6\ mm)} \right\} \tag{3.4}$$

3.6.2 Compression Mechanical Testing

Cylindrical particulate leached foams with an average diameter of about 10 mm were tested in compression at a frequency of 1 hz for 50% strain deformation using the 450 N load cell. Prior to testing, the sample was placed on the lower compression plate and raised until it came into contact with the upper compression plate and the load gauge recorded a negative force reading of about -0.05 N. The plate was then clamped at that

point and auto-tared before commencing with testing. The distance between both plates, which was equivalent to the height of the sample was about 5 mm on average. Stress and strain in compression was calculated as shown in Equation 3.5 and 3.6 on page 88.

$$\text{Stress in Compression} = \left\{ \frac{Force}{pi \; * \; (radius \; of \; scaffold)^2} \right\} \tag{3.5}$$

$$\text{Strain in Compression} = \left\{ \frac{Deformation}{Height \; of \; scaffold} \right\} \tag{3.6}$$

3.7 Biological Characterization

In order to evaluate the suitability of fabricated scaffolds as useful constructs for bone tissue engineering and optimise regeneration conditions for the development of an *in vitro* model, biological characterization was carried out on both electrospun and particulate leached scaffolds. Characterization was performed using osteoblasts and progenitor cells from human or animal established cell lines. It involved seeding and culturing cells on scaffolds under physiological conditions for a period of time, for *in vitro* analysis and implanting scaffolds into animal models for *in vivo* studies.

This section of the chapter, examines various cells and cell culture mechanisms used as part of this study. It also details various cell viability and matrix production staining protocols, *in vitro* and *in vivo* histological analysis, immunohistochemistry, second harmonic generation analysis of deposited collagen matrix, micro-ct quantification of mineralized matrix, as well as scanning electron microscopy.

3.7.1 Cultured Cells

As part of biological characterization, the MLO-A5 osteoblast-like cell line kindly donated by Professor Lynda Bonewald and Human Embryonic Stem Cell Mesenchymal Progenitor cells (hES-MPs) from Cellartis, Sweden were cultured in both 2-D and 3-D environments. In 2-D, cells were cultured in well plates and T75 flasks to study cell morphology and

viability, and also to proliferate sufficient cell quantities for other experiments. In 3-D, cells were seeded on fabricated scaffolds to investigate cell attachment and migration, proliferation, viability and differentiation, matrix production and mineralization, and also to characterize the nature of bone matrix produced. Earlier on in the project, preliminary cell culture experiments also utilised MG-63 osteosarcoma cells to practice cell culturing techniques and develop standardization curves.

3.7.1.1 MLO-A5 Murine Cells

MLO-A5 cells derived from a transgenic mouse was developed as a model for studying osteoblast to osetocyte differentiation due to the difficulty associated with the isolation and culture of primary osteocytes (Kato et al., 2001). These osteoblastic cells have characteristics of postosteoblast/preosteocytes and are very large in size ($\sim 100\,\mu$m). They express late osteoblast markers such as bone sialoprotein, high levels of alkaline phosphate and osteoclacin (Rosser and Bonewald, 2012). In culture, these cells rapidly mineralize in sheets rather than in nodules within three days of culture, and hence ideal for studying bone mineralization (Kato et al., 2001). The MLO-A5 cells are also extremely sensitive to fluid flow shear stress (Bonewald and Johnson, 2008) as compared to other osteoblast and fibroblast cell lines, and have been used in studying the effect of mechanical loading on biomineralization (Sittichockechaiwut et al., 2009) and the osteoblast to osteocyte differentiation process (Dallas et al., 2009).

3.7.1.2 Human Embryonic Stem Cells

Human mesenchymal stem cells (hMSCs) aspirated from bone marrow and other adult tissues are a suitable cell choice for bone regeneration, they posses the ability to differentiate toward the osteogenic lineage (Pittenger et al., 1999). However, despite their promise, hMSCs present with several limitations for tissue engineering which may interfere with an optimal clinical outcome. This includes the possibility of using cells with a high degree of heterogeneity resulting from inefficient aspiration and isolation methods (Ho et al., 2008). Also, limited proliferation potential (Bonab et al., 2006),

progressive loss of functionality upon protracted *in vitro* expansion (Baxter et al., 2004), and age-associated decline in cellular fitness restrict the use of hMSCs for large-scale bone regeneration (Stolzing et al., 2008).

On the other hand, human embryonic stem cell mesenchymal progenitor cells (hES-MPs) derived from human embryonic stem cells present a suitable stem cell line alternative to hMSC's (de Peppo et al., 2010). As hES-MPs display significantly higher proliferation ability and faster mineralization capacity *in vitro*, in addition to displaying lower amounts of HLA class II proteins compared to hMSCs. This suggests that hES-MPs may be well qualified for the successful treatment of musculoskeletal conditions. De Peppo *et al*, compared the dynamic culture of hMSC's and hESMPs on porous 3D coral scaffolds and reported findings that indicate that, hES-MPs is a suitable alternative cell source to hMSCs, and hold great potential for bone tissue engineering applications (de Peppo et al., 2012).

3.7.1.3   MG-63 Human Osteosarcoma Cells

Finally, MG-63 cells, another popular human osteoblastic cell source used in bone tissue engineering were utilised in this study. Similar to other osteosarcoma-derived cell lines such as Saos-2 and U-2 OS, they proliferate more rapidly than non-cancerous osteoblast-like cells and attach firmly to culture surfaces (Clover and Gowen, 1994). However, compared to osteoblasts derived from normal human bone, these cancerous cells are derived from malignant bone tumours (osteosarcomas) and exhibit heterogeneous but characteristic labelling profiles. Hence they produce extracellular matrix with different compositions. They also differ significantly from normal osteoblasts in terms of collagen types III and IV production, proliferation kinetics and osteoid formation (Pautke et al., 2004).

3.7.2   2-Dimensional Cell Culture

For all biological experiments, MLO-A5 cells were used at passage 29-35, whilst hES-MPs and MG-63 cells were kept at passage 2-8 and passage 68-75, respectively. For all 2D

experiments, cells were proliferated in T75 flasks and cultured in well plates for a period of time, at 37 °C in a humidified incubator supplied with 5% CO_2. All reagents were obtained from Sigma-Aldrich, UK unless otherwise stated.

Working culture media for MLO-A5 and MG-63 cells was made of Dulbeccos Modified Eagles Medium (DMEM) from Biosera, UK, supplemented with 10% fetal calf serum (FCS), 1% L-glutamine (L-G), 1% penicillin and streptomycin (P/S), and 0.25% Fungizone (F), all at volume by volume concentrations. Additionally, working culture media for hES-MP cells was Alpha Modified Eagles Medium (α-MEM) from Lonza, UK, supplemented with 10% fetal calf serum, 1% L-glutamine, 1% penicillin and streptomycin, all at volume by volume concentrations and 4 nM fibroblast growth factor-basic recombinant human (β-FGF). All T75 flasks used in culturing hES-MP cells were coated with 0.1% gelatin to enhance cell adhesion.

To facilitate osteogenesis, aid phosphate deposition and collagen hydroxylation, and also enhance cell and mineral growth, all working media was supplemented with 50 μg/ml AA_2P and 5 mM βGP. As both agents are essential for bone cell matrix maturation and mineralization (Beresford et al., 1993). Additionally, hES-MP working media was further supplemented with 100 nM of Dexamethasone (Dex) to stimulate the differentiation of progenitor cells towards an osteogenic lineage once β-FGF was removed.

3.7.2.1 Thawing and freezing down of cells

In order to have an adequate number of each cell type at identical passage numbers, thawing, expansion and freezing of cells was frequently carried out as part of this project. This was to enhance reproducibility of experiments and prevent the cells from loosing their distinct morphological and biological characteristics.

3.7.2.1.1 Thawing Cells

To resurrect or thaw cells that had previously been frozen in the liquid nitrogen, 20 ml of working media in a universal tube was warmed in a water bath at 37 °C for 10 mins. One cell vial containing approximately 1 ml of cell suspension was then removed from the liquid nitrogen and thawed in the water bath for about 4 mins or until there was only a

small ball of ice in the vial. Both the vial and universal tube containing media were then transferred to the tissue culture cabinet and mixed to attain 21 ml in the universal tube.

The universal tube was then centrifuged at 1000 rpm for 5 mins after which the supernatant was disposed off. The remaining cell pellet was then re-suspended in 1 ml of working media and split into 1:20 for MLO-A5 cells, and 1:10 for hES-MPs and MG-63 cells, before being transferred into a T75 flask containing about 14 ml of working media. The flasks were gently rocked and then placed in an incubator and media was changed every 2-3 days. All cells were monitored for proliferation and morphological changes and passaged into new T75 flasks at about 70-80% confluency for cell expansion, using trypsin-EDTA.

3.7.2.1.2 Freezing Cells

Alternatively, to freeze down cells at a particular passage number after culture, old media was removed from each T75 flask, before the flask was washed with Phosphate-Buffer Saline (PBS) twice to remove traces of remaining media. 3 ml of trypsin-EDTA was added to each flask and incubated to aid in detaching cells from the bottom of the flask. After 5 mins, the flask was removed and checked under the microscope to confirm that all cells had completely detached.

12 ml of fresh media was then added to the flask to stop the action of the trypsin-EDTA and attain a total of 15 ml which was placed in a universal tube and centrifuged at 1000 rpm for 5 mins. The supernatant was disposed and the pellet re-suspended in media. 15 μl of cell suspension was placed in the heamocytometer and the cells countered under a light microscope. The total number of suspended cells in media was estimated from the average number of counted cells. The appropriate volume of cell suspension needed to attain the nearest million cells was calculated, aspirated and re-centrifuged.

Freezing media containing 90% FCS and 10% DMSO was added to the cell pellet and re-suspended. The cell suspension was finally aliquoted into cyrovials and frozen in an isopropanol container, at 1 million cells/ml for 24 hours at -80 °C, before being transferred to the liquid nitrogen for long-term storage.

3.7.2.2   2D Experiments

For each 2D experiment, the required number of cells was calculated and added to the required volume of media in a well plate and gently rocked to ensure an even distribution. Media was changed every two days and the cells were examined for differences in cell morphology and proliferation density using light microscopy.

Standard calibration curves were created in a similar culturing protocol. In brief, cells were seeded at different densities in polystyrene tissue culture well plates and allowed to attach for about 4 hours. Standard cell viability assays such as MTT or alamar blue were then performed on the seeded cells and the results used to create calibration curves.

3.7.3   3-Dimensional Cell Culture

Since the mid 1950's, the culture of cells on 2-dimensional polystyrene or glass surfaces has become a fairly routine procedure in the biological sciences. Although several key advances has been made to date, it is argued that the presentation of eukaryotic cells on a 2D surface is not an accurate representation of the extracellular matrix found in native tissue (Freshney, 2005; Tibbitt and Anseth, 2009).

Consequently, many complex biological responses such as cellular migration, apoptosis and transcriptional expression, are known to differ quite significantly when cultured in a monolayer versus a 3D environment. The argument goes further to suggest that culturing cells in a 2D monolayer is far too simple and overlooks many important parameters such as mechanical cues and communication between the cell and its matrix, which is known to enhance accurate reproduction of cell and tissue physiology (Haycock, 2011).

Additionally, a likely important criteria for tissue engineering is to be able to create a growth environment that mimics the native tissue as closely as possible, by culturing cells on a porous biocompatible scaffold. Although not all three-dimensional culture models require a scaffold, the use of scaffolds for 3D models has certainly become extremely popular. It is also known that depending on the fabrication process used, scaffolds with different architectures can be produced.

3.7. BIOLOGICAL CHARACTERIZATION

3-Dimensional cell culture as part of this study utilised MLO-A5 cells and hES-MP cells on selected electrospun and particulate leached scaffolds. This was to identify the best fabrication process, scaffold material composition and cell culture conditions that enhanced bone matrix production and facilitated long-term static culture.

3.7.3.1 Scaffold Preparation & Sterilization

Prior to cell culture on electrospun scaffolds, both random and aligned scaffold mats were placed in large petri dishes and covered with PBS for 3 days to leach out any possible remaining solvent. The scaffolds were then cut to a diameter of 1.6 cm using the Epilog laser as described in Section **3.4.3** on page 82, and sterilised with 0.1% paracetic acid for 3 hours at room temperature. After sterilization, the scaffolds were washed three times with PBS each sitting for 5 minutes to remove all traces of the peracetic acid.

Particulate leached scaffolds were cut in a similar manner, with an internal diameter of 0.5 cm and an external diameter of 1.5 cm. These scaffolds were sterilized with the S20 laboratory autoclave and not 0.1% paracetic acid. Prior to sterilization, cut scaffolds were placed in an autoclavable glass bottle containing 0.1% gelatin to promote cell attachment onto the entire scaffold.

Once sterilized, all scaffolds were securely sealed and kept in the refrigerator for 2 months and only opened under sterile conditions in a tissue culture cabinet.

3.7.3.2 Cell Culture on Electrospun Scaffolds

3D cell culture on random and aligned electrospun scaffolds utilized PU and composite scaffolds made from either Z3A1 or Z9A1 pellets. Preliminary experiments to identify the best solvent combination and solute concentration used random scaffolds denoted as Z9-100, Z9-70, Z9-50 and Z3-100, Z3-70 and Z3-50, as shown in **Table** 3.3 on page 95.

Additionally, composite scaffolds with random fibres were made with either 25 %wt Z9A1 or 15 %wt Z3A1 in 70/30 DMF/THF solvents. These PU solutions were doped with either micro or nano-sized HA particles in a ratio of 5:1 PU: HA for Z9A1 and 3:1 for Z3A1, respectively. These were subsequently denoted as Z9-PU,

Z9-mHA and Z9-nHA and Z3-PU, Z3-mHA and Z3-nHA, as shown in table 3.3. Note that this concentration of PU in the Z9A1 composite group is lower than that used in the non-composite formulations (solvent group) described above, this is because the 27 wt% PU solutions were too viscous to enable adequate distribution of HA particles.

Also, all aligned scaffolds, denoted as A_Z3-PU, A_Z3-mHA and A_Z3-nHA were fabricated in a similar manner using only 15 %wt Z3A1 in 70/30 DMF/THF solutions, with a 3:1 doping ratio for composite scaffolds. All solvent and fabricating conditions used in making electrospun scaffolds for biological characterization is summarized in table 3.2 on page 73, and also listed in the nomenclature section of this thesis.

Table 3.3: Electrospun scaffolds used for biological characterization

Electrospun Group	Scaffolds
Z9 & Z3 Random Solvent Group	Z9-100, Z9-70, Z9-50, Z3-100, Z3-70 & Z3-50
Z9 & Z3 Random Composite Group	Z9-PU, Z9-mHA, Z9-nHA, Z3-PU, Z3-mHA & Z3-nHA
Z3 Aligned Composite Group	A_Z3-PU, A_Z3-mHA & A_Z3-nHA

Initial experiments with electrospun scaffolds in the Z9 composite group, thus Z9-PU, Z9-mHA & Z9-nHA, were seeded with MLO-A5 cells at 1.5 x 10^5 cells per scaffold. This cell volume was reduced to 1.0 x 10^5 cells per scaffold for all other electrospun scaffolds as the cells become over-confluent after Day 14 and started to peel from the scaffold. Hence, cell seeding for 28 day experiments on all other fabricated electrospun scaffolds (except the Z9 composite group) was performed using stainless steel rings with either MLO-A5 at passage 33-36 or hES-MP cells at passage 3-6, at a concentration of 1.0 x 10^5 cells per scaffold in a 12 well plate with 1 ml of working media. All well plates with seeded scaffolds were incubated at 37 °C in a humidified environment with 5% CO_2 after seeding. The stainless steel rings were removed after 24 hours and an additional 1 ml of working media was added to each scaffolds, media was changed every two days during the culture period.

3.7. BIOLOGICAL CHARACTERIZATION

3.7.3.3 Particulate Leached (PL) Scaffolds used for Cell Culture

To allow for easy comparison and reduce variability in cell culture conditions only particulate leached scaffolds made with Z3A1 PU were used for 3D PL cell culture. As shown in table 3.4, layer-by-layer, homogenized and physically mixed PU-PL scaffolds were made from 15 %wt Z3A1 in 70/30 DMF/THF. Additionally, composite scaffolds doped with either micro HA or nano-sized HA particles, in a ratio of either 3:1, 2:1 or 3:0.5:0.5 PU:HA were also used for 3D biological PL analysis.

Table 3.4: PL scaffolds used for biological characterization

PL Group	Scaffolds
Layer-by-Layer	LbL-PU-only, LbL-PU+mHA(3:1), LbL-PU+mHA(2:1) & LbL-PU+nHA(3:1)
Homogenized	H-PU+mHA(3:1), H-PU+nHA(3:1) & H-PU+cHA(3:0.5:0.5)
Physically Mixed	PM-only, PM-PU+mHA(3:1), PM-PU+nHA(3:1) & PM-PU+cHA(3:0.5:0.5)

3.7.3.3.1 Optimisation of Cell Seeding Density on PL Scaffolds

As this was the first time any cell type was being cultured on the fabricated PL scaffolds, optimisation of cell seeding density was carried out prior to experimental cell culture. This was to identify the best cell quantity to scaffold volume ratio that promotes good cell attachment and sufficient coverage.

In brief, already cut and sterilized layer-by-layer PL scaffolds were placed in a 12 well plate after almost all of the gelatin solution contained in the scaffolds had been removed. 2.5 ml of DMEM working media was added to each well and incubated for 2 hours to allow the scaffold to absorb as much media as possible. The soaked scaffolds were then transferred into new well plates to avert excess or unabsorbed media. Using only MLO-A5 cells at passage 34, cells were seeded in a clockwise pattern at either 2.5×10^5, 5.0×10^5 or 7.5×10^5 cells per scaffold.

The scaffolds were then incubated for 6 hours to allow cell attachment, after which MTT cell viability assay was used to identify the best seeding density for PL scaffolds.

3.7.3.3.2 Cell Culture on PL Scaffolds

Similar to the procedure described for optimising cell seeding density on PL scaffolds, all layer-by-layer, homogenized and physically mixed PL scaffolds used for biological characterization (listed in table 3.4 on page 96 and the nomenclature section of this thesis) were seeded at 5 x 10^5 cells per scaffold with either MLOA-5 cells at passage 33-36 or hES-MP cells at passage 3-6. The scaffolds were incubated at 37 °C in a humidified environment supplied 5% CO_2 for 24 hours to allow cells to attach firmly.

After 24 hours, cell seeded scaffolds were transferred into new well plates, and osteogenic media containing 50 μg/ml Ascorbic acid-2-phosphate and 5mM βGP was added and 2.5 ml changed every two days. hES-MP osteogenic media further contained 100 nM Dexamethasone (Dex).

3.7.3.4 Cell Culture with Titanium Implants in PL Scaffolds

2 mm cortex and 3 mm osteopenia titanium alloy (Ti-6Al-4V) screws from Smith and Nephew, UK were used to investigate bone matrix deposition as part of this study. The screws were cut into smaller 10 mm length dimensions prior to cell culture as discussed in Section **3.4.4** on page 83. After cutting, the cut-ends of all screws were filed with a sand paper to attain a smooth finish, before being washed with warm water and mild soap to remove metal chippings and leftover powder. The screws were then sonicated in an ultrasound bath for 180 seconds before being sterilized in an autoclavable glass bottle containing 0.1% gelatin solution.

For biological analysis, cortex or osteopenia sterilized screws were inserted into the inner 5 mm diameter portion of PU-only and PU+mHA 3.1 layer-by-layer or physically mixed PL scaffolds, as shown in Figure 3.8 on page 98. As well as comparing two different titanium screws, two different PL fabrication methods, and PU-only vs composite scaffolds, two culture conditions using passage 34 MLO-A5 cells at 5 x 10^5 cells per scaffold were also explored with the titanium-PL experiments.

One culture condition involved inserting each screw type into either a LbL or PM PL scaffold before seeding with cells. Whilst the second culture condition involved inserting

3.7. BIOLOGICAL CHARACTERIZATION

screws the into scaffolds, after the scaffolds had been seeded and cultured cells for 28 days. The aim of comparing the two culture conditions was to investigate the best time point for inserting screws that enhanced maximum matrix deposition onto the screws(Figure 3.8).
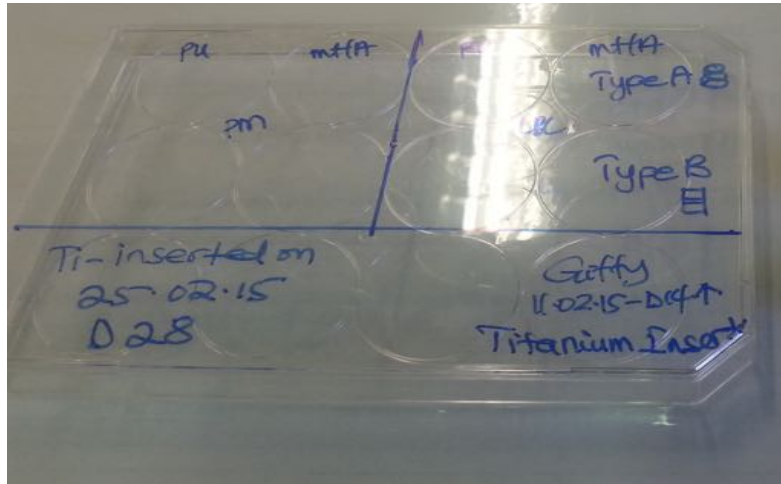
(a)
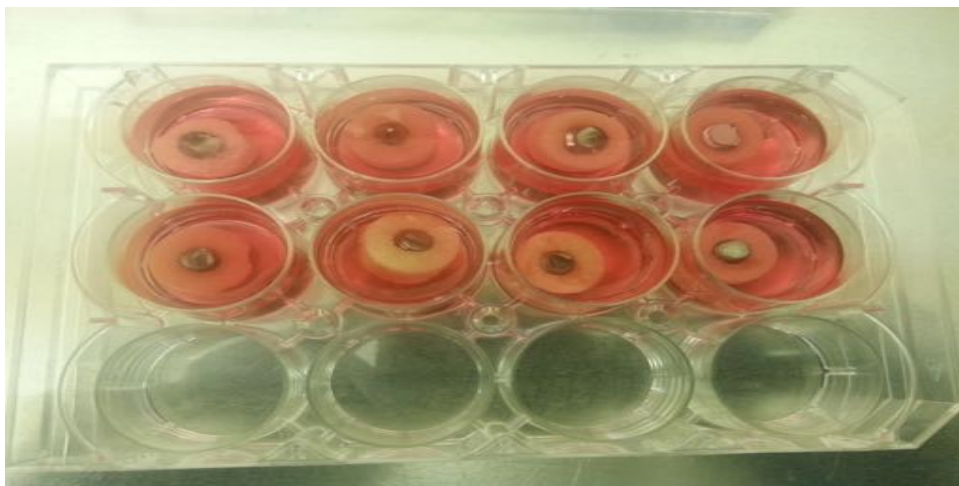
(b)

Figure 3.8: Cortex and osteopenia titanium screws in PL scaffolds

3.7.4 Cell Viability

Several cell viability assays including Alamar Blue and MTT that analyse whole populations were run as part of this study. This was to establish the number of healthy cells in a scaffold over a period of time in culture. Generally, cell viability assays operate based on membrane integrity, metabolic activity, proliferation rate or total protein content of the cell population (Gloeckner et al., 2001). Such whole populations assays are more

rapid as compared to those that analyse individual cells, but are however known to give less detailed results. Although several cell viability assays exist in literature, the choice of an optimal assay depends on the cell type, culture conditions applied, and the specific questions being asked (Stoddart, 2011).

One of the earliest and most common method for assessing cell viability is the trypan blue exclusion assay (Black and Berenbaum, 1964). This assay was used in this study to count viable cells in a heamocytometer ahead of experiments to estimate the number of viable cells ahead of cell culture. It operates on the principle that viable cells possess intact cell membranes that prevent the penetration of certain dyes, such as trypan blue, Eosin or propidium, whereas dead cells do not. Hence, dead cells can take up trypan blue, and appear blue as a consequence, as their membranes are no longer able to control the passage of macromolecules (Strober, 2001).

Furthermore, live/dead staining is a one-step staining procedure that is simple and fast, and can be directly used in cell culture media. It describes a number of potential dyes that specifically stains live cells (usually with green fluorescence) while the other dye stains dead cells (usually with red fluorescence) and is more sensitive than Trypan blue. An example is calcein AM with ethidium homodimer-1, which is membrane permeable, and cleaved by esterases in live cells to yield cytoplasmic green fluorescence. The membrane-impermeable ethidium homodimer-1 labels nucleic acids of membrane-compromised cells (i.e. dead) with red fluorescence. The ratio of live to dead cells can therefore be easily determined by simple counting (Stoddart, 2011).

Beyond trypan blue and live/dead staining, dyes which rely on the metabolic activity of cells, such as, XTT, MTT and MTS, as well as Resazurin-based methods such as Alamar Blue are also commonly used for viability analysis. Although it was not explored as part of this study, XTT and MTS have been reported to be less cytotoxic, have increased sensitivities and require fewer experimental steps as they are used in the presence of phenazine methosulphate (Scudiero et al., 1988; Cory et al., 1991).

3.7. BIOLOGICAL CHARACTERIZATION

3.7.4.1 MTT Cell Viability

MTT (3-(4,5-Dimethylthiazol-2-yl)-2,5-diphenyltetrazolium bromide) is a type of tetrazolium salt used as colorimetric reduction assay to determine the level of metabolic activity in eukaryotic cells. It was used as part of this study to investigate cell viability and proliferation after seeding MLO-A5 and hES-MPs on electrospun and PL scaffolds.

It is a versatile and popular viability assay useful for estimating cell numbers and proliferation. It is also useful for measuring cell growth in response to mitogens, antigenic stimuli, growth factors and other growth promoting reagents, for conducting cytotoxicity studies, easy identification of cell attachment on scaffolds and for deriving growth curves. Also, MTT is a very robust dye and can be metabolised by most cell types, whereas some of the newer alternatives such as MTS and XTT are not suitable for all cells (Stoddart, 2011).

MTT functions by reducing or converting water soluble yellow MTT dye to a purple formazan stain by the mitochondrial reductase enzyme in living cells. The process primarily takes place in the cytoplasm, and to a lesser extent in the mitochondria and cell membrane (Berridge and Tan, 1993; Bernas and Dobrucki, 2002). The needle-like formazan crystals produced as a result can be solubilized by mixing thoroughly in different organic solvents, mainly alcohols such as Ethanol and Isopropanol.

Using ethanol to destain has been reported to cause precipitation of proteins in the culture medium, hence, Isopropanol, an equally good solvent which lacks the adverse effects of ethanol can be used as a suitable alternative (Mosmann, 1983). Other detergents such as 10% sodium-dodecyl-sulfate, Triton X-100 and Nonidet P-40 have also been tested and used when isopropanol is incompatible (Tada et al., 1986). Although these detergents work without thorough mixing with the medium, they require overnight incubation as opposed to using alcohols which only require a few hours. Dimethyl sulfoxide has also been reported to dissolve formazan effectively (Jabbar et al., 1989).

The toxic nature of MTT however makes it only to be used once on cultured cells, hence all subsequent MTT analysis on future samples has to be done at the same conditions in order to allow for effective comparison. Additionally, organic solvents used

to destain purple formazan could cause precipitation of serum proteins, which could interfere with the absorbance reading. It is also possible for the formazan crystals to not be completely dissolved after destaining and this could lower the sensitivity of the assay (Kupcsik, 2011).

As part of this study, MTT stock solution at 12 mM (at 0.5 mg/ml) concentration was prepared by dissolving MTT powder in PBS. The solution was wrapped with foil to protect from light, and was vortexed and filtered to remove particulate materials. For each assay, scaffolds were rinsed with PBS after media had been removed from the wells. An appropriate amount of MTT stock solution was then added to each well to cover the entire scaffold before incubating at 37 °C for a period of time. The yellow MTT dye was reduced to purple formazan after the incubation period and destained with 0.125% acidified isopropanol, and its absorbance read with the spectrophotometer at 563 nm reference 630 nm.

3.7.4.1.1 MTT Cell Viability on Electrospun Scaffolds

MTT assay was carried on both aligned and random thin electrospun scaffolds on days 1, 4, 7, 14, 21 and 28 after seeding. As described above, culture media was removed from the scaffolds before being washed with 2 ml of PBS thrice, with a 5 mins waiting time between washes. 1 ml of MTT stock solution was added to each well and incubated for 40 mins in foil wrap. After incubation, the excess MTT solution was removed and the purple stain was destained with 1 ml of 0.125% acidified isopropanol before reading its absorbance with the plate reader.

3.7.4.1.2 MTT Cell Viability on PL Scaffolds

MTT assay was carried on Layer-by-Layer PL scaffolds to optimize the number of cells required for experimental cell seeding. Similar to the description of MTT on electrospun scaffolds, culture media was removed from the PL scaffolds after 6 hours of incubation and cell seeding, before being washed with 3 ml of PBS, thrice, with a 5 mins waiting time between washes. 2.5 ml of MTT stock solution was added to each well and incubated for 1 hour in foil wrap. After incubation, the MTT solution was removed and the purple stain

was destained with 2 ml of 0.125% acidified isopropanol before reading its absorbance with the plate reader.

3.7.4.2   Alamar Blue Cell Viability

Resazurin-based alamar blue assay is another popular and versatile way of measuring cell proliferation and cytotoxicity. It was routinely undertaken as part of this study to create preliminary calibration curves and also monitor continuous cell viability of PL scaffolds seeded with either MLO-A5 or hES-MP cells over a 56-day culture period.

The alamar blue assay functions by reducing resazurin, an oxidized blue and non-fluorescent dye to resorufin, a pink and highly fluorescent stain by cell activity, which can be further reduced to hydroresorufin, an uncoloured and non-fluorescent stain. The reduction process of alamar blue cell viability is likely to be by oxygen consumption through metabolism (Fields and Lancaster, 1993). Although it has been arbitrarily postulated as being reduced by mitochondrial enzymes, it is not known whether this occurs intracellularly, at the plasma membrane surface or just in the medium as a chemical reaction (De Fries and Mitsuhashi, 1995).

Compared to MTT, water soluble alamar blue is non-toxic to cells and does not need to kill the cells to obtain measurements. This allows precious cells, especially primary tissue cultures, to be re-used for further investigations, saving time and money (Ahmed et al., 1994). It is also a rapid and simple tool as it does not require the destaining step of MTT assays. Furthermore, it provides an advantage of being measured by either colourimetry or fluorimetry, although greater sensitivity has been reported when using the fluorescent property to give a reproducible and sensitive signal (O'Brien et al., 2000a).

It is however important to be careful when measuring fluorescence at higher cell densities to avoid over-reduction of alamar blue into the colourless and non-fluorescent hydroresorufin. Additionally, it is also necessary to test all assays based on reduction without any cells in the medium to determine any cross reactivity with the compound being tested (Stoddart, 2011).

During the 56-day cell culture period of PL scaffolds as part of this study, the alamar

blue assay was carried out on days 1, 4, 7, 14, 21, 28, 35, 42, 49 & 56. On each of these days, old culture media was removed from the scaffolds and washed with PBS twice, with a 5 mins wait time per wash. 2 ml of alamar blue solution at 10 μg/ml (in PBS) was added to each scaffold under light sensitive conditions and incubated for 2 hours at 37 °C.

After incubation, two 200 μl aliquot of reduced alamar blue solution were collected from each cell seeded scaffold as well as the blank scaffold into a labelled 96 well plate. The well plate was then read at 540 nm in a fluorescent plate reader. Excess alamar blue solution was then removed from the scaffolds before being washed with PBS thrice to remove remaining traces of alamar blue. Fresh osteogenic working media was then added to each scaffold and incubated, with media being changed every two days.

3.7.5   Sirius Red Collagen Staining

Sirius Red staining is a rapid, specific, sensitive and highly reproducible method for determining collagen (Junqueira et al., 1979), as it has an ability to qualitatively and quantitatively precipitate collagen in picric and acetic acid solutions (Marotta and Martino, 1985). It also enables quantitative morphometric measurements to be performed on histologically defined tissue areas and also on stained *in vitro* constructs (Malkusch et al., 1995).

Sirius Red staining was used as part of this study to stain and quantify the total collagen content synthesized by MLO-A5 and hES-MP cells under 2D and 3D culture conditions and also examine extracellular matrix production. Since its introduction as a histological technique in 1964 (Sweat et al., 1964), it has become a routine protocol for estimating total collagen content due to the fact that it stains collagen vigorously and permanently. It has also been widely accepted as a better alternative to determining collagen from its hydroxyproline content and a substitute for fuchsin in Van Gieson's method, as its simple, less time consuming and very sensitive (Junqueira et al., 1979).

It's function is based on the binding of the dye Sirius Supra red F3BA to collagen, followed by an elution process, and finally an estimation of the bound dye with a

spectrophotometer. The elongated Sirius Red molecule binds to all triple helical collagen molecules including types I, III and IV in a parallel fashion, but would not bind to denatured or degraded collagen or to other proteins which do not possess the typical collagenous triple helical structure (Lee et al., 1998).

As part of this study, Sirius Red staining was carried out on cultures terminated at weekly time-points, on both MLO-A5 and hES-MP cells seeded either in 2D or 3D, from D7 or D14 until the end of the experiment. The Sirius Red solution was prepared by dissolving Direct red dye from Sigma-Aldrich, UK at 1 mg/ml in saturated picric acid. Cells or cell-seeded scaffolds were washed trice with PBS with a 5 minutes waiting time per wash. The cells were then fixed with 3.7% formaldehyde for 15-20 minutes and again washed trice with PBS and then trice with distilled water with a longer waiting time of 10 minutes per wash.

For all 3D scaffolds, 3-6 ml Sirius Red solution (depending on the size of the scaffolds) was added to each well and left on the rocker for 18 hours, whilst 2D analysis used 2 ml of the solution for 3 hours. After staining, excess Sirius Red solution was removed under running tap water until the solution turned clear. Samples were allowed to air dry for 4 hours and photographic images were taken for qualitative analysis. For quantitative analysis, 2-4 ml (depending on the size of the scaffolds) of 0.2 M of NaOH and methanol at 1:1, was used to destain Sirius red on a platform rocker at 30 rpm for 24 hours. The absorbance of the eluate was read with a spectrophotometer at 490 nm.

3.7.6 Alizarin Red Calcium Staining

Pure synthetic alizarin, in the form of its soluble salt sodium alizarin monosulphonate, has been largely used in staining preserved skeleton specimens since 1900's (Lundvall, 1905). To date, several different types of the alizarin dye, each with varying advantages and disadvantages have been used. These include acid alizarin black R, alizarin-black SR, alizarin-blue Br3G, alizarin-black-Bayer NR, alizarin brown R B, alizarin red S and many others (Batson, 1921).

However, alizarin red S which reacts with calcium cations to form a chelate, has been used successfully for decades as a vital staining agent for developed bone (Puchtler et al., 1969), for differentiating cartilage and bone (Wassersug, 1976; McLeod, 1980), for detecting of calcium in synovial fluid (Paul et al., 1983), and also for evaluating the morphological integrity of corneal endothelium (Taylor and Hunt, 1981). Alizarin red (AR) is also very useful for staining extracellular calcified matrix deposition in tissue engineered bone and evaluating calcium-rich deposits by cells in culture. Additionally, it is particularly versatile in evaluating mineral distribution and also for inspecting fine structures by phase contrast microscopy. It can also be extracted from stained monolayer and assayed to attain quantified data (Gregory et al., 2004).

Although other staining assays such as fluorescent calcein binding (Hale et al., 2000), Von Kossa staining (Anselme et al., 2002) and xylenol orange staining (Rahn and Perren, 1971) can be used to access bone mineralization in tissue engineered constructs, only alizarin red and xylenol orange staining were used for calcium analysis as part of this study due to their simplicity and efficiency.

1% w/v of alizarin Red S powder from Sigma-Aldrich, UK was dissolved in distilled water to create an AR solution with an initial pH of 3. The pH of the solution was adjusted with drops of NaOH to 4.1 to enhance staining. Prior to 3D staining, all scaffolds were washed and fixed with 3.7% formaldehyde in a similar manner as done for collagen staining. The scaffolds were then washed trice with distilled water with a waiting time of about 5-10 minutes per wash.

Enough AR solution was then added to cover each sample for two hours under dynamic rocking. After which excess AR solution was removed and the samples washed with distilled water until the excess water became clear. The samples were then dried at room temperature for 4 hours . Photographic images of blank and cell seeded scaffolds were taken for quantitative analysis. For quantitative analysis, 5% v/v perchloric acid in distilled water was used to destain AR on a platform rocker at 30 rpm for 24 hours. The absorbance of the eluate was read with the spectrophotometer at 405 nm.

3.7. BIOLOGICAL CHARACTERIZATION

3.7.6.0.1 For Electrospun Scaffolds

AR staining was done on days 14, 21 and 28 of culture to stain for calcium on MLO-A5 or hES-MPs seeded scaffolds for two hours under dynamic rocking at 30 rpm. Prior to staining, scaffolds were washed and fixed with 2 ml of 3.7% formaldehyde as per the procedure described for collagen staining. Excess AR solution was removed after staining and samples washed 3 times with 2 ml of distilled water.

3.7.6.0.2 For PL Scaffolds

AR staining was carried out on days 14, 28, 42 and 56 of culture to stain for calcium on MLO-A5 seeded scaffolds for two hours under dynamic rocking at 30 rpm. Prior to staining, scaffolds were washed and fixed with 4 ml of 3.7% formaldehyde as per the procedure described for collagen staining. Excess AR solution was removed after staining and the samples washed 5 times with 5 ml of distilled water, each sitting for 5 minutes.

3.7.7 Xylenol Orange

As part of this study, xylenol orange staining presented an alternative approach for estimating newly developed mineralized nodules in fabricated PU-HA composite scaffolds, which contained varying amounts of calcium phosphate even in blank scaffolds without cells. This was particularly helpful since xylenol orange only binds to newly formed calcified tissue as compared to alizarin red staining, which stained both the calcium contained in blank scaffolds and the calcium secreted by the cells in culture.

Xylenol orange tetrasodium salt from Sigma-Aldrich, UK was prepared at 20 mM stock solution with distilled water and stored in the fridge at 4 °C. Prior to staining, the XO stock solution was diluted in culture medium at 1:1000 dilution, to attain a final concentration of 20 μM. 2 ml of the final concentration was added to each electrospun scaffold for a minimum incubation time of 12 hours. The XO solution was removed after incubation and the scaffolds washed with PBS twice with a 3 mins waiting time between washes.

Fresh medium without β-GP was added to the scaffolds prior to imaging to reduce

the fluorescent background from unbound XO. Imaging was carried out with the confocal microscope at an excitation wavelength of 543 nm. To examine the effect of XO staining on HA composite scaffolds, blank control scaffolds without cells were also stained to assess the effect of HA on XO staining.

3.7.8 Micro-CT on Cell Seeded Scaffolds

Following on from using Micro-Computed Tomography to investigate pore interconnectivity and porosity in Section **3.4.2** on page 81, micro-ct was also used to detect and analyse extracellular calcified regions in PL scaffolds, cultured *in vitro* with MLO-A5 cells.

In addition to minimum sample preparation, non-invasive and non-destructive high resolution imaging, using micro-ct for such *in vitro* analysis was particularly beneficial for examining deposited calcified matrix in PU-HA composites. This served as a challenge when alizarin red calcium staining was used to detect bone mineralization in engineered *in vitro* constructs.

The Skyscan 1172 micro-CT scanner in the Bone Analysis Laboratory was used to scan both blank and cell seeded PM-PL scaffolds. PM-PU and PM-PU+mHA scaffolds seeded with MLO-A5 cells at 5 x 10^5 cells per scaffold, were scanned after 14, 28, 42 and 56 days in culture. Prior to scanning, media was removed from the scaffolds and washed twice with PBS. 3.7% formaldehyde was then used to fix the cells for 15-20 minutes before being washed trice with PBS. The scaffolds were then kept in the last PBS wash in the fridge until imaging.

Similar to the settings used for the porosity analysis, acquisition conditions of 44 kV, 226 uA, no filter, with an image pixel size of 9.08 μm, a rotation step of 0.7º and an exposure time of 295 ms was used to scan scaffolds after all the PBS had been removed with tissue paper. Reconstruction of the acquired image slices was also done with the NRecon® software version: 1.6.9.4 from Skyscan, Belgium, and a GPUReconServer engine version: 1.6.9.

Reconstructed images were processed with CTAn software version: 1.13.11.0+ from

SkyScan, Belgium. Selected regions of interest (ROIs) were saved and loaded as new data sets. An appropriate threshold of (PU:148-high & $\sim$40-low) was applied to the ROI's for PU-regions whereas a threshold of (mHA and nHA: 255-high & $\sim$148-low) was applied HA regions. Standard 3D analysis and 3D models were also generated for each ROI.

3.7.9 DAPI and Phalloidin Staining

As most cellular components appear transparent under the microscope, cell staining using one or more dyes enhances visualisation of cell parts. The use of such dyes also highlights metabolic processes and structures, and facilitates enumeration. As part of this study, cells were stained with DAPI and Phalloidin-FITC or Phalloidin-TRITC fluorescent dyes to enhance the visualization of cell attachment, proliferation, cell morphology and extracellular matrix production.

DAPI (4', 6-diamidino-2-phenylindole dihydrochloride), is a fluorescent nuclear stain that binds to DNA (at Adenine-Thymine repeats of the DNA double helix) and shows as blue fluorescence upon excitation with ultraviolet light. Similar to Toluylene red, Hoechst 33342 and Nile blue, DAPI allows for easy imaging of live cell nuclei, although Hoechst 33342 and DAPI can also be used on fixed cells.

Phalloidin-FITC (Fluorescein Isothiocyanate) or Phalloidin-TRITC (Tetramethyl Rhodamine Isothiocyanate) were also used to counter stain DAPI and enhance visualization of the cytoskeleton by binding to the actin filaments in the cells. Although both Phalloidin-FITC or Phalloidin-TRITC have very similar operating mechanisms, the TRITC conjugate produces an orange-red colour and is considered less susceptible to photobleaching than the FITC conjugate (Faulstich et al., 1983) which produces a green colour.

As part of this study, both electrospun and particulate leached scaffolds were washed and fixed in a similar manner as for calcium and collagen staining with 3.7% formaldehyde for 20 minutes. Fixation allowed the morphology of the cells to be preserved and for it to be able to withstand harsh preparations conditions prior to imaging. After fixation, scaffolds were washed three times with PBS with a 5 minute waiting time per wash, and

later permeablized with 1% Triton X-100 in PBS for 5 minutes. Permeabilization using such a mild surfactant facilitated the dye molecules to penetrate the cell membrane. The scaffolds were then washed with PBS three times with a 5 minute waiting time per wash.

1% Bovine Serum Albumen (BSA) was added as a block non-specific binding agent for 30 minutes before either 1% Phalloidin-TRITC or Phalloidin-FITC was used to stain the cytoskeleton for 30 minutes. The scaffolds were then washed twice with PBS and stained with 0.1 μg/ml DAPI solution for a further 10 minutes. The scaffolds were finally washed with PBS and visualized with either the AXON Instruments ImageXpress 5000A, USA or the Confocal Microscope.

3.7.9.1 Electrospun Scaffolds

Z3-70 and Z9-70 electrospun scaffolds from the solvent group seeded with MLO-A5 cells at 1 x 10^5 cells per scaffold, were stained with DAPI and phalloidin-TRITC on days 1, 4 and 7 after seeding to enhance visualisation of cell attachment and cell morphology.

MLO-A5 cells on these scaffolds were fixed and prepared with 2 ml of each regent per scaffold using the protocol described in Section **3.7.9**. Stained scaffolds were subsequently imaged with the AXON Instruments ImageXpress 5000A, USA.

3.7.9.2 For Particulate Leached Scaffolds

For particulate leached scaffolds, only layer-by-layer and physically mixed scaffolds were stained and imaged. In brief, Plain PU, PU+mHA(2:1), PU+mHA(3:1) and PU+nHA(3:1) layer-by-layer scaffolds seeded with either hES-MPs or MLO-A5 cells at 5 x 10^5 cells per scaffold were stained with DAPI and phalloidin-FITC on day 4. However, Plain PU, PU+mHA(3:1), PU+nHA(3:1) and PU+cHA(3:0.5:0.5) physically mixed scaffolds were only seeded with MLO-A5 cells at 5 x 10^5 cells per scaffold and stained with DAPI and phalloidin-TRITC on days 1, 4, 7 and 14.

Each PL scaffold was fixed and prepared with 3 ml of regent per scaffold using the protocol described in Section **3.7.9** on page 108. Stained scaffolds were subsequently imaged at 512x512 pixels with the upright microscope confocal microscope (Axioskop 2

FS MOT Microscope, Carl Zeiss Ltd, UK) equipped with the 10x objective. DAPI was detected at excitation/emission wavelength of 800/461 nm whilst Phalloidin-FITC was detected at 495/517 nm and Phalloidin-TRITC at 550/573 nm.

3.7.10 Second Harmonic Generation Imaging

SHGI is a dynamic high resolution optical microscopy technique used in visualising the structure and function of cells and tissues. It is based on the non-linear optical process of second harmonic generation, in which high energy photons of the same frequency interacts with a non-linear material to generate new photons with twice the energy and frequency, and half the wavelength of the initial photons.

As part of this study, SHG was used to visualize collagen deposition and organisation on Z3 aligned electrospun scaffolds on days 14, 21 and 28 after seeding with MLO-A5 cells at 1 x 10^5 cells per scaffold. In brief, scaffolds were removed from culture media and washed once with PBS. They were then placed in a petri dish without fixation and covered with a cover slip prior to imaging.

Imaging was performed using the Zeiss LSM 510 Meta upright laser scanning microscope in conjunction with the two-photon Ti-Sapphire multiphoton laser. The laser was equipped with a 40x 1.3 NA oil immersion objective and operated at an excitation power of 20 mW. Cell-deposited collagen was illuminated at 950 nm and SHG emissions collected in a 10 nm bandpass filter centred around 475 nm. Additionally, cell-free PU and PU-HA fibrous scaffolds were also illuminated at 840 nm and collected in a 10 nm bandpass filter centred around 421 nm.

3.7.11 *In vivo* studies

In vivo studies consisting of subcutaneous and cortical defect implantations were carried out by Dr. Maksym Pogorielov's laboratory in Sumy State University, Ukraine. All experiments and animal housing conditions were in accordance with the European Convention for the protection of vertebrate animals used for experimental and other scientific purposes (de l'Europe, 1986), Directive 2010/63/EU of the European Parliament

(Parliament and Union, 2010) and the general ethical principles for experiments on animals, which was accepted at the First Bioethics National Congress (Kordyum, 2001). All the experiments were also approved by the Commission on Biomedical Ethics of Sumy State University on 15/12/2014.

3.7.11.1 Subcutaneous Implantation

36 laboratory rats aged between 4–5 months with body weights of 180–195 g were subcutaneously implanted with layer-by-layer PL scaffolds to further assess biocompatibility, and investigate inflammatory response and vascularization. The rats were housed at a temperature of 22±2 °C with a 12 hour light/dark cycle and received food and water ad libitum. They were further divided into three groups, with 12 rats in each group and labelled as Group 1 for LbL-Plain PU scaffolds, Group 2 for LbL-PU+mHA(3:1) scaffolds and finally Group 3 for LbL-PU+nHA(3:1) scaffolds, with n=6 for each time point and group.

The procedure of implantation included a 10 mg/kg of animal weight ketamine injection as general anaesthesia and peripheral vein catheterization. Prior to implantation, the intrascapular region in the back of the animals was shaved and treated with C-4 solution. A longitudinal incision was then made at the implantation site before separating the subcutaneous tissues from the skin above the left scapula. One of the fabricated scaffolds (graft) which had already been sterilized in 96% ethanol for 30 mins was then placed under the skin at about 1.5 cm from the incision. The wound was then closed with simple interrupted sutures and an aseptic dressing was applied.

The animals were later sacrificed on day 7 and 45 post-implantation as first and second time points respectively with an overdose of narcosis using ketamine at 70 mg/kg of animal weight.

3.7.11.2 Cortical Defect Implantation

Cortical defect implantation was also carried out as part of this study to further access the suitability of the fabricated scaffolds in restoring damaged bone. In brief, 36 rabbits

of the chinchillas breed, aged between 6–7 months with body weights of 2.5–3.0 kg were implanted with layer-by-layer PL scaffolds. All rabbits were housed at a temperature of 22±2 °C with a 12 hour light/dark cycle and received food and water ad libitum. Similar to the subcutaneous experiments, the rabbits were divided into three groups according to the type of scaffolds ahead of implantation.

For the implantation process, a combined dose of 7 mg/kg Ketamine and 10 mg/kg thiopental injection was used as general anaesthesia. A peripheral vein was catheterized and the left thigh was shaved to prepare the site. The surgical site was then treated with C-4 solution before a longitudinal incision on the lateral surface of the thigh was made. The muscles were then separated in order to provide access to the bone. Using a 10 mm diameter drill, a round defect was made into the bone until the bone marrow. The defect was then filled with one already sterilized 10 mm graft. The wound was sutured after implantation, and antibiotics was administered for a week as prophylaxis to prevent postoperative bacterial complications.

As with the subcutaneous implantation, the animals were later sacrificed on day 7 and 45 post-implantation with an overdose of narcosis using ketamine at 70 mg/kg of animal weight.

3.7.12 Histology

Histology entails the preparation and examination of thin slices of biological samples to attain detailed information about structural composition, pathology and the interactions within its structures.

As part of this study, cell-seeded scaffolds were histologically analysed *in vitro* to investigate cell attachment, depth penetration and possible tissue formation. Histology of scaffolds that had previously been implanted *in vivo* was also carried out to examine cell migration and tissue ingrowth, inflammatory response and vascularization, fibrous and osteiod tissue formation, and possible bone remodelling.

3.7.12.1 Histology of Samples Tested *In vitro*

Histology was conducted on *in vitro* samples of non-aligned and aligned electrospun scaffolds as well as particulate leached scaffolds in the homogenized and physically mixed groups. Non-aligned electrospun scaffolds seeded with either MLO-A5 or hES-MP cells at 1×10^5 cells per scaffold were analysed on days 14, 21 and 28 after seeding. In addition, aligned scaffolds seeded with only hES-MP cells at the same concentration were also analysed *in vitro*. Furthermore, all scaffolds in the homogenized and physically mixed PL groups which had previously been seeded with MLO-A5 cells at 5×10^5 cells per scaffold were also analysed on days 14, 28, 42 and 56 of culture.

For each histological process, media was removed and the samples washed with PBS twice. The samples were then fixed with 3.7% formaldehyde for 20 minutes and then washed twice with PBS. The samples were later soaked in 1% sucrose solution for an hour before being embedded in OCT$^{\mathbf{TM}}$ compound media, and then frozen with liquid nitrogen prior to sectioning. However, particulate leached samples were placed in well plates and put in a vacuum chamber, for 3 alternating cycles of vacuum and aeration of 3 minutes each, before quenching in liquid nitrogen to make the thick PL scaffolds aspirate the OCT media and prevent fragmentation.

All samples were cryo-sectioned at 15 μm as complete transverse-sections across the centre of all scaffolds and stained with Haematoxylin and Eosin. Stained sections were imaged with a light microscope with x20 objective.

3.7.12.2 Histology of Samples Tested *In vivo*

Following implantation of layer-by-layer PL scaffolds in rats and rabbits for subcutaneous and cortical defect analysis, *in vivo* histology of the implanted scaffolds was also carried out by Dr. Pogorielov's laboratory in Ukraine.

At each post-implantation time point, thus Day 7 for the first and Day 45 for the second, the animals were sacrificed and the grafts removed with surrounding bone or tissue to prevent graft damage. All samples were fixed in 10% formaldehyde for 24 hours and decalcificated in 4.5% acetic acid for 48 hours. The samples were then dried in

varying concentrations of alcohols and set with paraffin wax. 12-15 μm thick sections were prepared and stained with Haematoxylin and Eosin. Stained sections were imaged using a light microscope at a magnification of 360x.

3.7.13   Statistical Analysis

All experiments were performed a minimum of two times with triplicate samples for each condition where possible. All data are reported as mean $\pm$ standard deviation. Comparison of sample means of fibre diameter and mechanical analysis was performed by one-way analysis of variance using GraphPad Prism 6 software, whilst alamar blue and MTT cell viability, calcium and collagen absorbance data were analysed by two-way repeated measures analysis of variance. Differences between two groups were defined as statistically significant if $p \leq 0.05$ as determined by the Tukey's multiple comparisons post-hoc test. For imaging of samples, some experiments were limited to one sample per condition per experimental run due to time constraints. Single images are always chosen to be representative of the experimental outcome.

4 | Results and Discussion Section One

Fabricating Non-aligned Polyurethane & Polyurethane Hydroxyapatite Fibrous Mats for Bone Regeneration

4.1   Introduction

Bone tissue engineering involves the use of materials to either induce formation of bone from the surrounding tissue or to act as a carrier or template for implanted bone cells. It requires four key components which include a morphogenetic signal, responsive host cells, a suitable carrier to serve as scaffolding for the growth of host cells, and a viable and well vascularised host bed (Croteau et al., 1999; Burg et al., 2000). Scaffolds used for this purpose provide a three dimensional porous structure that facilitate cell attachment, growth and matrix deposition.

4.1. INTRODUCTION

An ideal scaffold should possess a suitable surface chemistry that supports cell attachment, proliferation, migration and growth. Additionally, it should serve as a biocompatible template for osteoprogenitor cell growth and aid in the differentiation of mesenchymal stem cells into osteoblasts, as well as supporting the production, organization and maintenance of an extracellular matrix (Gogolewski, 2007; Gorna and Gogolewski, 2003). In addition to being biocompatible, scaffolds are required to be composed of highly interconnected macro and micro-porous networks to facilitate cell migration and nutrient distribution.

Several polymers of both natural and synthetic origin can be used to create scaffolds for bone tissue engineering; however polyurethanes are of particular interest due to the flexibility associated with their versatile chemistry (Guelcher, 2008). This makes it possible to customise polyurethane scaffolds in order to attain desirable physical, chemical and mechanical properties such as durability, elasticity and fatigue resistance, by altering the choice and quantity of the starting materials (Zdrahala and Zdrahala, 1999). Biocompatible and biodegradable polyurethanes have been investigated as scaffolds for tissue engineering applications for almost thirty years (Guelcher et al., 2004), and also as heart valves, stents, intra-aortic balloons and pacing lead insulators, amongst others (Grad et al., 2003).

Mechanically, polymers are noted for their extensive deformation and high toughness whilst ceramics, such as hydroxyapatites (HA), are noted for their high compressive strength but brittle failure. Combining polyurethane with hydroxyapatite has been shown by a number of researchers to improve the mechanical properties of the resulting composite, as long as a strong interfacial bond strength is established between the ceramic phase and the polymer matrix (Attawia et al., 1995; Boccaccini and Maquet, 2003; Bonzani et al., 2007; Martinez-Valencia et al., 2011).

Electrospinning is an efficient, simple and relatively easy polymer fabrication technique that produces scaffolds with nano and micro polymer fibres that have non-aligned or aligned orientations, and the advantage that it can be performed with different polymers in both solution and melt states. Such thin fibres provide

116

high surface area to volume ratios, high porosity, flexibility in surface functionalities, superior mechanical performance and membrane technology (Demir et al., 2002). In the field of biomaterials and tissue engineering, electrospinning has been utilised for producing scaffolds that mimic the morphological characteristics and biological function of the natural extracellular matrix, by providing an optimal template for cell attachment, proliferation and growth (Carlberg et al., 2009; Huang et al., 2003). Several different polymers such as polyurethanes, poly(lactic acid), poly(glycolic acid) poly(ε-caprolactone), and their co-polymers have been successfully spun for musculoskeletal, nerve, skin, vascular and drug delivery applications (Bashur et al., 2009; Clarke et al., 2008; Nirmala et al., 2011). Electrospinning may be an ideal technique for bone tissue engineering where repair of a thin defect is required, for example a cleft palate repair (Bye et al., 2013), or electrospun sheets may be layered or rolled for larger defects (McMahon et al., 2011).

Demir et al. (2002) studied the effect of electrical field, temperature and conductivity on electrospun polyurethane-urea fibres and reported that the morphology of electrospun fibres is strongly correlated with viscosity, equivalent concentration and temperature. In their study, they reported that solution temperature, a key parameter that affects fibre morphology and spinning ability was essential to spin polymer concentrations beyond 12.8wt%. Khan et al. (2008) and Mi et al. (2014) electrospun polyurethane composites with micro and nano sized hydroxyapatite for dental and bone tissue engineering applications, respectively. In their studies, Khan and co-workers developed a novel non-aligned composite material by chemically binding HA particles to the diisocyanate component of the polyurethane backbone through solvent polymerisation, whilst Mi and co-workers studied the effect of polymer properties and particle size on electrospun PU-HA scaffolds. They reported reduced tensile properties with the inclusion of micro HA (mHA) and nano HA (nHA) particles, although the reduction was more significant with the inclusion of mHA.

4.2 Aim

The aim of this study was to identify polyurethane solutions with appropriate concentrations and solvent properties that can successfully be electrospun at room temperature to attain consistent non-aligned fibre mats without beads and irregularities. It was also to examine the effect of incorporating HA particles into these non-aligned scaffolds. The hypothesis was that HA would reinforce the mechanical properties of polymers and improve the bioactive properties compared to polymer-only scaffolds.

The overall aim is to create a range of scaffolds, with appropriate tensile mechanical properties that support bone cell and matrix growth. In this study, the effect of dimethylformamide (DMF) and tetrahydrofuran (THF) solvent combinations on the fibre morphology and mechanical properties of electrospun thermoplastic polyurethane polymers were investigated. Additionally, the effect of including nano and micro size HA particles on fibre morphology, mechanical properties, biocompatibility, extracellular and calcified matrix production, and histology were also investigated.

4.3 Results and Discussion One

Bone, the major load bearing tissue of the human body is subjected to varying degrees of loading and unloading on a daily basis. Hence, designing a scaffold for bone tissue engineering requires a material that is mechanically compatible, in order for it to be able to undergo varying degrees of deformation without rupturing. Polyurethane remains a popular choice amongst polymers for its advantageous properties of biocompatibility, biodegradability, mechanical flexibility and versatile chemistry. Such properties allow PU to be tailor-made for several applications including biomaterial design. As part of this study, it was necessary to optimise electrospinning conditions for creating PU based scaffolds for bone regeneration.

Scaffolds discussed in this chapter were fabricated as outlined in Section 3.3.1 on page 70 using PU and PU-HA solutions described in Sections 3.2.2.2 and 3.2.3, on

page 68 and 69 respectively. Cell culture and other biological characterization analysis on the selected scaffolds were done as described in Section 3.7.3.2 on page 94 and Sections 3.7.4 - 3.7.12 on page 98 and 112, respectively.

In brief, Z3A1 and Z9A1 PU pellets were dissolved in graded concentrations of DMF/THF solvents to attain uniform PU solutions with ideal concentrations of 28 wt% and 15 wt% for Z9A1 and Z3A1, respectively. These solutions were then electrospun to attain non-aligned fibrous scaffolds in the Z9A1 and Z3A1 solvent scaffold group. Composite scaffolds containing HA particles were also fabricated as part of this study, using 25 wt% Z9A1 and 15 wt% Z3A1 PU solutions doped with micro or nano-HA particles. All fabricated scaffolds were later characterized chemically and mechanically, using state of the art equipment and biologically using MLO-A5 and hES-MP cells.

4.3.1 PU Solutions

Medical grade thermoplastic polyurethane Z9A1 and Z3A1 were dissolved in graded concentrations of solvents to study the effect of solvent combinations on polyurethane dissolution, electrospun fibre morphology and mechanical properties. The PU polymers, with different molecular weights thus Z9A1 (Mn-100,428 & Mw-197,459 g/mol, PD-1.97) and Z3A1 (Mn-143,566 & Mw-272,857 g/mol, PD-1.90), but identical chemical structures and composition of 4,4'-diphenylmethane diisocyanate, polyether diol, and 1,4 butane diol, were dissolved in solvents of Dimethylformamide, Tetrahydrofuran, Dichloromethane, Xylene, Dioxane and Ethanol.

Polymer dissolution plays a key role in scaffold fabrication, as the nature of the dissolution process affects optimization and processing conditions, which is also in turn largely dependent on the choice of solvent. It was therefore important to optimise the dissolution process in order to attain consistent and uniform solutions prior to electrospinning. As with all high molecular weight polymers, these PU pellets were made up of long chains of tightly folded coils which are entangled together by strong intra and intermolecular dipole-dipole and hydrogen bonding forces. The strong nature of such interactions coupled with the coiled nature of the chain segments and high molecular

4.3. RESULTS AND DISCUSSION ONE

weight resulted in a slow dissolution process. On average the dissolution of both types of PU in an appropriate solvent required 24-48 hours for complete dissolution to occur.

DMF and THF, are popular organic solvents used in dissolving and synthesising polyurethane (Khil et al., 2003; Tsui and Gogolewski, 2009). In addition to DMF and THF, other solvents including Dichloromethane, Xylene, Dioxane and Ethanol were also assessed at different concentrations to identify the best solvent for dissolving the PU pellets. These earlier experiments showed that the PU pellets dissolved completely in 100% DMF solvent as well as solvent combinations of DMF and THF, but not 100% THF solvent. The pellets also did not dissolve in Dichloromethane, Dioxane and Ethanol, but greatly swelled in size when they came into contact with Dichloromethane.

The solubility of PU in a solvent is largely dependent on polarity, solvent compatibility and the nature of chemical bonds present in the backbone chain. Solvents with similar dispersion forces, intermolecular and hydrogen bonding forces to PU such as DMF and THF, dissolve faster and relatively more easily than solvents with dissimilar properties. The solvents used in this study differed in chemical composition, polarity, viscosity, evaporation rate and electrical conductivities, all of which are key to dissolution.

Such key parameters affect the swelling ability of the pellets which takes place prior to dissolution, as well as the overall solution viscosity, by increasing intermolecular friction and surface tension of the final solution. They also affect polymer solubility by influencing the degree of disentanglement of the polymer chains, the dispersion forces between the segments and the diffusion of the chains through the polymer-solvent interaction (Grassino, 2000). These features in turn affect electrospinning, since the creation of polymer fibres is largely dependent on surface tension, solution viscosity and electrical conductivity.

For successful dissolution to occur, polymer-solvent interactions should exceed polymer-polymer attraction forces. This happens in order for the the chain segments to absorb solvent molecules and increase in volume by swelling in size (Miller-Chou and Koenig, 2003). Such strong polymer-solvent interactions between the PU pellets and DMF caused the chain entanglements to loosen and the pellets to initially swell in a

gel-like manner. This created an opportunity for the magnetic bead stirrers to disperse the gel in solution and further increase the polymer-solvent surface contacts until all the pellets disintegrated to form a consistent and uniform solution.

On the contrary, polymer-polymer interactions exceeded polymer-solvent interactions when the PU pellets came into contact with DCM, Dioxane and Ethanol, hence dissolution was not achieved even after several weeks. However, in the case of DCM, the interaction was able to cause an initial swelling of the pellets, but not strong enough to cause disintegration and loosening of the coiled chains. Hence, only PU solutions made with 100% DMF, 70/30 DMF and 50/50 DMF/THF were used to electrospin scaffolds for this work.

4.3.2   PU Scaffolds

Polymer solutions can be electrospun to produce scaffolds with submicron to nanoscale fibers, as long as a proper solvent and polymer concentration is used to control the intrinsic conductivity, viscosity and surface tension of the solution.

For this study, PU-only scaffolds electrospun from solutions containing 100% DMF had more nano-diameter fibres and beads than other solvent combinations of DMF and THF for both types of PU as shown in Figures 4.1 and 4.2 (in greater detail with fibre diameter histogram distributions) on page 122 and 124, respectively. Reducing the amount of DMF, by replacing with THF eliminated the presence of beads and resulted in fibres with a more uniform morphology for Z9A1 scaffolds, and a combination of nano and micro fibres for Z3A1 scaffolds.

For both types of PU, scaffolds made from solutions containing 50% THF solvent had fibres with significantly larger diameters to those fabricated from 100% DMF and 70/30 DMF/THF combinations. It has been reported that the formation of beads and beaded fibres is driven by the surface tension and surface tension coefficient of the polymer and solvent (Doshi and Reneker, 1995).

Although both DMF and THF are organic solvents with similar densities, they have different evaporation rates, electrical conductivity, dielectric constant and dipole
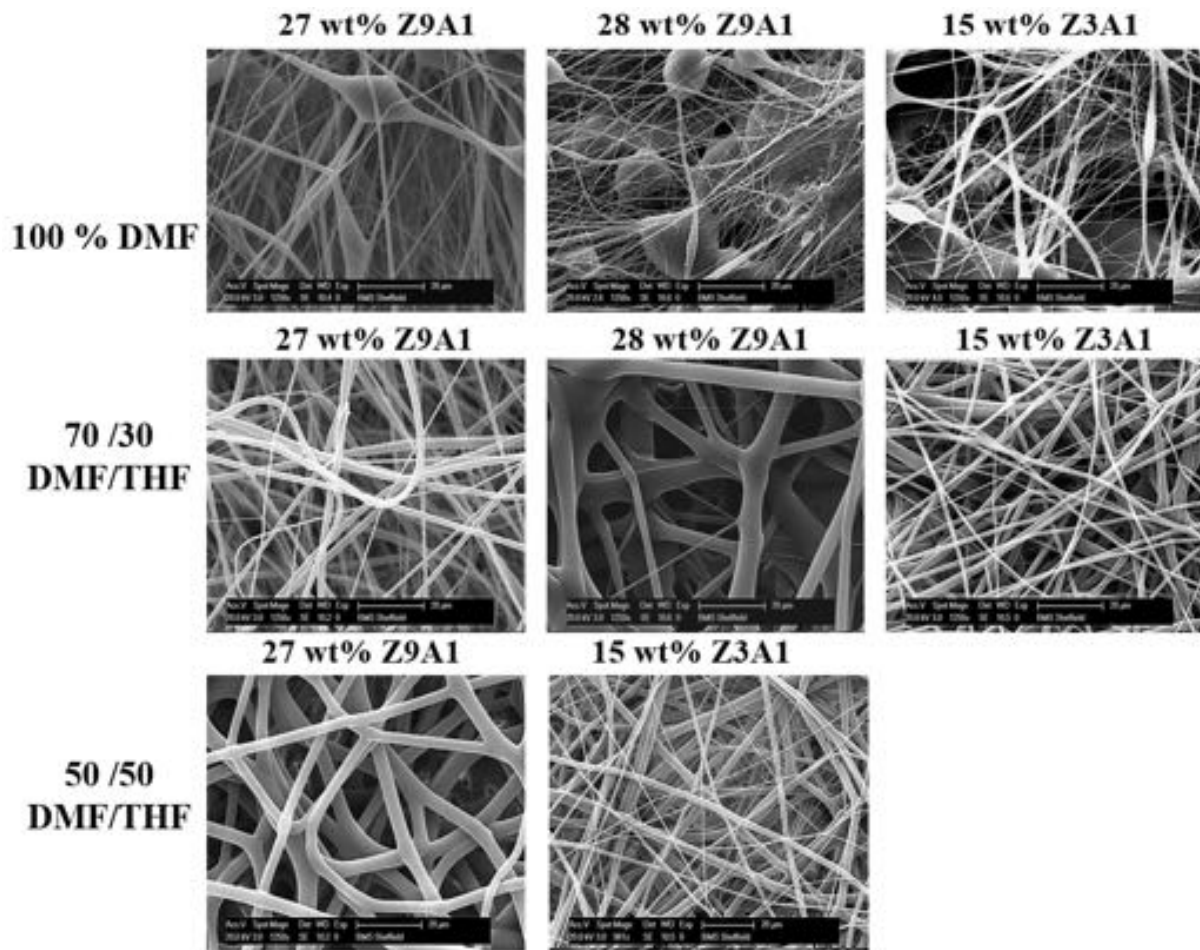
Figure 4.1: Combined SEM images of Plain Z9 and Z3 PU Electrospun Scaffolds at different wieght and solvent concentrations.
Scale Bar of SEM images=20 µm

moments, all of which affect fibre formation during electrospinning (Garg and Bowlin, 2011). DMF is more polar than THF, and has a higher dielectric constant, boiling point and dipole moment as compared to THF. It however has a lower evaporation rate than THF. This caused PU solutions containing only DMF to be more viscous than those with both DMF/THF. The high viscosity and low evaporation rate caused the thin fibres to land on the grounded collector wet and flatten on impact. This is because, highly viscous solutions are likely to overcome surface tension and transform solution droplets into polymer jets along with the voltage.

Shawon and Sung (2004) studied the effect of THF/DMF on electrospun polycarbonate nanofibres and reported a significant role of varying solvent combinations on fibre morphology. From their study, fibre diameter decreased due to the evaporation of

122

Table 4.1: Parameters used in preparing non-aligned electrospun scaffolds

Z9 & Z3	PU wt%	micro/nano HA wt%	Vol. ratio of DMF (%)	Vol. ratio of THF (%)	Spin Speed (rpm)	Diameter of the Rotating Drum (cm)
Solvent Group						
Z9-100	27	0	100	0	150	6
Z9-70	27	0	70	30	150	6
Z9-50	27	0	50	50	150	6
Z3-100	15	0	100	0	150	6
Z3-70	15	0	70	30	150	6
Z3-50	15	0	50	50	150	6
non-aligned Composites						
Z9-PU	25	0	70	30	150	6
Z9-mHA	25	5	70	30	150	6
Z9-nHA	25	5	70	30	150	6
Z3-PU	15	0	70	30	300	8
Z3-mHA	15	5	70	30	300	8
Z3-nHA	15	5	70	30	300	8

the solvent that led to an increase in the forces from the surface charge density. They also reported that increasing THF to DMF ratios, increased the presence of bead formation and bead density. This is in contrast to what was observed in this study, and could have resulted from the different polymer-solvent interaction of the thermoplastic polyurethane as compared to polycarbonate, since the PU has a more flexible chemical composition and an ultra-high molecular weight.

As discussed in Section **3.2.2.2** on page 68, each of the PU pellets from the Z**n**A1 series (**n**=1/3/9), underwent the most consistent and uniform dissolution in 70/30 DMF/THF solvent after 24 hours of mixing compared to the other solvents studied. Z3A1 was best at 15 %wt whilst the Z9A1 pellets dissolved best at a maximum concentration of 25 %wt for electrospinning with composite particles and a maximum concentration of 28 %wt for electrospinning without HA particles. The effects of molecular weights of Z3A1 versus Z9A1 could not be directly compared in this study as spinning parameters were slightly different between these two sets of scaffolds. However in general, Z3A1 dissolved faster and more uniformly than Z9A1 prior to electrospinning, and presented with a more

4.3. RESULTS AND DISCUSSION ONE
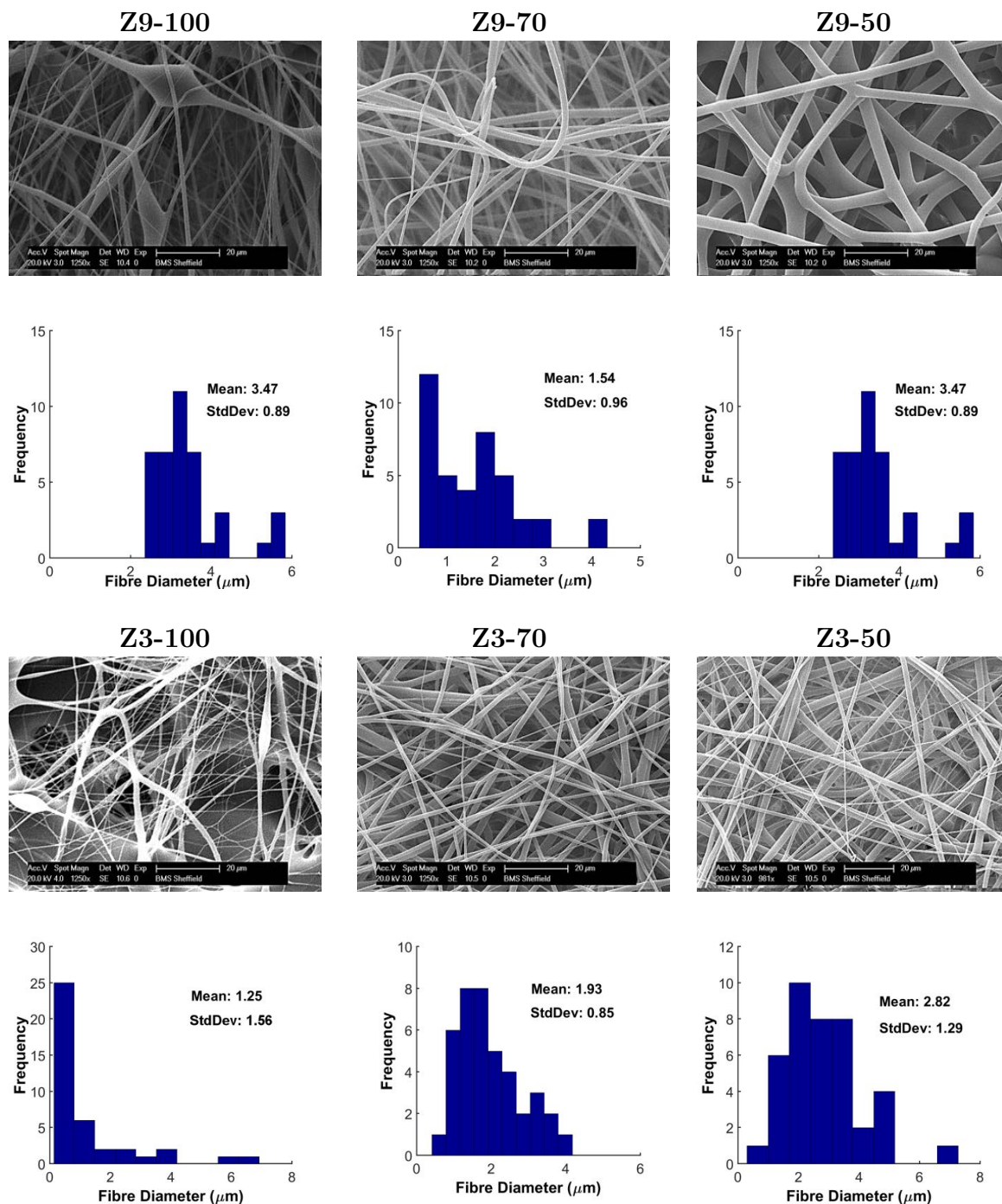
Figure 4.2: SEM images of Electrospun scaffolds synthesised with different combinations of DMF & THF.
(Scale Bar of SEM images=20 μm), with binned histogram distributions of the fibre diameters below (n=40).

uniform viscosity and was easier to fabricate.

Armentano et al. (2010) reported that the solvent choice used in fabricating polymer films influences several scaffold properties, including the heterogeneity of the surface

structure, reorientation or mobility of the surface crystal segment, as well as swelling and deformation. In this study, differences in electrospun morphology which resulted from changing the amount of DMF contained in solution are supported by the work of Oprea (2005) who studied the effect of N-methyl-2-pyrrolidone (NMP), DMF, toluene and ethyl acetate on the properties of polymer films. They reported differences in morphology and mechanical properties of films fabricated from solutions containing NMP and DMF solvents. They suggested that NMP was a better solvent than DMF for developing polyurethane films.

Wannatong et al. (2004) also studied the effect of five different solvents on electrospun polystyrene (PS) and reported that DMF was the best solvent for preparing beadless PS scaffolds. This is in contrast to what was observed in our study, but these different results could be due to differences in concentration of solutions, molecular weights and polymer choice, as PU and PS have different chemical and physical properties.

4.3.3 PU-HA Composites

Mimicking the ductile properties of collagen and the strength of the mineralised phase of bone with PU and HA particles combined in micro or nano composites has been proposed for bone substitute materials for a number of reasons. The elastomeric nature of PU serves as a matrix, reinforced by the HA particles. Nano HA and micro HA differ in several ways including surface area and the degree of crystallinity which both affect overall sample constitution.

By including both particle types in separate solutions, it was possible to assess the effect of particle size on fibre morphology and mechanical properties. Note that all solutions, including the PU scaffolds without HA for this set of experiments were spun from a 70/30 solution of DMF/THF because this enabled the best fibre morphology (without beads), however the processing conditions for Z9-PU and Z3-PU are slightly different from those used in the Z9-70 and Z3-70 groups (detailed in table 4.1) so these are not expected to have identical morphological and mechanical properties.

Electrospun 25wt% Z9A1 and 15wt% Z3A1 dissolved in 70/30 DMF/THF solvents
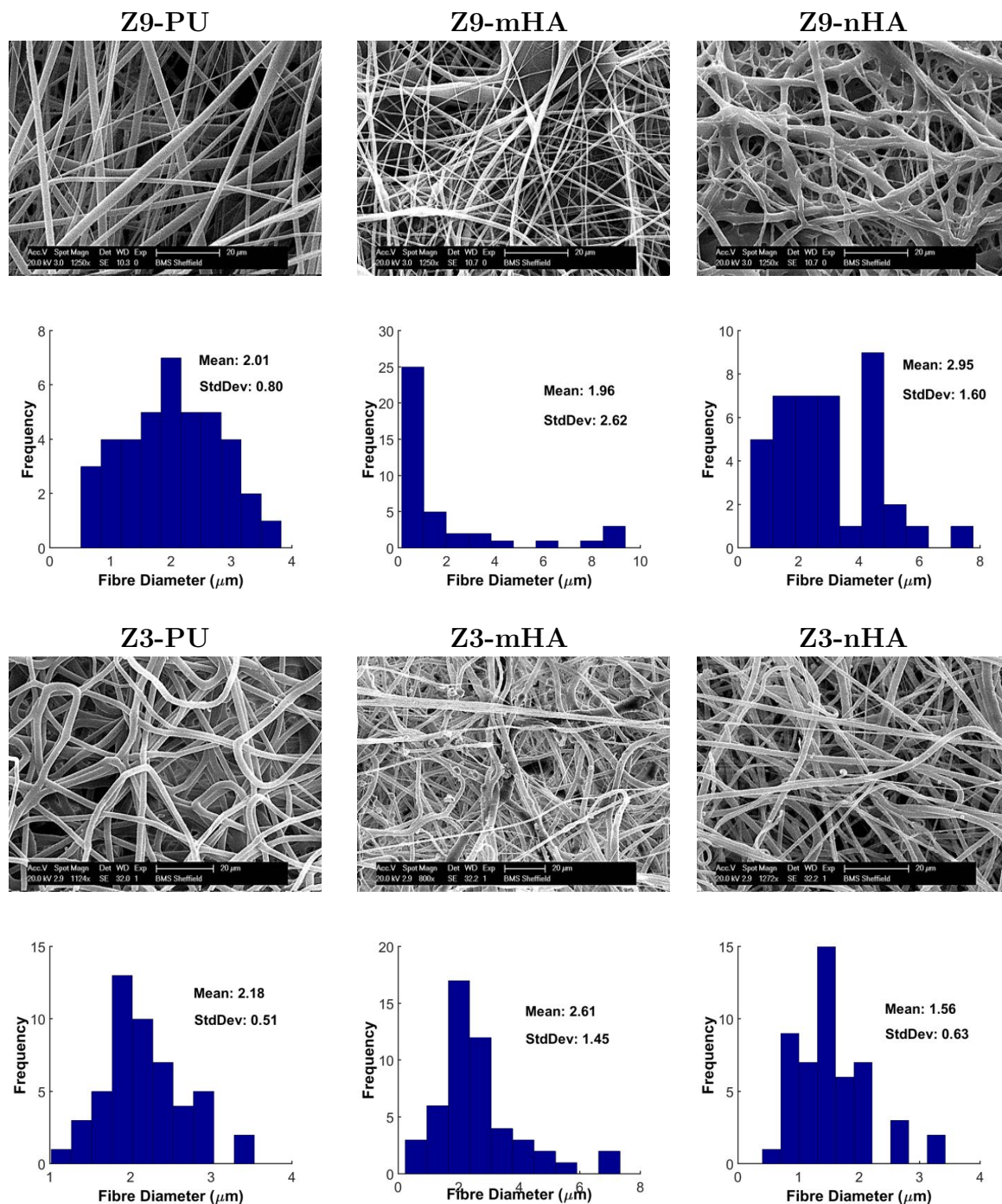
Figure 4.3: SEM images of Electrospun Composite Scaffolds; PU (left column), mHA (middle column) and nHA (right column) composite scaffolds.

(Scale Bar of SEM images=20 μm), with histogram distributions of the fibre diameters below (n=40). Note that the axes for each histogram are to different scales reflecting the variability in fibre size between scaffold compositions and the histogram for Z9-mHA excludes a single 35 μm fibre which is included in the mean values presented in table 4.3 on page 135.

showed relatively uniform fibre diameter distributions. However, the inclusion of mHA and nHA particles resulted in changes to fibre morphology. For both types of PU, nHA particles with a higher surface area and smaller particle size, blended well with PU and resulted in more uniform fibres compared to composite scaffolds containing mHA particles, which presented with a beaded morphology and generally reduced fibre diameters but with some particularly large fibres (Figure 4.3 on page 126).

It is likely that the particularly large fibres contain large chunks of mHA leading to a bimodal distribution of fibre size and large standard deviation (detailed in Table 4.3 on page 135). There was a single extremely large fibre of 35 μm in the field of view examined which was not included in the frequency plot (Figure 4.3) as it would have made it difficult to visualise the rest of the data, but this is included in the fibre average diameter data shown in Table 4.3 on page 135.

Reduction in fibre diameter with the inclusion of mHA particles to create composites was also observed by Nirmala et al. (2011) who electrospun nanofibrous polyurethane with micro Calcium Chloride particles and by Mi et al. (2014) who suggested that that mHA particles may have stretched the polymer jets while the fibres were being deposited. The effect of more fibres at a lower diameter and a few fibres at a much larger diameter caused by the inclusion of mHA is much less marked when the Z3A1 polymer is used. This may be explained by the smaller molecular weight and polymer chain length of Z3A1 compared to Z9A1 and its lower viscosity.

It has been reported that the higher surface area of nHA compared to mHA enables better bonding between the nano-sized HA particles and PU enabling greater reinforcement of the polymer matrix and ultimately, enhancing mechanical and functional properties of nanocomposites compared to conventional microcomposites (Armentano et al., 2010). This probably explains why the nHA fibres are much more consistent in their size and morphology as the particles would be better distributed within, and bound to their polymer matrix.

4.3.4 FTIR Spectroscopy

The polar nature of PU and HA makes FTIR characterisation, which elicits differences in dipole moments, an ideal characterisation technique for analysing the chemical composition of composite scaffolds. An infrared spectrum generated with FTIR spectroscopy represents the chemical fingerprint of a sample and hence useful for qualitative and quantitative analysis. It operates on the principle that chemical bonds or groups of bonds vibrate at characteristic frequencies, and that, molecules have specific vibrational modes that can be activated when hit by photons of a specific energy level (Dimitrova et al., 2009).

The FTIR spectrum of both Z9A1 and Z3A1 non-aligned electrospun scaffolds were generated with the Nicolet 8700 FTIR spectrometer but with different sampling accessories. Z3A1 scaffolds were characterized with the PAS sampling accessory whilst those of Z9A1 were done with ATR sampling. This allowed an investigation into the best FTIR sampling tool for characterizing PU-HA constructs. The FTIR spectra for Z3A1 scaffolds are presented in Figure 4.4 on page 129, and those of Z9A1 composites are presented in Figure 4.5 on page 131.

For Z3-PU as shown in Figure 4.4a, the peak at 3325 cm^{-1} is attributed to the stretching ν(N—H). The peak at 3121 cm^{-1} was the overtone of 1533 cm^{-1} and 3039 cm^{-1} attributed to the ν(C—H) in benzene ring. The peaks at 2940, 2857 and 2795 cm^{-1} were CH$_2$ peaks of the polyether. The peak at 2940 cm^{-1} was the asymmetric stretching peak of CH$_2$ and the peak at 2857 cm^{-1} was the symmetric stretching of CH$_2$. The carbonyl absorption region was observed in between 1730 to 1700 cm^{-1}, the carbonyl absorption band classified into two peaks.

The peak due to bonded C==O stretching was at 1701 cm^{-1} and the free C==O stretching appeared at 1730 cm^{-1}. The peak at 1597 cm^{-1} was assigned to ν(C=C) in the benzene ring and 1533 cm^{-1} was the amide II δ(N-H) + ν(C==N). 1478 cm^{-1} was the weak CH$_2$ peak and the 1413 cm^{-1} attributed to the strong ν(C-C) in benzene ring. The peak at 1310 cm^{-1} was assigned to amide III δ(N-H) + ν(C==N), β(C-H) peak and

(a)

(b)

(c)

Figure 4.4: FTIR Spectra of non-aligned Z3A1 Composites (a): Stacked FTIR spectra of Electrospun Z3-PU, Z3-mHA and Z3-nHA. (b) Combined FTIR spectra of Z3-PU, Z3-mHA and Z3-nHA at Common Scale with Hydroxyl, Carbonyl, Phosphate and bending Phosphate groups highlighted as $*$, β, π and Φ, respectively. (c) A combined spectra of Z3-PU, Z3-mHA and Z3-nHA at common scale for a wavenumber region of 1800 - 450 cm^{-1}.

δ(N-H) + ν(C==N) appeared at 1225 cm^{-1}. The region between 1103-916 cm^{-1} was the ν(CH$_2$—O—CH$_2$) of ether peak and 1018 cm^{-1} was the weak β(C—H) in benzene ring. The peak at 817 cm^{-1} was the γ(C-H) from butane diol. These observations were similar to those reported by (Khan et al., 2008) in their study of polyurethane composites for dental restoration applications.

Figure 4.4b shows the combined spectra of Z3-PU, Z3-mHA and Z3-nHA at common scale, with emphasis on the hydroxyl, carbonyl, phosphate and bending phosphate groups whilst Figure 4.4c shows the combined spectra in greater detail for a wave number region

of 1800 - 450 cm^{-1}. The characteristic peak of stretching O—H was observed at 3570 cm^{-1} (Rehman and Bonfield, 1997). The bands at 1060, 961, 603 and 571 cm^{-1} were assigned to vibration of the phosphate group, PO$_4$. The peak at 1078 cm^{-1} was the triply degenerated vibration $\nu 3$, and 961 cm^{-1} was the non-degenerated symmetric stretching mode $\nu 1$ of the P—O bond of the phosphate group which apparently are active in the infra-red because the lower symmetry in the lattice sites introduces distortion (Fowler et al., 1966). The peak at 603 and 571 cm^{-1} were assigned to a triple degenerated bending mode $\nu 4$, of the O-P-O bond. The peak at 633 cm^{-1} was due to the phosphate $\nu 4$ bending.

The stretching O—H and P—O (stretching and bending) peaks were not present in the Z3-PU (polyurethane-only) spectrum. However, after mixing the micro and nano hydroxyapatite in polyurethane, the appearance of characteristic peaks of HA were observed and it was noted from the shifting and appearance of new peaks in the region of 1100-916 cm^{-1} that nano-HA with a higher surface area and more crystalline structure was mixed better than micro-HA and affected the shifting of peaks $\nu 3$ P—O from 1078 cm^{-1} for Z3-mHA to 1060 cm^{-1} for Z3-nHA. It has been mentioned in the literature that the width and intensity of peaks in FTIR spectrum have explicit dependence on the particle size.

As particle size increases, the width of the peak decreases and intensity increases. The restoring force of nano particles created by surface polarisation charge is responsible for the frequency difference. The difference in the frequency of vibrational modes is attributed to dipolar interactions, interfacial effects, surface amorphousness, surface free energy etc (Mo et al., 1993; Martin, 1996; Bobovich, 1988).

As with the Z3 scaffolds, a similar FTIR characterization pattern was also observed with the Z9 scaffolds as shown in Figures 4.5a and 4.5b. However, the characteristic peak of stretching and liberation modes of O—H usually seen at 3570 cm^{-1} and 630 cm^{-1}were not present in the Z9-mHA and Z9-nHA composites.

For the Z9-PU spectra, typical bands present at (800–1050) cm^{-1} were assigned to weak β and γ(C-H) bonds in the benzene ring; (1010–1250) cm^{-1} was assigned to (CH$_2$-O-CH$_2$) bonds, and (1180–1230) cm^{-1} was allotted to the strong δ(N-H) + ν(C-N).
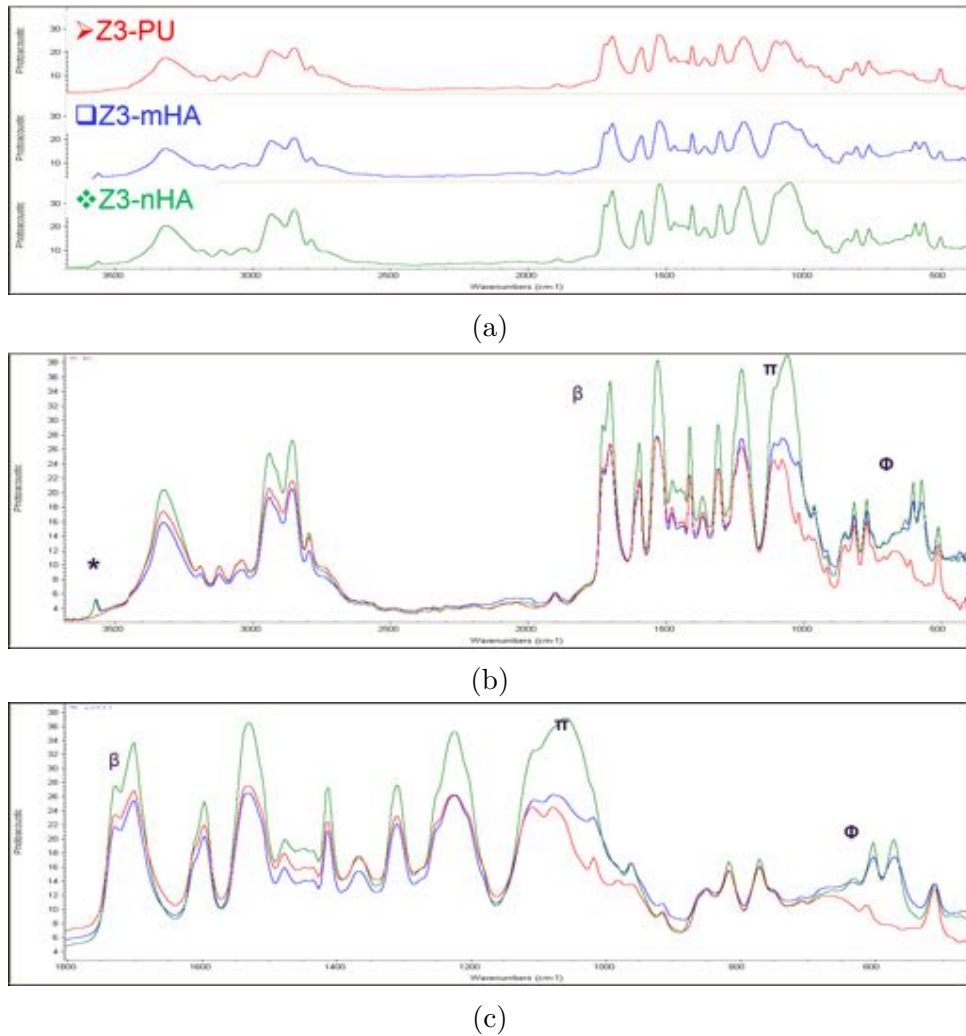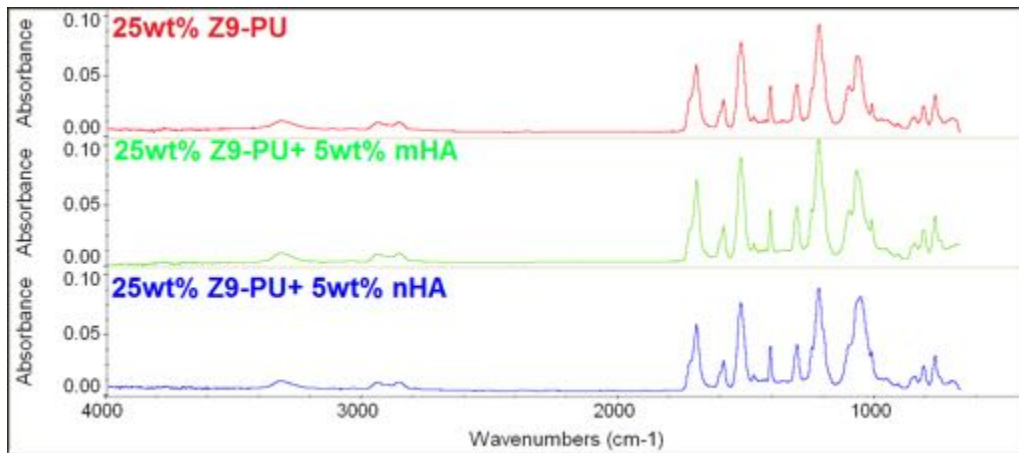
(a)
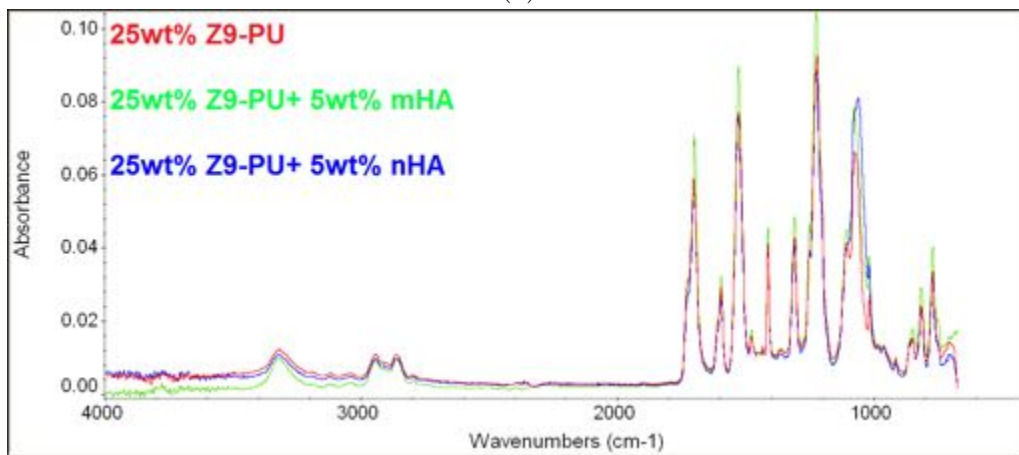
(b)
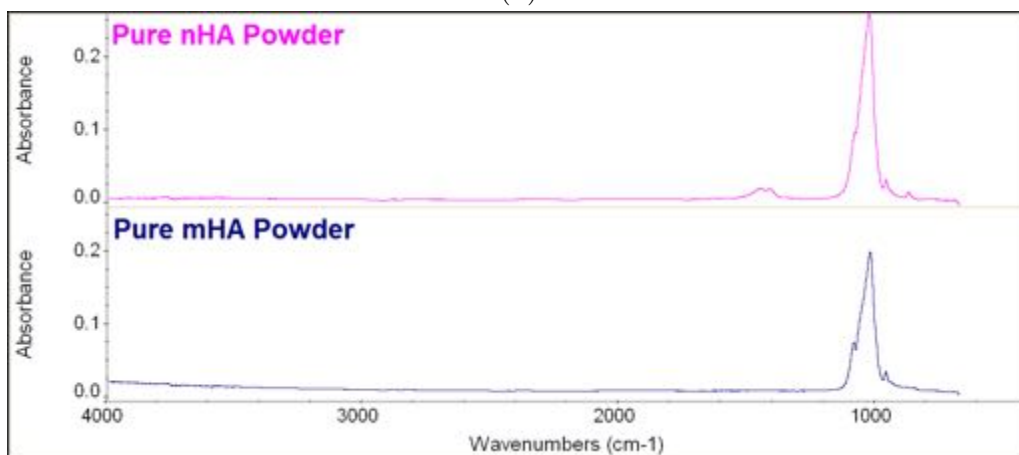
(c)

Figure 4.5: FTIR Spectra of non-aligned Z9A1 Composites (a): Stacked FTIR spectra of Electrospun Z9-PU, Z9-mHA and Z9-nHA. (b): Combined FTIR spectra of Z9-PU, Z9-mHA and Z9-nHA at Common Scale (c): A combined spectra of Pure mHA powder and Pure nHA powder at common scale. All spectra shows a wavenumber region of 4000 - 450 cm^{-1}.

4.3. RESULTS AND DISCUSSION ONE

1283 cm^{-1} and (1375–1630) cm^{-1} were ascribed to strong C=C bonds whilst (1750–1780) cm^{-1} was assigned to free and bonded C=O. In addition, peaks present at (2800–2950) cm^{-1} were attributed to strong vs (CH$_2$) bonding whilst those found at (3300–3400) cm^{-1} were ascribed to hydrogen non-bonded and bonded N-H stretching vibration.

Although the stretching and liberation modes of OH- groups usually observed at 3570 and 630 cm^{-1} were also not present in the HA spectra of pure Nano-HA powder and Pure Micro-HA powder without PU (Figure 4.5c), the phosphate and CO$_3$ group stretching at (960 – 1080) cm^{-1} and (1410–1475) cm^{-1} respectively indicates that both samples were indeed hydroxyapatite. This anomaly could be due to the fact that Attenuated Total Reflectance (ATR) sampling accessory was used to image the thicker Z9 scaffolds and the pure micro and nano-HA powders, instead of the Photo-acoustic sampling (PAS), which has been reported as a better technique for imaging biomaterials (Rehman and Bonfield, 1997).

Although ATR sampling requires less sample preparation or does not need to be purged with helium gas as compared to PAS sampling, not all samples are ATR compatible. ATR sampling requires an Schwarzchild IR objective which contains a ZnSe, Ge or diamond crystal that needs to be in contact with the material being tested. This allows the ATR crystal to absorb leaked out light that is normally reflected inside the crystal. This loss in reflection is then used to create a spectrum of the sample after it has been corrected for penetration depth as a function of wavelength (Miller, 2002).

Samples must therefore be thin and firm, or mounted onto stiff surfaces in order to establish good contact interaction between the crystal and the sample to allow an accurate spectral representation of the sample to be generated. Since Z9 scaffolds were thicker than the Z3 scaffolds, and both types of pure HA (micro and nano) were in a powdered state, this could have accounted for the absence of characteristic peaks of O—H in the spectra of both HA powders, as well as the Z9-mHA and Z9-nHA composites, shown in Figure 4.5 on page 131.

4.3.5 Mechanical Analysis of PU scaffolds

Microphase segregation, a key characteristic of thermoplastic polyurethane elastomers occurs as a result of the thermodynamic incompatibility of the hard and soft segments of PU and is known to play a key role in the mechanical properties of PU. Factors known to affect the degree of separation include segment polarity, hydrogen bonding responsible for hard/soft segment interaction, molecular weight and overall sample composition.

In general, Z9A1 scaffolds were stronger than Z3A1 scaffolds and presented with higher mechanical properties for all combinations of DMF and THF solvents. With identical chemical structures, differences in the mechanical properties of Z9A1 and Z3A1 probably resulted from the differences in molecular weights, which would have affected the interaction between the hard and soft segments, causing differences in the microphase segregation.

Table 4.2: Morphological and mechanical properties of Z9A1 and Z3A1 scaffolds with different solvent combinations.

Electrospun Scaffolds	Fibre Diameter (μm)	Thickness (mm)	Young's Modulus (MPa)	Yield Strength (MPa)
Z9-100	2.06 ± 3.09^c	0.27 ± 0.02	60.09 ± 10.1^{bc}	$2.13 \pm 0.55c$
Z9-70	1.54 ± 0.96^c	0.29 ± 0.06	25.89 ± 4.54^a	1.73 ± 0.79
Z9-50	3.47 ± 0.89^{ab}	0.36 ± 0.04	30.11 ± 0.78^a	1.27 ± 0.29^a
Z3-100	1.25 ± 1.56^{bc}	0.06 ± 0.01	18.54 ± 2.31^{bc}	1.56 ± 0.34^{bc}
Z3-70	1.93 ± 0.85^{ac}	0.18 ± 0.03	7.61 ± 0.76^{ac}	0.71 ± 0.03^a
Z3-50	2.82 ± 1.29^{ab}	0.10 ± 0.01	3.38 ± 1.25^{ab}	0.50 ± 0.04^a

(mean $\pm$ S.D., n= 40 for fibre measurements and 6 for all other measurements)
a=significantly different from scaffolds made from 100% DMF, at p $\leq$ 0.05
b=significantly different from scaffolds made from 70/30 DMF/THF, at p $\leq$ 0.05
c=significantly different from scaffolds made from 50/50 DMF/THF, at p $\leq$ 0.05

Decreasing the proportion of DMF in the solvent reduced the Young's Modulus and strength of Z9A1 and Z3A1 scaffolds. Z9-100 (100% DMF) showed a brittle stress-strain profile with plastic deformation occurring at 30% strain as shown in Figure 4.6a. Z9-100 also had the highest Young's Modulus and yield strength, significantly higher than those of Z9-50 for both properties, however, only Young's Modulus was significantly higher than that of Z9-70 scaffolds (Table 4.3 on page 135).

133
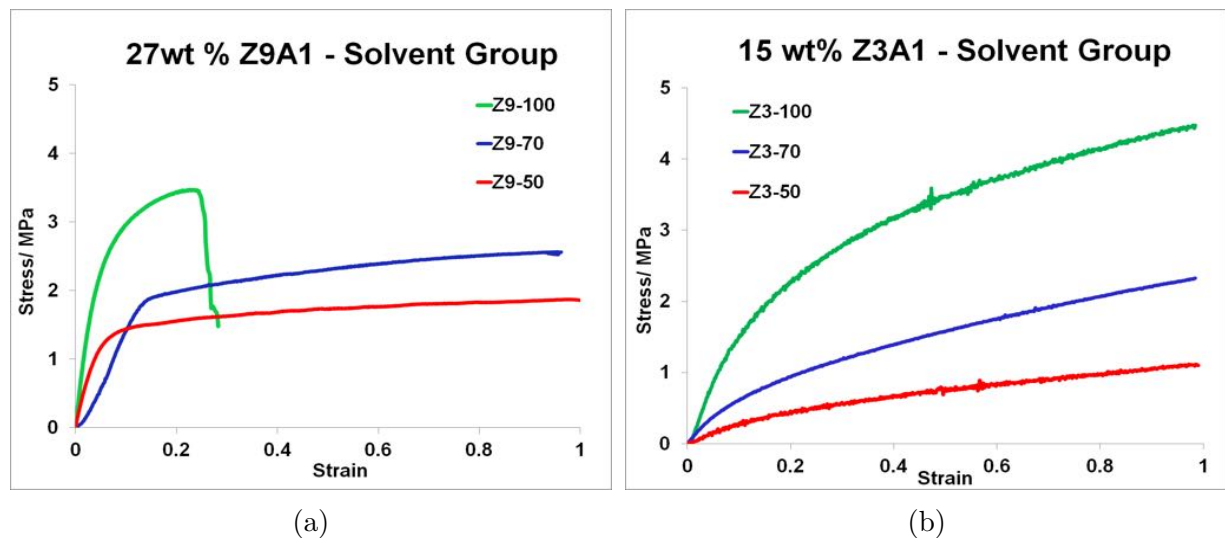
Figure 4.6: Example stress/strain curves of fabricated scaffolds, (a) Effect of solvent combination on Z9A1 scaffolds (b) Effect of solvent combination on Z3A1 scaffolds.

A similar pattern was observed with the Z3 groups as shown in Figure 4.6b. Values of Young's Modulus for Z3-100, Z3-70 and Z3-50 were significantly lower with less DMF in the electrospinning solvent (Table 4.2 on page 133). For both polymers, these differences in mechanical properties are likely to be the result of differences in fibre morphology (Figure 4.2 on page 124) which in turn may have resulted from differences in the solvent properties of DMF and THF. Beads present in scaffolds fabricated with 100% DMF solvent (Figure 4.2 on page 124) probably created short regions of large fibre cross-sectional area, which would have caused there to be a greater amount of material relative to void space within the sample, which would in turn create an overall stronger scaffold but with a reduced ability to undergo strain.

4.3.6 Mechanical Analysis of PU-HA Composites

Mechanical properties of composites are controlled by several micro-structural factors such as the properties of the matrix, interfacial bonding strength, processing methods and the properties and distribution of fillers. The interface strength between PU and HA particles greatly affects the effectiveness of load transfer from the polymer matrix to micro and nanocomposites. For composite scaffolds, inclusion of HA particles improved the tensile properties of both Z9A1 and Z3A1 scaffolds, Young's Modulus and yield

strength of composite scaffolds were significantly higher than those of plain PU scaffolds, for both Z9A1 and Z3A1.

Table 4.3: Morphological and mechanical properties of Z9A1 and Z3A1 scaffolds with different types of HA.

Electrospun Scaffolds	Fibre Diameter (μm)	Thickness (mm)	Young's Modulus (MPa)	Yield Strength (MPa)
Z9-PU	2.01 ± 0.80	0.36 ± 0.01	9.56 ± 3.03^d	0.61 ± 0.18^d
Z9-mHA	2.86 ± 6.01	0.30 ± 0.01	88.69 ± 20.20^{ce}	3.02 ± 0.80^{ce}
Z9-nHA	2.95 ± 1.60	0.42 ± 0.02	10.21 ± 2.99^d	0.79 ± 0.16^d
Z3-PU	2.18 ± 0.51^e	0.43 ± 0.09	2.42 ± 0.21^{de}	0.29 ± 0.04^{de}
Z3-mHA	2.61 ± 1.45^e	0.31 ± 0.01	4.77 ± 0.29^{ce}	0.46 ± 0.03^c
Z3-nHA	1.56 ± 0.63^{cd}	0.09 ± 0.01	3.09 ± 0.30^{cd}	0.52 ± 0.09^c

(mean $\pm$ S.D., n= 40 for fibre measurements and 6 for all other measurements)
c=significantly different from PU scaffolds, at $p \leq 0.05$
d=significantly different from scaffolds made with mHA, at $p \leq 0.05$
e=significantly different from scaffolds made with nHA, at $p \leq 0.05$
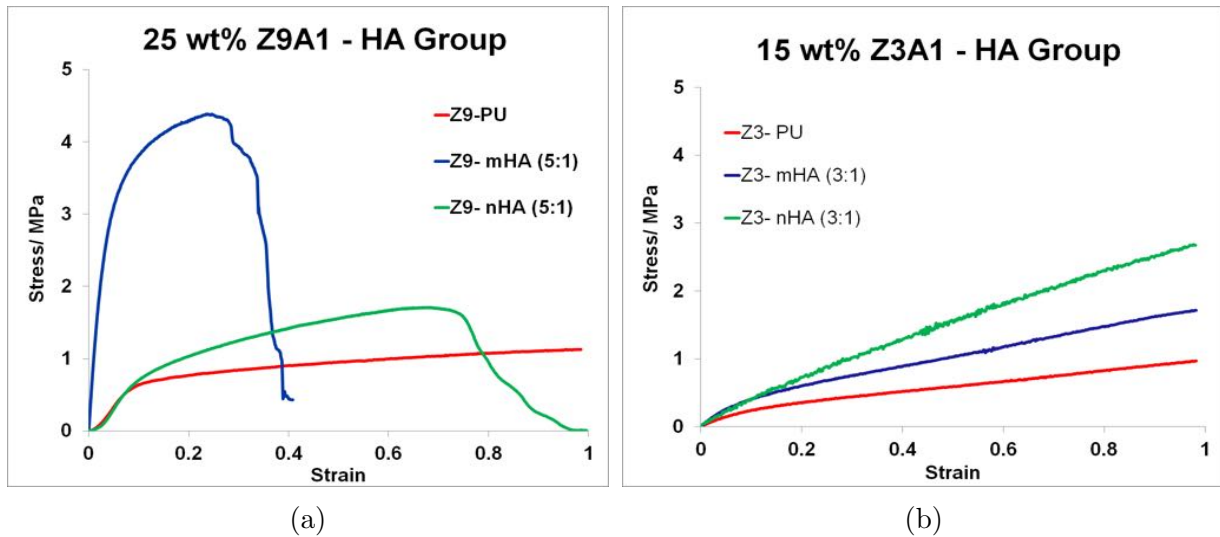
Figure 4.7: Example stress/strain curves of fabricated scaffolds, (a) Effect of HA particles on Z9A1 scaffolds, (b) Effect of HA particles on Z3A1 scaffolds.

SEM images of electrospun composites (Figure 4.3 on page 126) show that nHA, with its smaller size and higher surface area, properly integrated with the PU fibres compared to mHA which can be seen sticking out of the fibres and creating lumps and beads. Better mixing of nHA particles with PU as compared to mHA particles was also confirmed with FTIR for the Z3 composites. It was therefore expected that the nano-composites would

be stiffer and stronger than the micro-composites However, for Z9A1, both yield strength and Young's Modulus of mHA scaffolds were significantly higher than those of Z9-nHA scaffolds. Interestingly, the yield strength of Z3-nHA scaffolds was higher than that of Z3-mHA, although not statistically significant. These differences in behaviour between Z9A1 and Z3A1 composites scaffolds could have resulted from the difference in the PU:HA ratio between Z9A1 (5:1) and Z3A1 (3:1) and the molecular weight of the polymers. Z9A1 has a higher molecular weight and produces scaffolds that are high in Young's modulus and strength but more brittle, hence the addition of HA further increases the brittleness of the electrospun scaffold.

In contrast, Z3A1 has a lower molecular weight and is more flexible and the addition of HA, albeit at a higher concentration than that for Z9, has a smaller effect on the properties of the electrospun scaffold. Molecular weight, concentration and size of HA would all have resulted in differences in interactions between solvents, macromolecular chains of the polymer and the HA particles. These difference in interactions have been reported to affect microphase separation between the hard and soft segment of PU, hence ultimately affecting its mechanical properties (Oprea, 2005).

4.3.7 Cell Viability on PU Scaffolds

Electrospun polyurethane scaffolds have been used for several tissue engineering applications for more than 10 years (Khil et al., 2003; Clarke et al., 2008; Carlberg et al., 2009) as almost all of human tissue is deposited on nanofibrous structures. It is therefore ideal to mimic some of the structure and biological function of the natural extracellular matrix (ECM) with cells grown on electrospun scaffolds.

MLO-A5 cells were seeded on Z9A1 and Z3A1 PU scaffolds fabricated from solutions containing varying combinations of DMF/THF solvents, to assess the effect of varying fibre morphology resulting from solvent combination on cell viability. MLO-A5 cells have characteristics of a post-osteoblast and pre-osteocyte cell type, and rapidly mineralize in sheets rather than nodules. These cells have been used to extensively study the osteoblast to osteocyte differentiation process, bone mineralization and the effects of

mechanical loading on biomineralization (Sittichockechaiwut et al., 2009; Rosser and Bonewald, 2012).

pH Studies on Z9-PU Scaffolds in PBS
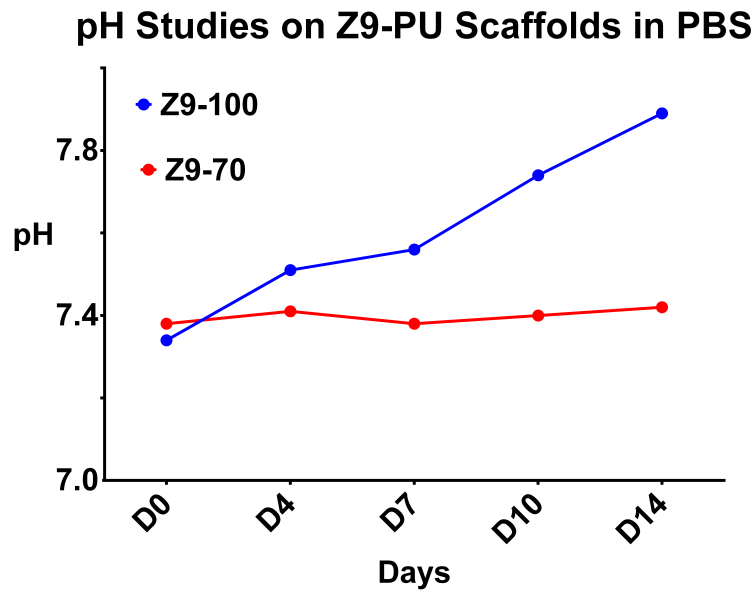
Figure 4.8: pH readings of Deionised Water Treatment on 28wt% Z9-PU Scaffolds, Z9-100 made from 100% DMF and Z9-70 made from 70/30 DMF/THF.

Prior to cell culture, the electrospun scaffolds were placed in PBS for a two week period to investigate the possibility of any remaining solvent leaching from the scaffolds. As shown in Figure 4.8 on page 137, Z9-PU scaffolds manufactured from solutions containing 70/30 DMF/THF content had a fairly stable pH reading over the period where as scaffolds made from 100% DMF solvent showed an increasing pH over the period. This indicated that although all scaffolds were placed in a vacuum chamber in an attempt to remove all traces of remaining solvent, some DMF solvent was still present in the 100% DMF scaffolds probably due to the low vapour pressure and slow evaporation rate of DMF as compared to THF.

This slow evaporation of DMF was also reported by Shawon and Sung (2004) in their study of polycarbonate nanofibres. They reported that polycarbonate solutions with higher ratios of THF to DMF solvent mixtures had more solvent evaporation occurring due to the higher vapour pressure of THF. On the other hand, since DMF has lower vapour pressure, it evaporates slowly, leaving solvent traces in the scaffold even after

4.3. RESULTS AND DISCUSSION ONE

electrospinning. Therefore at higher THF to DMF ratios, the rate of solvent evaporation from the fibre surface increased. This was likely due to large volume of THF in the polymer solution which caused the fibres to carry more charges per unit mass.

As a result of this observation, scaffolds were always placed in PBS solutions prior to cell culture to remove potential remaining solvent, as this could be toxic to the cells. PBS solutions were changed every 24 hours over a 3 day period.

(a)   (b)
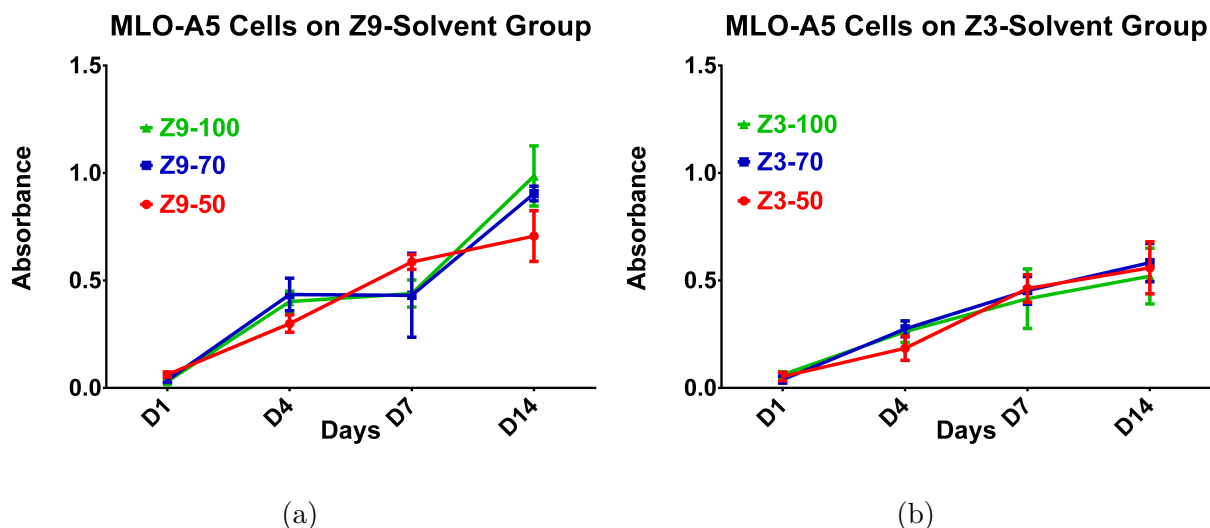
Figure 4.9: MTT absorbance for MLO-A5 cells seeded on (a) Z9A1 PU scaffolds (b) Z3A1 PU Scaffolds.
(mean ± S.D. n=6) For statistical analysis see text.

For biological characterisation, cells were viable on all scaffolds during the 14 day culture period. Cells had similar viability on all Z9A1 on day 1, indicating that, there were no differences in the cell's ability to attach to scaffolds. Viability increased steadily from day 1 to day 4 with similar values on Z9-100 and Z9-70 scaffolds between day 4 and day 7. On day 14 of culture, there was no significant difference between MTT absorbance on Z9-70 and Z9-100, however, cell viability on Z9-50 scaffolds was significantly lower than that on Z9-100 and Z9-70 ($p \leq 0.05$) (as showed in Figure 4.9a). This could have been the result of morphological differences in fibre diameter, as Z9-50 fibre diameters were significantly larger than Z9-70 and Z9-100 fibres.

For Z3A1 scaffolds, there was a steady increase in cell viability on all Z3-100, Z3-70 and Z3-50 scaffolds during the culture period (in Figure 4.9b). There was however, no significant difference between all groups of scaffolds, except that Z3-50 did not support

as high a cell viability on day 4 (p≤0.05). The ability of electrospun scaffolds to mimic the natural three-dimensional environment of the *in vivo* extracellular matrix whilst providing structural support with a high surface area to volume ratio, makes them excellent structures for tissue engineering applications.
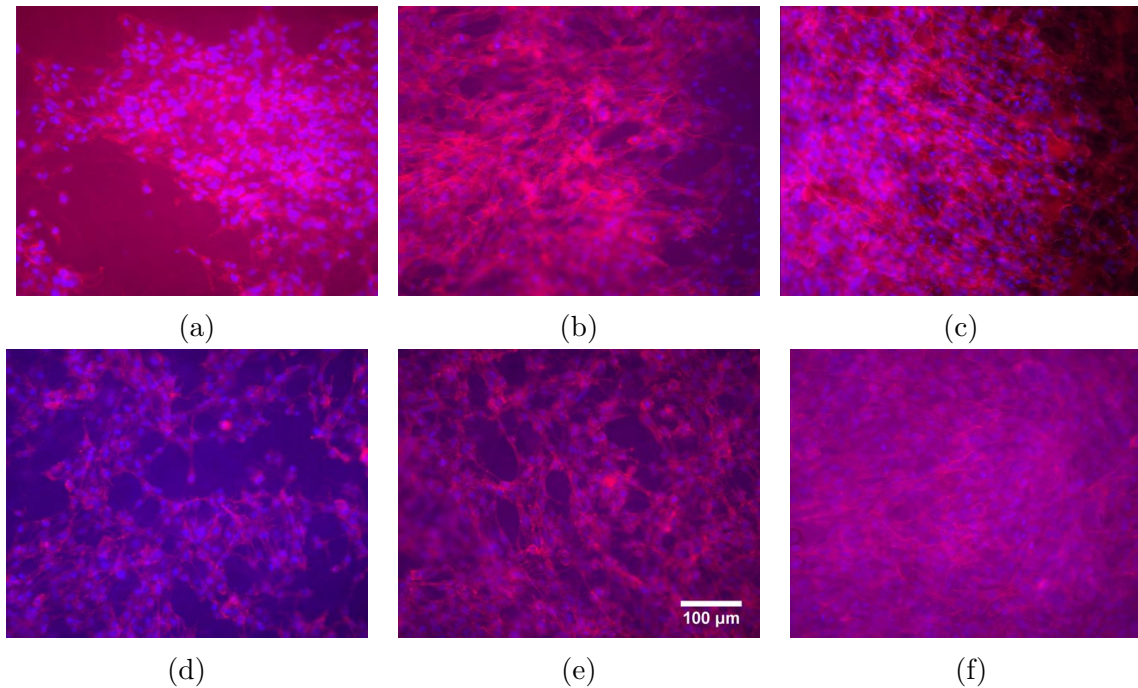
Figure 4.10: Fluorescent micrographs of DAPI (blue=nucleus) and Phalloidin (red=actin) staining of MLO-A5 Cells on Z3-70 scaffolds on (a) Day 1 (b) Day 4 and (c) Day 7 & for Z9-70 scaffolds on (d) Day 1 (e) Day 4 & (f) Day 7.
Scale Bar at 100 µm.

It has been reported that cells assume a more spindle-shaped morphology with increasing fibre diameters and rather orient parallel to fibres with aligned meshes (Bashur et al., 2009; Delaine-Smith et al., 2014). DAPI (nucleus) and Phalloidin (actin cytoskeleton) staining over a seven day period confirmed the MTT data indicating increasing numbers of cells attached to the scaffolds over time. Figure 4.10 shows representative micrographs of cell attachment over the period indicating that cells were well spread on the scaffolds with an elongated morphology for Z3-70 (Figure 4.10a - 4.10c) and Z9-70 (Figure 4.10d - 4.10f) scaffolds. The cells however appeared to be very confluent and less spread out by day 7, especially on the Z9-70 (Figure 4.10f) scaffolds. This observation was further reinforced with histological analysis of the scaffold's cross-section as discussed in Section 4.3.10. This confirmed that both MLO-A5 and hES-MP cells did

not only reside on the surface of the electrospun mats but penetrated the porous regions to occupy the entire scaffold.

4.3.8   Cell Viability on Composite Scaffolds

Hydroxyapatite $(Ca_{10}(PO_4)_6(OH)_2)$, HA has been widely used as a biocompatible material in many areas of medicine. HA is well established as a synthetic material for bone replacement due to its chemical resemblance to the inorganic component of bone and tooth. Additionally, HA is known to promote faster bone regeneration and direct bonding to regenerated bone without intermediate connective tissue (Patel et al., 2002).

Z9-PU, Z9 bioactive scaffolds (Z9-mHA & Z9-nHA) fabricated with 25wt% PU + 5wt% HA were seeded with MLOA-5 cells at a concentration of 1.5 x 10^5 cells per scaffold for an initial 14-day experiment. This concentration was later reduced to 1.0 x 10^5 cells per scaffold, for longer 28 day experiments as the scaffolds quickly become over confluent with some of the cells starting to peel of after day 14.

(a)	(b)
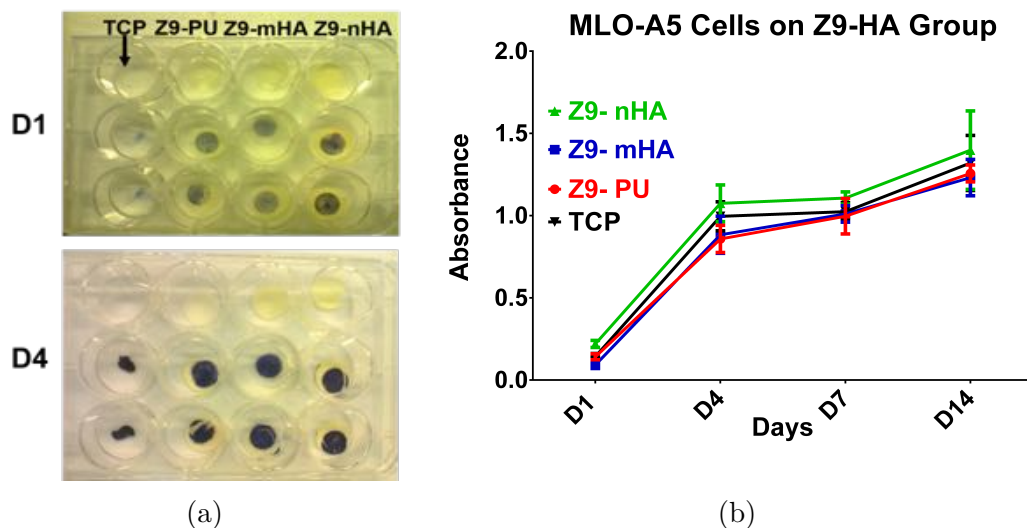
Figure 4.11: MTT of MLO-A5 cells on Z9A1 composite scaffolds, (a) Before Destaining (b) Quantitative absorbance after destaining with acidified Isopropanol - TCP control (black) *(Mean ± S.D. n=6), For statistical analysis see text.*

As shown in Figure 4.11b, Z9A1 non-aligned scaffolds fabricated with 5wt% nano-HA particles showed a higher cell viability across all time points (including day 1) as compared to Z9-PU, Z9-mHA and the Tissue Culture Plastic (TCP) control. Cells grown on TCP

had the second highest viability, whilst Z9-PU showed the lowest viability amongst the group after day 1. It was interesting to observe that Z9-mHA scaffolds with micro-HA particles had viabilities similar to those of Z9-PU polyurethane-only scaffolds. Although viabilities varied amongst the various materials during the 14-day culture period, there was no significant difference between their ability to support cells on days 1, 7 and 14. The only significant difference in the Z9-composite group was observed on Day 4, where the MTT absorbance of cells cultured on Z9-nHA scaffolds were significantly higher than those cultured on Z9-PU and Z9-mHA scaffolds.

nHA particles have been reported to favour interface adhesion between the nanoparticles and the polymer matrix ensuring an even and balanced blend in the nanocomposite as compared to the microcompostite (Rezwan et al., 2006). However, although a higher viability was observed for Z9-nHA scaffolds, further experiments were undertaken with a longer 28 day culture period, and another cell type or PU-nHA composite such as Z3-nHA. This was necessary to corroborate that the higher viability observed, resulted from the bioactive ability of nano-HA particles and not the biocompatible features of the Z9 polyurethane.

Z3A1 composite scaffolds which were easier to fabricate, consistently presented with a more uniform combination of nano and micro fibre diameters, were also less brittle than their Z9A1 counterparts. They were therefore used to examine the growth of hES-MP cells as well as MLO-A5 on composite scaffolds over a 28 day period. As human cells have been reported to attach and organize well around fibres with diameters smaller than those of cells, a combination of micro and nanoscale fibrous scaffolds have been said to provide an optimal template for cells to attach, migrate and grow (Huang et al., 2003; Laurencin et al., 1999).

Similar to Z9-nHA scaffolds, MLO-A5 cells seeded on Z3-nHA scaffolds had the highest cell viability at all-time points after day 1, being 22% higher by day 28 (Figure 4.12a), this implies that cell proliferation rate was higher on these scaffolds as MTT absorbance at day 1 was the same for all groups. This is similar to the effects of nHA observed with the Z9 composite group and in previous studies (Bianco et al., 2009; Mi et al., 2014).

4.3. RESULTS AND DISCUSSION ONE

This probably resulted from the bioactive nature of HA coupled with the higher surface area and crystallinity of nHA particles.

(a)   (b)
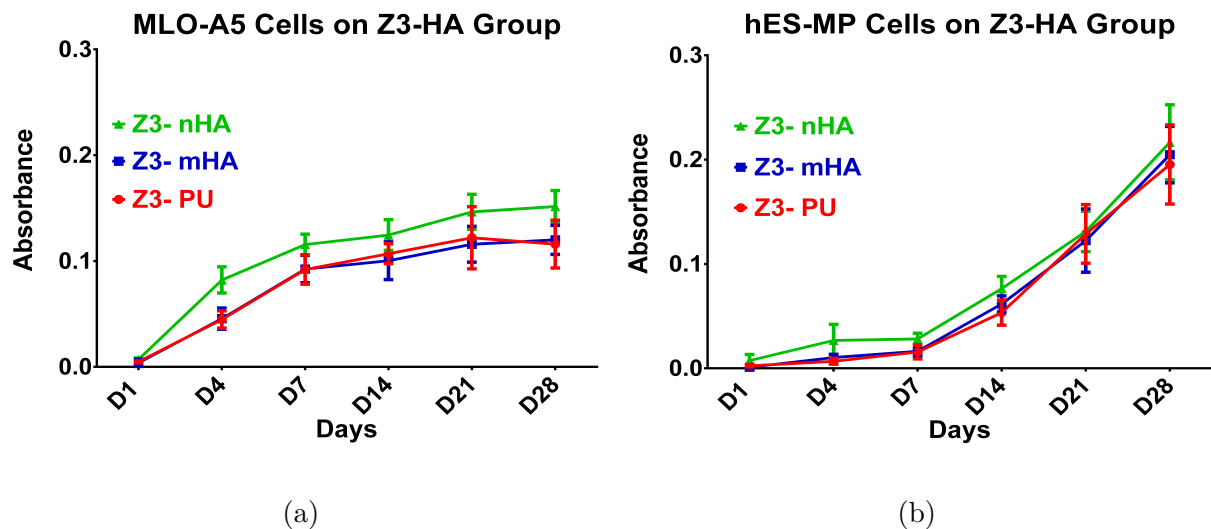
Figure 4.12: MTT absorbance on Z3A1 composite scaffolds. (a) MLO-A5 cells on Z3 PU, Z3-mHA and Z3-nHA scaffolds (b) hES-MP cells on Z3 PU, Z3-mHA and Z3-nHA scaffolds.
(Mean ± S.D. n=6), For statistical analysis see text.

A high HA surface area facilitates a strong interaction between the polymer and ceramic phase, and allows protein attachment. For example, it has been reported that initial calcium absorption to nanoceramic surfaces enhanced binding of vitronectin, that subsequently promoted osteoblastic adhesion and proliferation (Webster et al., 2001). It might be expected that mHA would also elicit cell viabilities as high as those attained by the nano-composites but that was not observed for MLO-A5 in this study. This may have been due to the lower scaffold porosity that was observed with the inclusion of mHA particles, which could have hindered cell proliferation, migration, and nutrient transfer.

To investigate the ability of these composites to support progenitor cells, hES-MPs, embryonic derived mesenchymal progenitor cells were also seeded on Z3A1 electrospun scaffolds and cultured in only osteogenic media (Figure 4.12b). hES-MPs have been used in several studies as a model cell for bone tissue engineering (Karlsson et al., 2009). In the presence of osteogenic supplements, hES-MP cells have been shown to differentiate towards the osteogenic lineage *in vitro* (Delaine-Smith et al., 2012).

As shown in Figure 4.12b, there was an increase in hES-MP cell viability over all

142

time-points on Z3A1 scaffolds however, in contrast to MLO-A5 cells, there was no significant difference between Z3-nHA, Z3-mHA and Z3-PU scaffolds in their ability to support cell proliferation. There is no obvious reason for this different effect of nHA on cell proliferation of the two types but it may be related to cell size and their different stages in the osteogenic differentiation pathways. It will therefore be interesting to investigate the osteoinductive ability of both micro and nano-HA composites, by culturing hES-MP cells in non-osteogenic media.

4.3.9 Collagen and Calcium Staining

The ultimate test of a scaffolds ability to support bone tissue engineering is its ability to support bone-like extracellular matrix deposition. Collagen and calcified matrix staining using Sirius red and alizarin red, respectively, were used to study matrix production on scaffolds in the Z3A1 composite group on days 14, 21 and 28 of culture.
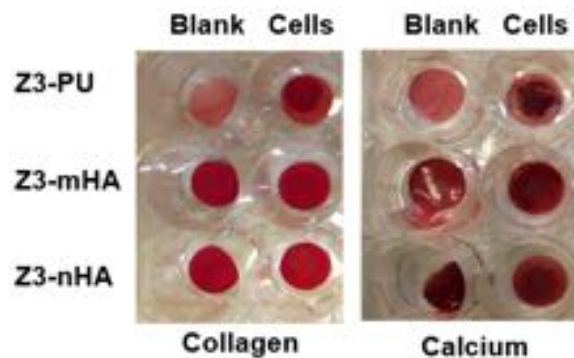
Figure 4.13: Day 14 Sirius Red Collagen Stain and Alizarin Red Calcium Stain on non-aligned Electrospun Scaffolds seeded with MLO-A5 cells.

Staining and destaining was done as described in Sections **3.7.5** and **3.7.6** on page 103 and 104, respectively. Photographic images of the samples as shown in Figure 4.13, taken after staining showed a good deposition of both mineralisation and collagenous extracelluar matrix on the scaffolds. Appropriate destaining solutions were then added to the samples to elucidate the deposits and allow for quantitative analysis.

Collagen production by MLO-A5 cells on Z3 scaffolds was highest for Z3-nHA scaffolds at all-time points (Figure 4.14a) with the highest deposition measured on day 28,

significantly higher than that produced on Z3-mHA and Z3-PU scaffolds. This is the same scaffold that supported the highest number of viable MLO-A5 cells. A similar pattern was observed with hES-MP cells (Figure 4.14b). It will therefore be interesting to establish if this occurred due to proliferating cell numbers by normalizing the Sirius red data with MTT or Pico-green DNA data. This would confirm if more cells resulted in more collagen, or that a fewer number of cells secreted a high amount of collagen.

(a)

(b)

(c)

(d)
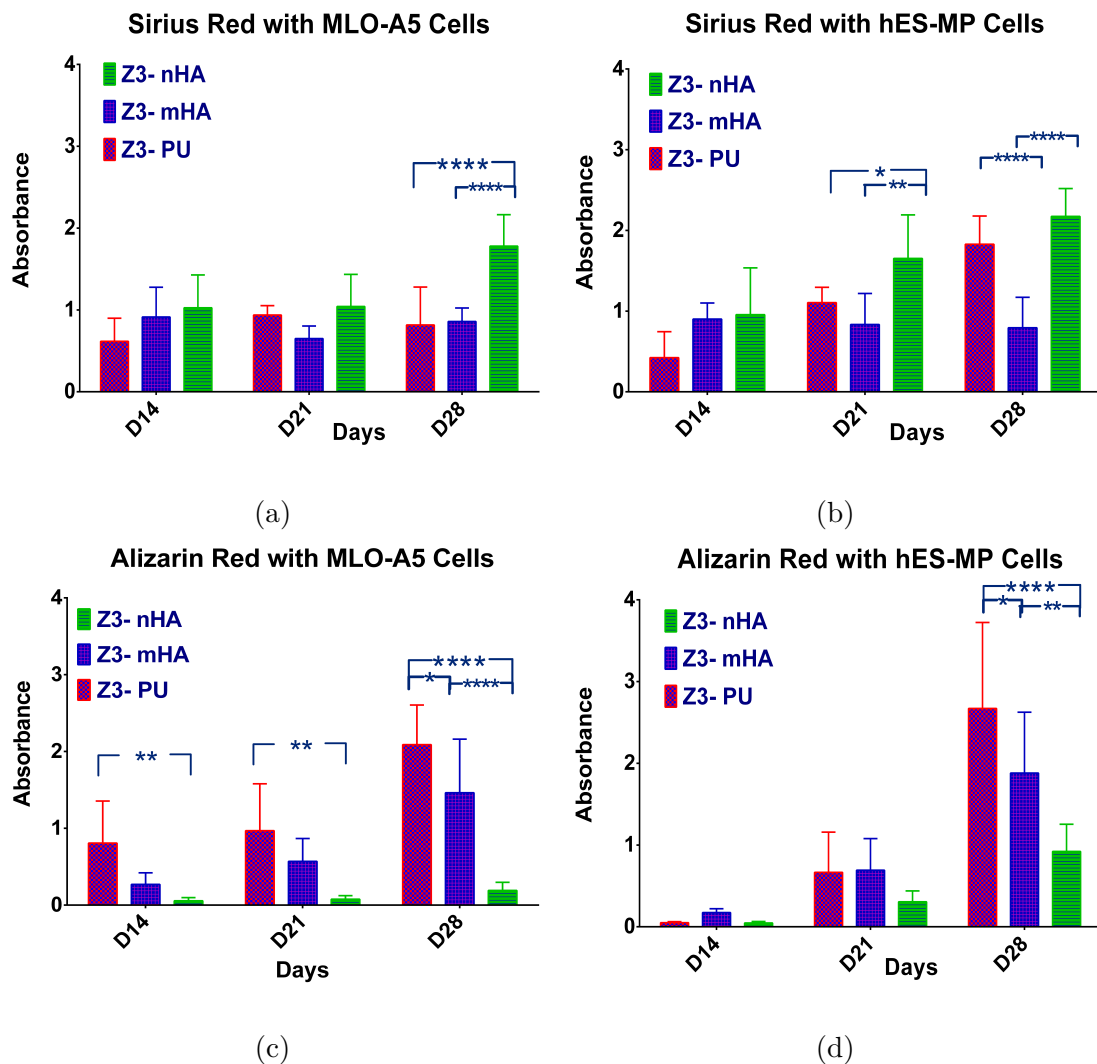
Figure 4.14: Collagen and calcium Staining on Z3-PU, Z3-mHA and Z3-nHA scaffolds on D14, D21 and D28. (a) Sirius Red absorbance of MLO-A5 cells, (b) Sirius Red absorbance of hES-MP cells, (c) Alizarin Red absorbance of MLO-A5 cells (d) Alizarin Red absorbance of hES-MP cells.
*(Mean ± S.D. n=6) * p ≤0.05, ** ≤0.01, * * ** ≤0.0001.*

Interestingly, calcium production appeared to elicit results opposite to those attained for collagen production. Alizarin red absorbance on cell-seeded Z3–PU scaffolds was

higher for both MLO-A5 (Figure 4.14c) and hES-MP cells (Figure 4.14d) than for HA composite scaffolds (after subtraction of the background absorbance). However, unsurprisingly, alizarin red strongly stained the blank (no cells) control scaffolds that contained HA (Figure 4.13 on page 143). As this is a single blank and not the same sample on which cells are seeded, any variability in HA content between scaffold samples would have made it more difficult to distinguish between the scaffold HA and cell-deposited HA. It would be interesting to image mineralisation in the same scaffold over time using techniques such as μCT scanning or Xylenol orange as used in subsequent chapters to determine if there was truly less cell deposited calcium in the composite scaffolds.

4.3.10 Histology

Histological sections were used to examine how far cells seeded on the scaffold surface penetrated into the scaffolds in the Z3 composite group. Hematoxylin and eosin staining, a popular biological characterization technique that stains nucleus purple and cytoplasm pink, was used to assess how deep MLO-A5 cells and hES-MP inflitrated the scaffolds on day 14, 21 & 28 of culture.

As shown in Figure 4.15, MLO-A5 cells were generally densely distributed on the surface of all scaffolds on day 14 as compared to hES-MP cells which exhibited thinner coverage in Z3-PU and Z3-mHA scaffolds and were more loosely dispersed throughout the scaffold interior.

hES-MPs cells cultured on Z3-nHA scaffolds appeared to penetrate to the greatest depth and were found in more locations compared to all other groups, although no cells were seen at the bottom of the scaffold at the day 14 time-point. Although infiltration of hES-MP cells into the scaffolds was greater on day 21 as compared to day 14, the cells did not reach the bottom of scaffolds. However, as shown in Figure 4.16, hES-MP cells on days 28 of culture penetrated the entire depth of the scaffolds, although the highly dense distribution of the cells were still present on the surface.

This penetration along the depth of the scaffold was greatest in the Z3-nHA scaffold on day 28, as it had a much smaller thickness as compared to the Z3-mHA and Z3-PU
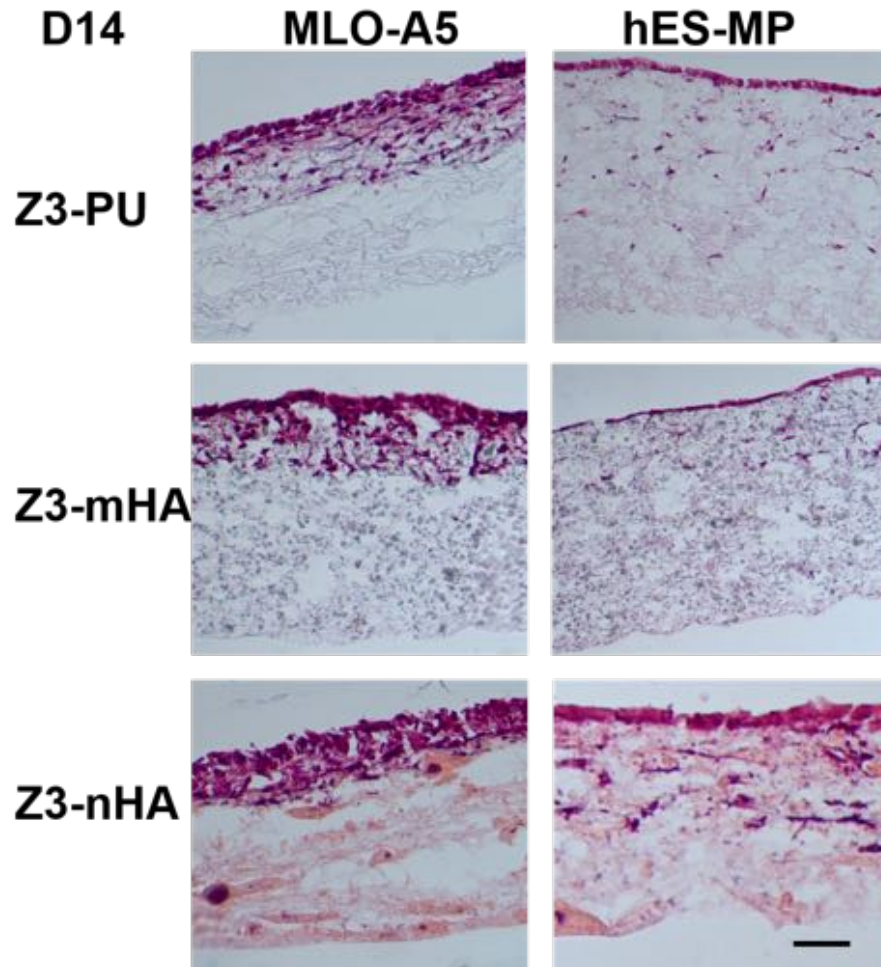
Figure 4.15: H & E staining on Z3-PU, Z3-mHA and Z3-nHA scaffolds on Day 14 of culture for MLO-A5 and hES-MP cells.
Scale Bar at 100 µm

scaffolds. It is also interesting that hES-MPs appear to penetrate deeper than MLO-A5 which may be related cell size or differences in attachment and migration cell surface molecules. The lack of adequate cell penetration into these scaffolds may have resulted from the low porosity, pore size and interconnectivity of scaffolds associated with the closely packed arrangement of the fibres.

This observation of low cell and matrix penetration has also been reported extensively in the literature as a major limitation of traditional electrospun sheets (Bergmeister et al., 2013; Leong et al., 2010). It would therefore be advantageous to increase the porosity of thicker electrospun scaffolds by opening up spaces between the fibres. Electrospinning with a cryogenic mandrel, controlling fibre deposition with air-flow impedance and electrospinning with porogens amongst others have reported to enhance scaffold porosity
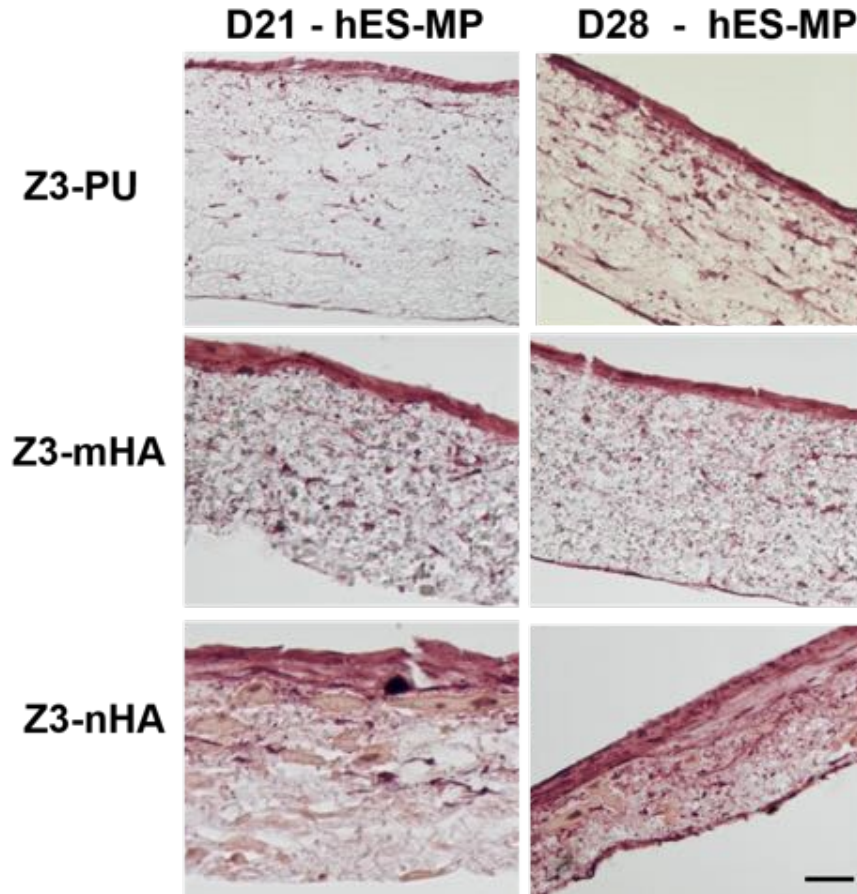
Figure 4.16: H & E staining on Z3-PU, Z3-mHA and Z3-nHA scaffolds on Days 21 & 28 of culture for hES-MP cells.
Scale Bar at 100 µm

and cell penetration (McClure et al., 2012).

It is also possible to increase porosity by co-spinning polymer solutions with a very fast degrading or water-soluble polymer (Milleret et al., 2011), and using mechanical techniques such as ultrasonication (Lee et al., 2011) and static stretch to force fibres apart and thus facilitate greater cell penetration, nutrient diffusion and transportation of metabolic products.

4.4   Chapter Summary and Key Points

- Both Z9A1 and Z3A1 PU pellets dissolved in 100% DMF, 70/30 DMF/THF and 50/50 DMF/THF solvents. Varying the amount of DMF and THF in solution affected solution and electrospinning properties, fibre morphology and mechanical

4.4. CHAPTER SUMMARY AND KEY POINTS

properties

- Increasing the amount of THF in solution eliminated the presence of beads seen in scaffolds fabricated from solutions containing only DMF. However, increasing the amount of DMF in solution increased Young's Modolus and yield strength of scaffolds in the solvent group.

- PU-only and PU-nHA scaffolds in the non-aligned composite group had more uniform fibre diameter than their PU-mHA counterparts.

- PAS-FTIR and ATR-FTIR confirmed the presence of HA in all composite scaffolds.

- Z9A1 scaffolds were generally stronger than Z3A1 scaffolds and presented with higher mechanical properties. Inclusion of HA particles reinforced the mechanical properties of both Z9A1 and Z3A2 composites.

- mHA composites had the highest Young's Modulus but nHA composites had the highest yield strength, whilst Z9-PU and Z3-PU had the lowest mechanical properties amongst the composite groups.

- nHA composites had the highest cell viability across all time-points for both MLO-A5 and hES-MP cells.

- H & E histology showed in-depth cell penetration throughout the entire scaffold, although hES-MP cells penetrated much further than MLO-A5 cells.

5 | Results and Discussion Section Two

Developing Aligned Polyurethane-Hydroxyapatite Reinforced Electrospun Composites: Analysing the Orientation and Directionality of Deposited Collagen using Second Harmonic Generation Imaging

5.1 Introduction

With the emergence of tissue engineering and regenerative medicine, there is enormous potential to employ treatment strategies that involve the use of biosynthetic constructs to overcome muscoluskeletal defects. Such defects can be caused by congenital malformation, infection, tumour resection, trauma and age-related pathologies. Human bone functions to provide mechanical integrity for locomotion and structural rigidity to the body. Hence the mechanical properties of bone is of great importance. Its high tensile strength and fracture toughness stems from the tough and flexible collagen fibres reinforced with hydroxyapatite crystals (Rezwan et al., 2006). Electrospun polymer-ceramic composites with ultra-fine continuous fibres and versatile mechanical properties are therefore a suitable template for engineering damaged bone tissue.

The inorganic phase of bone mostly referred to as hydroxyapatite, is an impure form of the naturally occurring calcium phosphate. However, the hydroxyapatite of bone

5.1. INTRODUCTION

is not 100% pure hydroxyapatite. It contains impurities such as potassium, magnesium, strontium and sodium (in place of the calcium ions), carbonate (in place of the phosphate ions), and chloride or fluoride (in place of the hydroxyl ions)(Keaveny et al., 2001). This is due to its tiny apatite crystals with average dimensions of 2-5 nm thickness, 15 nm width and 20-50 nm in length.

Electrospinning is a simple technique for fabricating scaffolds with surface modification flexibility and large surface area to volume ratios. Such advantages make electrospun constructs ideal for a wide range of potential applications including textiles, electrical, optical and biomedical applications, amongst others (Huang et al., 2003). Additionally, the possibility of large scale production combined with the simplicity of the process makes this technique very attractive for many biomedical applications, such as tissue engineering, tailored drug release and delivery, wound dressing and enzyme immobilization (Agarwal et al., 2008). This is because electrospinning can be used to fabricate aligned and random fibres with diameters in the nano to micrometre scale ranges, which mimic the length scales of native cellular environments and enhance matrix deposition.

The previous chapter focussed on improving the mechanical properties of electrospun PU scaffolds by incorporating HA particles to create micro and nano-composites. It also explored dissolution mechanisms of polyurethane in graded solvent combinations of DMF and THF. This made it possible to attain consistent, homogeneous and spinnable PU-only and PU-HA solutions, and also examine ideal conditions for electrospinning scaffolds. Optimising these conditions led to the development of a range of electrospun mats with random fibres that can be used for various bone tissue engineering applications. It was also demonstrated that, random PU-HA scaffolds with micro-HA particles had almost twice the yield strength and Young's Modulus of PU-only scaffolds.

These PU-mHA scaffolds which had the highest Young's Modulus and yield strength of 4.77 MPa and 0.46 MPa, respectively within the Z3 random composite group, are still relatively weaker than developing bone. It has however been reported in the literature that fabricating scaffolds with aligned fibre orientation can greatly increase the strength

and stiffness of scaffolds. These can be up to 9 times higher than those of random scaffolds made from the same polymer (Greiner and Wendorff, 2007). Although the previous study provided in-depth understanding, analysis and practical knowledge of creating electrospun composites with random fibres, I hypothesised that creating aligned electrospun scaffolds could provide better tensile mechanical properties that mimic the protein phase of bone and allow cells to deposit bone mineral. This would be suitable for applications where thin sheets of bone are needed with good resistance to tension and shear such as cleft palate repair.

Electrospun scaffolds with aligned fibres have been focus of many regenerative research groups for several years. Such scaffolds have been fabricated from polymers including cellulose, polystyrene, polylactic acid, polyurethane, poly ε-caprolactone and collagen. These have been used for replacing impaired tendon (Yin et al., 2010), skeletal muscle (Riboldi et al., 2008), anterior cruciate ligament (Lee et al., 2005), blood vessels (Xu et al., 2004), skin tissue (Zhong et al., 2006), as nerve guidance conduits (Huang et al., 2015), and also for wound management applications (Xie et al., 2010).

Using scaffolds with aligned fibres rather than non-aligned fibres have been reported to promote cell attachment (Xu et al., 2004), guide cells in a preferred growth direction (Greiner and Wendorff, 2007) through contact guidance with the fibres, regulate preferential differentiation (Lim et al., 2010), facilitate matrix production and guide matrix deposition (Baker et al., 2008) especially when periodical mechanical deformation is applied (Lee et al., 2005). While aligned scaffolds show promise for fiber-reinforced tissues, cell infiltration into these dense structures is slow. This is because aligned scaffolds have increased fibre packing density and reduced pore size, thereby limiting cellular ingress (Baker et al., 2008).

Although there has been extensive research on using non-aligned electrospun polyurethane composites for tissue engineering, only a few have focussed on bone applications. Such non-aligned PU composites have been fabricated with cellulose acetate (Tang et al., 2008), hydroxyapatite (Khan et al., 2008), silica (Koh et al., 2013), proteins (Jia et al., 2013), carbon nanotubes (Sirivisoot and Harrison, 2011) and calcium

chloride (Nirmala et al., 2011) particles.

Moreover, there are even fewer open publications on aligned polymer composites in general, and very limited publications on aligned polyurethane composites to be specific. This is due to the difficulty experienced with creating uniaxial aligned fibres and the added complexity of including reinforcement particles. Such difficulty occurs because, the polymer jet trajectory during electrospinning is in a very complicated three-dimensional "whipping" way, rather than in a straight line (Huang et al., 2003).

The very few publications on aligned PU composites utilised cadmium selenide particles for electromagnetic applications (Demir et al., 2009), silica particles for nerve guide conduits and vascular regeneration (Huang et al., 2014), and carbon nanotubes for vascular and wound repair (Han et al., 2009; Meng et al., 2010; Mi et al., 2015). However, to the best of the author's knowledge, there isn't any published work on aligned polyurethane-hydroxyapatite reinforced fibres for tissue engineering applications to date, for both nano-sized and micro-sized HA particles. It would therefore be interesting to create aligned PU-HA composites with better mechanical properties and optimal cell penetration, that can influence matrix synthesis and guide collagen deposition.

5.2   Aim

The primary goal of this study was to develop polyurethane-based scaffolds with aligned fibres that promote osteoid matrix production and guide collagen deposition. PU solutions that had already been optimized for electrospinning non-aligned fibrous mats were used for this study. The hypothesis was that increasing the speed of the rotating drum would create scaffolds with aligned fibres that have better mechanical properties which resemble the tensile properties of the collagenous fibres in bone.

The overall aim of the study was to determine whether the fibrous structure would guide MLO-A5 cell migration and subsequent orientation of deposited matrix. Second Harmonic Generation Imaging and FIJI image analysis were used to investigate how the orientation and directionality of collagen changed with increasing depth. It was also used

to compare variation in collagen deposition amongst composite and plain polyurethane scaffolds.

A secondary goal was to assess the extent to which hES-MPs cells infiltrated and penetrated the entire depth of the aligned scaffolds, since they are noted for their reduced pore size and increased fibre packing density. An analysis of mineral deposition using Xylenol Orange staining and Scanning Electron Microscopy was also undertaken. RAMAN and FITR spectroscopy were also used to chemically characterize fabricated scaffolds and compare the spectra of non-aligned and aligned scaffolds.

5.3   Results and Discussion Two

Polyurethane remains a popular choice of polymer for creating regenerative bone templates due to its advantageous mechanical properties. Such properties stem from its versatile chemistry and microphase segregation. This microphase separation between the hard and soft segments enables polyurethane to withstand physical stresses and posses desirable mechanical properties useful for dynamic bone tissue engineering (Wen et al., 1997). Therefore combining polyurethane with hydroxyapatite, the main component of bone mineral, creates suitable composites with beneficial osteoconductive and bioactive properties, which are essential for bone regeneration.

Scaffolds discussed in this chapter were fabricated as outlined in Section 3.3.1 on page 70 using PU and PU-HA solutions described in Sections 3.2.2.2 and 3.2.3, on page 68 and 69, respectively. Cell culture and other biological characterization analysis on the selected scaffolds were done as described in Section 3.7.3.2 on page 94 and Sections 3.7.4 - 3.7.12 on page 98 and 112, respectively.

Table 5.1: Parameters used in preparing aligned electrospun scaffolds

Z3A1	PU wt%	micro/nano HA wt%	Vol. ratio of DMF (%)	Vol. ratio of THF (%)	Spin Speed (rpm)	Diameter of the Rotating Drum (cm)
Z3-PU	15	0	70	30	1300	6
Z3-mHA	15	5	70	30	1300	6
Z3-nHA	15	5	70	30	1300	6

5.3. RESULTS AND DISCUSSION TWO

In brief, 15 wt% Z3A1 PU solutions made with 70/30 DMF/THF solvent were electrospun using parameters outlined in Table 5.1 on page 153 to attain semi-aligned fibrous scaffolds. The scaffolds were spun at room temperature at a voltage of $+ 16.5$ kV, a flow rate of 3 ml/hr, a tip to collector distance of 20 cm, and a rotating drum speed of 1300 rpm. Composite scaffolds containing HA particles were also fabricated as part of this study, using 15 wt% Z3A1 PU solutions doped with micro or nano-HA particles in a ratio of 3:1, PU:HA. All fabricated scaffolds were later characterized chemically and mechanically using state of the art equipment. They were also characterized biologically using MLO-A5 and hES-MP cells. In addition, Second Harmonic Generation Imaging as described in Section 3.7.10 on page 110 was also used to investigate how the alignment of scaffold fibres influenced the orientation and directionality of deposited collagen.

5.3.1 Electrospun Scaffolds

PU-only and PU-HA electrospun scaffolds with semi-aligned fibre orientations were created by rapidly rotating the cylindrical collector of the electrospinning set-up (Figure 3.2 on page 71) at 1300 rpm. This rotational speed was a 1000 rpm faster than the 300 rpm speed used for creating non-aligned scaffolds in the previous chapter. Increasing the speed of the rotating drum, whilst maintaining the composition of the solutions, the tip to collector distance, the size of drum, the pumping rate and high electrical voltage led to the creation of scaffolds with an interesting fibre morphology and semi-aligned orientation.

Scaffolds made from polyurethane-only solutions had the most interesting fibre morphology (Figure 5.1). Its fibres self-assembled very closely together to form thick aligned bundles, which were large enough to be seen with the naked eye. A closer inspection of the aligned Z3-PU scaffolds using the scanning electron microscope, revealed a pattern of large fibril bundles interspersed with grooved portions of individual fibres. These large and highly aligned fibre bundles which were about 20 μm in diameter, were observed to consist of a collection of very thin PU fibres, each with a diameter of ~1.2 μm (Figure 5.2).
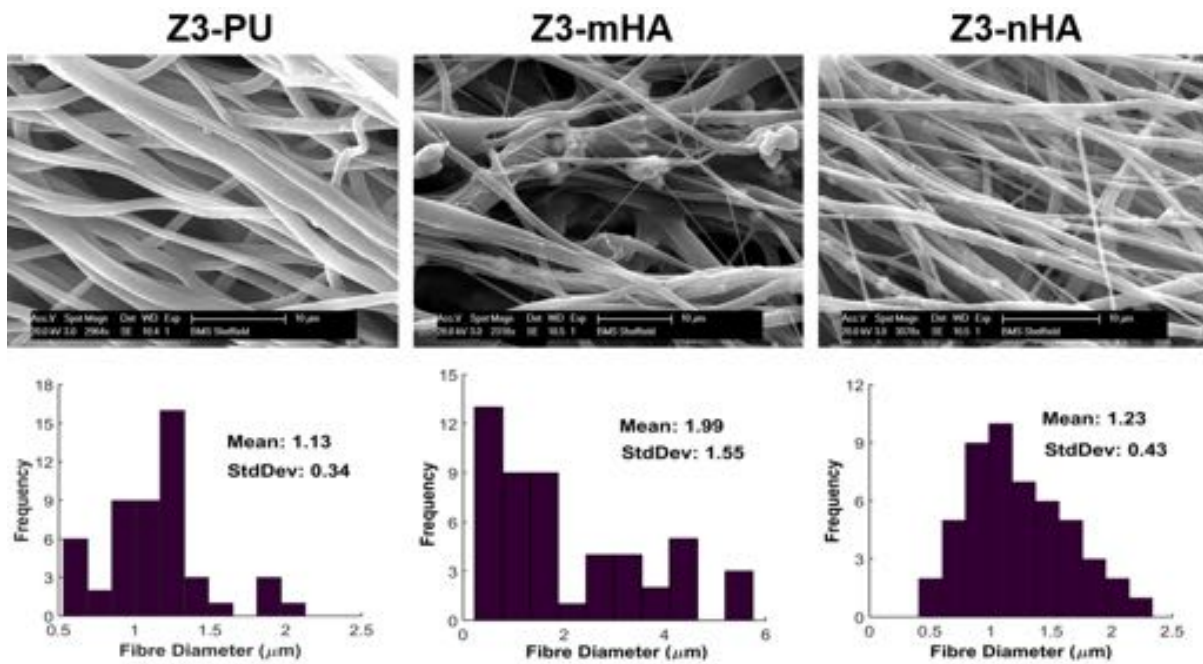
Figure 5.1: SEM images of Scaffolds in the Aligned Electrospun Composite Group. *Scale Bar of SEM images=10 µm, Histogram distributions of fibre diameters (n=50).*

The large nature of these fibre bundles caused Z3-PU to be the thickest scaffold amongst the aligned Z3 group. Its thickness of 0.59 mm was approximately twice the thickness of Z3-mHA and Z3-nHA composites, which had thickness's of 0.30 mm and 0.23 mm, respectively (Table 5.4 on page 168). This was because, the bundling behaviour of the fibres observed in PU-only scaffolds, was not observed in both aligned micro and nano-composites, although they both contained 75% of PU and only 25% of HA.
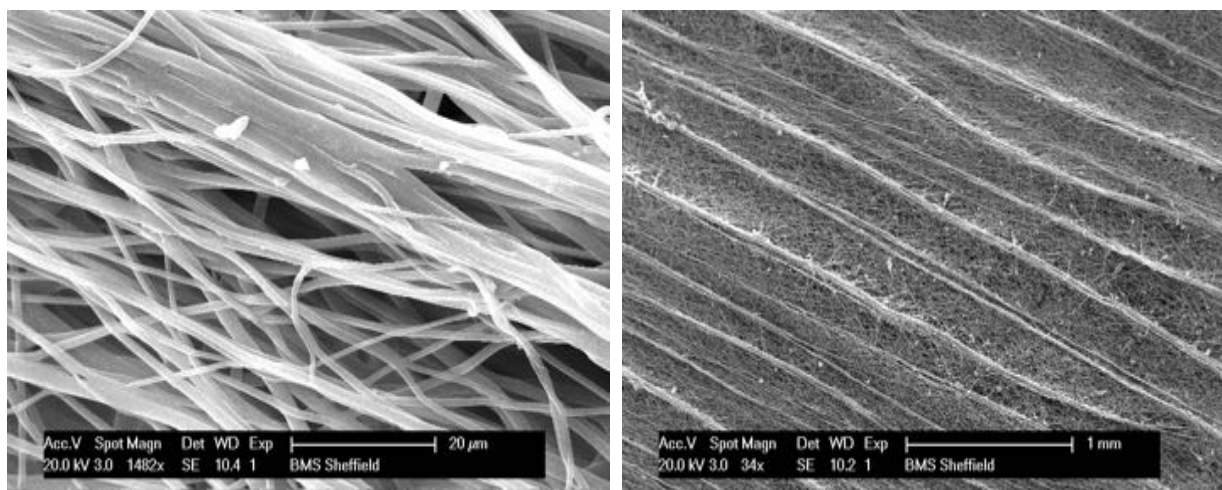
(a) At 20 µm

(b) At 1 mm

Figure 5.2: SEM images of Z3-PU scaffolds at Different Magnifications.

5.3. RESULTS AND DISCUSSION TWO

It is possible that this occurred as a result of the high rotational speed of the collector, which caused more fibres to be deposited on the collector in a short period. This could have caused a higher amount of solvent to be retained in the fibres, as the fibres had shorter time to be exposed before the next set of fibres landed on the collector. Such wet fibres have a high affinity of sticking together in the direction of the electric field (Doshi and Reneker, 1995), as the fibres are no longer strained by the electric field when they reach the collection drum (Zong et al., 2002). This could have also caused portions of the fibres to melt and bond together once they are in contact.

This also decreases the local resistance and enhances the electrical charge transfer between the deposited fibres and the collector through the fibrous network. This charge transfer grounds the fibres and makes them the preferential sites for the deposition of subsequent fibres. Driven by a set of electrostatic forces, the electrospun fibres were deposited in a self-aligned, consistent fibre-by-fibre manner to form an arbitrarily shaped 3D structure (Luo et al., 2015). Moreover, DMF and THF solvent properties such as large surface tension, slow evaporation rate and strong intermolecular interactions also played a role in accounting for this bundle fibre phenomenon. The influence of the solvents was however amplified by the 1300 rpm high rotational speed, as this interesting morphology was observed in only aligned Z3-PU but not in non-aligned Z3-PU scaffolds.

As shown in Figure 5.1, Z3-mHA composites had the largest fibre diameters and showed the least fibre alignment. With particle sizes ranging from 2-12 μm, the large nature of micro-HA particles coupled with the high spin speed greatly distorted the aligned orientation of the Z3-mHA fibres. These scaffolds had a combination of very thin fibres suspected to be composed of only PU and large chunky fibres embedded with micro-HA particles. This resulted in a bimodal distribution of the fibre diameter with a large standard deviation of 1.55 μm for an average fibre diameter of 1.99 μm. Another possible explanation for this is that the conductivity of the Z3-mHA solutions increased with the addition of micro-HA particles to the PU solution (Zhang et al., 2010).

It may be possible to attain more consistent Z3-mHA solutions by using an ultrasound sonicator or a homogenizer to further distribute the mHA particles in solution and
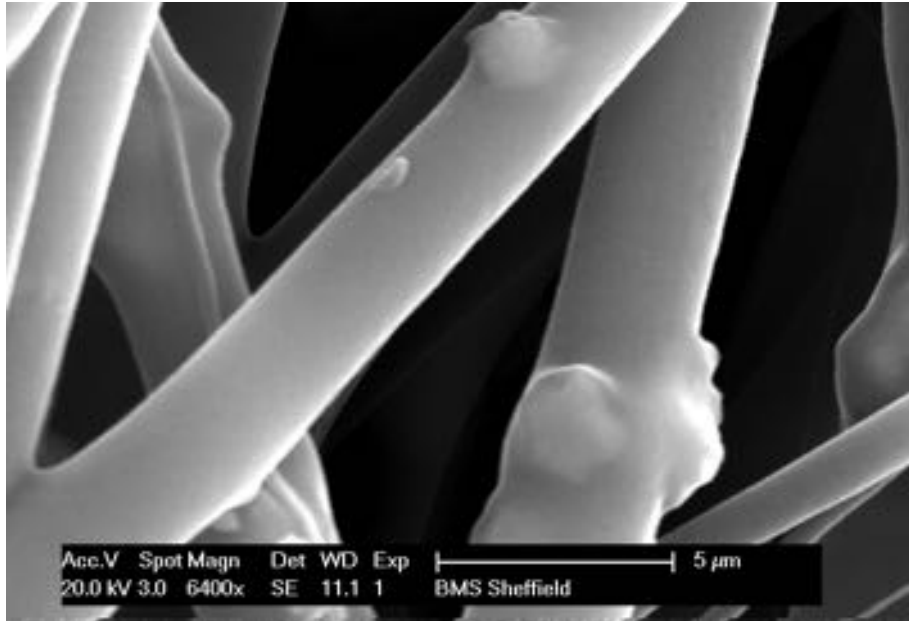
Figure 5.3: SEM images of Z3-mHA Scaffolds at 5 μm.

properly integrate the particles after the initial physical mixing using the magnetic beads. It would also be interesting to experiment other techniques that can be used to create aligned scaffolds which may cause the mHA particles to create less distortion and better alignment in morphology. Such techniques include using an auxiliary electrode or electrical field to circumferentially orient deposited fibres or by simply placing a rectangular frame structure under the spinning jet. Reducing the distance between electrodes to a few centimetres or millimetres is also another technique that can be used circumvent the difficulties experienced with creating aligned Z3-mHA scaffolds (Huang et al., 2003; Greiner and Wendorff, 2007).

On the other hand, Z3-nHA scaffolds had the most uniform fibre morphology. These composites had very even fibre diameters and showed sufficient porosity with interconnected pores. They also had a much better fibre alignment and a less beaded morphology compared to its mHA counterparts. As showed in Figure 5.4 on page 158, nHA particles in these scaffolds were well integrated in the fibres and aligned in a uniaxial manner.

With more than 50% of its fibres having diameters less than 1.5 μm, these scaffolds had a good representation of nanofibres that mimic the nanoscale dimensions of native
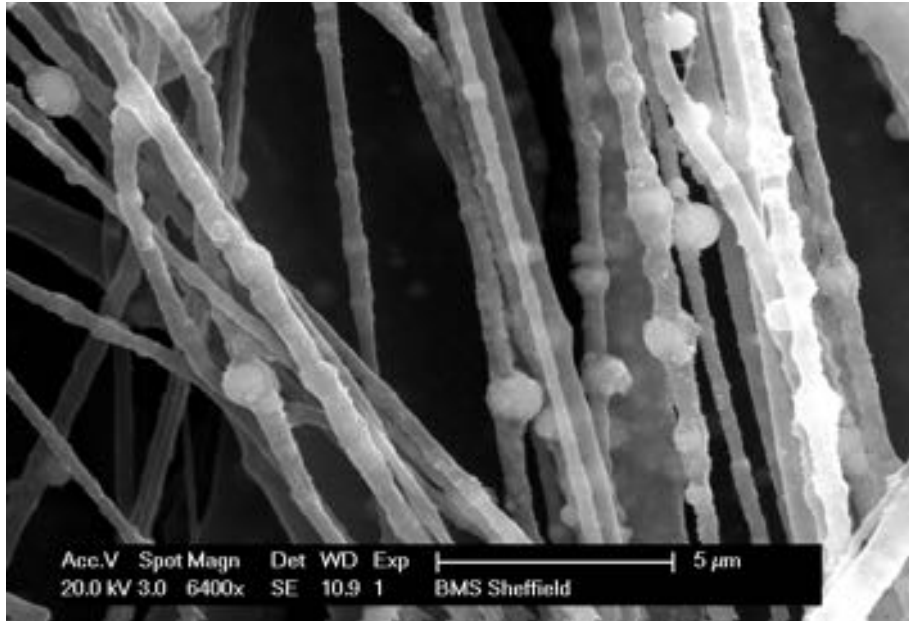
Figure 5.4: SEM images of Z3-nHA Scaffolds at 5 μm.

extracellular matrix. Moreover, the smaller nature of the nHA particles (<200 nm) and its corresponding higher surface area (>9.4 m^2/g) facilitated the distribution of nHA particles in the PU solution. This led to a more homogenous and spinnable solution compared to Z3-mHA solutions which were observed to settle quickly in the syringes during spinning.

Following on from the uniform nanofibrous structure and good fibre alignment exhibited by Z3-nHA composites, it would be interesting to create other aligned Z3 composites with carbon nanotubes. Using carbon nanotubes to fortify fibres has attracted considerable attention (Han et al., 2009; Meng et al., 2010; Mi et al., 2015) due to their fibre-like structure and exceptional electrical, thermal and mechanical properties. This makes them particularly attractive to be used as reinforcements for electrospinning both non-aligned and aligned fibres, as long as uniform dispersion of nanotubes within the polymer matrix is achieved, as it tends to easily agglomerate in polymer solutions.

5.3.2 RAMAN & FTIR Characterization

Raman and FITR are two complimentary spectroscopy techniques that provide detailed information about materials by detecting the vibrational levels of molecules and ions.

Raman spectroscopy was used to characterize fabricated scaffolds and confirm the presence of HA in composites. FITR spectroscopy which was used to in previous chapter to characterize non-aligned scaffolds was also used in this chapter to identify differences in the spectra of aligned and non-aligned Z3 scaffolds.

Both techniques require minimum sample preparation, are non-invasive and useful for identifying most calcium phosphate phases. Carbonate, phosphate, water and hydroxide ions are the main species that can be identified by FTIR and Raman spectroscopy, although apatites are also known to contain a variety of other ions. The effect of such ions have been compiled by Curzon and Cutress (1983).

Both spectroscopy techniques are especially useful for easily distinguishing apatite phases that cannot be identified by X-Ray Diffraction (XRD). This gives them a principal advantage over XRD, as they can be used for identifying fine structural details in apatite nanocrystals and poorly crystalline apatites with great accuracy (Ducheyne et al., 2011). Additionally, they can be used for phase quantification using standard mixtures and standardization curves.

Although they have many similarities, they however differ in instrumentation and how photon energy is transferred to molecules upon collision with light (Lin-Vien et al., 1991). Compared to Raman spectroscopy, which examines scattering and changes in the polarisability of chemical compounds, FTIR spectroscopy focusses on absorption and changes in the dipole moment of covalent compounds (Mahadevan-Jansen and Richards-Kortum, 1996). Additionally, FTIR can only be applied to non-aqueous samples whilst Raman spectroscopy can be applied to both aqueous and non-aqueous samples.

5.3.2.1 RAMAN Spectroscopy

Hydroxyapatite is an intense Raman scatterer which is indicated by the exceptional signal to noise ratio. As a consequence, the direct determination of Ca/P ratio of a calcium phosphate mixture is not possible with Raman spectrometry. However, the sensitivity of this method allows the detection and accurate identification of compounds that are considered as impurities.

5.3. RESULTS AND DISCUSSION TWO
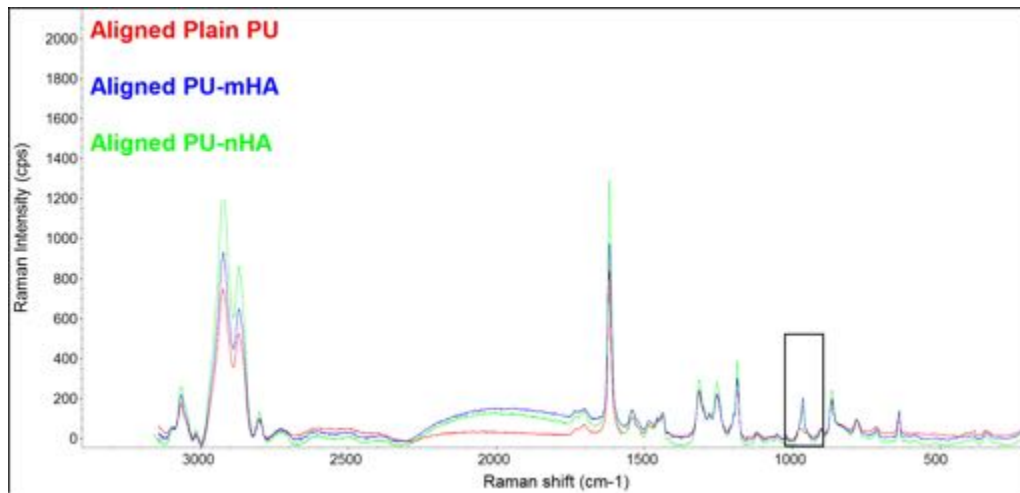
(a)
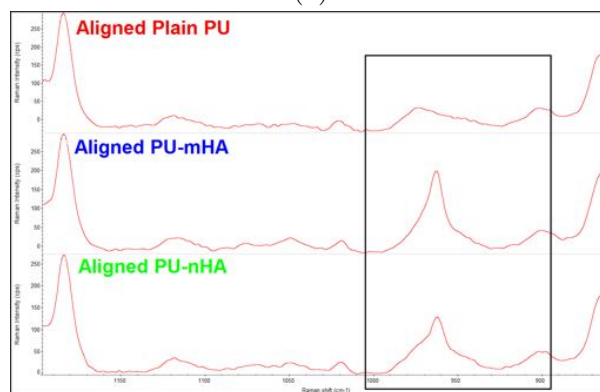
(b)

Figure 5.5: Raman Spectra of aligned Z3A1 Scaffolds(a): Combined spectra of Z3-PU, Z3-mHA and Z3-nHA scaffolds at 3400-200 cm^{-1}. (b): Zoomed Spectra higlighting the presense of HA in the composite Z3-mHA and Z3-nHA scaffolds at 1200-860 cm^{-1}.

Figure 5.5a shows the Raman spectra of the different regions of interest for all aligned scaffolds. Its corresponding peaks are also tabulated in Table 5.2. For Z3-PU, the sharp peaks at 2922 cm^{-1} and 2869 cm^{-1} can be assigned to (CH_2) antisymmetric stretching and (CH_3) symmetric stretching vibrations, respectively. The broad Raman shift at 1704 cm^{-1} was assigned to stretching urethane mode of $(C=O)$, whilst the very strong shift at 1615 cm^{-1} was attributed to the $(C=C)$ aromatic ring mode of the Z3A1 ether group. There was also a bending NH and stretching CN mode at 1536 cm^{-1} and $\delta(CH_2)$ at 1484, 1452 and 1436 cm^{-1}.

Additionally, $\nu(C-N)$ and $\nu(C-O)$ were observed at 1313 cm^{-1}. The twist $\delta(CH_2)$ was at 1277 cm^{-1}, whilst the stretching $C-N$ in the aromatic ring was at 1253 cm^{-1}. A sharp shift corresponding to the symmetrical urethane $\nu(C-O-C)$ and $\delta(CH)$ aromatic

160

ring was noted at 1184 cm^{-1}. 973 cm^{-1} was assigned to stretching CH and stretching CN aromatic ring, whilst 865 cm^{-1} was attributed to δ(C$-$O$-$C) and δ(C$-$C$-$C). These Raman shifts are similar to those observed by Janik et al. (2003) and Gupta et al. (2013).

Table 5.2: Peak Assignment of Raman Shifts for Z3-PU, Z3-mHA and Z3-nHA

Raman Shift (cm^{-1})	Peak Assignment
PU	
2922	as. ν(CH$_2$)
2869	s. ν(CH$_3$)
1704	urethane ν(C=O)
1615	(C=C) aromatic ring
1536	δ(NH) and ν(CN)
1484, 1452 and 1436	δ(CH$_2$)
1313	ν(C$-$N) and ν(C$-$O)
1277	t. δ(CH$_2$)
1253	νC$-$N in the aromatic ring
1184	s. urethane ν(C$-$O$-$C) and δ(CH) aromatic ring
973	ν(CH) and ν(CN) aromatic ring
865	δ(C$-$O$-$C) and δ(C$-$C$-$C)
Phosphate & Carbonate Shifts	
964	s. ν_1 (PO$_4^{3-}$)
432	ν_2 (PO$_4^{3-}$)
1029 and 1048	ν_3 (PO$_4^{3-}$)
1076	ν_3 (PO$_4^{3-}$) and ν_1 (CO$_3^{2-}$)
581, 591 and 607	ν_4 (PO$_4^{3-}$)

(Key: as=Asymmetric, s=Symmetric, t=Twist)

In addition to these peaks, composite scaffolds containing HA particles showed phosphate and carbonate Raman shifts. There were four vibrational modes present for phosphate (PO$_4^{3-}$) ions. These are ν_1, ν_2, ν_3 and ν_4, all of which are Raman and infrared active. As shown in Figure 5.5a, there was a very strong ν_1 (symmetric stretch) phosphate mode observed at 964 cm^{-1}. The ν_2 phosphate bending mode observed at 432 cm^{-1} was similar to that in dentine and bone samples (Penel et al., 1998). ν_3 PO$_4^{3-}$ was at 1048 cm^{-1} with a weaker shift at 1076 cm^{-1}, however, the 1076 cm^{-1} shift cannot be assigned to only phosphate ions as it also corresponds to the ν_1 mode of carbonate ions. The three main ν_4 PO$_4^{3-}$ (bending mode) were noted at 581 and 591 cm^{-1} with a weaker shoulder shift at 607 cm^{-1}. As both types of HA particles were synthetics, the band at

5.3. RESULTS AND DISCUSSION TWO

591 cm^{-1} exhibited the strongest intensity amongst the ν_4 PO$_4{}^{3-}$ shifts.

Although carbonate ions have four vibrational modes in theory, only two of these (ν_1 and ν_4) are usually observed in the Raman spectrum, where as FTIR spectrum boosts of three, mainly ν_1, ν_2 and ν_3 (Rehman et al., 1995). However, the ν_4 carbonate bands have seldom been observed in carbonate apatites. These bands are very weak and can only be detected in samples with an average-to-high carbonate content. These are usually observed at about 757, 740, 718, 692 and 670 cm^{-1} (Fowler et al., 1966). As mentioned earlier, the stretching mode of ν_1 CO$_3{}^{2-}$ which was observed at 1076 cm^{-1} was totally obscured by the ν_3 PO$_4{}^{3-}$ Raman shift. The bending mode of CO$_3{}^{2-}$ which is usually seen at 1036 cm^{-1} was observed at 1029 cm^{-1} and was also obscured by the ν_3 PO$_4{}^{3-}$ Raman shift.

(a) Z3-mHA

(b) Z3-nHA
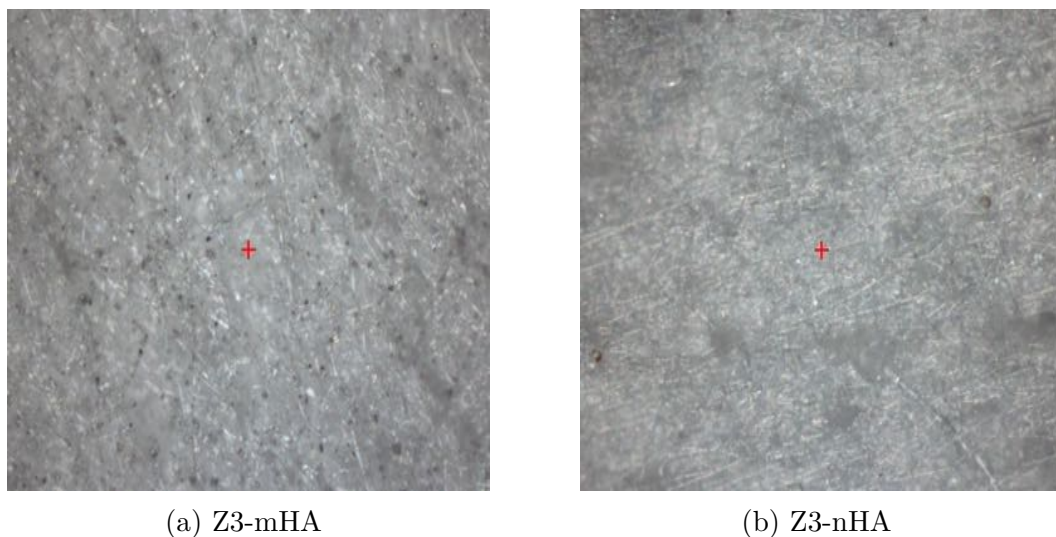
Figure 5.6: Images of Composite Scaffolds from the DXR Raman Microscope.

The strong ν_1 phosphate moiety peak is further highlighted in Figure 5.5b to emphasize the main spectral difference between PU-only and PU-HA composites. There was a major shift in this peak for both Z3-mHA and Z3-nHA scaffolds when compared to Z3-PU, although it was more pronounced in mHA composites. The ν_1 PO$_4{}^{3-}$ peak of Z3-nHA was broader than that of Z3-mHA which had a sharp and narrow band. This could have been due to the large size of the mHA particles, which caused the particles not to properly integrate with the PU fibres (as shown in the SEM images in

162

Figure 5.1 on page 155). This could have caused the mHA particles to have greater exposure than the nHA particles, and made them more susceptible to the vibrations. Moreover, the DXR microscope attached to the RAMAN spectrometer that was used to visualise HA distribution in PU composites, also showed more HA particles (black dots) in mHA composites (Figure 5.6a) than in nHA composites (Figure 5.6b) due to the spatio-resolution restrictions of the microscope.

5.3.2.2 FTIR Spectroscopy

In addition to Raman imaging, FTIR spectroscopy was also used to characterize the aligned scaffolds. Infrared (IR) spectroscopy which uses radiation in the mid-IR region and a changes in dipole moment of the molecules provided a good opportunity for analysing ions and molecular species that were inactive in Raman e.g. $\nu_3 \, CO_3{}^{2-}$. This also made it possible to compare the spectra of aligned Z3 scaffolds with those of non-aligned Z3 scaffolds reported in the previous chapter.

As shown in Figure 5.7, the FTIR spectra of aligned and non-aligned Z3 scaffolds were very similar. With the exception of vibrations in the $\nu 3$ phosphate peak highlighted in Figure 5.7c, there was no major difference in the spectra of composite non-aligned and aligned scaffolds. The spectra of plain polyurethane scaffolds had the same spectra for both non-aligned and aligned Z3-PU (Figure 5.7a). Both scaffolds exhibited the same PU peaks discussed in Section 4.3.4 on page 128. These peaks together with the peaks of the composite scaffolds are also tabulated in Table 5.3.

Since the Z3-PU scaffolds did not contain any hydroxyapatite particles, there were no stretching and bending O—H and P—O peaks in Figure 5.7a. However, upon inclusion of micro and nano HA particles in Z3-nHA and Z3-mHA, characteristic HA peaks were observed (Figures 5.7b and 5.7c). Comparing the spectra of non-aligned and aligned composite scaffolds reinforced the explanation for the shifting and appearance of new peaks in the region of 1100-916 cm^{-1} as discussed in Section 4.3.4 on page 128.

This relates to the fact that nano-HA with a higher surface area and more crystalline structure mixed better with the PU solution than micro-HA particles. This affected the
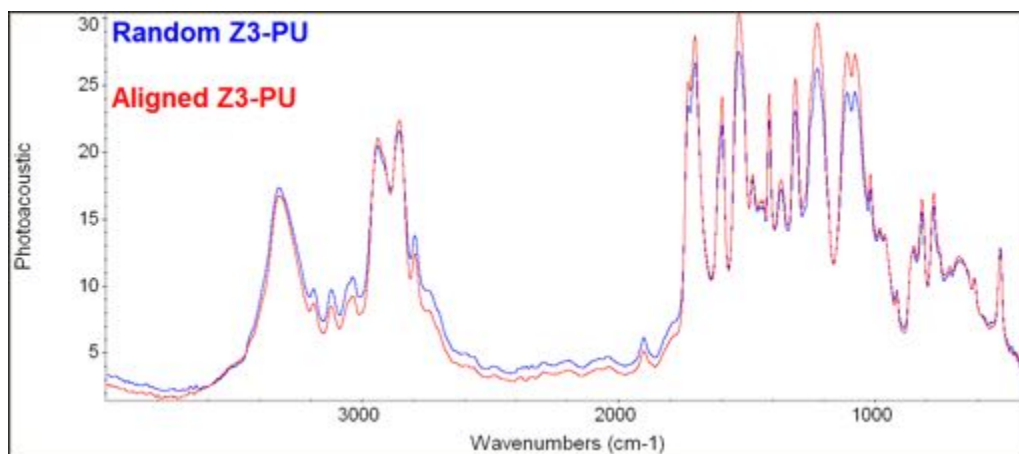
(a)
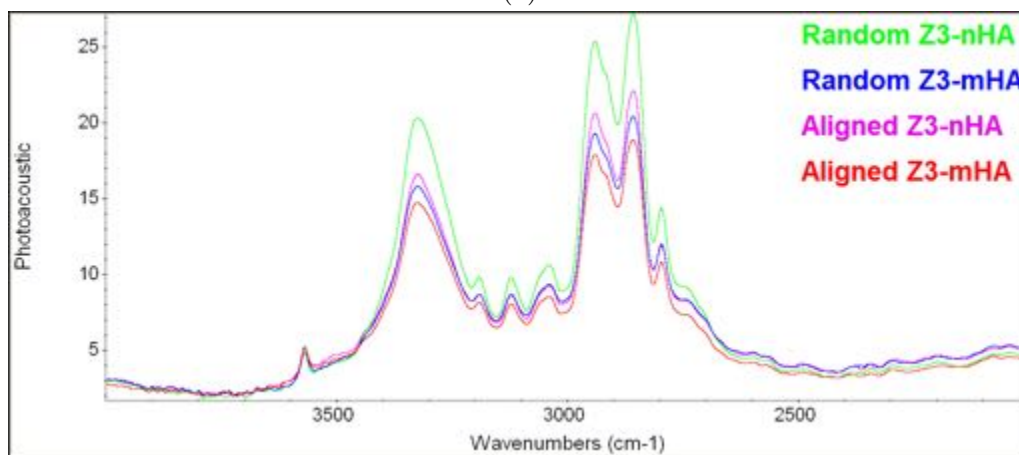
(b)
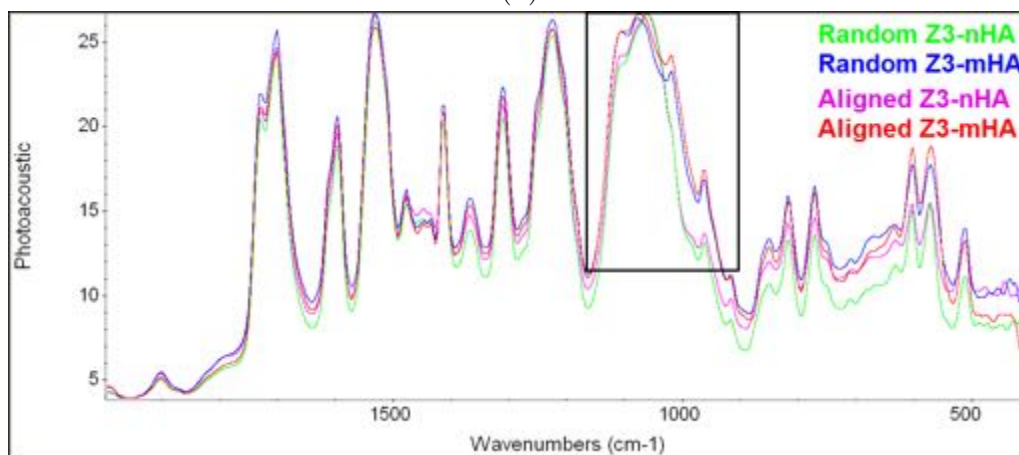
(c)

Figure 5.7: FTIR Spectra comparing non-aligned and aligned Z3A1 Scaffolds at common scale (a): FTIR spectra of Z3A1 PU-only Scaffolds. (b): Combined FTIR spectra of Z3-mHA and Z3-nHA Composites for a wavenumber region of 4000-2000 cm^{-1}. (c): Combined FTIR spectra of Z3-composites for a wavenumber region of 2000-401 cm^{-1}, highlighting main spectral difference between aligned and non-aligned composites.

Table 5.3: Peak Assignment of FTIR Spectra of Z3-PU, Z3-mHA and Z3-nHA

Wavenumbers (cm^{-1})	Peak Assignment
PU	
3325	ν (N—H)
3121	overtone of 1533 cm^{-1}
3039	ν (C—H) in benzene ring
2940, 2857 and 2795	CH$_2$ peaks of the polyether
2940	as. ν CH$_2$
2857	s. ν CH$_2$
1597	ν (C=C) in the benzene ring
1533	amide II δ (N-H) ν (C=N)
1478	weak CH$_2$
1413	strong ν (C—C) in benzene ring
1310	amide III δ (N—H) + ν (C=N)
1225	β (C—H) peak and δ (N—H) + ν (C=N)
1103-916	v(CH$_2$—O—CH$_2$) of ether peak
1018	weak β (C—H) in benzene ring
817	γ (C—H) from butane diol
Hydroxyl	
3570	O—H stretching
633	OH librational band
Carbonate	
1730 to 1700	carbonyl absorption region
1701	bonded (C=O) stretching
1730	free (C=O) stretching
Phosphate	
1060, 961, 603 and 571	vibrations of the phosphate group
1078	triply degenerated vibration ν 3
961	non-degenerated symmetric stretching mode ν 1
633	ν 4 bending
603 and 571	triple degenerated bending mode ν 4

(Key: as=Asymmetric, s=Symmetric)

shifting of the ν3 P—O peak from 1078 cm^{-1} for Z3-mHA to 1060 cm^{-1} for Z3-nHA. Moreover, the shoulder P—O peak at 1010 cm^{-1} which was observed in both non-aligned and aligned Z3-mHA scaffolds was not present in both nHA composites. This is because this particular peak is usually seen in poorly crystalline apatites at 1010 cm^{-1} but at 1030 cm^{-1} for highly crystalline apatite (Alvarez-Lloret et al., 2006). These peaks are important because the calculation of the 1030/1020 cm^{-1} intensity ratio is an index of

crystal size/perfection, and this increases as bone matures (Paschalis et al., 1996).

5.3.3 Mechanical Properties

In creating electrospun scaffolds for musculoskeletal regeneration, high mechanical strength and toughness are extremely important as even partial failure will significantly reduce the efficiency of the fibres within the mat and have strong effects on the overall stability of the structure (Blond et al., 2008). It is conceivable that incorporating robust ceramic particles into polymer solutions and aiming to attain a high degree of fibre orientation along a preferential or elongated direction (referred to as parallel orientation in this chapter) could greatly improve the strength and stiffness of electrospun scaffolds. Combining these two methods can create electrospun scaffolds with excellent mechanical properties that can be useful for musculoskeletal applications including bone and cartilage reconstruction.
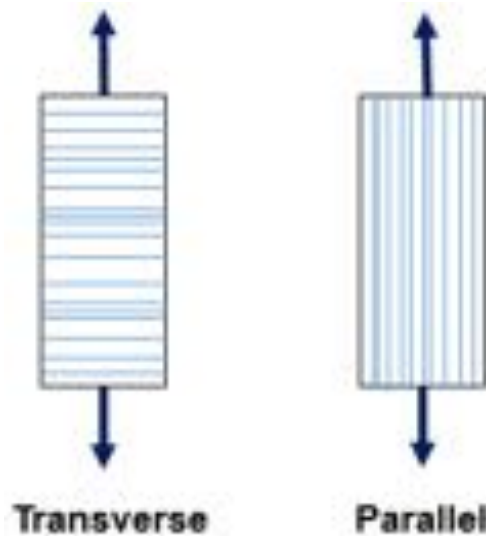
Figure 5.8: Orientations used to mechanically test aligned fibers in tension.

Compared to non-aligned scaffolds, aligned scaffolds were tested in tension in both transverse and parallel orientations as shown in Figure 5.8. Parallel orientation testing was done in the predominate direction of fibre alignment where as transverse orientation testing was done in a perpendicular alignment to the fibres. It was important to assess the tensile properties of the scaffolds as this can affect the scaffold's ability to mechanically

stimulate cells by stretching *in vitro* prior to implantation. This could also affect surgical handle-ability and regeneration of thin bone regions where bone might be in tension e.g. cleft palate and cranofacial applications.

(a) Transverse Orientation

(b) Transverse Orientation

(c) Parallel Orientation
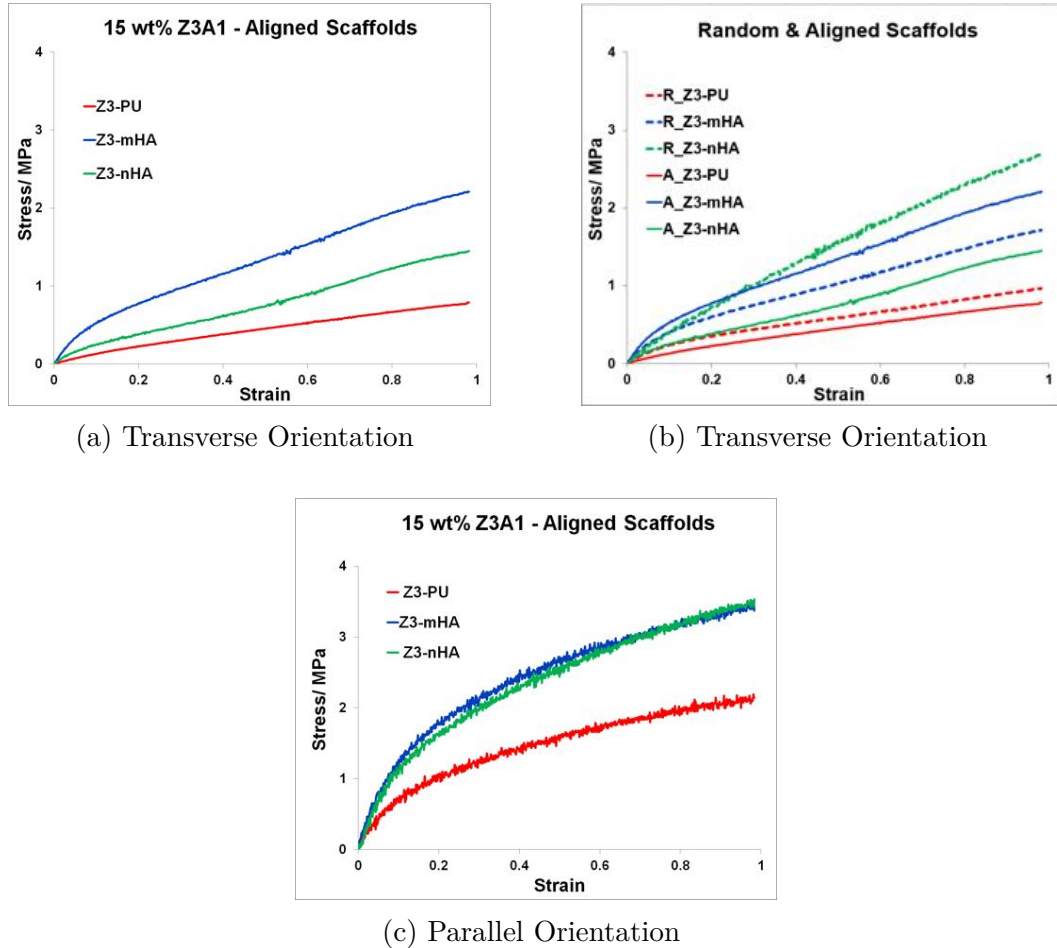
Figure 5.9: Example stress/strain curves of 15 wt% Z3A1 fabricated scaffolds (a): Aligned Scaffolds tested in Transverse Orientation (b): Comparing non-aligned and Aligned Scaffolds tested in Transverse Orientation (c): Aligned Scaffolds tested in Parallel Orientation.

As shown in Figure 5.9, stress-strain curves showed that the inclusion of both types of HA particles reinforced the mechanical properties of Z3-PU, when tested in both transverse and parallel orientations. When tested in the transverse orientation, Z3-mHA scaffolds had the highest Young's Modulus and yield strength. Its Young's Modulus of 6.41 ± 0.85 MPa, was about 80% higher than those of Z3-PU and 60% higher their Z3-nHA counterparts, whilst its yield strength of 0.37 ± 0.06 MPa, was about 50% higher than those of Z3-PU and Z3-nHA.

Comparing the mechanical properties of non-aligned and aligned scaffolds tested along

5.3. RESULTS AND DISCUSSION TWO

Table 5.4: Average Morphological and Mechanical properties of Aligned Z3A1 scaffolds

Aligned Scaffolds	Fibre Diameter (μm)	Thickness (mm)	Young's Modulus (MPa)	Yield Strength (MPa)
(above=transverse test results, below=parallel test results)				
Transverse				
Z3-PU	1.13 ± 0.34^b	0.59 ± 0.03	1.22 ± 0.17^{bc}	0.19 ± 0.03^b
Z3-mHA	1.95 ± 1.55^{ac}	0.30 ± 0.03	6.41 ± 0.85^{ac}	0.37 ± 0.06^{ac}
Z3-nHA	1.23 ± 0.43^a	0.23 ± 0.01	2.36 ± 0.37^{ab}	0.21 ± 0.03^b
Parallel				
Z3-PU			7.15 ± 0.93^{bc}	0.77 ± 0.33^{bc}
Z3-mHA			12.61 ± 2.65^a	1.40 ± 0.29^a
Z3-nHA			14.23 ± 1.87^a	1.31 ± 0.16^a

(mean $\pm$ S.D., n=50 for fibre measurements, n=6 for all other measurements)
a=significantly different from PU scaffolds, at p $\leq$ 0.05
b=significantly different from scaffolds made with mHA, at p $\leq$ 0.05
c=significantly different from scaffolds made with nHA, at p $\leq$ 0.05

the transverse orientation showed that Z3 scaffolds with aligned fibres were generally weaker than those attained for Z3 non-aligned scaffolds (Tetteh et al., 2014). As shown in Figure 5.9b, this was observed in both Z3-PU and Z3-HA scaffolds. There was a 50% reduction in Young's Modulus in Z3-PU whilst Z3-nHA showed a 30% reduction, respectively. These lower tensile mechanical properties for electrospun PU scaffolds tested in the transverse orientation is similar to those observed with PCL electrospun scaffolds (Delaine-Smith, 2013).
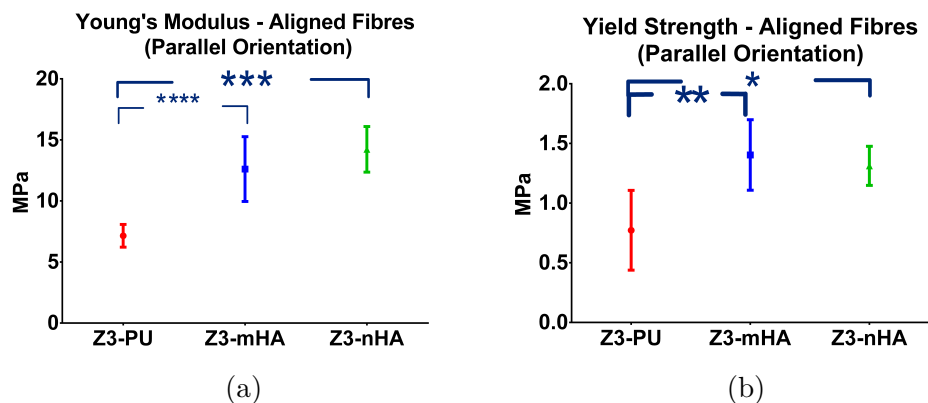
Figure 5.10: Mechanical Properties of 15 wt% Z3A1 aligned scaffolds tested in Parallel Orientation (a): Young's Modulus (b): Yield Strength

As shown in Figures 5.9c and 5.10, Z3-PU again had the weakest mechanical behaviour

within the parallel orientation group. However, it's Young's Modulus of 7.15 ± 0.93 MPa was about 7 times that of its transverse testing results. As tabulated in table 5.4, Z3-nHA and Z3-mHA scaffolds also showed a very similar stress-stain pattern.

When tested in the parallel orientation direction, aligned scaffolds displayed very high mechanical properties. Z3-nHA scaffolds the highest Young's Modulus of 14.23 ± 1.87 MPa and a yield strength of 1.31 ± 0.16 MPa. This was about 7 times greater than its stress value in the transverse orientation. Z3-mHA and Z3-PU also showed significant improvement in their mechanical properties when tested in the aligned direction.

Compared to non-aligned scaffolds, the yield strength and Young's Modulus of aligned scaffolds were four fold higher. It has been reported that compared to randomly oriented fibres, aligned fibres exhibit significantly improved resistance to tensile stress when tested parallel in the direction of fibre alignment (Subramanian et al., 2011). This is because non-aligned electrospun non-woven fibres usually exhibit poor mechanical performance due to the low degree of orientation and chain extension of the polymer chains along the fibre axis. Thus compared to corresponding textile fibres made from the same polymers, the mechanical properties of non-aligned electrospun nanofibers are often found to be poorer than their aligned counterparts (Yao et al., 2014).

5.3.4 MTT Cell Viability

Similar to Section 4.3.8 on page 140, Z3 scaffolds with aligned fibres were also seeded with MLO-A5 and hES-MP cells at a seeding density of 1.0×10^5 cells per scaffold. As shown in Figure 5.11, both cell types were viable on all scaffolds, with viability increasing from D1 to D28. Cell viability of both MLO-A5 and hES-MPs were generally higher on aligned scaffolds compared to the cell viabilities of scaffolds in the non-aligned group. This is contrary to what is usually observed with aligned scaffolds, as their reduced pore size and increased fibre packing density are known to inhibit cellular infiltration and cell proliferation (Bashur et al., 2009). Moreover, PU-only supported the highest viability across all time points for both MLO-A5 and hES-MP cells. This is opposite to what

was observed with non-aligned fibre scaffolds where Z3-nHA composites supported the highest viability across all time points.
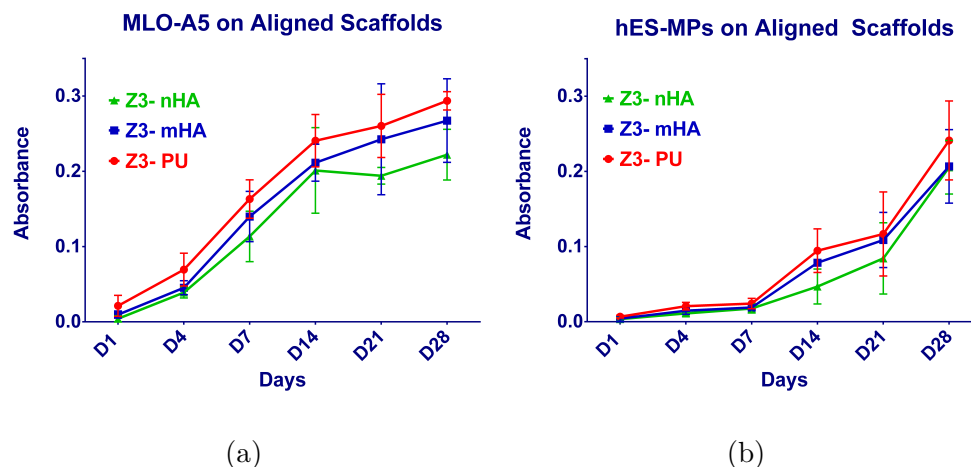
Figure 5.11: MTT absorbance of cells seeded on Z3A1 Aligned Scaffolds (a): MLO-A5 Cells (b): hES-MP Cells

Within the aligned fibre group, MLO-A5 cells had higher viabilities across all time points compared to hES-MPs. MLO-A5 cell viability increased sharply from D1 to D14 on all scaffold types. Although cells on Z3-PU and Z3-nHA supported the highest and lowest viability, respectively across these time points, the only significant difference in their viabilities was seen on D7. However, cell viabilities for both Z3-PU and Z3-mHA were significantly higher than that of Z3-nHA on D21. Furthermore, the highest MTT absorbance for scaffolds with aligned fibres on D28, which was by MLO-A5 cells on Z3-PU scaffolds was also significantly higher than that on Z3-nHA scaffolds.

A similar pattern was observed with hES-MP cells on aligned Z3 scaffolds. There was a gradual increase in cell viabilities from D1 to D7 for all scaffold types. Beyond D7, there was a sharp increase in the cell viabilities of all Z3 scaffolds, with a steep increase occurring between D21 and D28. The only significant difference within the hES-MP group was observed between Z3-PU and Z3-nHA on D14, all other differences in viabilities amongst the scaffolds were not significant.

It is well known that the alignment of fibres in electrospun scaffolds influences cell behaviour through initial cell spreading and elongation (Shin et al., 2012). Hence it is possible that, the bundling effect of the PU fibres discussed in Section 5.3.1 on page 154

caused the variations in cell viabilities. This bundling effect led to the creation of thicker PU scaffolds with larger fibres and greater porosity, promoting cell attachment and proliferation. This could account for the overall higher cell viabilities on Z3-PU for both MLO-A5 and hES-MP cells, compared to the other aligned Z3-composites, as cells seeded on PU scaffolds had more room for proliferation and migration, nutrient transfer and gaseous exchange.

It was very interesting to observe a contrasting cell viability behaviour between non-aligned and aligned Z3 scaffolds fabricated with exactly the same composition. It was expected that composite scaffolds which had the highest viability within the non-aligned scaffold group would also have a similar effect wtih the aligned scaffolds but this was not observed. Composite scaffolds made with bioactive HA particles supported lower cell viabilities than the PU-only scaffolds. This showed that it was possible to improve cell viability using only physical modifications to scaffold topography. The ability to control cell growth by topography may provide a more cost effective mechanism to encourage tissue growth on a scaffold compared to expensive biochemicals. It would still be interesting to repeat this experiment using a higher concentration of HA particles in the aligned composites and the same bundling Z3-PU scaffolds. This can ascertain if a higher amount of HA in composite scaffolds is needed to attain the same viability levels as that of aligned PU-only scaffolds.

5.3.5   Histology

Scaffolds seeded with hES-MP cells were also prepared for histology. This was to access the extent to which cells were able to penetrate the entire length of the fabricated scaffolds. The small size of hES-MP cells facilitated cellular penetration within the entire scaffold.

On D14, cells on Z3-PU showed about 50% penetration along the depth of scaffold. This was less than the almost 90% depth penetration seen in Z3-mHA but more than that of the Z3-nHA. Although cellular penetration in nHA composites improved by D21, such that there were even a few cells at the bottom of the scaffold, there were still a lot of cells on the surface of the scaffold. This is similar to what was observed in Z3-mHA

171
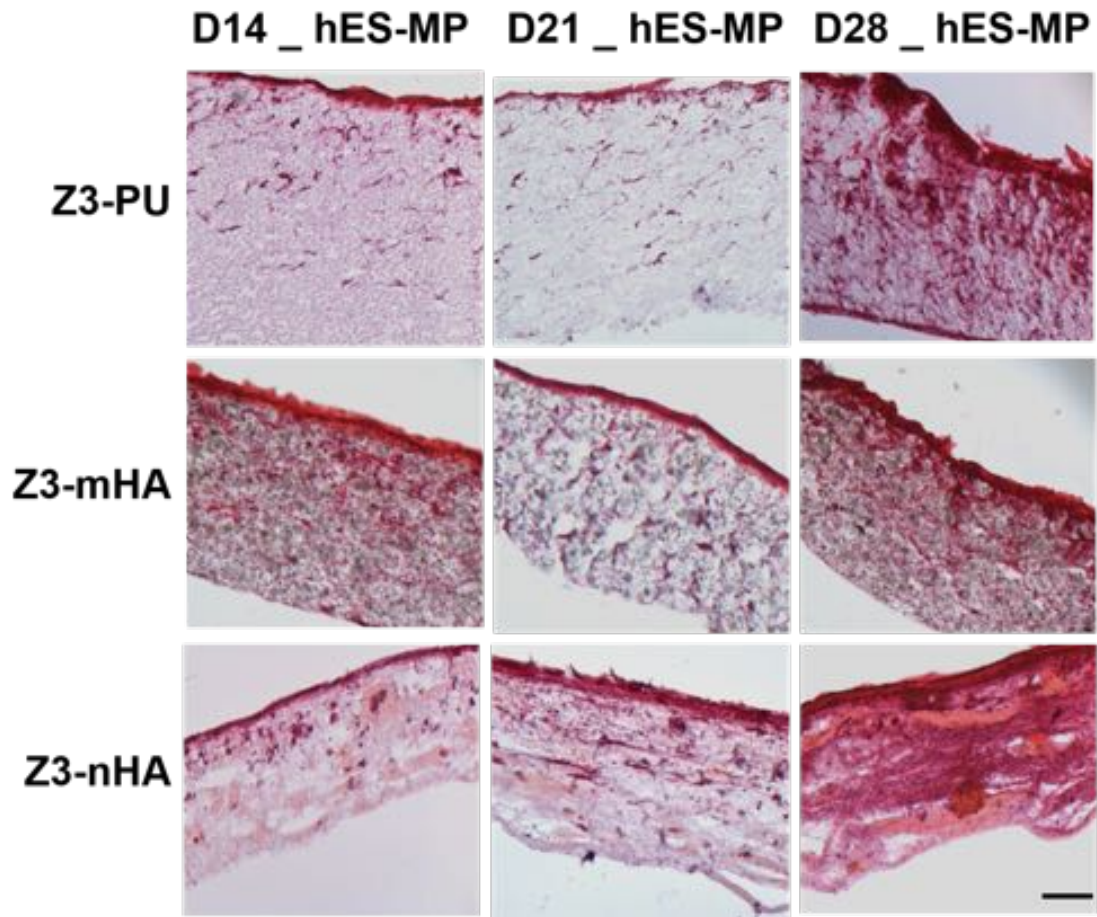
Figure 5.12: H & E staining on Z3-PU, Z3-mHA and Z3-nHA aligned scaffolds on Days 14, 21 & 28 of culture for hES-MP cells.
Scale Bar at 100 µm

composites.

Although the increased fibre packing density of aligned scaffolds is known to inhibit cellular infiltration, very good cell penetration and matrix deposition was observed on all scaffolds. The highest level of cellular penetration and extracellular matrix production was seen in PU-only scaffolds on D28. These Z3-PU scaffolds showed good cellular infiltration and matrix deposition throughout their entire depth. This was followed by mHA composites and finally Z3-nHA, showing a trend similar to that of the cell viability MTT absorbance. Although only aligned scaffolds seeded with hES-MPs cells were analysed histologically, its will be interesting to explore whether the histology of MLO-A5 cells on these scaffolds would also have a comparable cell growth and penetration.

5.3.6 XO Imaging

Xylenol orange, ($C_{31}H_{28}N_2O_{13}SNa_4$), a fluorescent compound that chelates to calcium and stains mineral red was also used used to label mineralized nodules *in vitro*. Once used, xylenol orange (XO), becomes fixed to newly formed calcified tissues where it remains until removal of the bone mineral, and produces clearly outlined fluorescence in regions which were calcified at the time of administration of the dye (Rahn and Perren, 1971).

As a fluorochrome, it has its own specific excitation and emission wavelengths of 440/570 nm and 610 nm, respectively and expresses a red color under the fluorescent microscope using a TRITC red filter (Pautke et al., 2005). Compared to other calcification assays such as Von Kossa and alizarin red S, which require fixation and culture termination ahead of staining, XO staining does not require fixation and thus enhances experimental efficiency. This makes XO imaging particularly useful in bone tissue engineering, where the onset time and location of osteogenesis are fundamental parameters for the characterization of directed bone formation and for determining osteoinductive and osteoconductive properties of scaffolds (van Gaalen et al., 2010).

As xylenol orange is not harmful to cells (Wang et al., 2006), it was used to stain osteoid mineral of live MLO-A5 cells seeded on aligned scaffolds. This provided an opportunity to monitor and observe dynamic changes during the formation of mineralized nodules in living MLO-A5 cultures. It also aided in creating a timed sequence overview of the *in vitro* osteoid deposition.

As shown in Figure 5.13, mineralized nodules emitted red fluorescence when stained with xylenol orange. D14 Z3-nHA scaffolds showed large chunky regions of deposited mineral indicating agglomeration, whereas Z3-mHA and Z3-PU scaffolds showed a good distribution of the mineralized nodules. Although XO images of Z3-PU (Figure 5.13b) and Z3-mHA (Figure 5.13c) scaffolds showed an even distribution of mineral nodules, Z3-mHA had a higher percentage of mineral area coverage compared to Z3-PU. This percentage of mineral area coverage was estimated as MineralArea/TotalArea, where MineralArea is the area of mineralization (red fluorescence), and TotalArea is the total

(a) **Blank Z3-PU**　　　　　　　　(b) **Z3-PU**

(c) **Z3-mHA**　　　　　　　　(d) **Z3-nHA**
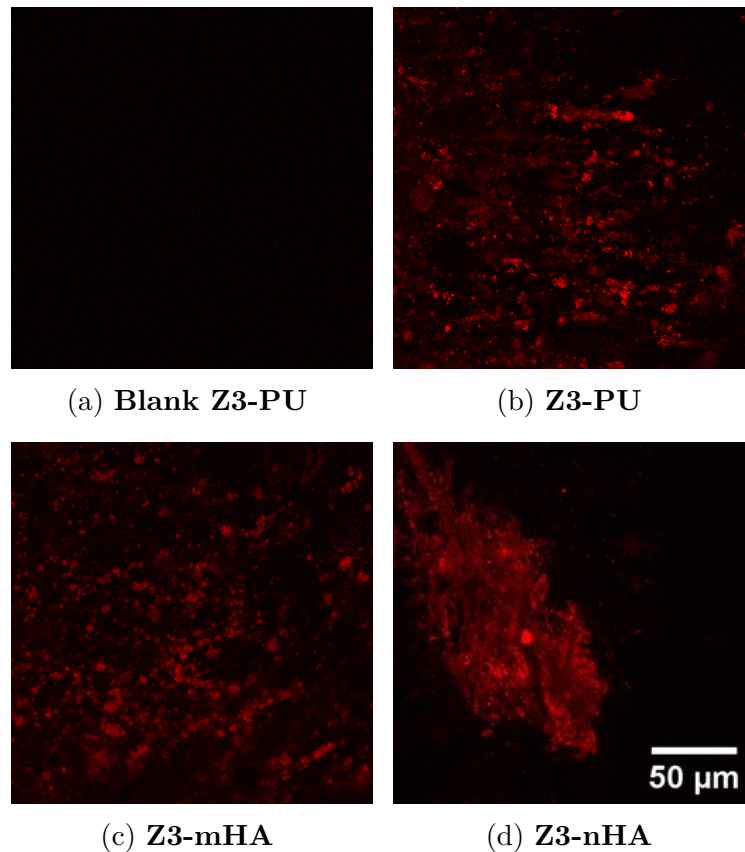
Figure 5.13: Xylenol Orange Staining on Z3A1 aligned scaffolds. A:Blank, B-D: Seeded with MLO-A5 cells *Scale Bar at 50 µm*

area of the field of view of the image (Zhao et al., 2010).

Furthermore, as shown in the standard deviation and maximum intensity images in Figure 5.14, the nodules in Z3-mHA were also more defined and mature, and appeared as distinct red spots which were easy to focus. On the contrary, Z3-PU scaffolds presented with several scattered speckles which caused its image to appear hazy with many softened and unfocussed regions. It is possible that this occurred due to the poorly crystalline and immature nature of the osteoid in PU-only scaffolds compared to those in the nano and micro-HA composites (Zhao et al., 2010). Mineralization however increased with time in all scaffolds.

A closer look at the cross-section along the maximum intensity images (Figure 5.14c), confirmed that the mineralized nodules in Z3-mHA penetrated almost the entire length of the scaffold compared to Z3-PU, which had only partial deposition with about 50% depth converge. It would be interesting to compare these findings with the SEM data of cells
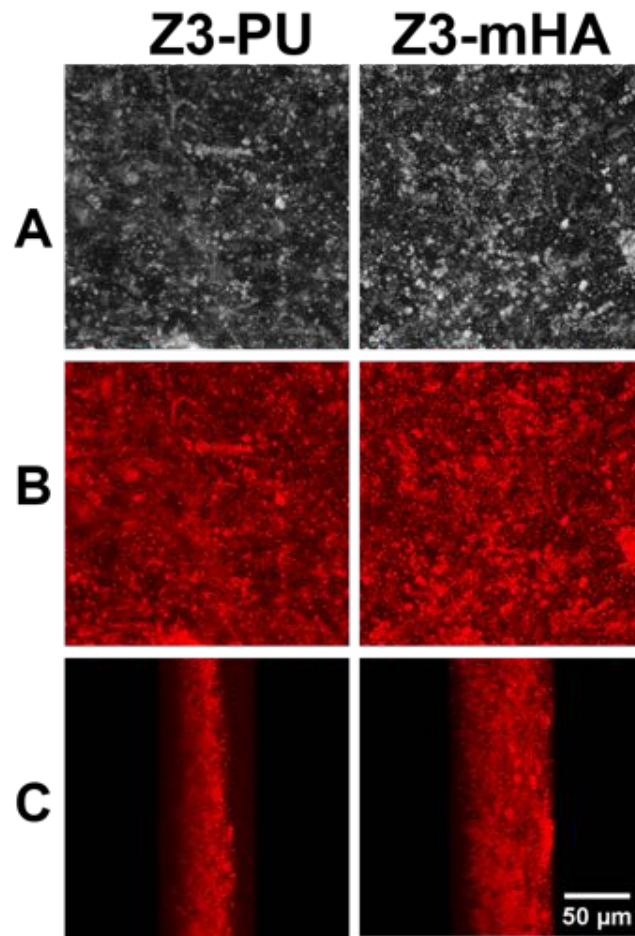
Figure 5.14: Comparing Xylenol Orange Staining on 15 wt% Z3-PU and Z3-mHA aligned scaffolds. (a): Standard Deviation Images of Deposited Calcium (b): Maximum Intensity Images of Deposited Calcium (c): Cross-Section along the Maximum Intensity Images. *Scale Bar at 50 µm*

on aligned scaffolds. Moreover, it would be interesting to establish if this phenomenon will be present in other cell types and also explore earlier time points such as D4 & D7, to attain a better overview of when mineralization starts.

5.3.7   SEM on Cells on Scaffolds

Following on from XO imaging, MLO-A5 cells seeded on fabricated scaffolds were analysed with Scanning Electron Mircroscopy. This provided an opportunity to explore cell attachment, extracellular matrix development and calcified mineral production.

MLOA-5 cells post-osteoblast and pre-osteocyte cell characteristics, rapidly mineralize in culture. They were therefore an ideal cell-type for examining how mineralization

175
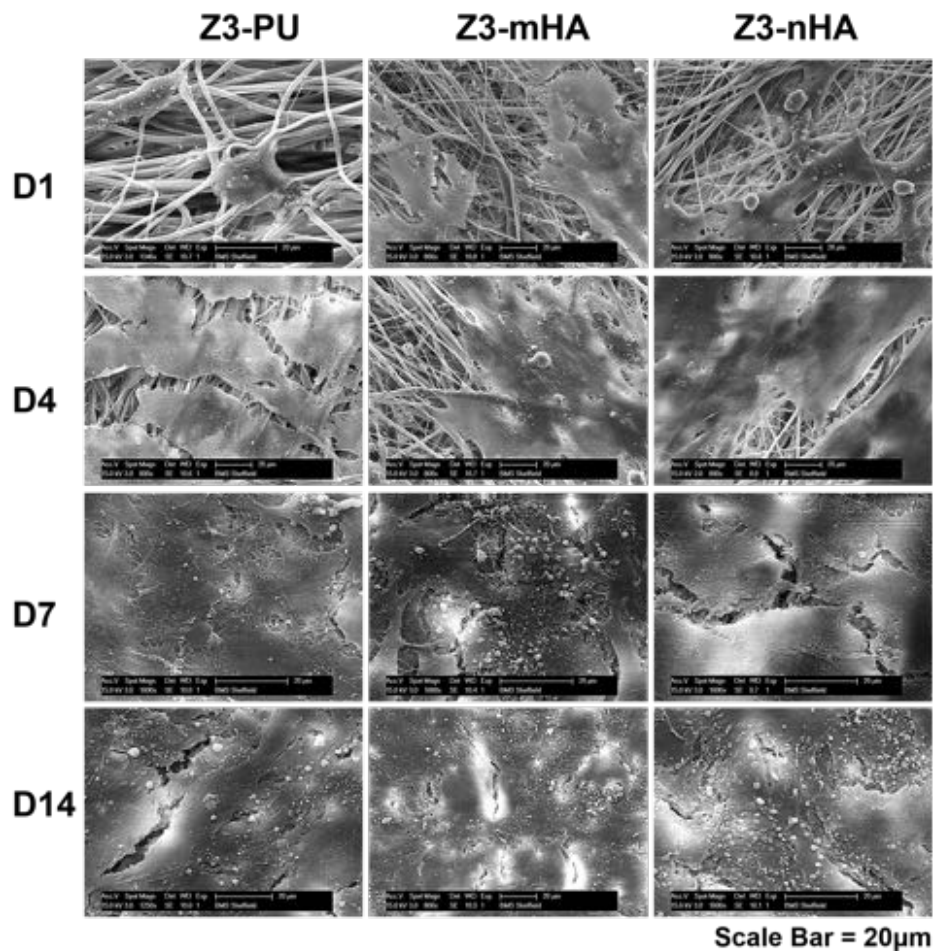
Figure 5.15: Combined SEM Images of MLO-A5 Cells on aligned Z3-PU, Z3-mHA & Z3-nHA scaffolds on Days 1, 4, 7 & 14. *Scale Bar at 20 μm*

occurred *in vitro*, due to their ability to form a honey-comb like mineralized matrix after only 7-9 days in culture (Rosser and Bonewald, 2012).

Figure 5.15 shows an SEM of how cells attached onto the various scaffolds. There was good cell attachment on all scaffolds on Day 1. The cells were well spread out on the scaffolds and anchored to the fibres of PU-only and composite scaffolds. By the day 4, cells had clustered on the surface of most parts of the scaffolds indicating cell proliferation which reinforces the MTT data.

Images from day 7 showed the cells were overly confluent and had completely covered the scaffolds, whilst secreting copious amounts of extracellular matrix. Several groups of mineralized nodules which appeared as bright regions at low magnification were also seen on both Z3-mHA and Z3-nHA scaffolds. Z3-PU however had very few mineralised

(a) **Seen on Z3-mHA by D7**

(b) **Seen on Z3-PU by D14**
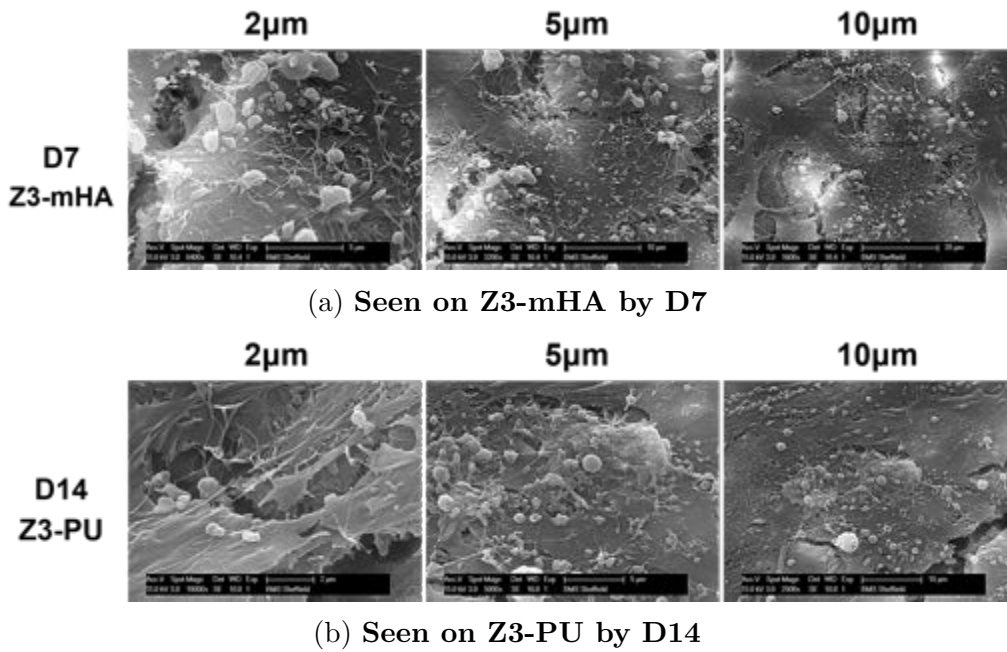
Figure 5.16: Higher Magnification SEM Images of MLO-A5 Cells on aligned Z3-PU & Z3-mHA scaffolds highlighting bight granules assumed to be mineralised nodules

regions but many threadlike cell extensions on day 7.
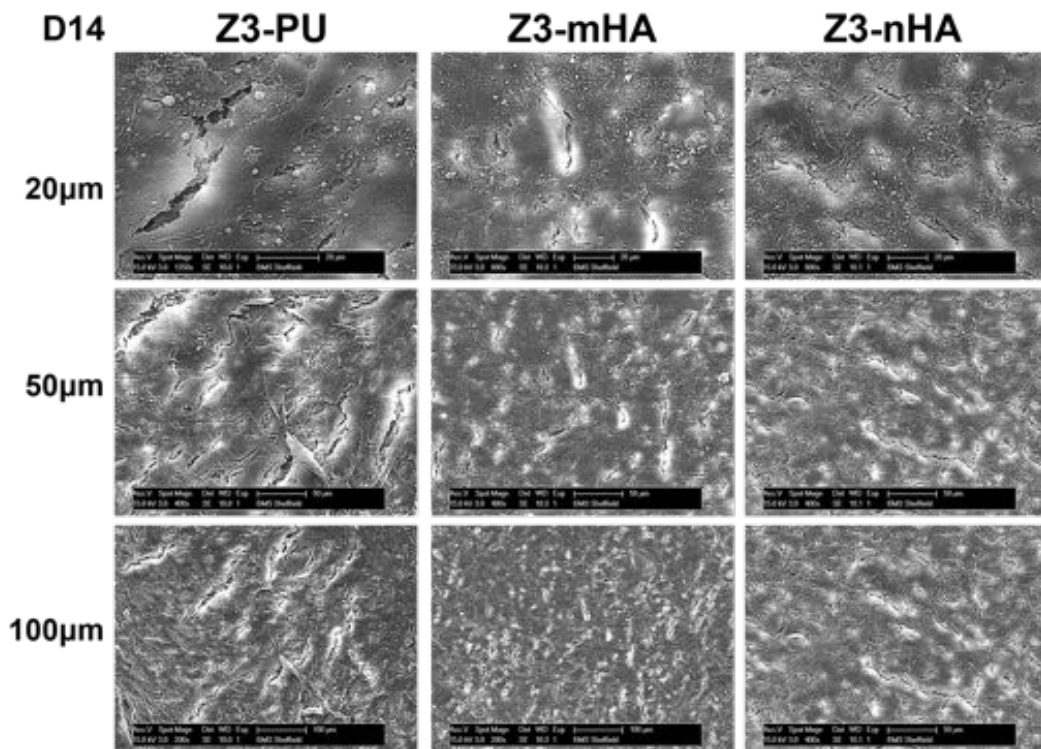
Figure 5.17: Combined D14 SEM Images of MLO-A5 Cells on aligned Z3-PU, Z3-mHA & Z3-nHA scaffolds highlighting bight regions assumed to be mineralised nodules at different magnifications.

The number of mineralized nodules on both HA composites and the PU-only scaffold greatly increased by day 14, indicating that all scaffolds supported MLO-A5 cells by providing a suitable growth environment that facilitates extracellular matrix deposition. As shown in Figure 5.16, the amount of mineralized nodules seen on day 14 Z3-PU scaffold is similar to that of day 7 Z3-mHA scaffolds.

This is similar to what was observed on the day 14 xylenol orange images, where there was a higher amount of calcified matrix production in Z3-mHA than in Z3-PU. Additionally, the bundling topography of the PU-only fibres which formed grooves and ridges were also covered with extracellular matrix and mineralization by day 14. As shown in Figure 5.17, mineralization on Z3-nHA and Z3-mHA were very similar.

It would be interesting to accurately confirm that the bright regions which look very similar to SEM of NaCl particles are indeed mineral deposits. This can be achieved by using TEM analysis to rule out apoptosis. It would also be interesting to explore whether this extent of early mineral deposition can also be achieved by mesenchymal cells such as hES-MPs. This would help to further compare the rate of mineralization of the two cell types.

5.3.8 Second Harmonic Generation Imaging

Second harmonic generation imaging (SHGI) was used to investigate the effect of fibre alignment on collagenous matrix production. Fibre alignment is known to influence cell behaviour starting from the initial cell spreading and elongation. This can in turn impact on matrix synthesis, and possibly on differentiation of bone cells and the calcification into bone tissues (Shin et al., 2012; He et al., 2014). On days 14, 21 and 28 of culture, scaffolds seeded with MLO-A5 cells were imaged with the Zeiss LSM 510 Meta upright laser scanning microscope equipped with the two-photon Ti-Sapphire multiphoton laser. $2\ \mu$m thick SHG image slices were analysed individually and also in small groups of $12\ \mu$m thickness's.

Compared to optical microscopy, SHGI attains contrast from a materials internal organizational structure rather than by variations in optical density and refractive

index. A highly polarizable or non-linear material, with non-centrosymmetric structures is therefore required to generate SHG signals due to the non-zero second harmonic co-efficient. This makes SHG an ideal imaging modality for biological components rich in highly ordered structural proteins such as collagen, muscle myosin and microtubles. Moreover, its high sensitivity for imaging and quantitatively analysing collagen fibril/fiber structure is said to be useful in detecting changes that occur in diseases such as cancer, fibrosis and connective tissue disorders (Chen et al., 2012; Han et al., 2005).

Similar to Two-Photon Excited Fluorescence TPEF, SHGI offers advantages of imaging deeper into thick 3D tissues by using near infrared wavelengths as opposed to confocal imaging (Campagnola et al., 2001). However, in contrast to TPEF, SHGI is energy conserving, since there is no loss in energy resulting from the relaxation of excited energy. It is therefore in principle not susceptible to phototoxicity and photobleaching compared to fluorescence microscopy (Campagnola and Loew, 2003). Furthermore, it provides very high axial and lateral resolution, and is also non-destructive, as it can be used on live cells without additional labelling.

5.3.8.1 Grouped Analysis

Prior to analysing the grouped SHG data, the entire collagen thickness for each scaffold type at each time point was subdivided into smaller 12 μm thickness's to allow for easy comparison i.e. 22-32 μm, 34-44 μm etc. Each 12 μm grouped image was compiled from six individual 2 μm slices. The directionality plug-in of the FIJI software was then used to calculate the average orientation of the collagen fibres in each 12 μm slice. All angles were measured between 0-180° in an anti-clockwise direction from the horizontal. Image slices are labelled alphabetically upwards, for example for D14 Z3-PU, **a**=first slice (portion closest to the scaffold) and **d**=last slice (furthest from the scaffold).

The amount of collagen produced by MLO-A5 cells which corresponds to the number of 12 μm slices varied across the various scaffolds and time points. Collagen deposition which appeared to be originally guided by the alignment of the scaffold fibres was observed to change orientation with change in depth. Moreover, the intensity/brightness

Table 5.5: Representative grouped SHG Images of MLO-A5 Cells on Z3-PU, Z3-mHA and Z3-nHA scaffolds on Days 14, 21 & 28. Each grouped image represents a merge of 6 individual (2 μm) slices with a total depth/thickness of 12 μm. *Scale Bar at 50 μm*
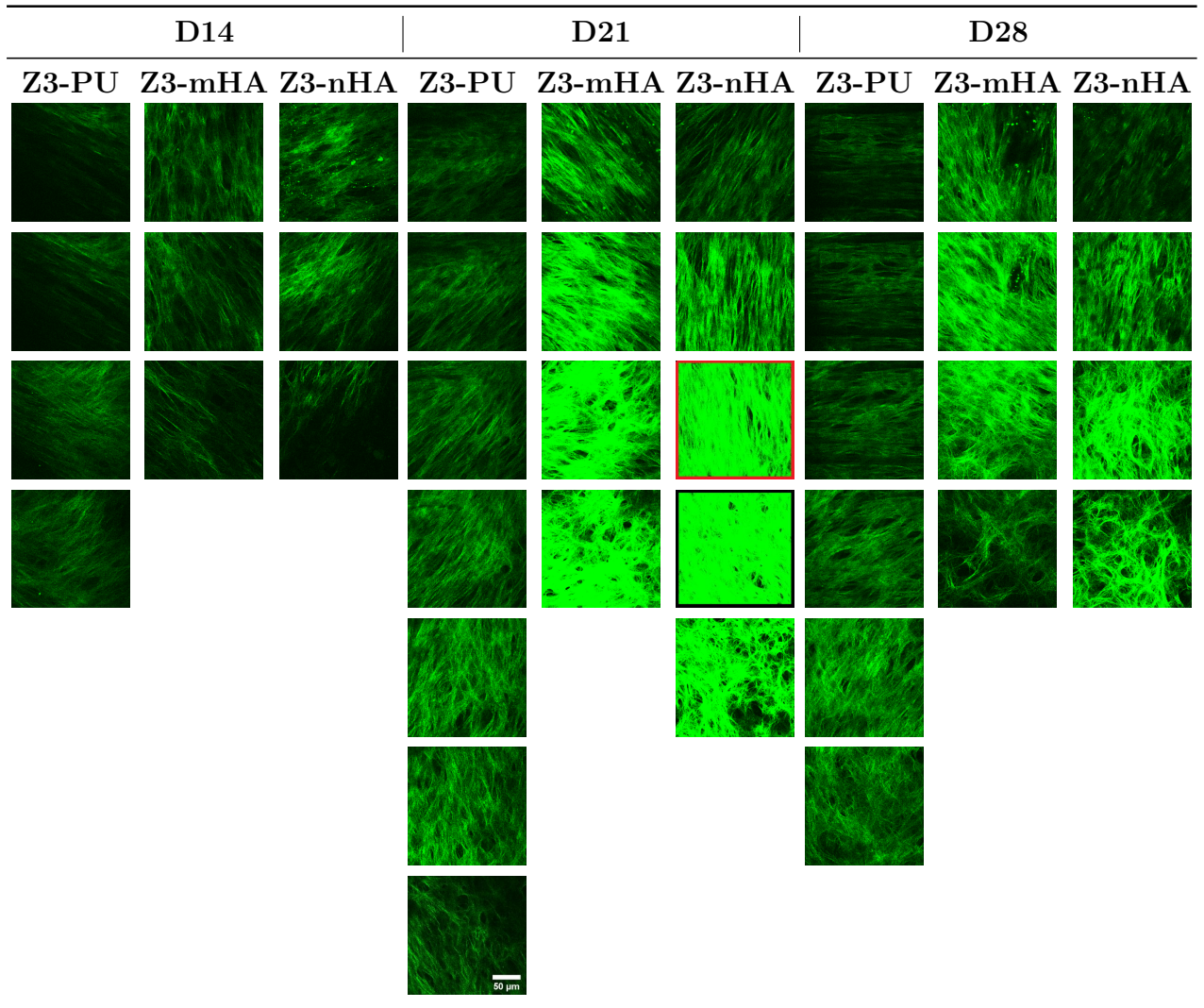
of deposited collagen also varied across materials. In general, there were higher amounts of collagen on the Z3-PU only scaffolds than on the composite scaffolds for all time points. Composite scaffolds however showed visibly brighter collagen intensities on D21 and D28 time-points compared to PU-only scaffolds.

For hard tissues such as bone, the alignment of collagenous fibres is of special importance. This is because calcified bone tissue exhibits different mechanical properties depending on the collagen alignment in the native structure (Sell et al., 2010; Shin et al., 2012). In addition, mature bone has a highly organised lamella microstructure. Its mineralised collagen fibrils are aligned mostly parallel within a single lamellae, but adjacent lamella have orientations at varying degrees from each other. For some osteons, this has been described as a 'twisted plywood' structure in which each lamellar has a small difference in the angle of orientation from the previous, such that the preferred orientation rotates through the layers (Giraud-Guille, 1988).

When bone cells are grown *in vitro* on planar substrates there is very little physical guidance of bone structure. This usually results in disorganised matrix and probably more representative of fast-growing immature woven bone. The exact mechanisms for collagen fibre alignment is still unclear but some intriguing information comes from tendon research in which the cell's primary cilia are aligned along the collagen fibrils of the tendon. Bashur et al. (2009) reported that bone marrow stromal cells assumed a more spindle-shaped morphology with increasing fibre diameter and degree of fibre alignment, and oriented parallel to fibres on aligned polyurethane meshes. Aligned electrospun scaffolds are therefore a promising tool for engineering fibrous musculoskeletal tissues as they reproduce the mechanical anisotropy of such tissues and can direct ordered neo-tissue formation (Baker et al., 2008).

Scaffolds with fewer slices had a thinner deposition of collagen. As tabulated in Table 5.5 on page 180, Z3-PU had four collagen slices on D14 compared to Z3-mHA and Z3-nHA scaffolds which had only three slices. However, compared to Z3-PU, changes in the average direction and orientation of collagen on the composite scaffolds was sharper than that of the Z3-PU. Figure 5.18 shows that collagen on Z3-PU which started at
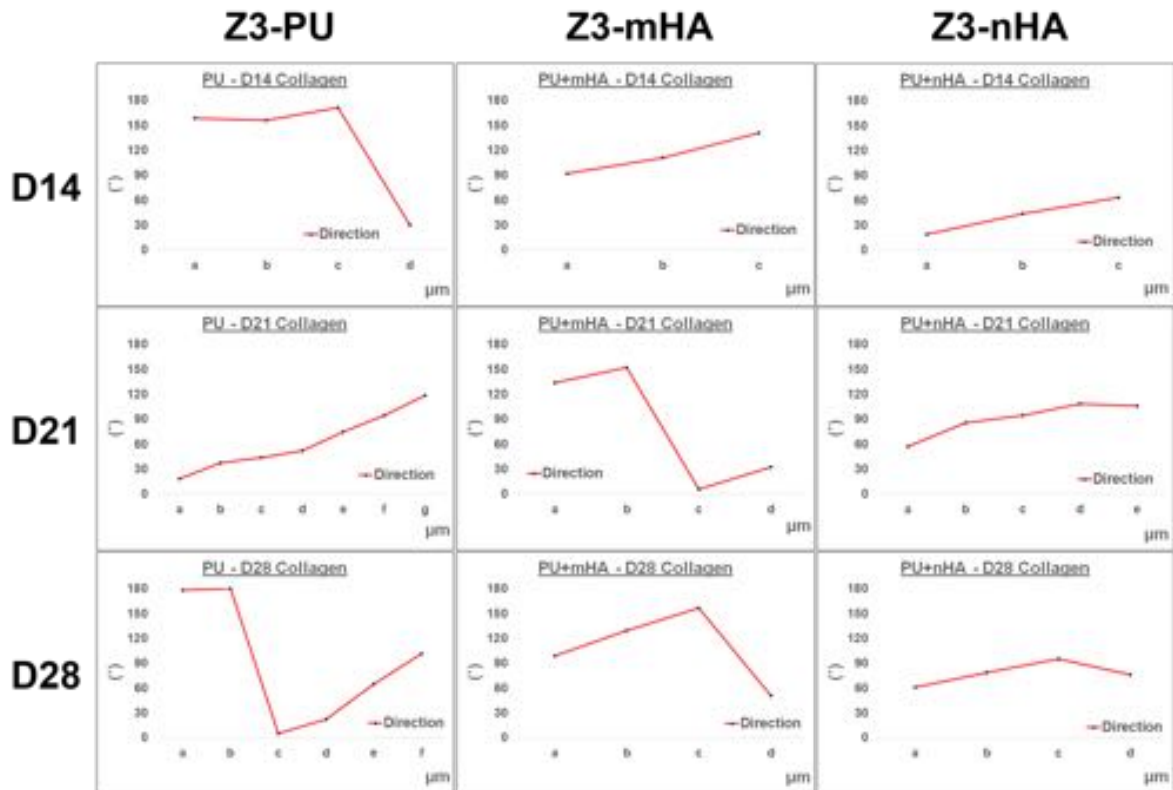
Figure 5.18: Directionality Analysis of Collagen Fibres in grouped (12 μm thickness) SHG Images of MLO-A5 Cells on aligned Z3-PU, Z3-mHA & Z3-nHA scaffolds on Days 14, 21 & 28.

158° had only a 3° change in directionality between slice **a** and **b**. Compared to the 19° difference for Z3-mHA which started at 91°, and the 24° difference for Z3-nHA which started at 19°. Slice **a** of Z3-nHA also contained several bright spot nodules believed to be nano-HA deposits.

The amount of collagen deposited on the Z3-PU scaffold on D21 was the highest observed during the 28 day period. Similar to that of D14, there were subtle changes in the directionality of the collagen on Z3-PU. With an initial average directionality of 18° for slice **a**, the directionality of deposited collagen which was initially guided by the fibre alignment, changed orientation in an anti-clockwise manner as it moved away from the fibres and ended with average directionality of 118° for slice **g**. Collagen on Z3-mHA quickly lost the guidance of the scaffold fibres after slice **b**, moving from an average directionality of 151° to 5°. On the other hand, collagen deposition on D21 for Z3-nHA was the brightest and most intense across the entire period. Its
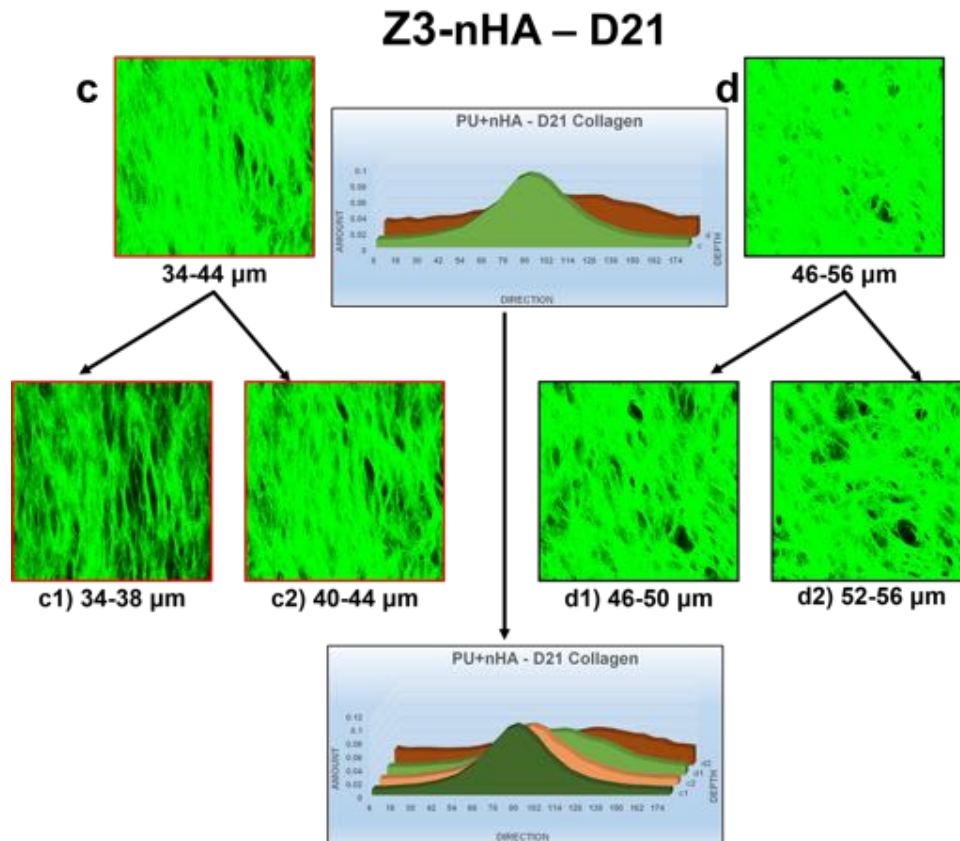
Figure 5.19: Grouped SHG D21-Z3-nHA slices **c**(third-red) & **d**(fourth-black) had very high collagen intensities/brightness. Hence each 12 μm image was further spilt into two 6 μm images. Thus image **c** (red) was split into two, c1 & c2 and image **d** (black) was split into d1 & d2.

third slice **c** (highlighted with a red border) and fourth slice **d** (highlighted with a black border) were overly bright. Each of these had to be split further into two smaller slices of 6 μm thickness (Figure 5.19) to highlight the changes in their directionality. There was a 4° difference in the directionality of slices **c1** & **c2**, and a 24° difference in slices **d1** & **d2**.

The change in collagen orientation between the slices was small in some cases e.g.slices A-C of D28 Z3-nHA and in others large differences were observed between one depth and the next e.g. slices B & C of D28 Z3-mHA. The directionality of deposited collagen on D28 Z3-PU which appeared to be almost horizontally aligned for slices **a-c**, quickly changed its alignment in slice **d**, and assumed an almost vertical orientation in slice **e**, before finally losing alignment in slice **f**. Z3-mHA, which had a much higher intensity of collagen however started off with an almost vertical alignment of 98° in slice **a**, changing
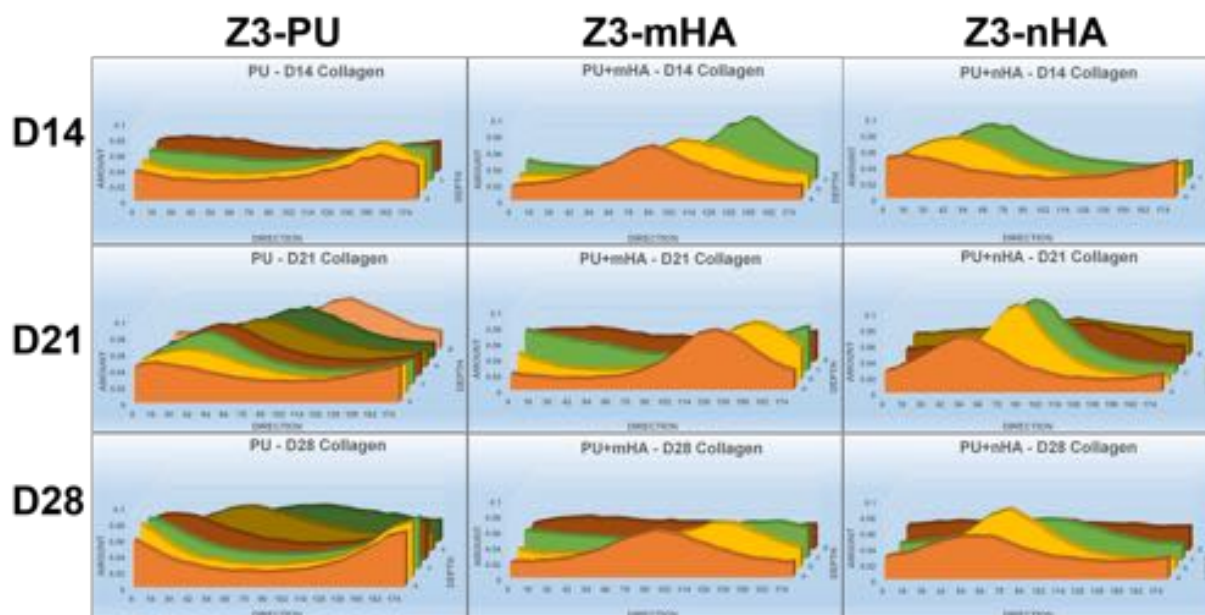
Figure 5.20: 3D histograms highlighting changes in directionality of collagen fibres in relation to depth for grouped (12 μm thickness) SHG slices. NB: Slide **c** & **d** Z3-nHA on D21 have not been split in this figure. Amount on the y-axis, refers to the ratio of fibers in each analysed image at a particular angle, thus on a scale of 0-1, how many fibers are at 0, 6, 12,18 ...180.

orientation in increments of approximately 30° per slice in slices **b** & **c**, before finally losing alignment in slice **d**. Furthermore, Z3-nHA which started of with a slightly lower amount of collagen than Z3-mHA, had a similar pattern of collagen deposition. With an initial alignment of 61° in slice **a**, it gently increased to 78° in slice **b** and 95° in slice **c**, before finally losing alignment in slice **d**. A 3D histogram summarizing the changes in the directionality of collagen deposition for the grouped slices is shown in Figure 5.20.

5.3.8.2 Individual Analysis

As shown in Table 5.5 on page 180, although collagen deposition on PU-only scaffolds were thicker than those of Z3-HA composites, its brightness and intensities were not as high as those of the composites. It was therefore very difficult to accurately compare collagen deposition on PU-only scaffolds to those of PU-HA scaffolds. The directionality of collagen fibres in individual 2 μm SHG slices, were analysed using the FIJI software. This made it possible to normalize the depth of collagen deposited on the scaffolds in a
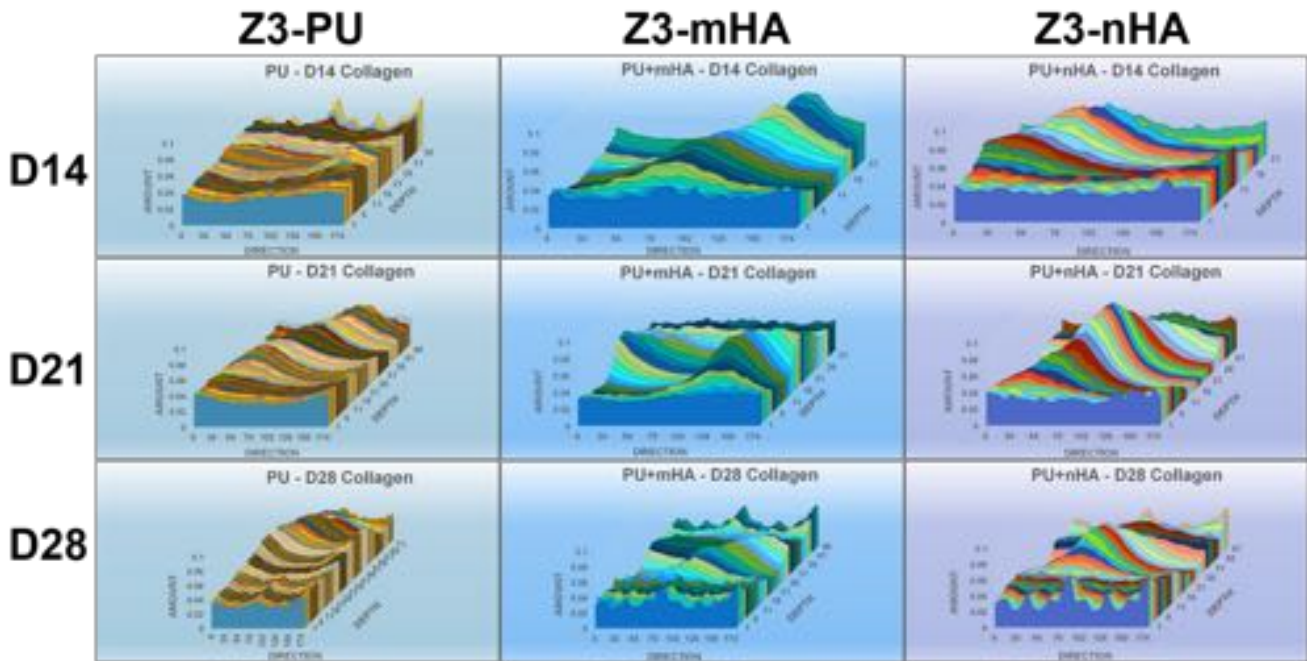
Figure 5.21: 3D histograms showing how the directionality of fibres changed in relation to depth in individual (2 μm thickness) SHG images .

scale of 0.0-1.0. There was however no specific trend amongst the materials and within the time points even after normalizing the collagen depth. 3D histograms of the individual SHG slices for all materials at the various time points is compiled in Figure 5.21.

Figure 5.22b highlights the individual 3D histogram of Z3-nHA on D21. This shows how the orientation of collagen fibres in the individual SHG slices changed along the 68 μm depth. Collagen deposition on these scaffolds, which were originally guided by the Z3-nHA fibres for the first 12 μm depth, gradually changed from a horizontal orientation through a 90° vertical orientation before losing alignment in the final 14 μm depth.

Bone has a twisted plywood structure which, to my knowledge has never been seen in culture to date. However, preliminary evidence from this study highlights changes to the directionality of collagen deposition that was originally guided by the orientation of scaffold fibres, suggests that it may be possible to recreate the twisted plywood structure *in vitro*. Although cell alignment in the same samples were not analyzed, evidence in the literature suggesting that it is likely that cells aligned along the fibres hence further investigation into cell alignment would be useful future work.
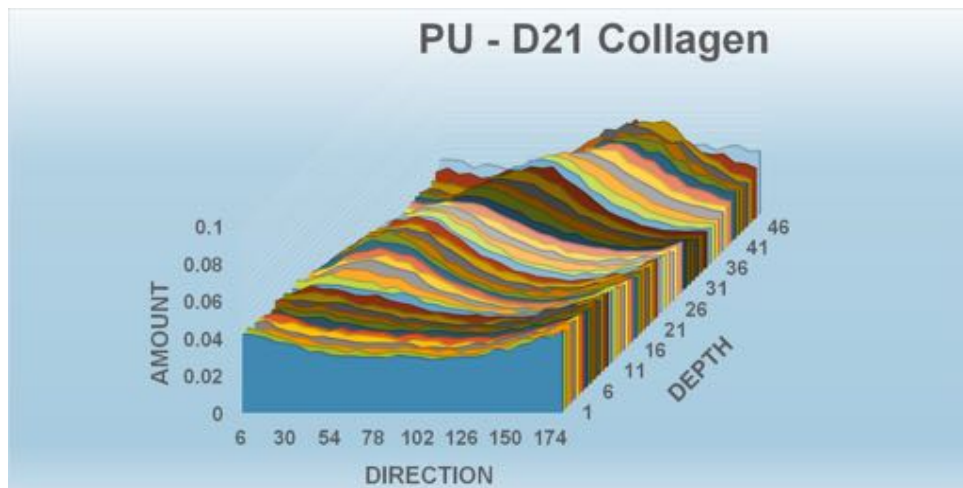
(a) **D21 Z3-PU scaffold**
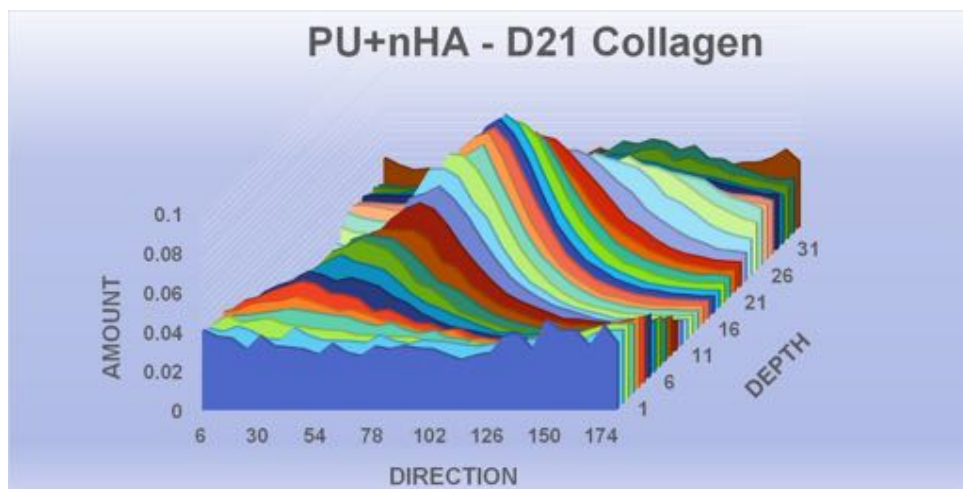
(b) **D21 Z3-nHA scaffold**

Figure 5.22: 3D histogram showing how the directionality of Collagen fibres changed in relation to depth for individual (2 μm thickness) SHG images.

5.4 Chapter Summary & Key Points

- Scaffolds made from polyurethane-only solutions had a distinct and interesting fibre morphology. Fibres of Z3-PU self-assembled very closely together to form thick aligned bundles, which were large enough to be seen with the naked eye

- Z3-nHA scaffolds had the most uniform fibre morphology. These nHA composites had very even fibre diameters and showed good porosity with interconnected pores. They also had a uniaxial fibre alignment and a less beaded morphology compared to its mHA counterparts

- Raman spectroscopy was used to characterize ν(C=O) urethane and (C=C) aromatic ring in PU, as well as ν_1, ν_2, ν_3 and ν_4 phosphate (PO_4^{3-}) ions and the ν_1 and ν_4 carbonate $CO_3{}^{2-}$ bands and confirm the presence of HA in both micro and nano-composites

- The main distinction between the FTIR specrta of aligned and non-aligned scaffolds was observed at vibrations in the $\nu3$ phosphate peak

- The inclusion of both types of HA particles reinforced the mechanical properties of Z3-PU, when tested in both transverse and parallel orientations. Z3-mHA scaffolds had the highest Young's Modulus and yield strength when tested in the transverse orientation

- Z3-PU which had the weakest mechanical behaviour within the parallel orientation group, had a Young's Modulus of 7.2 MPa, which was about 7 times that of its transverse testing results

- When tested along the long axis of the fibres i.e. the parallel orientation direction, aligned scaffolds displayed very high mechanical properties. Z3-nHA scaffolds the highest Young's Modulus of 14.5 MPa and a yield strength of 1.5 MPa.

- MLO-A5 and hES-MP cells were viable on all aligned scaffolds, with viability

increasing from D1 to D28. Cell viability of both cell types were generally higher on aligned scaffolds than on scaffolds in the non-aligned group

- PU supported the highest level of cellular penetration and viability across all time points for both MLO-A5 and hES-MP cells. Although the increased fibre packing density of aligned scaffolds is known to inhibit cellular infiltration, very good cell penetration and matrix deposition was observed along the entire depth of all scaffolds

- XO images of Z3-PU and Z3-mHA scaffolds showed an even distribution of mineral nodules. Z3-mHA had a higher percentage of mineral area coverage compared to Z3-PU

- Mineralized nodules in Z3-mHA penetrated almost the entire length of the scaffold compared to Z3-PU, which had only partial deposition with about 50% depth converge whilst Z3-nHA scaffolds showed large chunky regions of deposited mineral

- SEM images showed that there was good cell attachment on all scaffolds on D1 and images from D7 showed the cells were overly confluent and had completely covered the scaffolds, whilst secreting copious amounts of extracellular matrix

- There was a higher amount of calcified matrix production in Z3-mHA than in Z3-PU

- The amount of collagen produced by MLO-A5 cells varied across the various scaffolds and time points

- SHG imaging showed that collagen deposition which was originally guided by the alignment of the scaffold fibres was observed to change orientation with changes in depth

- The intensity/brightness of deposited collagen also varied across materials. There was thicker collagen deposition on the Z3-PU only scaffolds than on the composite scaffolds for all time points

- Composite scaffolds however showed visibly brighter collagen intensities on D21 and D28 time points compared to PU-only scaffolds

- The amount of collagen deposited on the Z3-PU scaffold on D21 was the highest observed during the 28 day period whilst Z3-nHA was showed the visibly brightest and most intense collagen deposition across the entire period

This page was intentionally left blank.

6 | Results and Discussion Section Three

Engineering a 3-dimensional biomimetic *in vitro* bone model for testing small orthopaedic implants

6.1 Introduction

Three-dimensional (3D) cell culture systems have gained increasing interest in tissue engineering due to their evident advantages in providing more physiologically relevant information and predictive data (Edmondson et al., 2014). Such advances in tissue engineering have aided the development of several *in vitro* models for tissues such as skin (Harrison et al., 2006), kidney (Subramanian et al., 2010), lung (Mondrinos et al., 2007), nerve (Gingras et al., 2003), cartilage (Risbud and Sittinger, 2002; Martin et al., 2007) and cornea (Suuronen et al., 2004).

While substantial progress has been achieved in the development of *in vitro* bone tissue engineering constructs for regenerative purposes (Shea et al., 2000; Petite et al., 2000; Meinel et al., 2004), limited progress has been attained in developing an ideal 3-D bone model (Tortelli and Cancedda, 2009; Papadimitropoulos et al., 2011). Such 3D models could be used to understand disease progression associated with bone pathologies such as osteoporosis, infection control, and osseointegration. Moreover, such models could also provide extensive understanding of the bone-implant interface, and can also be used as alternative to animal models for implant testing.

6.1. INTRODUCTION

Although traditional 2D cultures are still useful for investigating the molecular mechanisms regulating cell differentiation, it is evident that they cannot be used to faithfully mimic bone and cartilage (Tortelli and Cancedda, 2009). Current 2-dimensional *in vitro* testing of implant materials using cell culture is limited by a lack of dynamic environment and an inability to investigate the mechanical strength of the attachment between the bone matrix and implant surface.

Such conventional 2D cell cultures are not capable of mimicking the complexity and heterogeneity of bone turnover as they lack the specific organization and architecture observed in 3D conformations. Moreover, numerous signals that govern different cellular processes are lost when cells are grown on 2D plastic substrates (Zanoni et al., 2016). Current 3-dimensional tests to examine osseointegration are carried out in animals. These tests consist of embedding sections of implant and control samples into holes, cut or drilled in an animal's bone for a period of time. At the end of the study, the animal is sacrificed and the area of implantation is examined meticulously for local and systemic adverse effects, and possible osseointegration.

The costly nature of these long term *in vivo* tests, the differences in behaviour and structure in human and animal cells as well as the difficulty of replicating the effects of human aging are key setbacks to using an *in vivo* model. Moreover, there are many pieces of legislation that restrict the use of animals for scientific testing (European-Commission, 2013). There is therefore a clear demand to develop a novel 3D models that can be used to validate new implant designs since current *in vitro* tests fail to provide a 3-Dimensional dynamic environment.

In attempt to develop a 3D *in vitro* bone model, Tortelli and Cancedda (2009) seeded murine primary osteoblasts and osteoclast precursors on a resorbable 3D ceramic scaffolds and investigated bone cell interactions. They observed an enhancement in osteoblastic differentiation that promoted osteoclast differentiation and enhanced extracellular matrix deposition. Papadimitropoulos et al. (2011) also developed a 3D osteoblastic-osteoclastic endothelial cell co-culture system. Their aim was to create an *in vitro* model that mimics the process of bone turnover. They co-cultured osteoprogenitor and endothelial lineage

cells in 3D porous ceramic scaffolds using a perfusion-based bioreactor device. They intend to use their co-culture system to capture aspects of the functional coupling of bone-like matrix deposition and resorption.

With several scientific groups now focusing on cancer research, recent developments of *in vitro* bone models have also focussed on cancer since bone is one of the most common metastatic sites of breast cancer (Chen et al., 2010). Zhu et al. (2016) utilised 3D printed hydroxyapatite nanocomposites to create a biomimetic bone-specific environment for evaluating breast cancer invasion into the bone. Holen et al. (2015) also used a novel 3D model to investigate tumour cell-bone cell interactions and study breast cancer bone metastasis, *in vitro* and *in vivo*.

However, to the best of our knowledge an *in vitro* 3D bone model for implant testing has not yet been developed. Creating this three-dimensional organotypic model may reduce the use of complex and costly animal models, while gaining clinical relevance. Developing this advanced biomimetic model requires a scaffold that resembles trabeculae bone structure as close as possible. This scaffold should have the right chemical composition, desirable physical properties with characteristic pore sizes and porosity, ideal mechanical properties and support excellent biological response. Moreover, the scaffold should be easy to manufacture in bulk, imaged by μ-ct and support osteoblastic and progenitor cells to make bone structure.

The random and aligned electrospun scaffold discussed in the previous chapters had good bone tissue engineering properties and it is possible to roll them into a 3D cylindrical shape. Such a cylinder could be used as *in vitro* constructs for implant testing. This however would present with challenges including how to hold the rolled sheet in place, preventing necrosis in the rolled up portions, and ensuring an adequate nutrient and waste transfer amongst the cells. The thin structure of elesctrospun scaffolds limits it use as an *in vitro* bone model suitable for implant testing. There was therefore a need to create thicker scaffolds with properties using other scaffold fabrication techniques.

As already mentioned in the previous chapters, polyurethanes are attractive candidates for scaffold fabrication due to their mechanical flexibility and biocompatibility.

6.2. AIM

This mechanical flexibility arises from the thermodynamic incompatibility between its hard and soft segments, providing its unique segmented structure. Moreover, its versatile chemical composition allows PU to range from thermoplastic to thermosetting, from stable to degradable materials, and from hydrophobic to hydrophilic depending on the composition and synthesis procedure applied (Kucinska-Lipka et al., 2013). PU can therefore be applied to various methods of porous scaffold fabrication, among which are solvent casting/particulate leaching, thermally induced phase separation and emulsion freeze-drying. The properties of the scaffold created with these techniques depend on the thermal processing parameters, porogen agent and solvents used (Janik and Marzec, 2015).

Similarly, particulate leaching combined with solvent casting is a relatively simple and common technique that combines either salt or sugar particles (as porogens) with polymer or composite solution. Together with phase separation, these techniques were explored for creating highly porous 3D structures as part of this study. This created an opportunity to produce thicker constructs with controlled pore sizes and enhanced pore interconnectivity that were essential for developing a 3D model.

6.2 Aim

The overall aim of this chapter was to develop and test a 3D *in vitro* bone model for implant testing. Firstly, it was to explore a series of 3D fabrication techniques, and identify the best technique for creating thick scaffolds with uniform pores and consistent pore interconnectivity.

The secondary aim was to fully characterize the fabricated scaffolds *in vitro* and assess their suitability for use in developing the *in vitro* model by undertaking in-depth physical, mechanical and biological characterisation. The suitability of these scaffolds to be sterilised by autoclaving was also explored as part of this study.

Moreover, cell culture protocols were developed for seeding and proliferating hES-MP and MLO-A5 cells on these foam scaffolds. Additionally, the scaffold's ability to support

calcified matrix production was assessed using μ-CT imaging. Besides using the fabricated scaffolds to create an *in vitro* 3D model, their potential to serve as a bone graft substitute was also examined by conducting cortical defect and subcutaneous studies.

6.3   Results and Discussion Three

The particulate leached, freeze dried and freeze extracted scaffolds discussed in this chapter were fabricated as outlined in Section 3.3.2.2, 3.3.3 and 3.3.4, respectively. These were fabricated using PU and PU-HA solutions described in Sections 3.2.2.2 and 3.2.3, on page 68 and 69, respectively.

Freeze drying was the first fabrication technique to be explored for this project, this was done prior to electrospinning. In brief, PU-only solutions made from 15 wt% or 20 wt% Z9A1 or Z3A1 PU solutions, made with either 70/30 DMF/THF or 50/50 DMF/THF solvents. The solutions were poured into glass disks and lyophilized with a freeze dryer at Sheffield Hallam University. However, freeze extracted scaffolds were fabricated with 20 wt% Z9A1, 15 wt% Z3A1 and 10 wt% Z1A1 solutions in 100% DMF solvent.

Although, some particulate leached scaffolds were made using sugar particles, only PL scaffolds made with salt particles were characterized biologically. These included layer-by-layer, homogenized and physically mixed scaffolds. Cell culture and other biological characterization analysis undertaken on these PL scaffolds are described in Section 3.7.3.3 on page 96 and Sections 3.7.4 - 3.7.12 on pages 98 and 112, respectively.

In developing a protocol for the particulate leached technique, all the three types of PU in the ZnA1 series were examined. Initial attempts at creating foam PL scaffolds used sugar particles. It was however difficult to leach the sugar particles from the solidified PU matrix, resulting in a non-porous constructs. The layer-by-layer (LbL) technique was therefore developed by alternating salt and polymer based solutions in a layer pattern to create porous PU and PU-HA-based composites. All fabricated scaffolds were later characterized physically and mechanically. They were also characterized biologically using

MLO-A5 and hES-MP cells.

Although, the salt based LbL-technique addressed the earlier porosity challenges encountered with the sugar particles, its mechanical properties were found to be much lower than that of human bone. An attempt to rectify this aimed at developing homogenized PL composites from PU-HA solutions that were mixed at super-high speeds with a homogenizer. This was done to improve the interfacial bond strength between the HA particles and the PU matrix. Additionally, the time consuming nature of the LbL-technique was also addressed by developing the physically mixed (PM) technique. This is a relatively easier and faster approach for creating highly porous PL foams.

The ability of these scaffolds to support cell attachment and proliferation was examined using DAPI and Phalloidin staining, and alamar blue cell viability as described in Section 3.7.9.2 on page 109. Furthermore, Micro-CT analysis described in Section 3.7.8 on page 107 was also used to investigate how MLO-A5 cells deposited calcified extracellular matrix on these fabricated PM scaffolds. Finally, the ability of engineered PU and PU+mHA models to support cortex and osteopenia titanium screws were also investigated as part of this study.

6.3.1 Alternate Foam Fabrication Techniques

Phase separation or inversion is a process of transforming a polymer in a controlled space, from a liquid state to a solid state. It can be initiated by solvent evaporation (as in the case of solvent casting), by thermal precipitation or by precipitation with a non-solvent (Tsui and Gogolewski, 2009). Freeze drying, freeze gelation and freeze extraction are variations of thermal precipitation.

Thermally-induced phase separation is a temperature sensitive technique based on a polymer solution's ability to induce a liquid–liquid separation and quench below the solvent's freezing point. This creates in a polymer-rich and poor phase, which solidifies and crystallises, respectively. A highly porous structure can therefore be created once the formed crystals are removed. The concentration and composition of the solution, quenching temperature, and the rate of quenching are factors that affect the structure of

scaffolds developed with this technique (Janik and Marzec, 2015).

6.3.1.1 Freeze Dried Scaffolds

Freeze drying is a user and material sensitive technique of fabricating scaffolds. It is also extensively used as a preservation method in the pharmaceutical and food industry, to improve the storage and shelf-life of products.
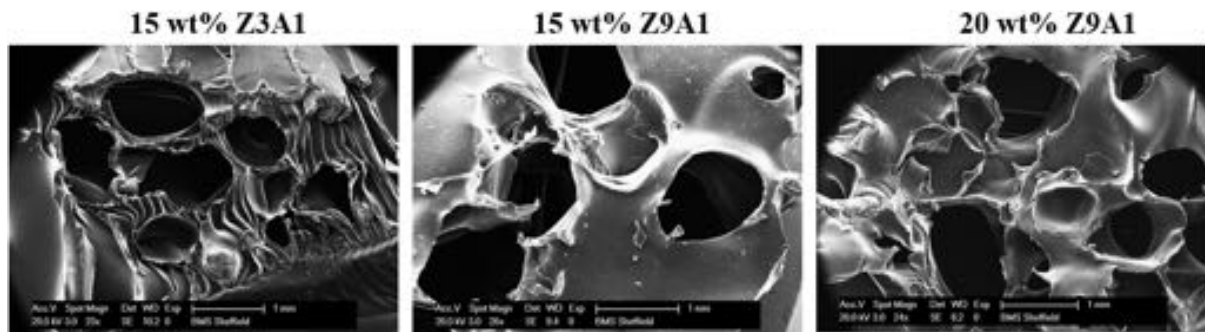
Figure 6.1: SEM images of Freeze Dried Polyurethane Scaffolds.
Scale Bar of SEM images=1 mm

As shown in Figure 6.1, scaffolds fabricated using this technique had very large and irregularly shaped pore structures. For all solvent combinations and concentrations, Z9A1 scaffolds had more bubbled and large pore sizes compared to Z3A1 scaffolds, which had relatively smaller and more uniform pore structures.

With some pore sizes greater than 1 mm, these transparent scaffolds were also exceptionally hard to handle and could not be used for biological characterization. Heijkants et al. (2006) used freeze drying in fabricating polyurethane scaffolds and reported of a high degree of interconnected macro and micro pore structures which enhanced cell attachment and proliferation. However, the freeze dried PU scaffolds fabricated as part of this study could not be used for cell work as the pore structures lacked interconnection and were far larger than the 200-300 μm pore size ideal for nutrients and cellular waste transfer in bone cell culture (Burg et al., 2000).

These differences in the behaviour of freeze dried polyurethane scaffolds could have been due to that fact that Heijkants et al. (2006) combined freeze drying with particulate leaching. They also utilized 1,4-dioxane solvent compared to the DMF/THF combinations used in this study. 1,4-dioxane is a popular solvent for freeze drying due to its ideal

6.3. RESULTS AND DISCUSSION THREE

Table 6.1: Mechanical Properties of Freeze Dried Scaffolds (n=6)

Freeze Dried Scaffolds	Thickness (mm)	Young's Modulus (MPa)	Yield Strength (MPa)
70/30 DMF/THF			
15wt % Z3A1	1.96 ± 0.27	5.02 ± 2.58	0.62 ± 0.14
20wt % Z3A1	4.05 ± 0.43	7.21 ± 2.35	0.99 ± 0.01
15wt % Z9A1	1.71 ± 0.04	35.47 ± 1.32	3.34 ± 0.80
20wt % Z9A1	1.47 ± 0.23	47.89 ± 7.81	4.49 ± 1.67
50/50 DMF/THF			
15wt % Z3A1	2.90 ± 0.71	1.68 ± 0.83	1.28 ± 0.64
20wt % Z3A1	5.41 ± 1.38	2.79 ± 1.59	0.60 ± 0.23
15wt % Z9A1	1.96 ± 0.22	28.03 ± 0.92	3.03 ± 0.70
20wt % Z9A1	1.67 ± 0.16	37.08 ± 7.19	2.92 ± 1.73

freezing properties, it however could not completely dissolve the PU pellets in the ZnA1 series. Moreover, the differences in PU behaviour could have also been due to variations in the chemical composition of polyurethane used. The chain extender used in the PU of Heijkants et al. (2006) is poly(tetramethylene adipate) based Estane whilst that of the ZnA1 series is 1,4 butane diol.

6.3.1.1.1 Mechanical Properties of Freeze Dried Scaffolds

Although these freeze dried scaffolds could not be used for biological characterization, they provided valuable insight into the mechanical properties of the polyurethane in the ZnA1 series. Since freeze drying was the first fabrication technique to be explored for this project prior to electrospinning. The tensile stress-strain curves of these scaffolds in Figure 6.2a & 6.2b, showed a clear distinction between the mechanical properties of Z9A1 and Z3A1 scaffolds. Made from the same 70/30 DMF/THF solvent combination, the stiffness values of Z9A1 scaffolds were almost 10-fold's higher than those of Z3A1.

As tabulated in Table 6.1, a similar observation was seen with the 50/50 DMF/THF solvent combination. For both Z3A1 and Z9A1 scaffolds, 20 wt% scaffolds containing a higher polymer to solvent ratio were stiffer than their 15wt% counterparts. Similar to random electrospun scaffolds, freeze dried scaffolds made from 70/30 DMF/THF solvent at the same solute concentration, had higher yield strength and Young's Modulus than their 50/50 DMF/THF counterparts.

(a) 70/30 DMF/THF

(b) 50/50 DMF/THF

(c) All Z3A1 Scaffolds

(d) All Z9A1 Scaffolds
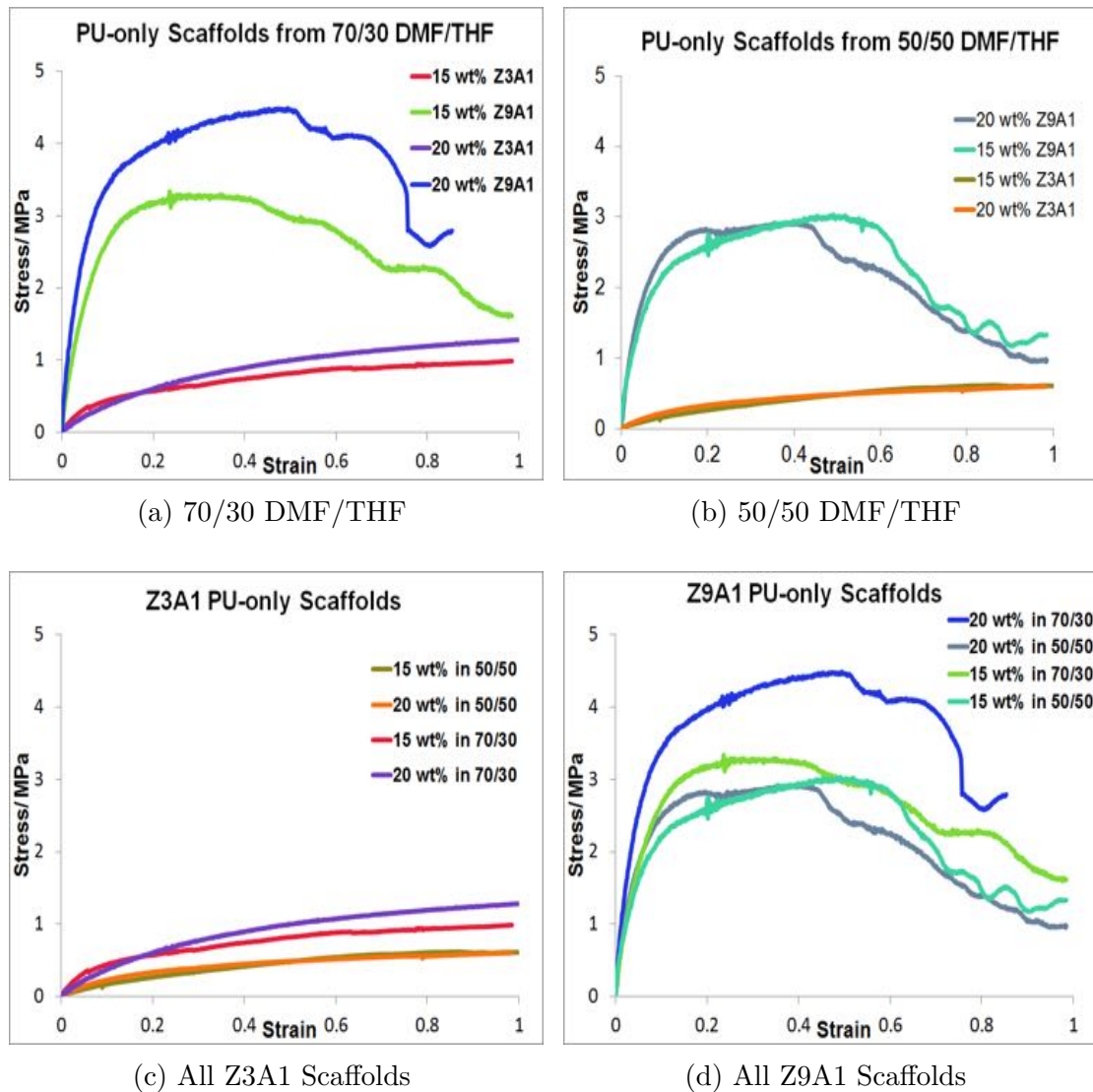
Figure 6.2: Example stress/strain curves of Freeze Dried Scaffolds.

6.3.1.2   Solvent Casting & Freeze Extracted Scaffolds

Solvent casting was used to create PU-only scaffolds at +20 ºC. These scaffolds dried into irregular shapes and felt very stiff to handle. They also appeared to be non-porous, although SEM images in Figure 6.3 showed a few pores in the scaffolds. Z1A1 scaffolds had the least pores, and showed a honey-comb porous surface in the 1 mm scale bar SEM image. Z9A1 had more pore structures compared to Z3A1. However, pore structures in both Z3A1 and Z9A1 appeared very shallow and were not interconnected.

Freeze extraction which combines thermal precipitation and precipitation with a non-solvent was also used to create a range of scaffolds at temperatures of

6.3. RESULTS AND DISCUSSION THREE
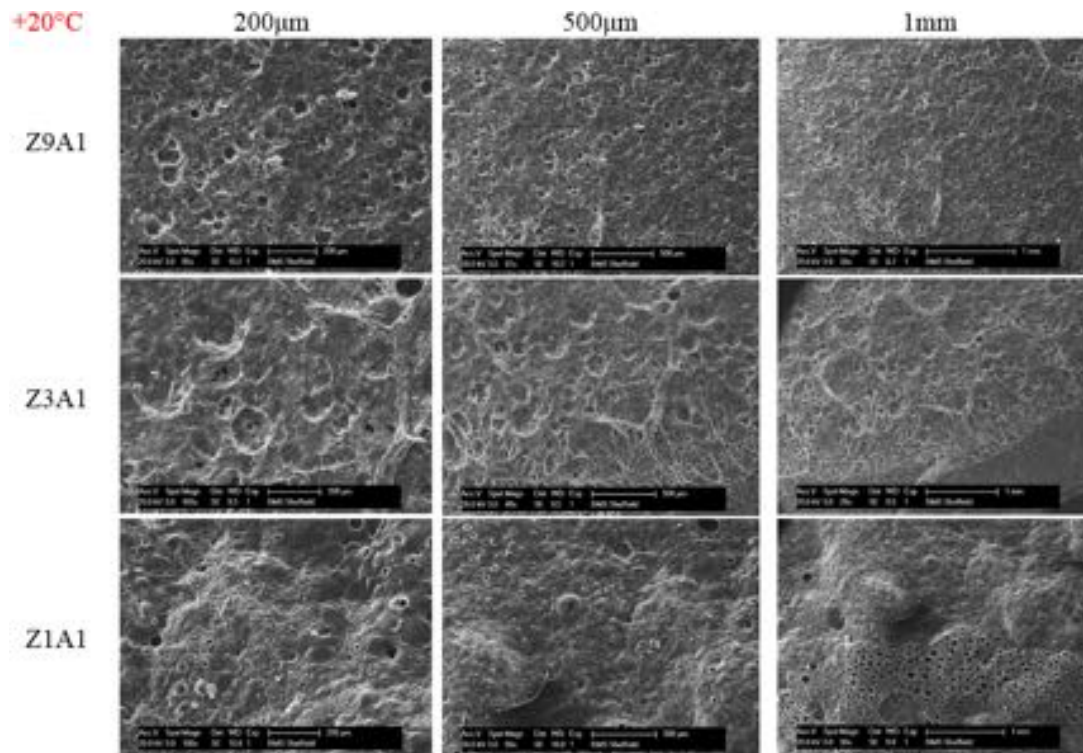
Figure 6.3: SEM images of +20° C Solvent Cast Polyurethane Scaffolds.
Scale Bar of SEM images=200 µm, 500 µm & 1 mm

-196 °C (Figure 6.4), -80 °C (Figure 6.5), -20 °C (Figure 6.6). Z1A1 freeze extracted -20 °C scaffolds had almost no pore structures, whereas Z3A1 and Z9A1 scaffolds contained large and irregular pores that appeared to have deep tunnels. These pores were however not connected. Similar morphologies were observed in scaffolds extracted in the -80 °C freezer. Scaffolds extracted at -196 °C had a very uneven morphology due to the fast quenching effect of the liquid nitrogen. They showed a small number of shallow pores under SEM for Z1A1 scaffolds but almost no pores in the Z3A1 scaffolds.

Similar to freeze dried scaffolds, the scaffolds fabricated by solvent casting and freeze extraction were not used for biological characterization. Their uneven and unrepeatable structures even made it impossible to attain any meaningful mechanical characterization data from them. Due to the challenges encountered with electrospinning and phase inversion fabrication techniques. Particulate leached foams were therefore considered as a suitable alternative for creating *in vitro* bone models.
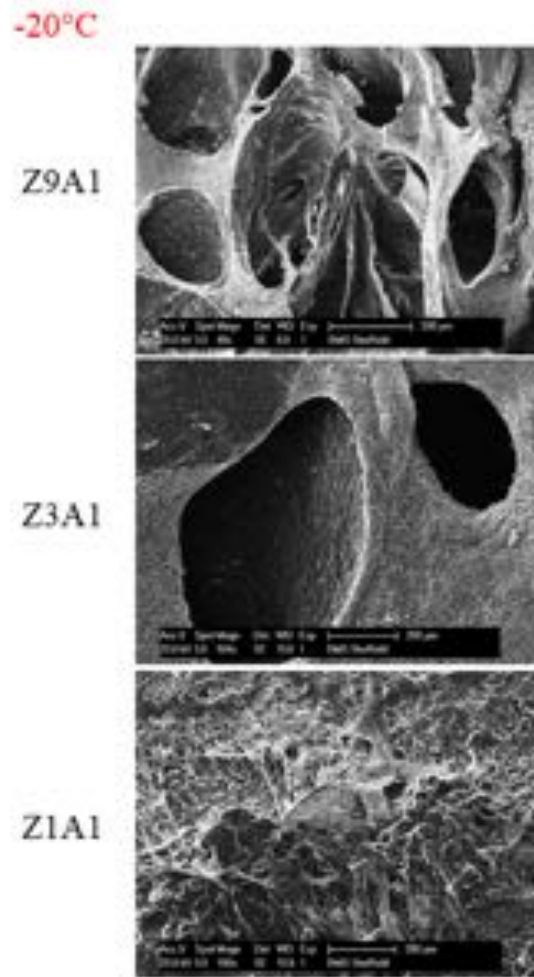
Figure 6.4: SEM images of -20° C Freeze Extracted Polyurethane Scaffolds.
Scale Bar of SEM images : Z9A1=500 µm, Z3A1 & Z1A1=200 µm

6.3.2   Particulate Leaching (PL) Scaffolds

Particulate leaching is a relatively simple technique used to fabricate scaffolds for various tissue engineering applications. It consists of combining either salt or sugar particles (as porogens) with a polymer or composite solution. These combined solutions are then contained in a predefined mold for a period of time to allow the solvent to evaporate. After the solvent has evaporated, the sugar or salt particles, which dissolve in water are leached away to obtain a porous three dimensional scaffold. This technique provides flexibility in controlling scaffold pore size by modifying the size of the porogen crystals, and ultimately its porosity by altering the salt/polymer ratio.
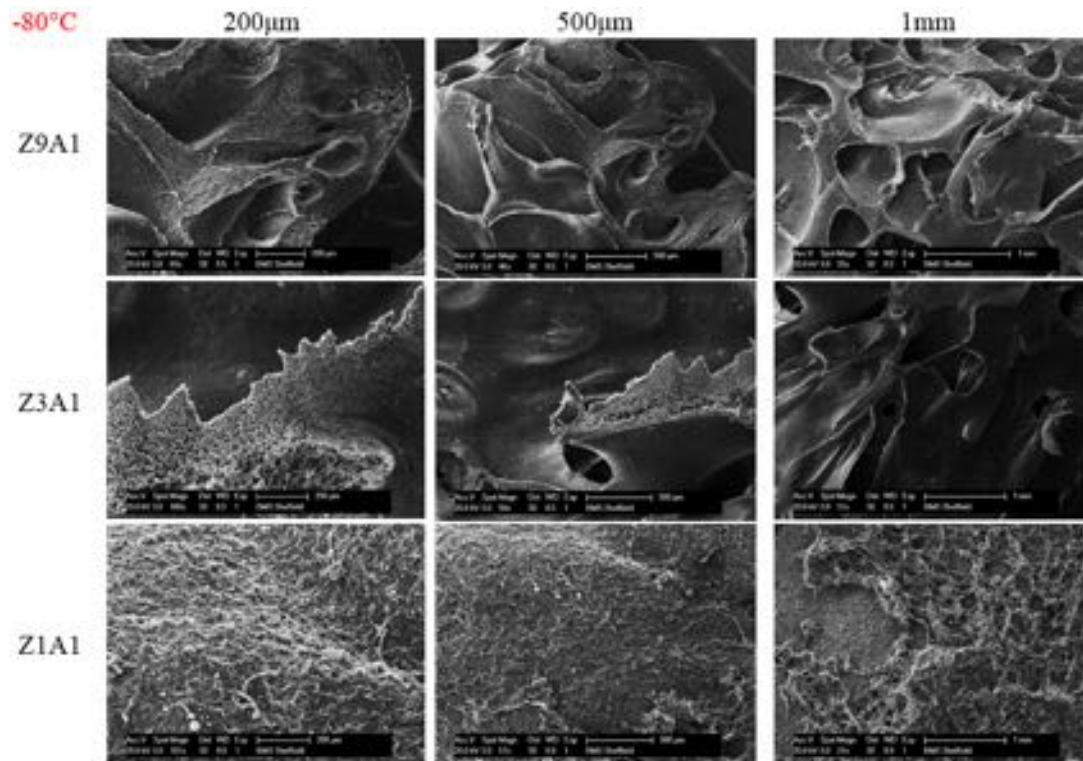
Figure 6.5: SEM images of -80° C Freeze Extracted Polyurethane Scaffolds
Scale Bar of SEM images=200 µm, 500 µm & 1 mm

6.3.2.1 Using Industrial PU Foam

Prior to fabricating PL scaffolds as part of this study, our group utilised an industrial PU foam kindly donated by Prof. Anthony Ryan as the main PU scaffold for *in vitro* analysis. As shown in Figure 6.7, these PU-only scaffolds had very large and interconnected pore structures. Most of these pores however appeared to be covered with a thin layer of PU coating across the edges or over the entire length of pore. Preliminary cell culture experiments, exposed the scaffolds to have pores that were too large for cell attachment.

With an average pore size of almost 400 μm, hES-MP cells seeded on these non-bioactive scaffolds fell straight through and did not attach well to the scaffolds. Subsequent MTT experiments showed that adjusting the cell seeding density, media and protocol could improve cell attachment in these scaffolds. A previous researcher in our lab was also able to optimise cell seeding well enough to use these foams as a model system for mechanical loading experiments (Sittichockechaiwut et al., 2009). However, fabricating our own foam scaffolds using particulate leaching could provide greater control
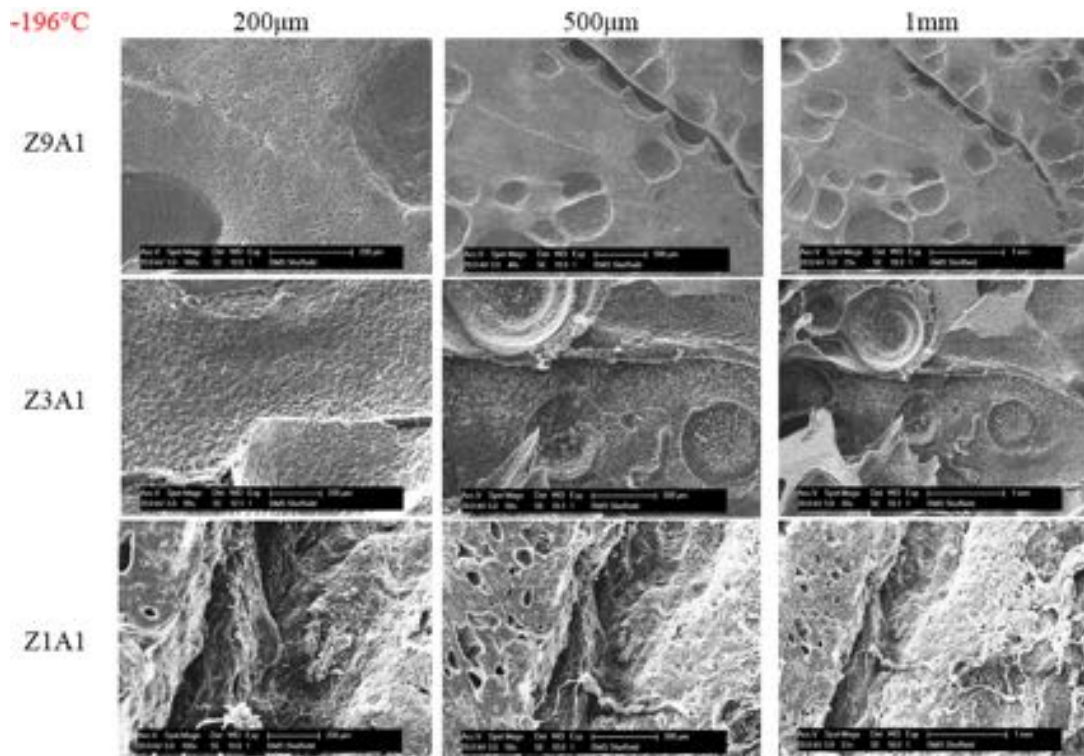
Figure 6.6: SEM images of -196° C Freeze Extracted Polyurethane Scaffolds
Scale Bar of SEM images=200 µm, 500 µm & 1 mm

of our scaffolds. These scaffolds could be customised to have an ideal pore size and interconnectivity, as well as be incorporated with nanocomposites and biomolecules to improve the mechanical and bioactive properties of the scaffold.
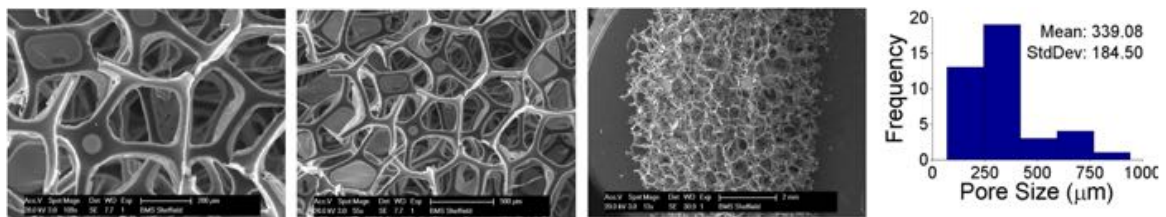
Figure 6.7: SEM image of Previously used Industrial PU Foam
Scale Bar of SEM images=200 µm, 500 µm & 2 mm

6.3.2.2   Using Sugar Particles

Initial attempts to fabricate foam PU scaffolds combined sugar particles with 15 wt% and 20 wt% Z9A1 solutions made from 100% DMF solution. The integration of a solid porogen within a 3D polymer matrix facilitates the creation of an inter-connected pore network with well-defined pore sizes and shapes (Guarino and Ambrosio, 2008).
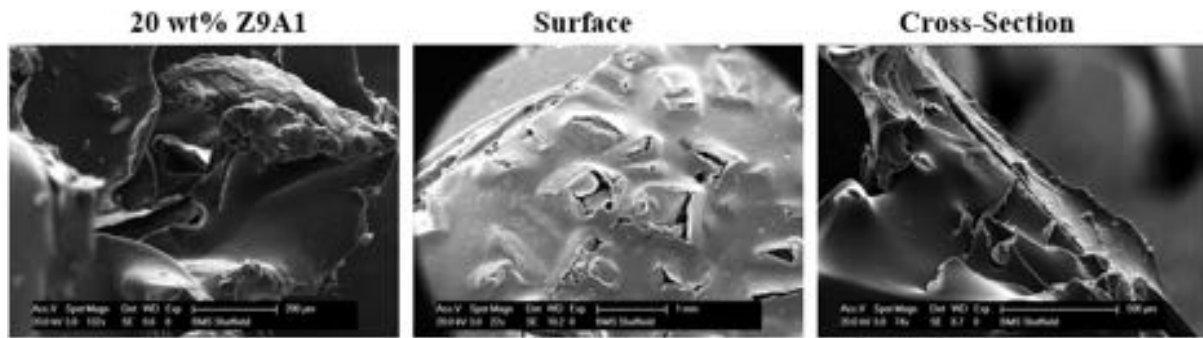
Figure 6.8: SEM images of 20 wt% of Z9A1 PL Scaffolds made with Sugar Particles
Scale Bar of SEM images=200 µm, 1 mm & 500 µm

For both 15 wt% and 20 wt% Z9A1 scaffolds fabricated with the particulate leaching method, it was difficult to leach out the sugar particles used. About 50% of porogens remained entrapped in the fabricated scaffold after more than a month of leaching under static conditions. As shown in Figure 6.8, the scaffold had trapped sugar particles and non-uniform morphology. This observation is typical of thick sugar-based particulate leached scaffolds and as such others have recommended fabricating thinner scaffolds by layering scaffolds with chloroform (Sachlos and Czernuszka, 2003). Although this layering technique is advantageous for removing porogens, the toxic nature of chloroform undermines its use for cell culture.

6.3.3   Layer-by-Layer PL Scaffolds

The layer-by-layer technique was developed to address the limitations encountered with fabricating PL foams with sugar. Following on from discussions with Dr.Frederik Claeyssens regarding creating sugar-based PL scaffolds, it became evident that the challenges occurred from the manner in which the particles were introduced. This trapped the particles in solution and prevented them from being accessible to water molecules.

This was because the large sugar particles were introduced into the high molecular weight Z9A1 PU solution after casting. Evaporation of the 100% DMF solvent had already commenced and started to create a sealed non-porous regions at the edges of the scaffolds. This caused the sugar particles to became trapped in the PU solution and be inaccessible to leaching, and hence inhibited the dissolution process. The layer-by-layer

technique was therefore created to fabricate highly porous PL scaffolds by alternating salt particles (Figure 6.9) and polymer solution in layered pattern.

Figure 6.9: SEM of nHA, mHA and NaCl particles used in fabricating PL scaffolds
Scale Bar of SEM images=10 µm, 10 µm & 1 mm

6.3.3.1 SEM of LbL-PL Scaffolds

The LbL-PL technique described in detail in Section 3.3.2.2.1 on page 74 was first used for creating PU-only scaffolds from 10 wt% Z1A1 solution, 15 wt% Z3A1 solutions and 20 wt% Z9A1 solutions made with 100% DMF solvent. SEM of these scaffolds shown in Figure 6.10, showed an impressive improvement over the sugar-based PL scaffolds in Figure 6.8.

These scaffolds showed an even porous structure and a combination of interconnected macro and micro pores which have been reported to facilitate cell culture and nutrient transport (Heijkants et al., 2006). Scaffolds made from all three types of PU in the ZnA1 series had a highly porous 3D structure and were significantly thicker than electrospun scaffolds. They were therefore seen as excellent templates for creating the *in vitro* 3D model.

However, to allow for consistency and uniformity in scaffold fabrication, only PL scaffolds made from Z3A1 and 70/30 DMF/THF solvent were used for biological characterization. Composite scaffolds were made by doping the Z3A1-70/30 solutions with either micro or nano-sized HA particles (Figure 6.9) in the ratio of 3:1, PU:HA.

As shown in Figure 6.11, PU-only Z3A1 scaffolds had the highest average pore size of 235 µm. Including both types of HA particles to create composites reduced this average pore size to 187 µm for mHA composites and 190 µm for nHA composites. SEM images
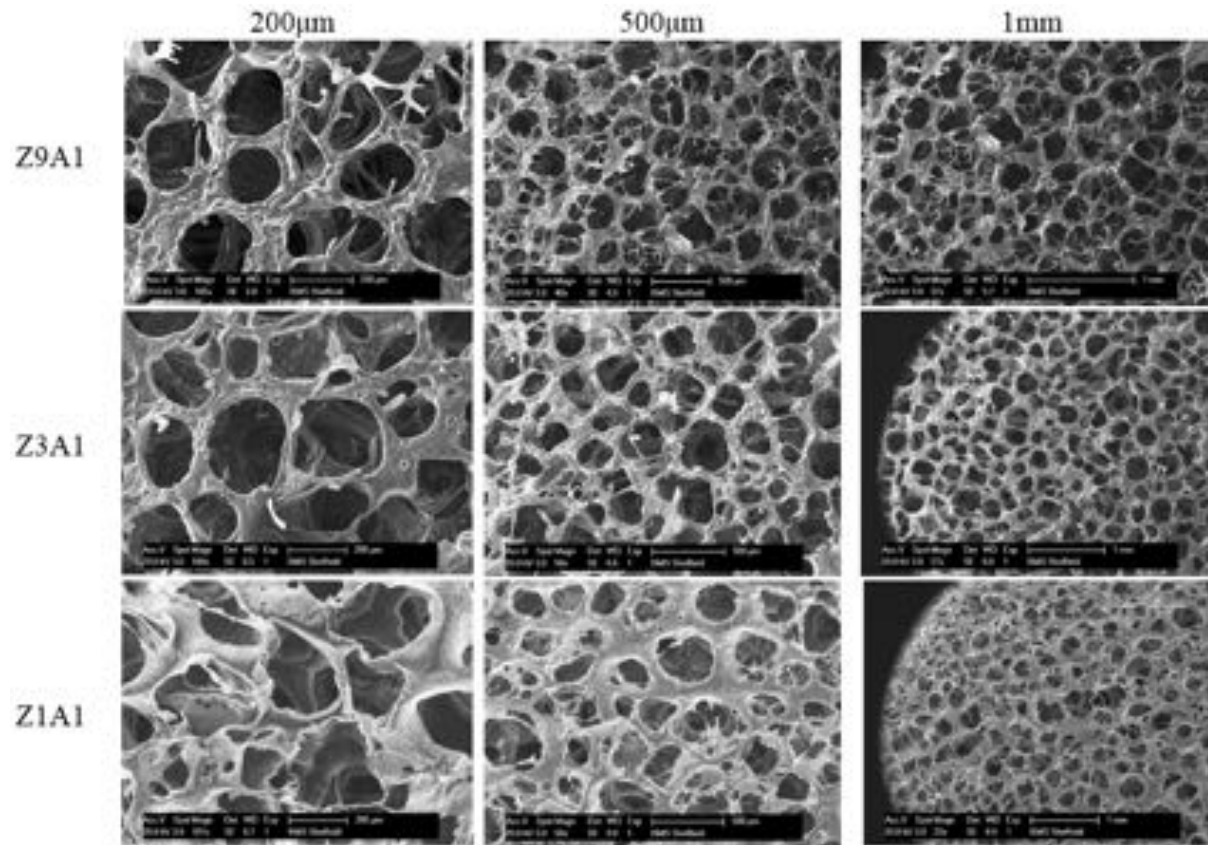
Figure 6.10: SEM of PL Z9A1, Z3A1 & Z1A1 PU Scaffolds made with NaCl Particles
Scale Bar of SEM images=200 µm, 500 µm & 1 mm

of the cross-sections also revealed a highly interconnected porous structure across the entire length of the scaffolds which comprised of a range of pore sizes. The larger pores may serve as channels to perfuse culture media or augment diffusion of nutrients to cells seeded within central pores. In turn, the smaller pores provide a potential space for tissue ingrowth. Taboas et al. (2003) also fabricated PLA/HA scaffolds with similar pore structures to mimic trabecular bone.

6.3.3.1.1 Optimisation of HA content

By weight, approximately 70% of bone tissue is mineral, with an estimated 95% of the mineral phase composed of a crystalline hydroxyapatite and the remaining 5% being impurities (Feldman et al., 2007). The remaining 30% of bone dry weight is the organic component of bone which is noted to be predominantly collagen Type 1 (Hollinger, 2005).

In an attempt to mimic the higher mineral content of bone, composite scaffolds containing micro-sized HA particles in the ratio 2:1, PU:HA, were also created to assess
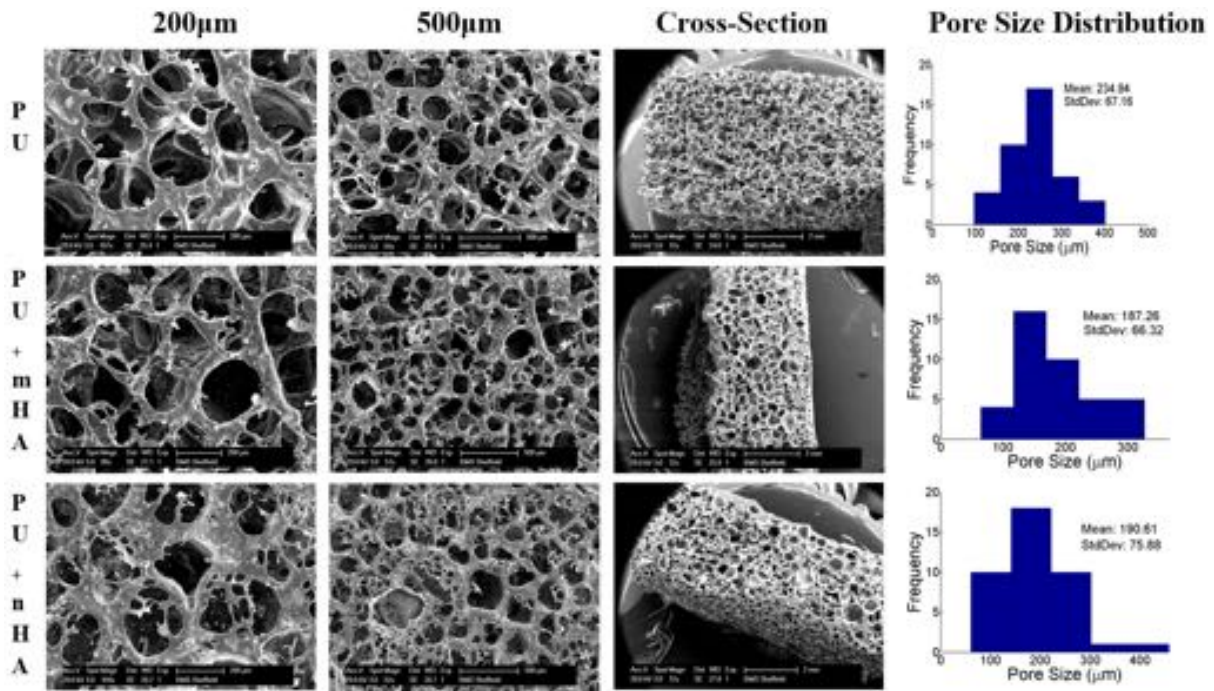
Figure 6.11: SEM images of 15 wt% Z3A1 Layer-by-Layer PL Scaffolds
Scale Bar of SEM images=200 µm, 500 µm & Cross-section=2 mm
Histogram distributions of pore sizes (n=40)

the effect of incorporating higher HA quantities in fabricated scaffolds. As shown in Figure 6.12, 2:1 PU+mHA scaffolds had an average pore size of 148 μm with some closed up pores. This was lower than the 187 μm attained with 3:1 mHA composites. It is possible that increasing the quantity of mHA powder in solution caused the reduction in quantity and size of the pores.

6.3.3.1.2 SEM and PAS-FTIR of Autoclaved Scaffolds

Sterilization of fabricated scaffolds prior to cell culture is an essential step that cannot be ignored as it avoids the introduction of micro-organisms to the cell culture and prevent infection. Ethylene oxide treatment, gamma irradiation, antibiotic treatment and liquid sterilisation such as ethanol and paracetic acid are possible sterilisation methods that have been used on scaffolds. Each of these however present with their own advantages and disadvantages. Some of these techniques have been shown to be unsuitable for polymer scaffolds because of deformation from lengthy degassing, chemical toxicity and deterioration due to decreased molecular weights (Athanasiou et al., 1996).

Electrospun scaffolds used in this study were sterilized with paracetic acid for 3 hours
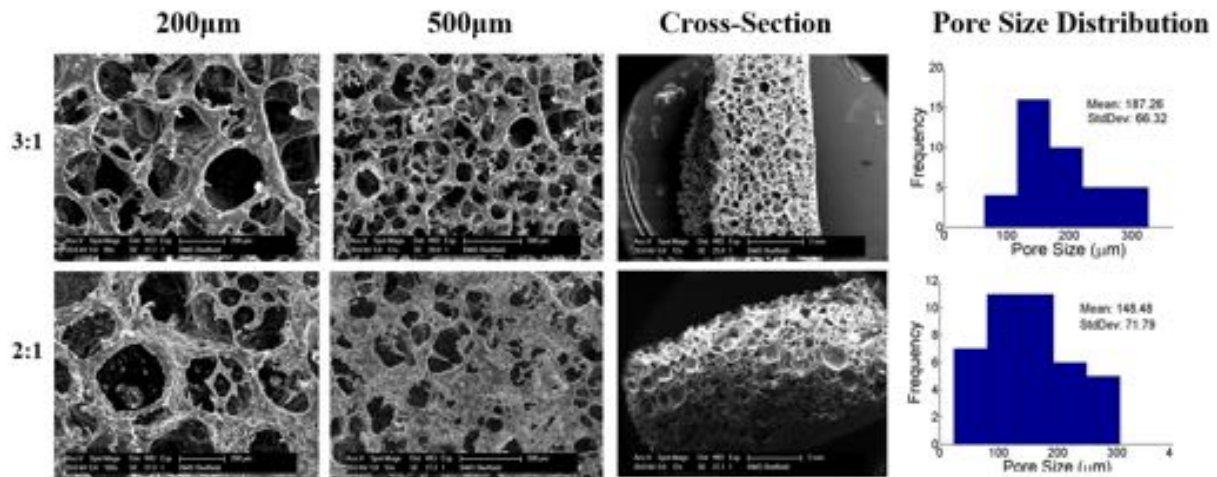
Figure 6.12: SEM images of 3:1 vs 2:1, 15 wt% Z3A1 PU+mHA LbL-PL Scaffolds
Scale Bar of SEM images=200 µm, 500 µm & Cross-section=2 mm
Histogram distributions of pore sizes (n=40)

prior to cell culture. However due to the large size of the PL scaffolds, an alternative method of sterilisation was required as sterilisation with paracetic acid did not suffice. Autoclaving, a typical medical sterilization method has been reported in the literature to be unsuitable for polymer scaffolds (Shearer et al., 2006). However using this method to sterilise the fabricated PL scaffolds proved effective and showed minor visible differences between the SEM images of before and after autoclaving scaffolds (Figure 6.13).

6.3.3.2 Micro-CT: Pore Interconnectivity and Porosity

Micro-computed tomography (μ-CT) combined with 3D image rendering provides an opportunity to access systematic variation in scaffold architecture (Jones et al., 2007). μ-CT made it possible to evaluate scaffold porosity, surface area per unit volume and the degree of interconnectivity by combining μ-CT imaging and computer aided manipulation of the scanned data. This provided an accurate quantification of the 3D structure and an ability to visualize the scaffolds internal conformations.

It was also used during the final stages of the project to access bone mineralization in cell-seeded scaffolds. As shown in Table 6.2, μ-CT imaging of plain polyurethane scaffolds showed a more porous morphology compared to composite scaffolds containing micro and nano-sized HA particles. This was further highlighted with an analysis of the scaffold's entire porosity. As shown in Figure 6.14, PU-only and PU+nHA scaffolds were

Before Autoclaving
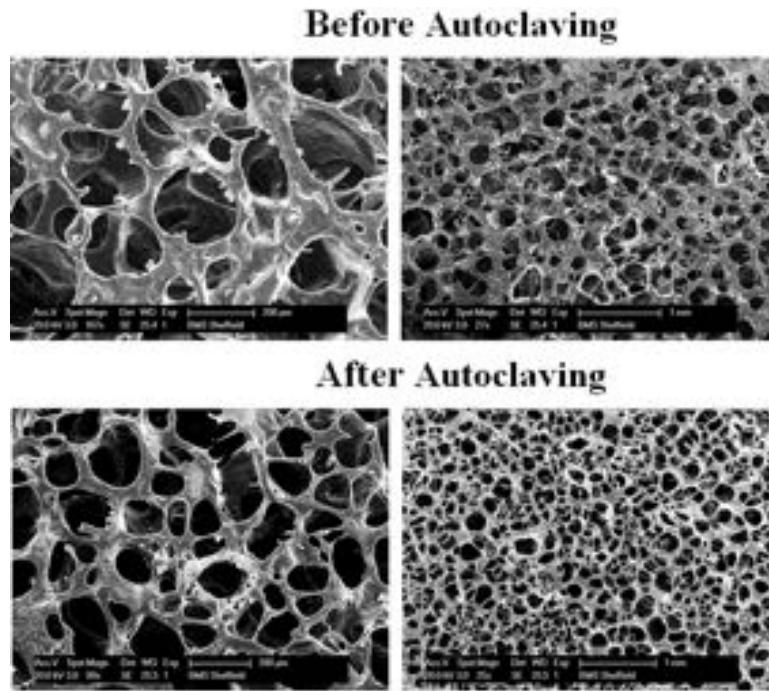
After Autoclaving

Figure 6.13: Before and After Autoclaving SEM images of LbL PU Scaffolds
Scale Bar of SEM images=200 µm & 1 mm

more porous than mHA based scaffolds.

With a porosity of 89.4%, PU scaffolds were about 6% more porous than both 3:1 and 2:1 PU+mHA scaffolds, but only 3% more porous than 3:1 PU+nHA. This trend is similar to the average pore size analysis of the SEM scaffolds. μ-CT showed a good distribution of HA particles throughout the entire volume of composite scaffolds. A comparison of 3:1 and 2:1 PU+mHA μ-CT images in Table 6.3, confirmed that composite scaffolds with 2:1 PU:mHA, had more HA particles than their 3:1 counterparts. However, compared to the 38.78 μm (20.71%) difference between the SEM average pore size of 3:1 and 2:1 PU+mHA scaffolds, there was only a 0.2% difference in their average porosities. This could have been due to the changes in the field of view of SEM images.

The three-dimensional structure and architecture of scaffolds play a critical role in bone formation and could influence the functionality of the engineered bone constructs (Ho and Hutmacher, 2006). Hence such quantitative analysis of the structure-function relationships is therefore important for optimizing the mechanical and biological performance of these scaffolds.

Table 6.2: Micro-CT Imaging of Blank LbL-PL Scaffolds to Examine Scaffold Porosity
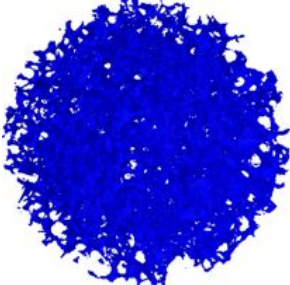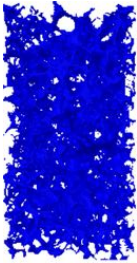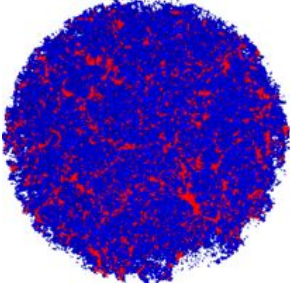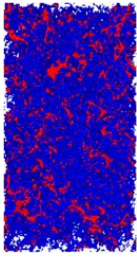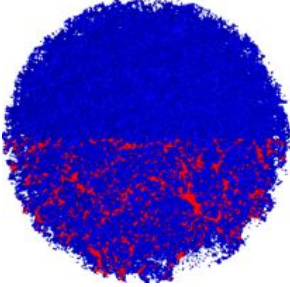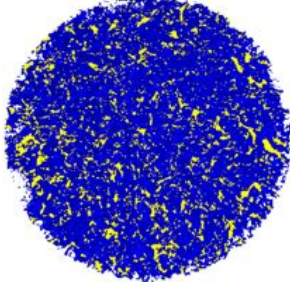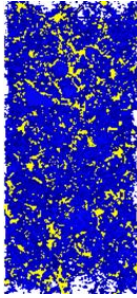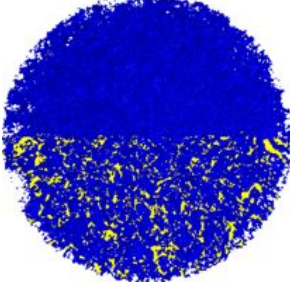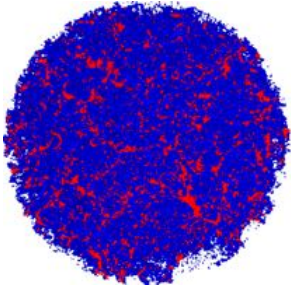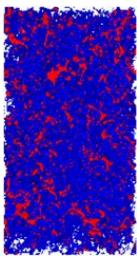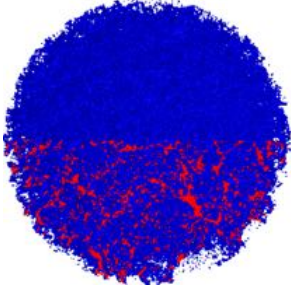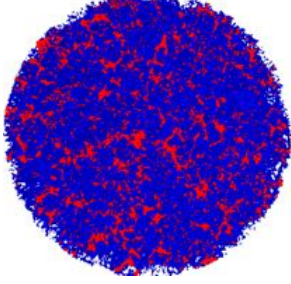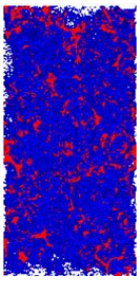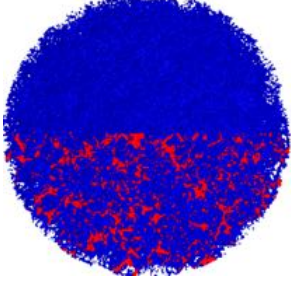
	Top View	Cross-section	Truncated HA
PU			
PU+mHA			
PU+nHA			

Table 6.3: Micro-CT Image Comparison of 3:1 vs 2:1 PU+mHA Scaffolds

	Top View	Cross-section	Truncated HA
PU+mHA 3:1			
PU+mHA 2:1			
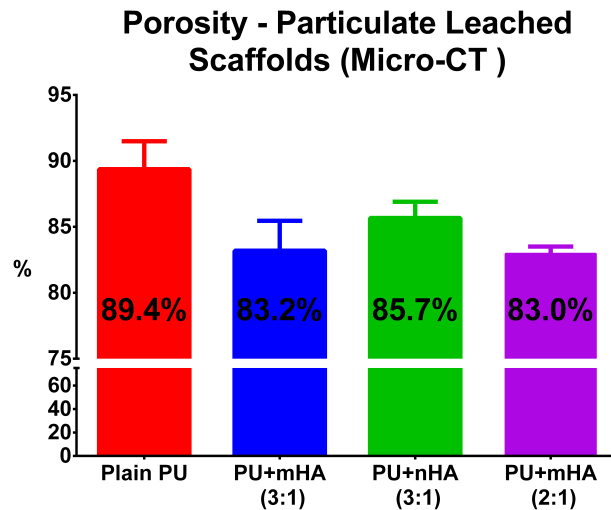
Figure 6.14: Micro CT Estimation of the Porosity of 15 wt% Z3A1 PU-LbL PL Scaffolds

6.3.3.3   Mechanical Properties

The mechanical properties of particulate leached scaffolds were assessed using compression plate accessories and the Bose 3200. Example stress/strain curves in Figure 6.15a showed that including HA particles reinforced the mechanical properties of composites compared to PU-only scaffolds.

Although 3:1 nHA composites had the highest Young's Modulus and yield strength in the LbL-PL group, its mechanical properties were not significantly different from 3:1 mHA composites. PU-only scaffolds had the lowest Young's Modulus (Figure 6.15b) in the group. It's Young's Modulus value of 0.32 MPa was significantly lower than the 0.63 and 0.67 MPa of 3:1 PU+mHA and 3:1 PU+nHA composites, respectively. Similarly, its yield strength value of 0.015 MPa (Figure 6.15c) was half that of 3:1 PU+mHA, and significantly lower than those of 3:1 PU+nHA composites.

As shown in Figure 6.16a, the mechanical properties of 2:1 and 3:1 PU+mHA composites were very similar. Although 2:1 PU+mHA scaffolds contained a higher ∽33% HA content, (8% more HA than its 3:1 counterparts), there was only a 0.05 and 0.004 MPa difference between its Young's Modulus and yield strength values of 3:1 and 2:1 mHA composites. With a yield strength of 0.035 MPa, 2:1 PU+mHA was 12.9% higher than

6.3. RESULTS AND DISCUSSION THREE
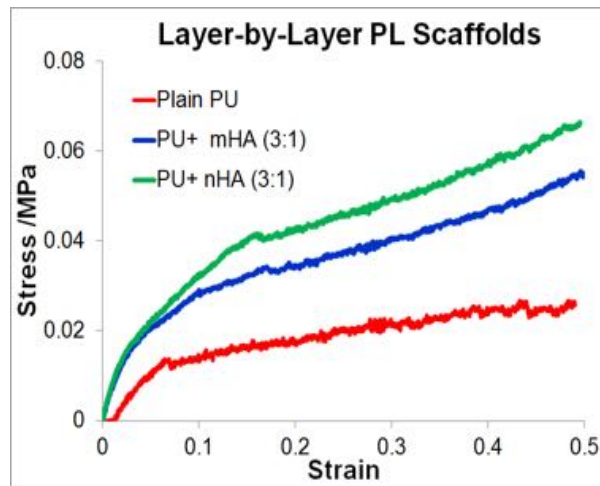
(a) Example stress/strain curves
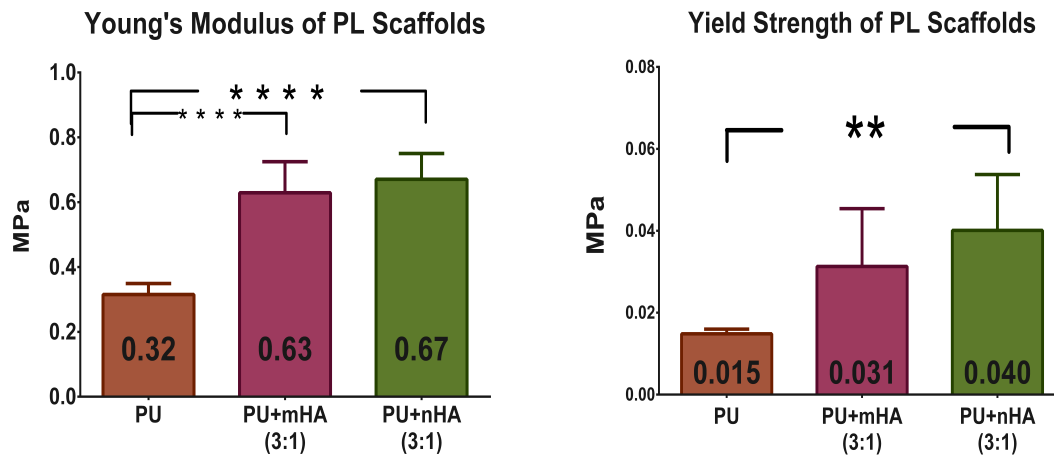
(b) Youngs's Modulus

(c) Yield Strength

Figure 6.15: Mechanical Properties of 15 wt% Z3A1 LbL-PL Scaffolds.

that of 3:1 PU+mHA. Interestingly, its 0.58 MPa Young's Modulus was 7.94% lower than that of the 3:1 composites.

6.3.3.4 Alamar Blue Cell Viability

Alamar blue cell viability assay was carried on LbL-PL scaffolds seeded with either MLO-A5 or hES-MP cells for 21 days. Compared to MTT, water soluble resazurin salt is non-toxic to cells and hence does not kill the cells to obtain viability measurements. This allows precious primary cells to be re-used for further investigations, saving time and money (Ahmed et al., 1994).

(a) Example stress/strain curves

(b)

(c)
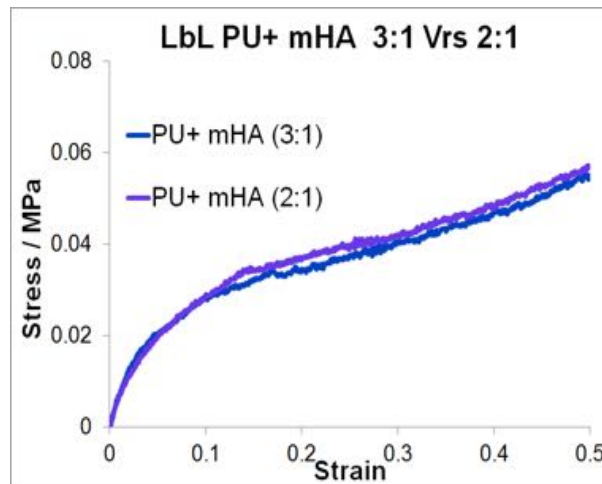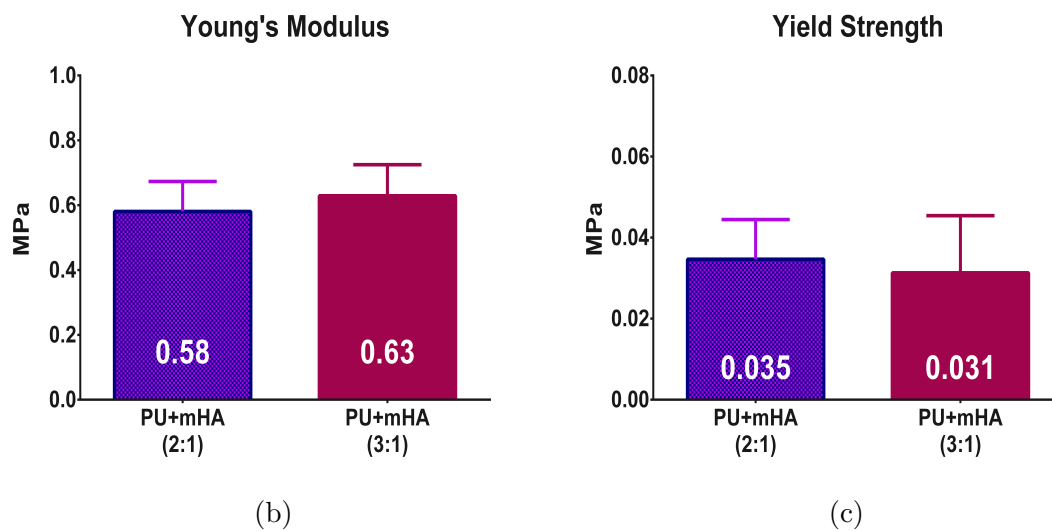
Figure 6.16: Mechanical Properties of 3:1 vs 2:1 15 wt% PU+mHA LbL-PL Scaffolds

6.3.3.4.1 MLO-A5 cells

As shown in Figure 6.17a, all scaffolds showed an increase in cell viabilities between D1 and D6 during the 21 day culture period. MLO-A5 cells cultured on PU scaffolds had the highest viability on D1 and D4. This was significantly higher than the viabilities of both PU+mHA and PU+nHA scaffolds on D1, but only significantly higher than PU+nHA on D4. There was no significance difference between cell viability on PU+mHA and PU+nHA on both D1 and D4.

MLO-A5 cell viability on PU+mHA was the highest amongst the groups between D6 and D21. This was followed by PU+nHA scaffolds, as cell viabilities on PU-only scaffolds

were observed to decrease between D6 and D14 before increasing from D14 to D21. It may be possible that multiple destaining washes carried out after an alamar blue assay may have washed some cells from the PU-only scaffolds and caused this decrease.

(a) (b)
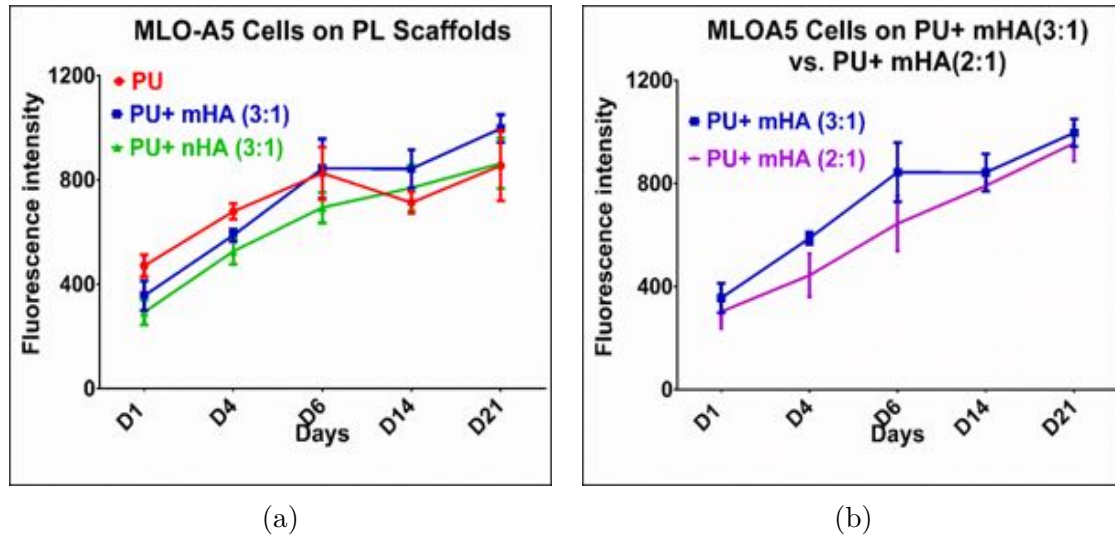
Figure 6.17: Alamar Blue Cell Viability of MLO-A5 cells on LbL-PL Scaffolds A:PU, PU+mHA 3:1 & PU+nHA 3:1 Scaffolds, B:Comparison of 3:1 vs 2:1 PU+mHA Scaffolds

Kindly refer to text in Section 6.3.3.4.1 on page 213 for statistical analysis

Although there was no significance difference between PU and PU+mHA scaffolds on D6, cell viability on PU+nHA scaffolds was significantly lower than on PU scaffolds and PU+mHA. The decrease in cell viability on PU scaffolds on D14 was significantly lower than on PU+mHA, but there was no significant difference between cells on PU+nHA and PU+mHA scaffolds. With cell viabilities increasing on all scaffolds between D14 and D21, PU+mHA supported a significantly higher cell viability than that of PU+nHA and PU-only scaffolds.

Similar to the work of Popescu et al. (2013), LbL-PL nHA composites did not support improved cell viability over PU-only scaffolds. This behaviour of PU+nHA scaffolds was in contrast to what was seen with random electrospun scaffolds but similar to aligned scaffolds. It may be possible that the cells preferred having more room for proliferation as opposed to the bioactive properties of nano-sized HA particles. It may also have been due to the fact that, the nano-sized HA particles were encapsulated in the PU matrix and were not exposed enough to allow the cells to interact with the HA particles.

MLO-A5 cells were seeded on 2:1 PU+mHA composites to examine whether a higher HA content could enhance cell proliferation and increase cell viability. As shown in Figure 6.17b, cell viability on 2:1 PU+mHA increased steadily from D1 to D21. With similar cell viability on D1, MLO-A5 cell viability on 3:1 PU+mHA was significantly higher than that 2:1 PU+mHA on D4 and D6.

Beyond day 6, cell viability increased on 2:1 PU+mHA, but was maintained on the 3:1 scaffolds until D14. Viability however increased on both scaffold types beyond D14, however, there were no significant differences between MLO-A5 cell viability on 3:1 and 2:1 PU+mHA scaffolds on D14 and D21. It may still be possible to improve the bioactive effect of PL scaffolds with a higher concentration ($< 40\%$) of HA particles in composites. This has have been shown by Kavlock et al. (2007); Du et al. (2014); Yang et al. (2015) who developed scaffolds with >40 wt% HA content . However, 2:1 PU+mHA did not show any superior biological properties when compared with 3:1 PU+mHA.

6.3.3.4.2   hES-MP cells
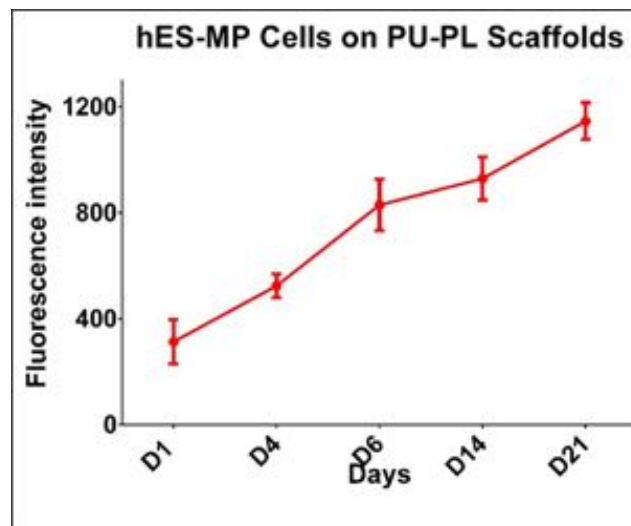
Figure 6.18: Alamar Blue Cell Viability of hES-MP cells on PU LbL-PL Scaffolds
Kindly refer to text in Section 6.3.3.4.2 on page 215 for statistical analysis

Based on the results of various characterization techniques undertaken on the fabricated LbL-PL scaffolds so far, it may be possible to use the scaffolds to not only develop an *in vitro* 3D model but also as a bone substitute. While MLO-A5 cells confirmed

that all scaffolds in LbL-PL group were biocompatible, hES-MP cells were also seeded onto PU scaffolds to assess the suitability of the scaffolds to support human progenitor cells. As shown in Figure 6.18, cell viability increased sharply between D1 and D6, and then gradually from D6 to D21.

6.3.3.5 Sirius Red Staining

LbL-PL scaffolds were stained with Sirius Red dye to examine the scaffold's ability to support extracellular matrix deposition. At the end of both MLO-A5 and hES-MPs alamar blue cell viability study, scaffolds were prepared for sirius red staining as described in Section 3.7.5 on page 103.
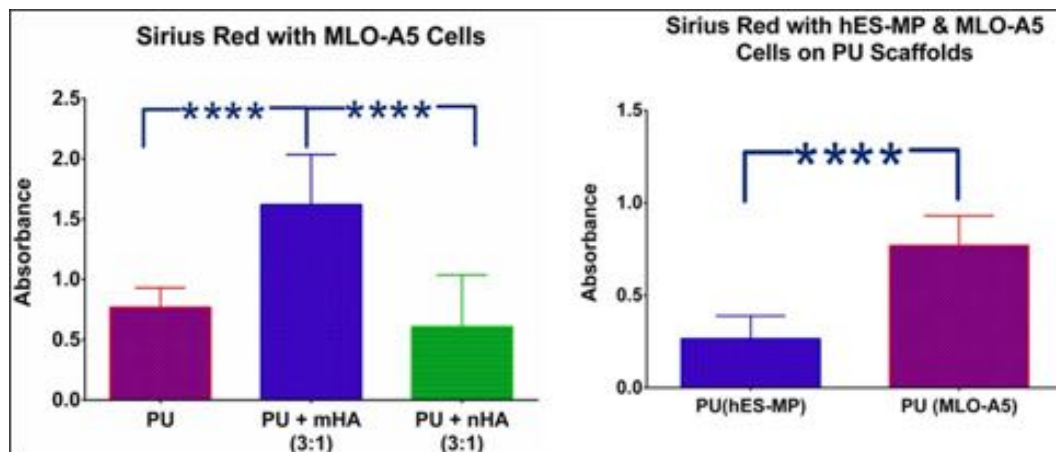
Figure 6.19: Quantitative Analysis of D21 Sirius Red Staining of MLO-A5 & hES-MP cells seeded on LbL-PL Scaffolds

As shown in Figure 6.19, PU+mHA scaffolds supported the most collagen deposition within the LbL-PL group. This was significantly higher than that of PU only scaffolds and PU+nHA scaffolds. It may be possible that the PU+mHA scaffolds had a higher amount of cells on the scaffolds and hence produced a higher amount of collagen, as these scaffolds also recorded the highest alamar blue cell viability on D21. It may be worth normalizing the alamar blue data with the Sirius red data to determine if more matrix was made per cell on a particular material.

Collagen production by MLO-A5 cells was also significantly higher than that of hES-MP cells. However, these cells have several differences between them which could have influenced this result. As shown in Figure 6.20, qualitative Sirius red images of these

(a) hES-MP cells   (b) MLO-A5 cells
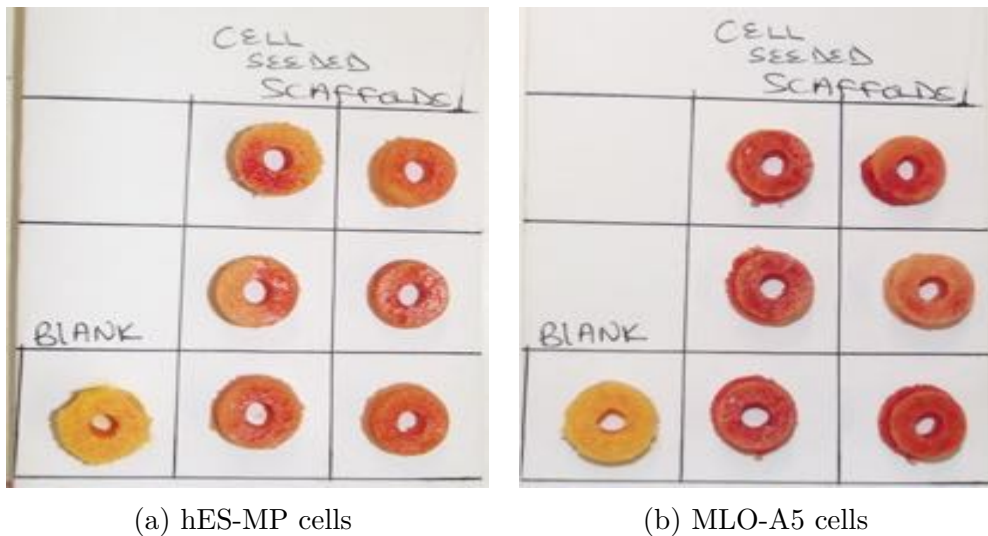
Figure 6.20: D21 Sirius Red Staining of MLO-A5 & hES-MP cells on PU LbL-PL Scaffolds

cell-seeded scaffolds highlights a thicker extracellular matrix deposition on PU scaffolds seeded with MLO-A5 (Figure 6.20b) cells compared to that of hES-MPs (Figure 6.20a). It is likely that this is predominately due to the late osteoblastic stage of MLO-A5 cells compared to the progenitor status of the hES-MPs.

6.3.3.6   *In vivo* Studies

Whilst the scaffold was primarily designed to be used as an *in vitro* 3D model, it may be possible to use it also as a bone substitute. *in vivo* studies were carried out as part of this study to access the suitability of the fabricated scaffolds as a bone substitute. Although *in vitro* analysis was successful at answering many biological questions, there was still the need to understand whether the scaffold could support vascularization and also attain an overall biological evaluation of the scaffolds under physiological conditions in a living organism. *in vivo* studies consisting of subcutaneous and cortical defect implantations were carried out as described in Section 3.7.11 on page 110, by Dr. Maksym Pogorielov's laboratory in Sumy State University, Ukraine. All explanted *in vivo* samples were analysed histologically and imaged in Ukraine.

6.3.3.6.1   Subcutaneous Implantation

After 7 days of implantation, all extracted scaffolds were still white in colour and

6.3. RESULTS AND DISCUSSION THREE

contained a dark-coloured substance within the pores (Figure 6.21). 5 out of the 6 implanted PU-only scaffolds appeared white in colour but were filled with a dark-color substance and covered with a thin connective layer. The tissue around the 5 scaffolds had a regular structure and no inflammation. However, the remaining PU scaffold was completely inflamed and filled with inflammatory exudate. This could have been caused by a wound infection during the postoperative period. This sample was subsequently excluded from the experiment and all data analysis.

(a) PU (b) PU+mHA (c) PU+nHA
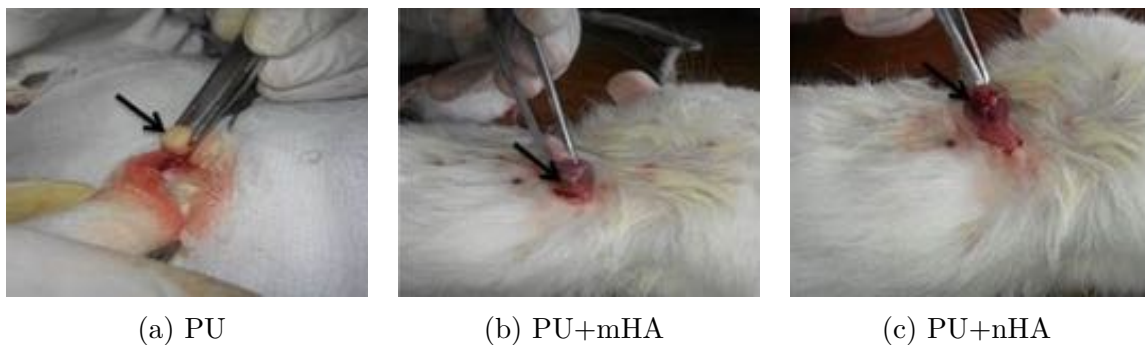
Figure 6.21: Pictures of Extracted LbL-PL scaffolds after 45 days of implantation

All the 6 retrieved PU+mHA scaffolds were covered with a thin connective tissue capsule. There were no undesirable inflammatory response in this group. However, one animal death was recorded on D3 within the PU+nHA group. Although an autopsy did not show any inflammation or other specific changes around the composite scaffold. Moreover, a detailed inspection of the main organs including the heart, brain, liver, kidney, lungs showed normal macroscopic structures. The group in Ukraine were unable to determine the cause of death and excluded this sample from all experimental analysis. The remaining 5 PU+nHA scaffolds included in the experimental analysis were also covered with a thin connective layer. Tissues around these scaffolds had a regular structure and showed no signs of an inflammation.

All animals scarified on D45 for the second time point were healthy and no death was recorded during the implantation period. All PU+mHA and PU+nHA scaffolds, as well as 4 PU scaffolds were located just underneath the skin, covered with a connective capsule and filled with the dark coloured tissue. The remaining (2) PU scaffolds which were white

in colour, were not covered with a connective capsule. A histological examination of these two scaffolds showed no tissue ingrowth.

Histology

12 μm thick sections of explanted samples were prepared and stained with hematoxylin and eosin, and analysed using light microscopy. The outer surface of all the scaffolds were covered with a thin connective tissue capsule by D7. As tabulated in Table 6.4, the thickness of this capsule ranged from 31.9$\pm$0.41 mcm(500 mcm=253.4mm^2) for PU+nHA scaffolds to 34.3$\pm$0.37 for PU-only scaffolds. There were no significant differences between these experimental groups.

Table 6.4: The Thickness (mcm) of the Capsule around LbL-PL Scaffolds

Time-point	PU	PU+mHA	PU+nHA
D7	34.3$\pm$0.37	32.6$\pm$0.16	31.9$\pm$0.41
D45	47.2$\pm$0.32	36.2$\pm$0.35	33.5$\pm$0.27

Empty Pores-(% from slide surface), Blood Vessels and Osteoblasts–(number per 1 mm^2)
a – Significantly different from plane PU
b - Significant difference between PU+mHA

This encapsulation could have resulted from a general inflammatory reaction to the presence of the foreign scaffolds. The capsules were composed of collagen fibres, fibroblast-like cells and inflammatory cells such as lymphocytes and neutrophils (Figure 6.22). The presence of such capsules inhibits further inflammatory and foreign body reactions and prevents additional tissue damage (Yaltirik et al., 2004). A closer inspection of the superficial regions (outermost part of the scaffold) showed an ingrowth of small blood vessels, filled with erythrocytes.

The superficial zone, located directly underneath the connective tissue capsule had a depth of $\sim$1 mm. As tabulated in Table 6.5, PU scaffolds in this zone were filled with inflammatory cells including lymphocytes and neutrophils which may have migrated from damaged vessels and subcutaneous tissues. In addition to these cells, erythrocytes and fibroblastic cells which formed a thin network of collagen fibres and granulation tissue, were also observed in the macro-pores of the scaffolds. The number of fibroblasts found

(a) PU (b) PU+mHA (c) PU+nHA
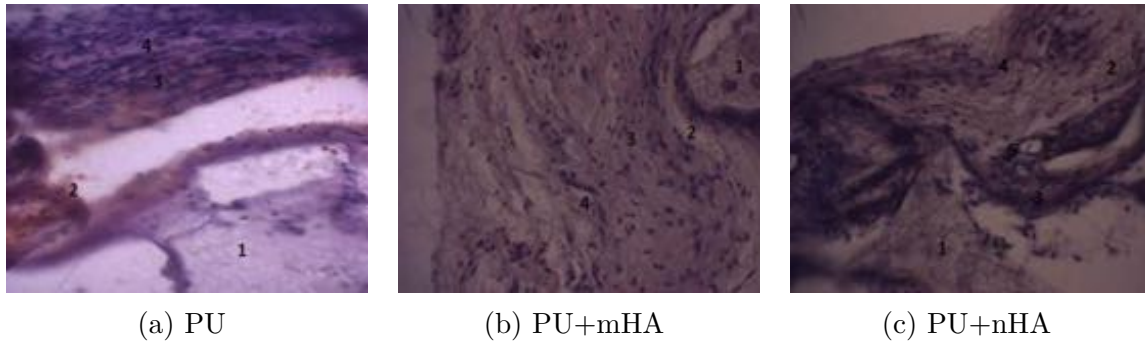
Figure 6.22: Histological Images of the Capsule that Covered the Scaffolds on D7
Magnification at 360x
Keys: 1–Scaffold, 2–Erythrocytes, 3–Lymphocytes, 4–Fibroblasts, 5–Blood Vessel
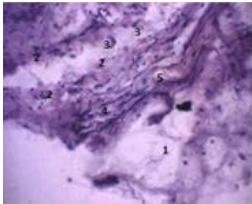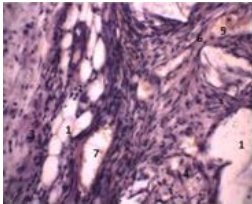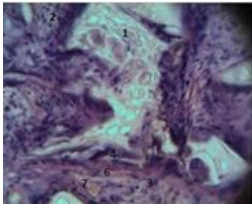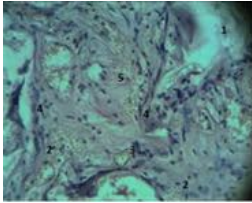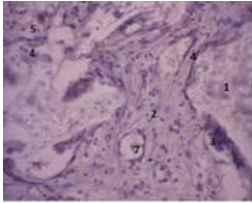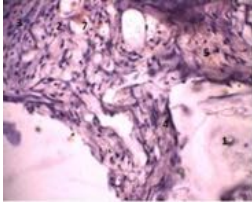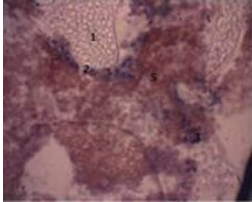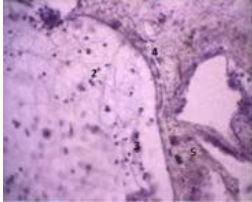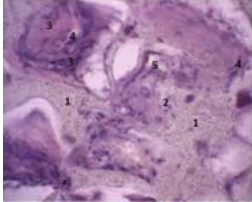
in composites were twice the amount in PU scaffolds. Although there were no major observational differences between micro and nano HA composites at D7, it is possible that the inclusion of these HA particles had a specific effect on the fibroblasts. As the PU scaffolds did not have any granulation tissue in their pores at D7.

It been reported in the literature that hydroxyapatite, especially nano-sized HA can stimulate fibroblast migration and adhesion during subcutaneous implantation (Kasaj et al., 2008; Pendegrass et al., 2012). A few blood vessels with varying diameters were observed in the PU scaffolds. They were however significantly lower than the amount seen in the HA composites. This supported the work of Tommila et al. (2009), who hypothesized that, macrophages recognize HA as foreign material, and hence phagocyte or hydrolyse it to release calcium ions. This is recognized by the calcium-sensing receptors expressed in many cells including hematopoietic progenitors, leading to endothelial cell migration and vessel growth.

The intermediate zone of the scaffolds were filled with neutrophils, lymphocytes and erythrocytes. As tabulated in Table 6.6, erythrocytes were the main cells present in this zone. For PU scaffolds, there was about 70% more erythrocytes in the intermediate zone than in the superficial zone. There were also traces of fibroblasts, which were believed to have migrated from the surrounding tissue. The amount of fibroblasts in HA scaffolds was significantly higher than that of PU scaffolds. However, there were less lymphocytes and neutrophils in the HA composites in this zone than the superficial zone.

Table 6.5: Histological Images of LBL-PL Scaffolds: **D7 Subcutaneous Implantation**

	PU	PU+mHA	PU+nHA
Superficial Zone			
Intermediate Zone			
Deep Zone			

Magnification at 360x
Keys: 1–Scaffold, 2–Lymphocyte, 3–Neutrophil, 4–Fibroblast, 5–Erythrocyte,
Granulation Tissue, 7–Blood Vessel

A closer inspection of the deep zone (the innermost part of the scaffold) showed significant differences between PU and PU:HA scaffolds, however, there were no visible differences between PU+nHA and PU+mHA scaffolds. The main cells present in PU-only scaffolds were erythrocytes, which are believed to have migrated from the damaged subcutaneous vessels. There were also a few lymphocytes and neutrophils present. The pores of PU-HA scaffolds had a significantly lower quantity of erythrocytes, but there were no significant differences in the amount of inflammatory cells between these HA composites.

As shown in Figure 6.23, all the scaffolds extracted on D45 were covered with a thicker capsule compared to D7. PU scaffolds had a capsule thickness of 47.2±0.32 mcm. This was significantly thicker than that of PU+nHA and PU+mHA, at 33.5±0.27 mcm and 36.2±0.35 mcm, respectively. Compared to the previous time point, these capsules contained a lot of blood vessels, especially around the HA based scaffolds. This led to better vascularisation of the capsule around the composites, leading to better oxygen

Table 6.6: **D7** Morphometric Parameters of Subcutaneous Implantation

LbL-PL Scaffold	Cells/Vessel	Zone		
		Superficial	Intermediate	Deep
	Lymphocytes	16.55±1.4	12.52±0.6	4.23±0.6
	Neutrophils	37.18±2.3	28.74±1.9	8.83±0.7
PU	Fibroblasts	17.54±2.9	9.87±1.1	0
	Erythrocytes	28.92±3.5	49.19±3.6	87.69±5.2
	Granulation Tissue	0	0	
	Blood Vessel	3.65±0.5	0	0
	Lymphocytes	28.1±3.1^a	16.27±0.9	9.25±1.7^a
	Neutrophils	15.4±0.9^a	23.04±1.1^a	19.59±2.4^a
PU+mHA	Fibroblasts	35.3±2.7^a	32.92±3.5^a	7.82±0.8
	Erythrocytes	21.3±1.4	28.11±1.8^a	64.91±3.4^a
	Granulation Tissue	12.6±1.5	0	0
	Blood Vessel	8.3±0.6^a	5.4±0.3	0
	Lymphocytes	27.4±1.8^a	15.52±1.3^a	11.36±0.8^a
	Neutrophils	12.4±1.6^a	21.48±2.8^a	22.50±1.6^a
PU+nHA	Fibroblasts	37.9±3.6^a	33.17±2.6^a	7.29±0.4
	Erythrocytes	22.5±1.3	29.95±1.1^a	58.49±5.3^a
	Granulation Tissue	11.8±0.6	0	0
	Blood Vessel	11.2±1.2^{a,b}	7.8±0.6^a	0

a – Significantly different from PU-only
b - Significant difference between PU+mHA

perfusion and a reduced capsule thickness. As a deficit in oxygen supply has been reported to lead to an overproduction of connective tissue (Parirokh et al., 2011).

(a) PU   (b) PU+mHA   (c) PU+nHA
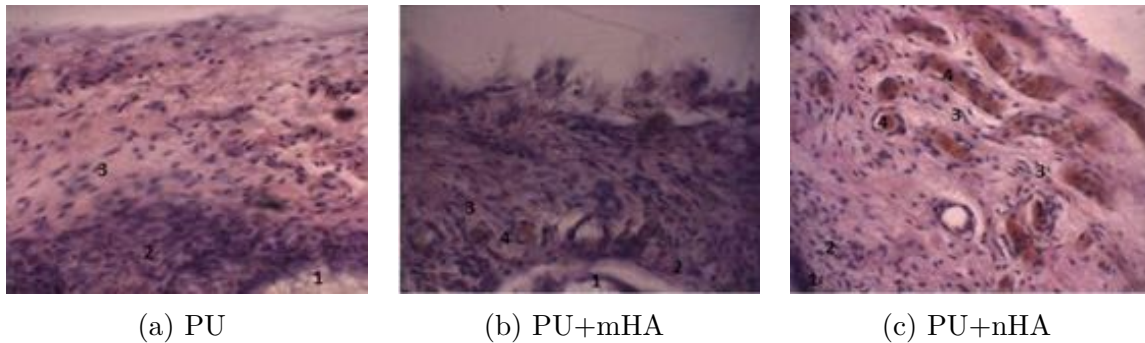
Figure 6.23: Histological Images of the Capsule that Covered Scaffolds on D45
Magnification at 360x
Keys: 1–Scaffold, 2–Lymphocytes, 3–Fibroblasts, 3–Blood Vessel

Similar to D7, histological analysis of the graft showed visible differences between PU and PU-HA scaffolds. At a lower magnification of 120x (Table 6.7), all the pores in the PU-HA scaffolds appeared to be filled with fibrous connective tissue compared to PU-only scaffolds, which were only partially filled. Fibroblast adhesion and proliferation observed in the D7 explanted samples led to a satisfactory development of fibrous connective tissue inside the scaffolds by D45. There were more PU+nHA pores filled with this connective tissue as compared to PU+mHA. This caused the percentage of empty pores in PU+nHA to be significant lower than its PU+mHA counterparts, indicating that nano-sized HA particles stimulated more fibroblastic activity and tissue ingrowth than mHA particles.

The level of vascularization in new fibrous tissue was also better in PU-HA composites than PU scaffolds. This could have been due to the earlier vessel ingrowth at the D7 time point. At a higher magnification of 360x, the fibrous connective tissue inside the PU pores was composed of chaotically arranged collagen fibres. However, the collagen fibres around the circumference of PU-HA pores were tightly packed but chaotically arranged in central zones of the pores.

6.3.3.6.2 Cortical Defect

Similar to the subcutaneous implantation studies, animals were sacrificed on D7 for the first time point. All scaffolds were still inside the bone defect but dark in colour. There

6.3. RESULTS AND DISCUSSION THREE

Table 6.7: Histological Images of LBL-PL Scaffolds: **D45 Subcutaneous Implantation**

	PU	PU+mHA	PU+nHA
x120			
x360			

Keys:1–Scaffold, 2–Empty Pore, 3–Blood Vessel, 4–Connective Tissue
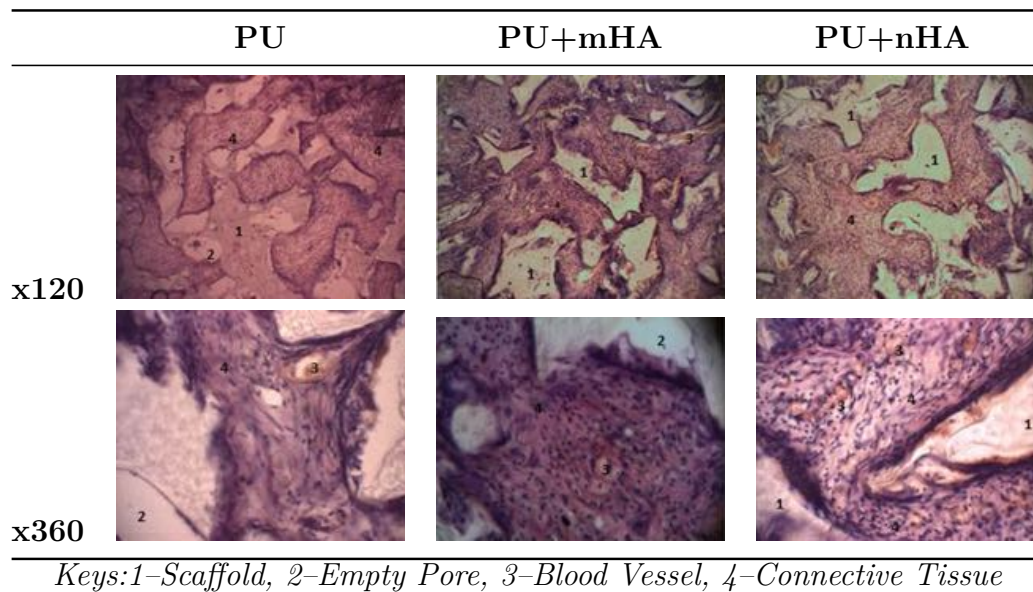
Table 6.8: **D45** Morphometric Parameters of Subcutaneous Implantation

	PU	PU+mHA	PU+nHA
% of Empty Pores per Slide	15.9±0.4	5.3±0.7^a	2.5±0.2^{a,b}
% of Fibrous Connective Tissue per Sample	32.2±1.4	44.8±2.1^a	52.4±1.2^{a,b}
Number of Blood Vessels per 1 mm^2	7.6±0.3	12.4±0.6^a	17.3±0.5^{a,b}

a – Significantly different from plane PU
b - Significant difference between PU+mHA

was no periosteal reaction between the surrounding bone and the scaffolds, however, a minor elevation was observed at the edge of the defect. In addition, there were no macroscopic differences between PU, PU+mHA and PU+nHA scaffolds. A bone-like tissue formation was however observed on the surface of extracted scaffolds at the second time-point, which was 45 days after implantation. Again, there were no macroscopic differences between the scaffolds and no fibrous capsule around the scaffolds.

Histology

12-15 μm thick sections of the extracted scaffolds were prepared for histology using H & E staining. All the scaffolds were filled with cells and fibrous tissue (Figure 6.24) after a 7 day implantation period. PU-nHA scaffolds had the highest percentage of pores filled with new fibrous tissue. As shown in Table 6.9, their percentage of empty pores was

significantly lower than that of PU+mHA scaffolds, and PU-only scaffolds which showed some empty pores. These empty PU regions were mostly located in the deeper regions of the scaffold that had minimum or no contact with blood vessels and bone marrow.

Table 6.9: **D7** Morphometric Parameters of Cortical Defect

	PU	PU+mHA	PU+nHA
Empty Pores	17.2±1.1	8.6±0.5^a	4.1±0.7^{a,b}
Blood Vessel	5.6±0.6	6.3±1.2	6.1±0.5
Osteoblast Density	8.4±0.8	15.3±0.5^a	21.7±0.7^{a,b}

Empty Pores-(% from slide surface), Blood Vessels and Osteoblasts–(number per 1 mm^2)
a – Significantly different from plane PU
b - Significant difference between PU+mHA

A number of blood vessels, ranging from 5.6±0.4 to 6.3±1.0 per 1 mm^2 were also observed in all scaffolds on D7. Fibroblasts and osteoblasts which are believed to have migrated from the cambial layer of the periosteum and bone marrow were also seen. The amount of osteoblasts varied amongst the scaffolds. PU scaffolds had the lowest density of osteoblasts in the group, however, PU-nHA has more osteoblast per 1 mm^2 compared to PU-mHA composites. A few leukocytes and bone marrow cells were also observed in the pores. Interestingly, bone tissue ingrowth in PU+mHA scaffolds was observed as early as D7. This was observed in the pores near the hosting bone as shown in Figure 6.24. The new bone tissue had less cells compared to the fibrous tissue, and differential staining confirmed it as an early stage mineralisation similar to an osteoid. It may be possible that the a good blood supply around the nano-HA particles stimulated more osteoblastic activity and accelerated early bone formation in the nHA composites.

However, by the second time point, all the pores in both PU+mHA and PU+nHA scaffolds had become filled with bone tissue, rich in osteoblasts. The orientation of collagen fibres in this tissue was quite irregular, a typical observation in immature bone. It is expected that subsequent bone remodelling from mechanical loading could alter this irregularity. Although more porous regions in the PU scaffolds were filled with fibrous tissue by D45, its percentage of empty pores was significantly higher than the HA composites.

6.3. RESULTS AND DISCUSSION THREE

|(a) PU|(b) PU+mHA|(c) PU+nHA|
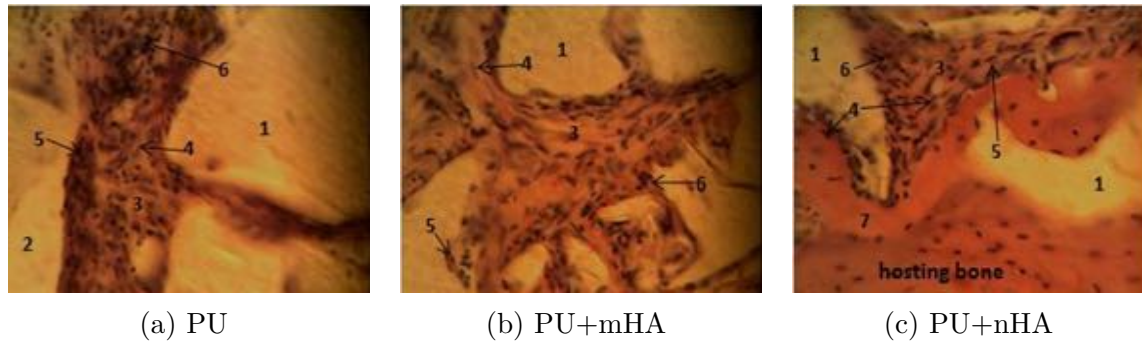
Figure 6.24: Histological Images of LBL-PL Scaffolds: **D7 Cortical Defect**
Magnification at 360x, Keys: 1-Scaffold, 2-Empty pore, 3-Fibrous tissue,4-Osteoblast, 5-Fibroblast, 6-Bone marrow Cells, 7-Osteoid

|(a) PU|(b) PU+mHA|(c) PU+nHA|
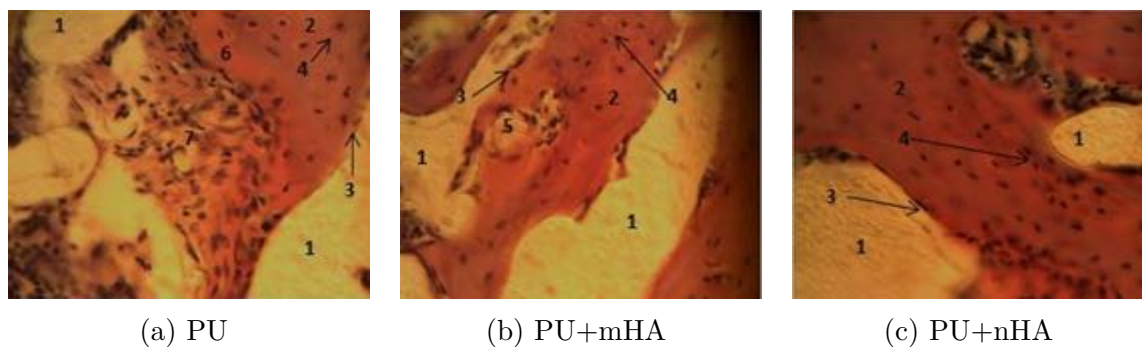
Figure 6.25: Histological Images of LBL-PL Scaffolds: **D45 Cortical Defect**
Magnification at 360x, Keys: 1-Scaffold, 2-Bone tissue, 3-Osteoblast, 4-Osteocyte, 5-Bone marrow, 6-Osteoid, 7-Fibrous tissue

The outer surface of the new bone trabeculae was observed to be lined with osteoblasts, while osteocytes were contained in the central portions around the bone tissue. As shown in Figure 6.25, the structure of new bone in both PU+mHA and PU+nHA scaffolds were very similar. Although bone formation started as early as D7 in PU+nHA, there were no major differences in the quality of new bone formed in both scaffolds by D45. It may be possible that bone formation in PU+nHA scaffolds finished earlier than PU+mHA, but it was not possible to confirm it as this time-point.

Most peripheral regions of the PU scaffolds were also filled with new bone tissue. This new tissue was similar in structure to those found in the HA composites. However, the central zones of some of the PU pores were not completely filled with bone tissue. These pores contained a combination of fibrous and bone tissue, and some showed a thin mineralization zone between the fibrous tissue and the osteoid.

The cortical defect *in vivo* study concluded that, both PU and PU-HA scaffolds have osteoconductive properties and fill with connective tissue and osteoblast-like cells after D7. However, compared to the PU-only and PU-mHA grafts, only PU+nHA scaffolds were able to stimulate bone ingrowth by D7 . Nonetheless, new bone tissue was seen in all the pores of PU+mHA and PU+nHA by D45, although PU scaffolds still had remnants of fibrous tissue.

Table 6.10: **D45** Morphometric Parameters of Cortical Defect

	PU	PU+mHA	PU+nHA
Empty Pores	12.4±0.8	5.9±0.4[a]	4.4±0.6[a]
Pores with fibrous tissue	10.6±1.3	-	-

Empty Pores-(% from slide surface)
a – Significantly different from plane PU

6.3.4 Homogenized Scaffolds

While LbL-PL scaffolds especially PU+nHA composites demonstrated an excellent bone formation capability *in vivo*, their mechanical properties of after fabrication were lower than the mechanical properties of bone (discussed in Section 2.2.5 on page 19). Although an incorporation of both micro and nano-sized HA particles reinforced the mechanical properties of the composites as opposed to PU-only scaffolds. The Young's Modulus and yield strength of 0.65 and 0.35 MPa were tens/hundreds in magnitude lower than that of cancellous/cortical bone tissue in humans (An and Draughn, 2000) .

The mechanical properties of PU-HA composites is however known to be dependent on the scaffolds ability to from a strong interfacial bond strength between the ceramic HA phase and the polymeric PU matrix (Attawia et al., 1995; Boccaccini and Maquet, 2003; Bonzani et al., 2007). It was therefore hypothesized that introducing HA particles into PU solutions at very high speeds with a homogenizer could create composite solutions with a stronger PU-HA physical bond and better mechanical properties. The aim was to identify the scaffold with the best mechanical properties to that of human bone, and optimise its properties in line with the overall aim of developing an *in vitro* 3D bone

6.3. RESULTS AND DISCUSSION THREE

model for implant testing.

In addition to the two main composite scaffold groups that were created with the LbL-PL scaffolds, namely 3:1 PU+mHA and 3:1 PU+nHA scaffolds, a third composite group that combines both micro and nano-HA particles was also created with these homogenized solutions. These combined mHA-nHA composites denoted PU+cHA, were created in a ratio of 3:0.5:0.5 PU:mHA:nHA to investigate whether combining different sizes of HA particles presented with any special features. All homogenized scaffolds were later fabricated into PL scaffolds using the LbL technique.

6.3.4.1   SEM of Homogenized Scaffolds

As shown in Figure 6.26, PU+mHA scaffolds fabricated from homogenized solutions had the largest pore sizes in the group. With an average pore size of 200 μm, its pores were generally larger than those of PU+nHA scaffolds at 138 μm and PU+cHA at 141 μm. A closer inspection of the surface SEM of PU+nHA and PU+cHA scaffolds showed larger pores to contain several smaller pores. This was not observed in PU+mHA scaffolds and could have occurred from an interactions between the nHA and NaCL particles.

6.3.4.2   Mechanical Properties

Similar to mechanical properties of the non-homogenized LbL composites, H-PU+nHA, had the highest mechanical properties within the homogenized scaffold group. However, its Young's Modulus and yield strength was not significantly different that of H-PU+nHA. It was expected that combining nano and micro HA particles would improve the mechanical properties of the H-PU+cHA scaffolds by capitalizing on the particles close packed structures. However, as shown in Figures 6.27a & 6.27b, the mechanical properties of these H-PU+cHA scaffolds were significantly lower than those of H-PU+mHA and H-PU+nHA. It may be possible that this was caused by a mechanical mismatch between the mineral/polymer phase of the scaffold.

The mechanical properties of the scaffolds in the homogenized group were very similar to those in the traditional non-homogenized LbL-PL
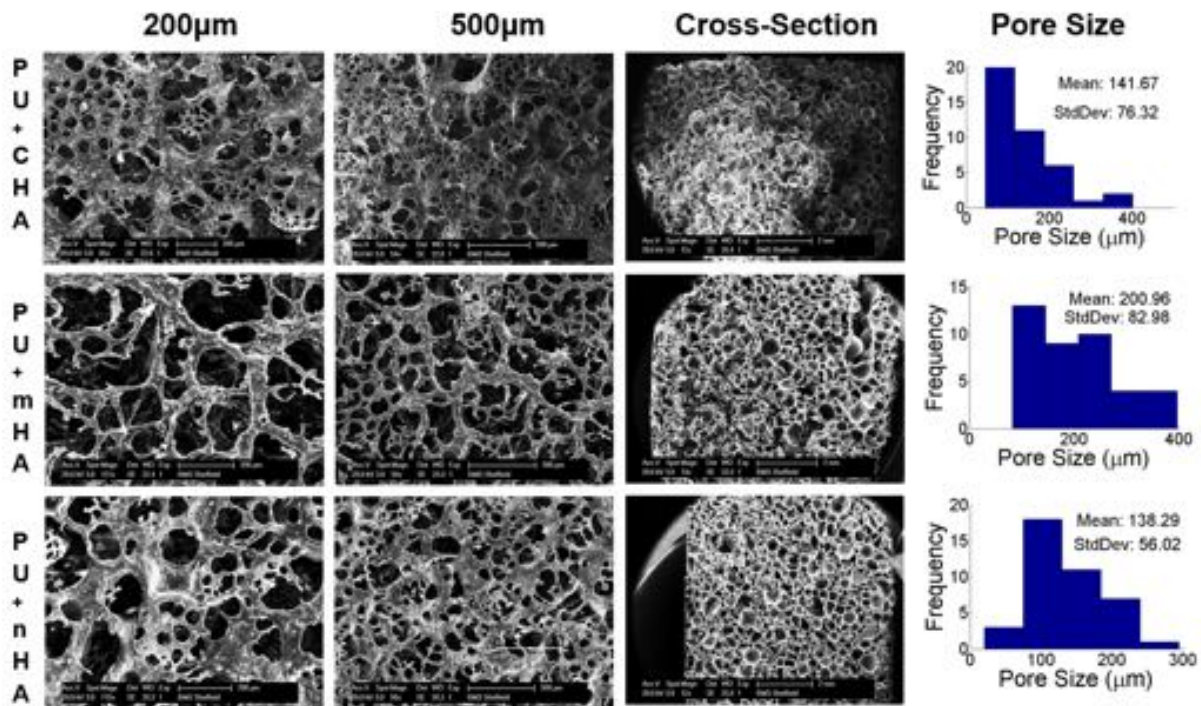
Figure 6.26: SEM images of 15 wt% Z3A1 Homogenized PL Scaffolds
Scale Bar of SEM images=200 µm, 500 µm & Cross-section=2 mm
Histogram distributions of pore sizes (n=40)

group (Figures 6.28a & 6.28b).   Interestingly, the Young's Modulus and yield strength of both H-PU+mHA (0.50 & 0.017 MPa) and H-PU+nHA (0.62 & 0.023 MPa) were lower than their non-homogenized LbL-PU+mHA (0.63 & 0.031 MPa) and LbL-PU+nHA (0.67 & 0.040 MPa) counterparts.   The hypothesis of improving the mechanical properties of LbL-PL scaffolds by introducing HA particles at very high speeds with a homogenizer was therefore rejected. Although these scaffolds were seeded with cells for biological characterization (data shown with PM-PL alamar blue studies), they were no longer pursued in the quest to develop an *in vitro* 3D bone model.

6.3.5   Physically Mixed Scaffolds

The LbL-PL technique required an average of 50 mins to cast one glass disk of scaffold. Although this is an effective fabrication method for making thicker and highly porous 3D scaffolds, the length of time it took to reproduce a large number of glass disks was too long for high throughput manufacturing.

A more efficient mass production method for creating reproducible PL scaffolds in a

6.3. RESULTS AND DISCUSSION THREE
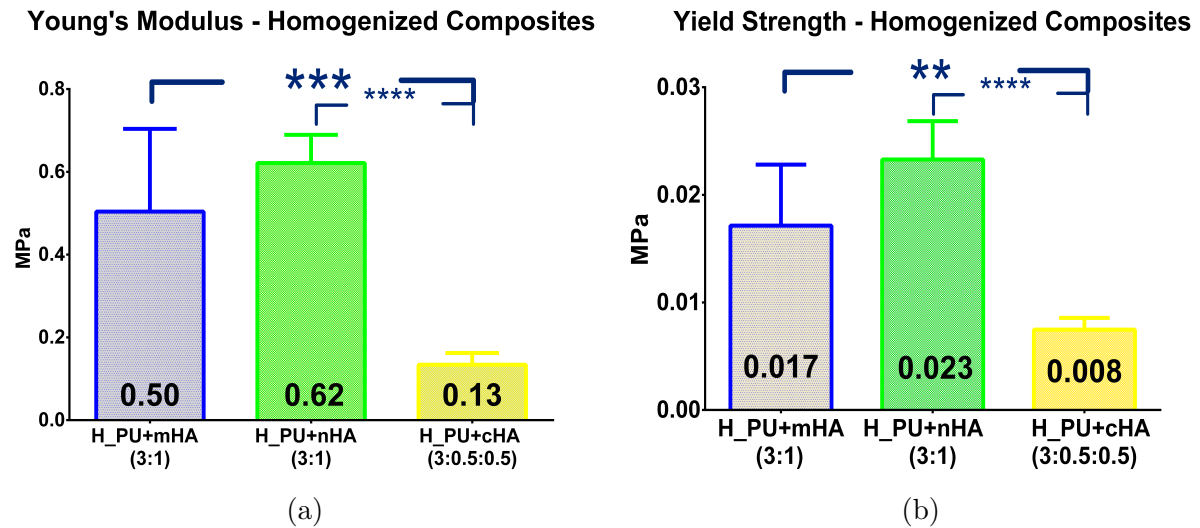
Figure 6.27: Mechanical Properties of Homogenized PL Scaffolds A: Young's Modulus of Homogenized Scaffolds B: Yield Strength of Homogenized Scaffolds

shorter period of time was therefore needed. A novel physical mixing (PM-PL) protocol was therefore developed to address this limitation. The modified technique required as little as 5 mins to efficiently create a PM-PL scaffold, which was a tenth of the time it took to create a LbL-PL scaffold.

The aim of developing these scaffolds was to decrease the fabrication time and maintain or improve the physical, mechanical and biological properties of the LbL-PL scaffolds.

6.3.5.1 SEM of PM-PL Scaffolds

As shown in Figure 6.29a, physically mixed PU scaffolds had the largest pore sizes within the PM-PL group, similar to that observed in the LbL-PL group. With an average pore size of 212 μm, these scaffolds showed a good pore interconnection within the entire scaffold and along the scaffolds cross-section.

PM-PU+mHA scaffolds followed with an average pore size of 171 μm. This was slightly lower than the average pore size of 187 μm for LbL-PU+mHA and the 200 μm of H-PU+mHA scaffolds. A physical examination of these scaffolds prior to SEM also revealed a thick non-porous section at the top of the mould (that is the bottom of the scaffolds). It may be possible that this was caused by insufficient NaCl particles, or that

(a)   (b)
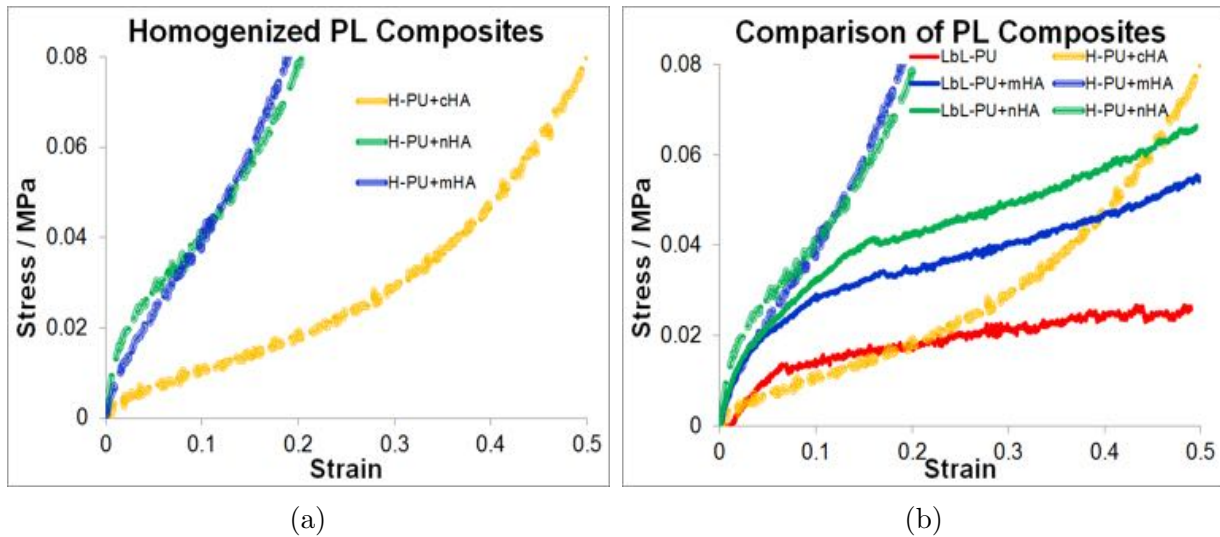
Figure 6.28: Mechanical Properties of Homogenized PL Scaffolds A: Example stress/strain curves of Homogenized PL Scaffolds, B: Comparing Example Stress/Strain Curves of Homogenized and Non-Homogenized LbL-PL Scaffolds

the NaCl particles sank to the bottom of the glass mould, leaving the top of the mould non-porous. These non-porous regions were cut from the scaffolds before mechanical characterization to allow a suitable comparison with the other PL composites.

PM-PU+nHA scaffolds contained the fewest pores and the smallest pore sizes. With an average pore size of 98 μm, PM-PU+nHA had the lowest average pore size within the entire foam scaffold group. However, combined HA composites containing both micro and nano-HA particles had an average pore size of 197 μm. This was interestingly larger than the average pore size of both PM-PU+mHA and PM-PU+nHA composites. It was also larger than the 141 μm average pore size of H-PU+cHA scaffolds.

6.3.5.2 Mechanical Properties

The mechanical properties of fabricated PM-PL scaffolds were assessed using the same compression testing parameters used for LbL-PL and H-PL scaffolds. As shown in Figure 6.30a, the PM-PL scaffolds had a very interesting mechanical profile that contrasted with previous fabricated scaffolds. PM-PU had the highest mechanical properties in the PM group. Moreover, the inclusion of neither nano, micro nor combined micro and nano-HA particles improved the mechanical properties of the PM-PU scaffolds.

231

(a) PM-PU Scaffolds

(b) PM-Composite Scaffolds
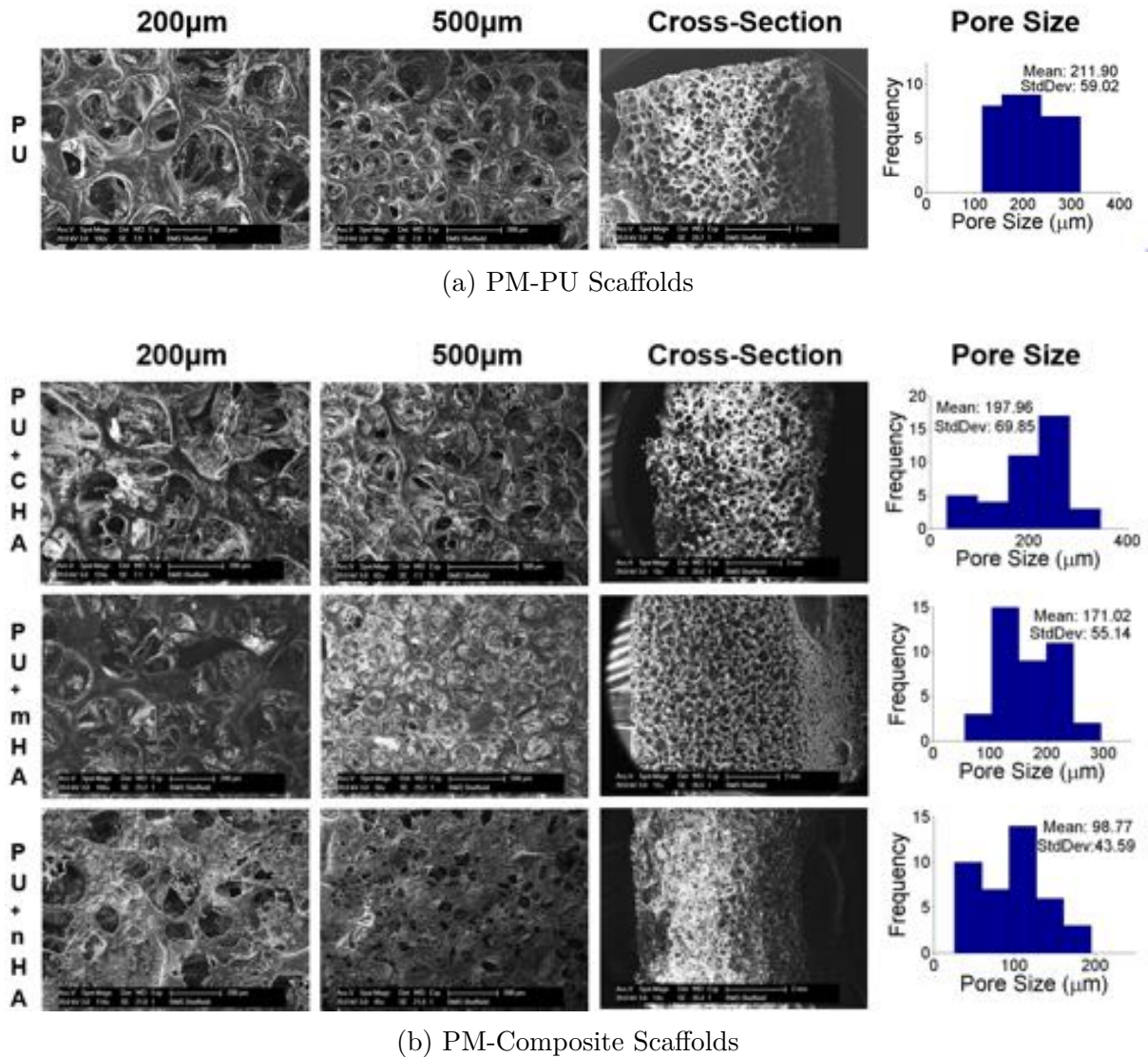
Figure 6.29: SEM images of 15 wt% Z3A1 Physically Mixed Scaffolds
Scale Bar of SEM images=200 μm, 500 μm & Cross-section=2 mm
Histogram distributions of pore sizes (n=40)

It was the first and only fabrication technique to display this contrasting pattern.

As shown in Figure 6.30b, the mechanical properties of these PM-PL scaffolds were compared to those in the LbL-PL group discussed in Section 6.3.3.3 on page 211. The Young's modulus and yield strength of PM-PU which were 0.54 & 0.041 MPa, respectively, was surprisingly similar to those of LbL-PU+nHA scaffolds at 0.67 & 0.040 MPa. They were however, much stronger than their LbL-PU counterparts which recorded only 0.32 & 0.015 MPa, for Young's modulus and yield strength, respectively.

PM-PU+nHA scaffolds had the highest Young's Modulus within the composite group,

(a)   (b)
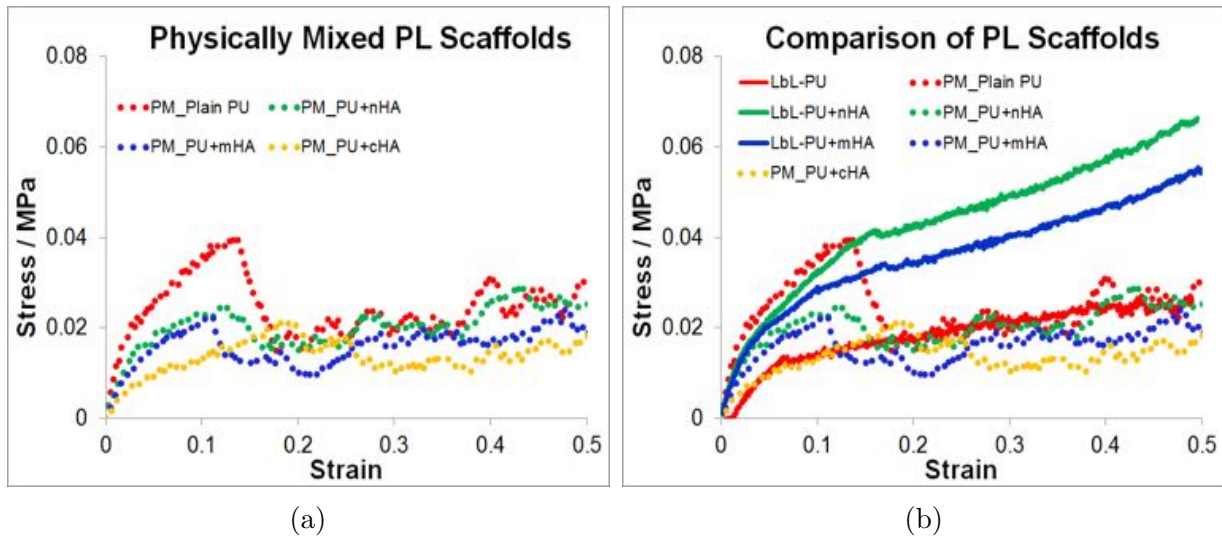
Figure 6.30:   Mechanical Properties of Physically Mixed Scaffolds, A: Example stress/strain curves of PM-PL Scaffolds, B: Example stress/strain curves comparing PM and LbL-PL Scaffolds

but their yield strength was the same as that of the PU+cHA. Although no significant differences were recorded amongst the yield strength of PM-PL scaffolds, only physically mixed PU+mHA and PU+cHA had no significant difference in their Young's modulus, as shown in Figure 6.31a, the Young's modulus of all other PM-PL scaffolds showed significant differences.

While using the physically mixed technique to create PL scaffolds shortened fabrication time by about 90%, the mechanical properties of its PU scaffolds did not improve after reinforcement with HA particles. It is possible that this resulted from the fast rates at which NaCl particles were combined with the composite solutions. This probably made it easier for the HA particles to leach out from the scaffolds during the salt leaching process.

As shown in Figure 6.32a, SEM images of PM-PU+mHA and PM-PU+nHA prior to autoclaving showed several unbounded HA particles that easily cleaved off from the scaffolds when agitated. Once autoclaved, these scaffolds had less visible HA particles on the scaffold and left a cloudy gelatin solution shown in Figure 6.32c. It is possible that the originally transparent and clear gelatin solution became cloudy during the autoclaving process, due to the agitation of liquid particles at the elevated temperature. This could
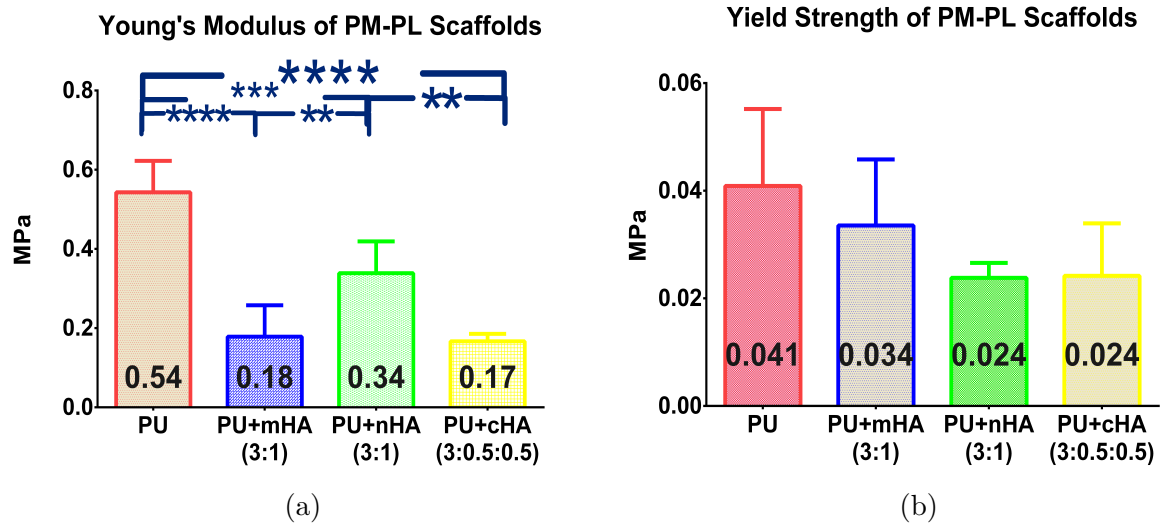
Figure 6.31: Mechanical Properties of Physically Mixed Scaffolds, A: Young's Modulus of PM-PL Scaffolds, B: Yield Strength of PM-PL Scaffolds

(a) PM-PU+mHA at 20 μm   (b) PM-PU+mHA at 100 μm   (c)
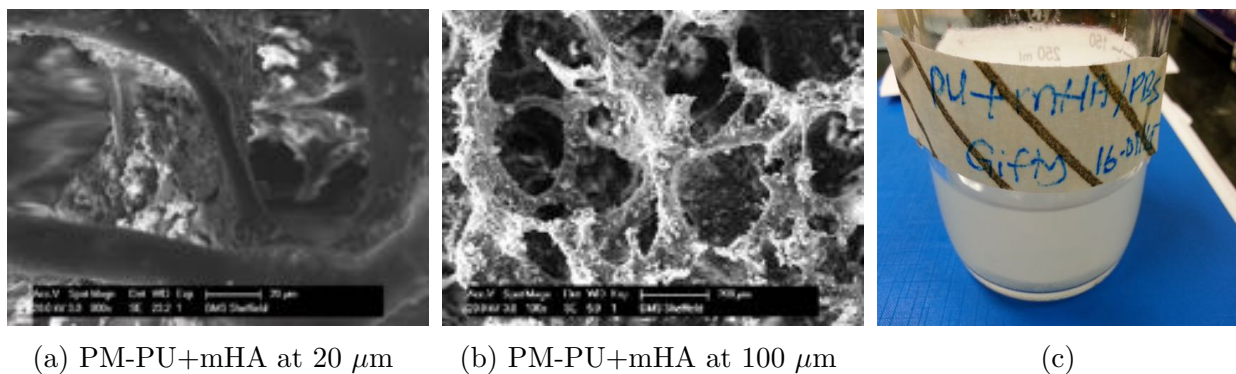
Figure 6.32: Unbounded HA particles easily cleaves from Composite Scaffolds A & B:SEM Images of PM Scaffolds Before Autoclaving, C:Autoclaved Gelatin Solution contaminated with HA particles

have caused the unbounded HA particles to cleave from the scaffold and remain in the gelatin solution, leading to the reduced mechanical properties of the composites.

Based on the fact that PM-PU scaffolds were from the same PU solution used in fabricating LbL-PU scaffolds, but had impressively higher mechanical properties than the LbL-PU scaffolds (Figure 6.33), its may be possible to further optimise the PM-PL technique to improve the mechanical properties of PM-composites, as long as the HA particles can be trapped in the polymeric matrix.
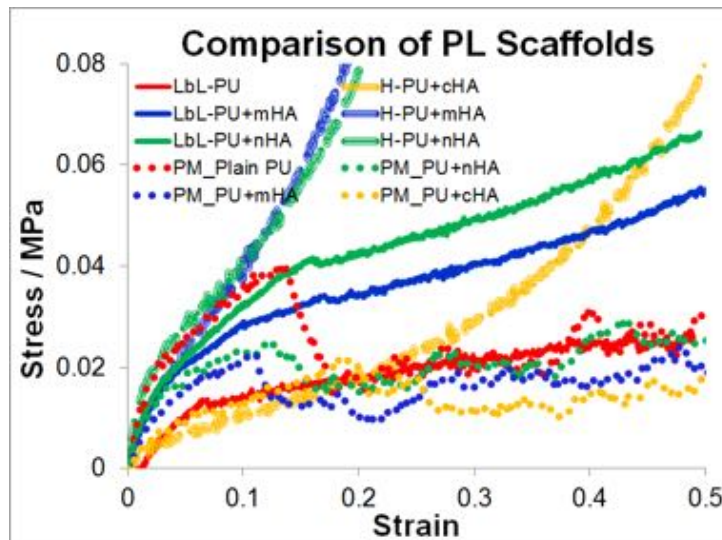
Figure 6.33: Example stress/strain curves of all PL Scaffolds Fabricated in this Project

6.3.5.3   Alamar Blue Cell Viability

As part of attempts to develop an *in vitro* 3D bone model for implant testing, alamar blue cell viability was carried out for a 56 day period to access the models ability to withstand long term cell-culture under static conditions. As shown in Figure 6.34a, MLO-A5 cells on all scaffolds grew rapidly from D1 to D7, with D7 recording the highest cell viability throughout the entire 56-day period.

Similar to the mechanical analysis of PM-PL scaffolds, PU-only scaffolds had the highest cell viability for all time-points. This was significantly higher than the viability of composite scaffolds with micro, nano and combined HA particles. Among the composite scaffolds, PU-mHA scaffolds had the highest viability for all time points. Cell viability on these scaffolds decreased dramatically between D7 and D14, recording its lowest reading on D14. This reduction in alamar blue was also observed on the other scaffolds, although the effect was more pronounced in composite scaffolds. It may be possible that this was caused from an extensive reduction of alamar blue by metabolically active cells leading to a final non-fluorescent product, and hence an underestimation of cellular activity (O'Brien et al., 2000b).

Resasurin fluoresence however increased gradually after D14 in all scaffolds until D28. Once again, the viability of cells after D28 reduced slightly in plain PU scaffolds but

6.3. RESULTS AND DISCUSSION THREE

(a) All PM-PL Scaffolds

(b) PM-PL and H-PL PU Scaffolds
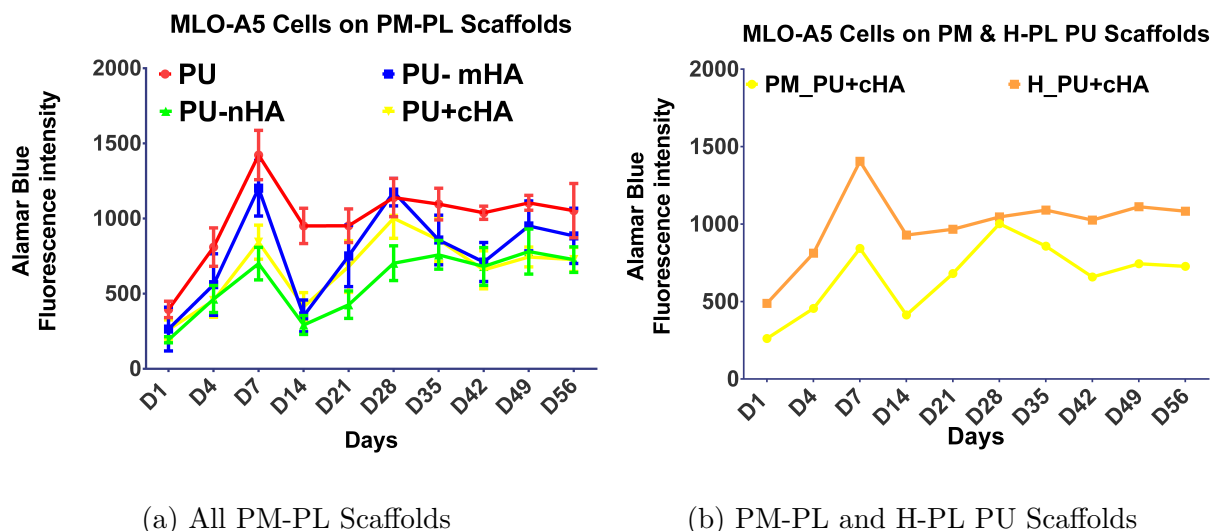
Figure 6.34: Alamar Blue Cell Viability of MLO-A5 Cells on PL Scaffolds

sharply in mHA and cHA composites. Viability however increased gradually after D42 until the end of the study. Plain PU scaffolds had the highest cell viability on D56. This was followed by PU+mHA, PU+cHA and PU+nHA. It may be possible to attribute this interesting variation in cell viability observed in physically mixed scaffolds to the differences in pore sizes observed in the scaffolds via SEM. As plain PU had the largest average pore size of 212 μm. This was followed by PU+mHA and PU+nHA at 171 and 98 μm, respectively.

Although homogenized scaffolds were not intended to be used for biological characterisation, a comparison of the alamar blue cell viability assay of MLO-A5 cells on H-PU+cHA and PM-PU+cHA scaffolds showed a similar pattern. As shown in Figure 6.34b, the viability of MLO-A5 cells on both scaffolds increased between D1 and D7 before reducing on D14. Although both scaffolds were made from solutions with the same composition, homogenized scaffolds showed very little variation the viability of MLO-A5 cells compared to their physically mixed counterparts. This could have been due to an alteration in the amount of HA particles that remained in the scaffolds after autoclaving, as PM-PL scaffolds seemed to have cleaved off easily after autoclaving.

6.3.5.4 DAPI & Phalloidin Staining

In addition to alamar blue cell viability data, DAPI (nucleus) and Phalloidin (actin cytoskeleton) staining over a 14 day period was also used to compare the cellular behaviour of MLO-A5 cells, including cell orientation, proliferation, and extracellular matrix (ECM) production on the fabricated PM scaffolds. Cell behaviour has been reported to be directly influenced by scaffold architecture since ECM production provide cues that influence specific integrin–ligand interactions between cells and the surrounding (Murphy et al., 2010).

Table 6.11 on page 247 shows a compilation of representative micrographs of nuclei and cytoskeleton visualisations over the 14 day period. These representative images were generated by merging images from the DAPI(blue) and Phalloidin-TRITC(red) channels. Images taken on D1 showed a few cells on plain PU and composite scaffolds as well as an auto-fluorescence HA background in the PU+cHA scaffold. Images from D4 staining, was similar to D1, an enhanced spindle-shaped morphology of the attached cells.

There was however a remarkable difference in cell proliferation between the images taken on D4 and D7. MLO-A5 cells were well spread and interconnected around the macro and micro-pores of plain-PU scaffolds. PU+mHA scaffolds showed the highest confluency of cells within the PM-PL group on D7, whilst PU+cHA scaffolds showed the least cells for the fields of view imaged. Cells on PU+nHA scaffolds had an elongated morphology, and their nuclei also appeared to be stretched.

By D14, the cells on all scaffolds appeared to be overly confluent and less spread out especially on the PU+mHA scaffold, and interestingly on the PU+cHA scaffold. PU and PU+nHA scaffolds also had improved cell and ECM coverage, and showed the location and position of MLO-A5 cells around the large pores. These highly porous and interconnected scaffolds facilitated cell migration within their porous structure and enabled cell growth whilst minimizing overcrowding. This observation of MLO-A5 cells on PU-only and PU-HA composite PL scaffolds is in line with published studies of PL PU-only (Loh and Choong, 2013; Rottmar et al., 2016) and electrospun PU-HA (Tetteh et al., 2014) scaffolds showing good cyto-compatibility.

6.3. RESULTS AND DISCUSSION THREE

6.3.5.5 Sirius Red & Alizarin Red
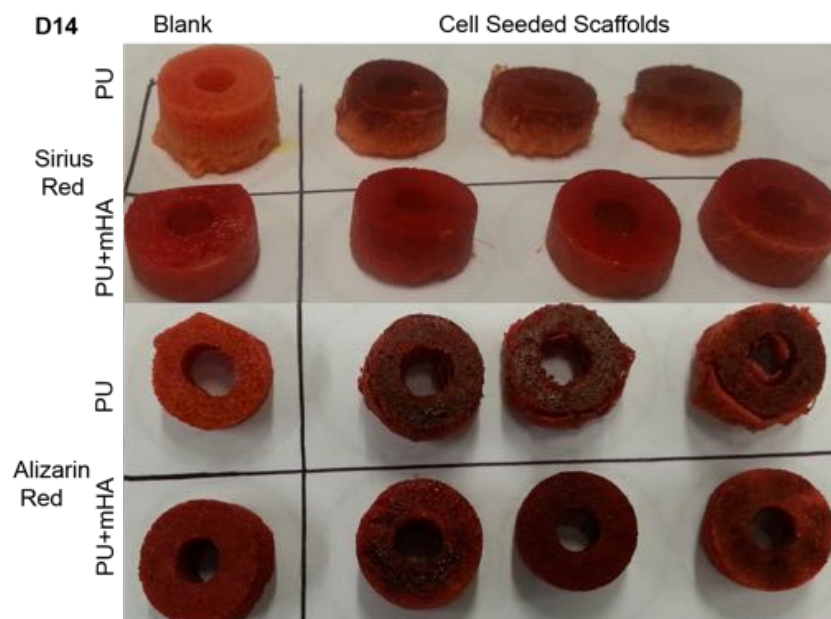
Figure 6.35: **D14** Images of Sirius Red and Alizarin Red staining of MLO-A5 Cells on PM-PL Scaffolds

Sirius red and Alizarin red staining discussed extensively in the previous chapters were also used on PM-PL foams to examine their ability to support extracellular matrix production and calcified matrix deposition. PU and PU+mHA scaffolds seeded with MLO-A5 cells were stained on D14, 28, 42 and 56.

As shown in the qualitative images in Figures 6.35-6.38, collagenous matrix deposition increased over the 56 day period in both scaffold types, however, this increasing effect was more pronounce in PU-only scaffolds as compared to their PU+mHA counterparts. A similar pattern was also observed with Alizarin red staining although the effect of the HA in the blank scaffolds was rather pronounced. Figure 6.39 on page 241, highlights the effect of HA contained in blank negative control samples on the total amount of mineral expressed by the cells on the seeded scaffolds.
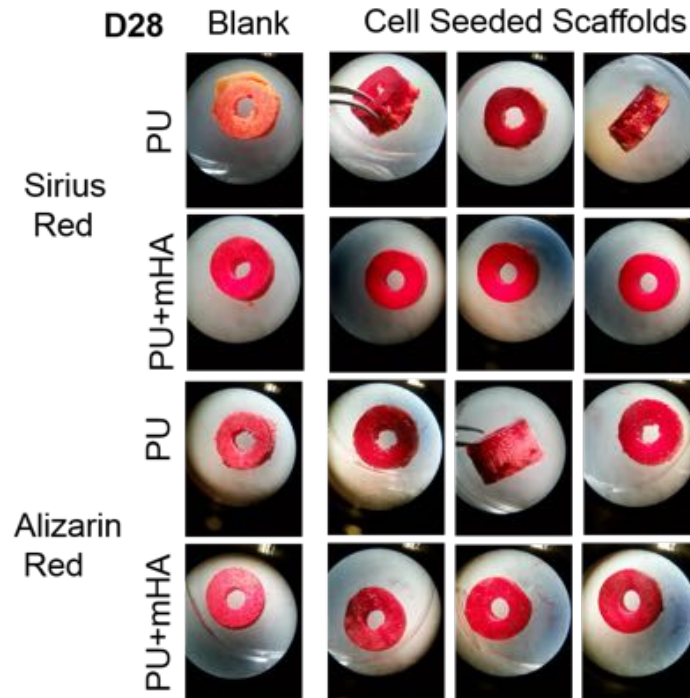
Figure 6.36: **D28** Images of Sirius Red and Alizarin Red staining of MLO-A5 Cells on PM-PL Scaffolds

6.3.5.6 MTT of Titanium Implants in Cultured Scaffolds

In order to assess the suitability of developed constructs to act as an *in vitro* bone model for small orthopaedic implants, 2 types of small titanium screws were investigated. These osteopenia and cortex titanium screws were cut and prepared for cell culture as described in Sections 3.4.4 & 3.7.3.4 on page 83 & 97, respectively.

The screws were inserted into the inner cylindrical rings of PU-only and PU+mHA scaffolds. These scaffolds were selected based on their alamar blue cell viability data. Layer-by-layer and physically mixed PU-only and PU+mHA scaffolds were also compared as part of this study. Furthermore, two main approaches were explored for press-fitting the titanium screws into the scaffolds. One approach inserted the screws into scaffolds that had already been in culture with MLO-A5 cells for 28 days, this was referred to as group 1. The other approach inserted the screws during cell seeding, and was referred to as group 2. The implanted constructs were subsequently cultured under static conditions for 28 days. After the 28 day culture period, the scaffolds were examined with MTT
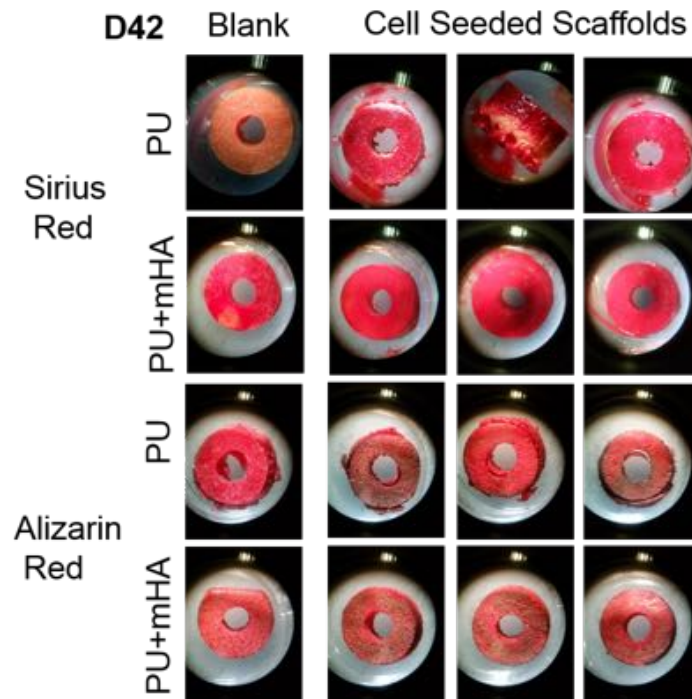
Figure 6.37: **D42** Images of Sirius Red and Alizarin Red staining of MLO-A5 Cells on PM-PL Scaffolds
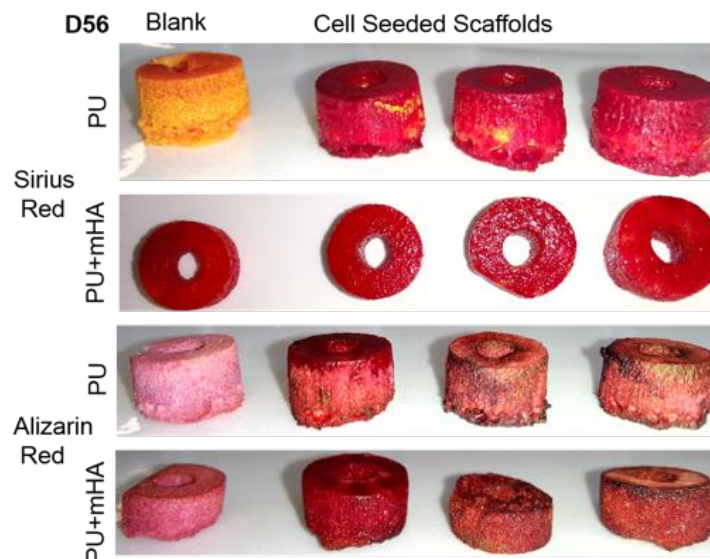
Figure 6.38: **D56** Images of Sirius Red and Alizarin Red staining of MLO-A5 Cells on PM-PL Scaffolds

(a) with negative control (b) without negative control
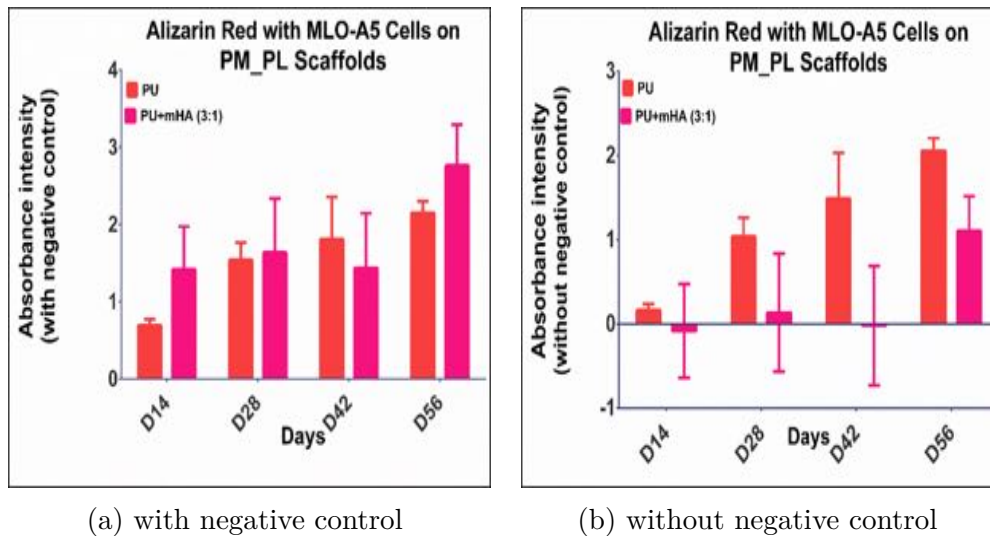
Figure 6.39: Quantitative Analysis of Alizarin Red Destaining of MLO-A5 Cells on PM-PL Scaffolds

assay before the titanium screws were explanted.

MTT made it possible to visualise and locate cells in the scaffolds and also on the implants. This created an opportunity to identify the best seeding approach for the *in vitro* 3D model. As shown in Figure 6.40, LbL and PM-PU scaffolds in group 1, had a denser MTT shade than those in group 2. This can be attributed to the fact that the scaffolds in group 1 were effectively cultured for 28 days longer than those in group 2. However, there were no other visible differences between the LbL and PM-PL scaffolds of group 1 and 2. One of the future work tasks, which is quite challenging, is to identify the best way to monitor cell growth in the constructs over time.

After 28 days of culture, its was expected that the cells would have migrated onto the implants and secreted enough matrix to attach the screws to the scaffolds but this was not observed. A closer inspection of the extracted titanium screws as shown in Figure 6.41a showed only a small MTT stain on one of the screws. This screw (Figure 6.41b) was extracted from a PM-PL PU scaffold in group 2. Although this requires further testing, it appears inserting the screws during cell seeding (group 2) is a better than inserting them after D28 (group 1).

As part of this study, implants grown for 28 days in the PL constructs remained sterile. Moreover, viable and live cells could be detected in these constructs however
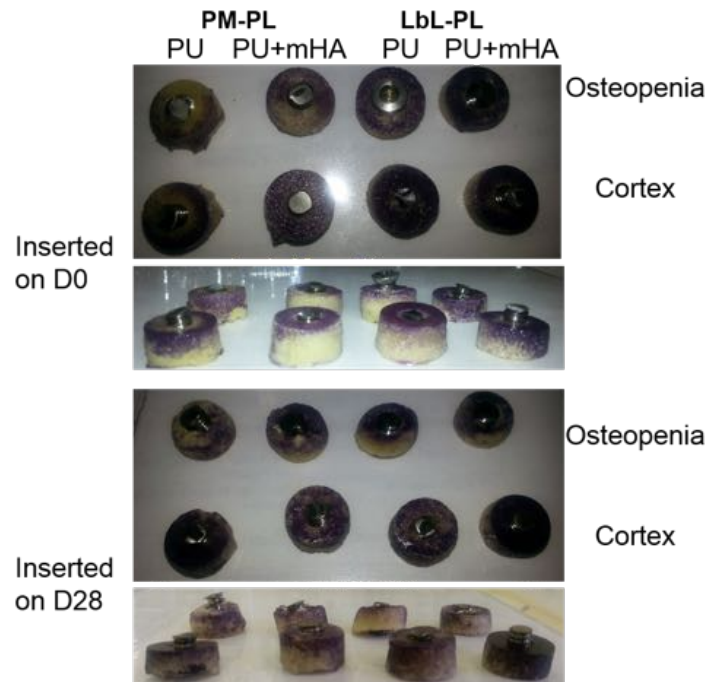
Figure 6.40: MTT of Group 1 & 2 LbL & PM-PL scaffolds implanted with Cortex and Osteopenia titanium Screws

(a)
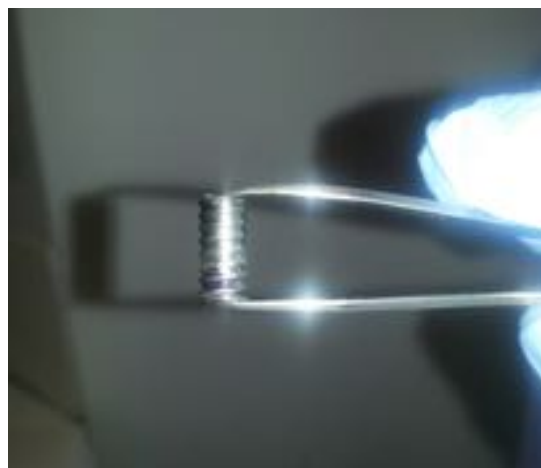
(b) Cortex and Osteopenia Screws in use

Figure 6.41: Titanium Implants Extracted from the *in vitro* Model A: All Extracted Cortex Screws, C: An Extracted Cortex Screw showing MTT stain

more work needs to be undertaken to be able to optimise the model. It may also be possible to achieve a higher level of integration between the scaffold and the implant with a longer culturing period. Such long-term experiments could combine dynamic cell seeding and continuous monitoring of the cell seeded scaffolds and implants in a perfusion bioreactor. This can facilitate efficient mass transfer between the scaffolds and the implants, and provide an opportunity to use biomechanical stimulations to stimulate extracellular matrix production, and seed cells at a higher density, uniformly and efficiently throughout the large PU scaffold (Hofmann et al., 2007; Vetsch et al., 2015).

Attaining a higher level of integration could provide an opportunity to investigate the engineered bone-implant interface and further enhance the usefulness of the model. This would allow the model to be used for push out and pull out tests akin to those carried out on explanted *in vivo* samples as described by An and Draughn (2000).

6.4 Chapter Summary & Key Points

6.4.1 Freeze Dried Scaffolds

- Scaffolds fabricated using the freeze dried technique had very large and irregularly shaped pore structures which lacked interconnection. These scaffolds could not be used for cell culture.

- Mechanical analysis of the freeze dried scaffolds showed a clear distinction between the mechanical properties of Z9A1 and Z3A1 polymers.

6.4.2 Solvent Casting & Freeze Extracted Scaffolds

- Solvent casting PU scaffolds created at $+20\,^{\circ}\text{C}$ dried into irregular shapes, appeared non-porous and felt very stiff to handle.

6.4. CHAPTER SUMMARY & KEY POINTS

- Z1A1 scaffolds extracted at -20ºC and -80ºC had almost no pore structures, whilst Z3A1 and Z9A1 scaffolds contained large and irregular pores and had deep tunnels.

- Scaffolds extracted at -196 ºC had a very uneven morphology due to the fast quenching effect of the liquid nitrogen.

6.4.3 Layer-by-Layer PL Scaffolds

- The layer-by-layer technique was developed to address the limitations encountered with fabricating PL foams with sugar.

- The LbL-PL technique was first used in creating PU-only scaffolds from 10 wt% Z1A1 solution, 15 wt% Z3A1 solutions and 20 wt% Z9A1 solutions made with 100% DMF solvent. Scaffolds made from all three types of PU in the ZnA1 series had a highly porous 3D structure and were significantly thicker than electrospun scaffolds.

- Only PL scaffolds made from Z3A1 and 70/30 DMF/THF solvent were used for biological characterization. 2:1, PU:HA scaffolds were also created to access the effect of incorporating higher HA quantities in fabricated scaffolds

- μ-CT imaging of plain polyurethane scaffolds showed a more porous morphology compared to composite scaffolds containing micro and nano-sized HA particles. With a porosity of 89.4%, PU scaffolds were about 6% more porous than both 3:1 and 2:1 PU+mHA scaffolds, but only 3% more porous than 3:1 PU+nHA.

- 3:1 nHA composites had the highest Young's Modulus and yield strength in the LbL-PL group. The Young's Modulus of plain-PU scaffolds was significantly lower than that of 3:1 PU+mHA and 3:1 PU+nHA composites.

- Although 2:1 PU+mHA scaffolds contained a higher HA content, there was only a small difference between the Young's Modulus and yield strength values of 3:1 and 2:1 mHA composites.

- An inspection of the superficial regions of explanted subcutaneous scaffolds showed an ingrowth of small blood vessels, filled with erythrocytes. The number of fibroblasts found in composites were twice the amount in PU scaffolds.

- The intermediate zone of explanted subcutaneous scaffolds were filled with neutrophils, lymphocytes and erythrocytes. All the pores in the PU-HA scaffolds appeared to be filled with fibrous connective tissue compared to PU-only scaffolds, which were only partially filled.

- For subcutaneous implantation, nano-sized HA particles stimulates more fibroblastic activity and tissue ingrowth than mHA particles.

- For cortical defect studies, nano-HA particles stimulated more osteoblastic activity and accelerated early bone formation in the nHA composites by D7, however new bone tissue was seen in all the pores of PU+mHA and PU+nHA by D45, although PU scaffolds stilled had remnants of fibrous tissue.

6.4.4 Homogenized PL Scaffolds

- With an average pore size of 200 μm, H-PU+mHA had the largest average pore size in the H-PL group, compared to H-PU+nHA scaffolds at 138 μm and H-PU+cHA at 141 μm.

- H-PU+nHA, had the highest mechanical properties within the homogenized scaffold group. The Young's Modulus and yield strength of both H-PU+mHA (0.50 & 0.017 MPa) and H-PU+nHA (0.62 & 0.023 MPa) were lower than their non-homogenized LbL-PU+mHA (0.63 & 0.031 MPa) and LbL-PU+nHA (0.67 & 0.040 MPa) counterparts.

6.4.5   Physical Mixed PL Scaffolds

- A novel physical mixing (PM-PL) protocol was used to mass produce reproducible PL scaffolds in a shorter period of time, as the PM-PL technique shortened fabrication time by about 90%. PM-PU scaffolds had the largest pore sizes within the group, whilst PU+nHA scaffolds the fewest pores and the smallest pore sizes.

- PM-PL scaffolds had a very contrasting mechanical profile to previous fabricated scaffolds. PM-PU had the highest mechanical properties in the PM group and the inclusion of neither nano, micro nor combined micro and nano-HA particles enhanced the mechanical properties of the PM-PU scaffolds.

- Young's modulus and yield strength of PM-PU was surprisingly similar to those of LbL-PU+nHA scaffolds.

- PM-PU-only scaffolds had the highest cell viability for all time-points. This was significantly higher than the viability of composite scaffolds with micro, nano and combined HA particles.

- Collagenous matrix deposition increased over the 56 day period in both scaffold types, however, it was more pronounce in PU-only scaffolds as compared to their PU+mHA counterparts.

- Inserting the titanium screws during cell seeding is a better method to inserting them after a D28 culture period.

Table 6.11: Dapi and Philloidin Staining of the Nucleus and Cytoskeleton of MLO-A5 Cells on PM-PL Scaffolds
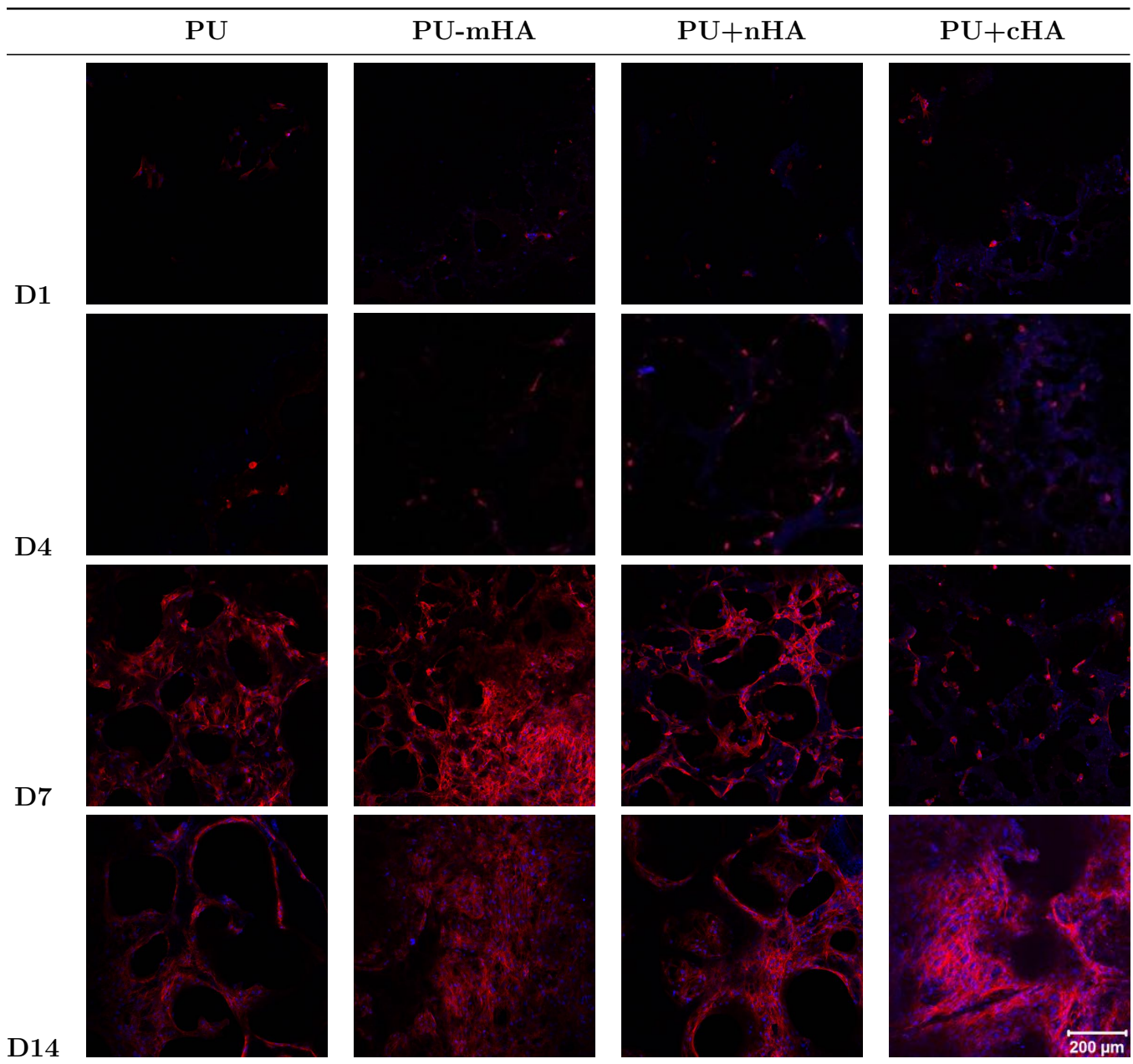
This page was intentionally left blank.

7 | CONCLUSIONS & FUTURE WORK

This final chapter of the thesis summarises the key findings of this project, and discusses possible follow up experiments that evolved from this project but could not be undertaken due to time constraints and circumstances beyond our control. These experiments can serve as PhD topics and final year undergraduate and MSc student projects.

7.1 Non-Aligned Fibrous Scaffolds

The results from electrospun non-aligned PU-only scaffolds showed that the choice of solvents, on their own or in combination, strongly influences the final properties of solution, hence fibre morphology during the electrospinning process. Two types of thermoplastic polyurethane Z9A1 and Z3A1 were electrospun from solutions made with varying combinations of DMF and THF solvents. For both types of PU reducing the amount of DMF contained in the solution, increased fibre diameter, resulting in fibres with a more uniform morphology, and also eliminated beads which were found in the scaffolds fabricated from 100% DMF solvent.

In addition, reducing the DMF solvent content led to lower tensile properties of electrospun scaffolds, whilst incorporation of nano and micro HA particles in both Z9-PU and Z3-PU solutions reinforced the mechanical properties of electrospun composites. Young's Modulus and yield strength values of composites were higher than that of PU scaffolds; these differences were significantly higher with mHA composites compared to nHA composites. nHA composites however exhibited smoother fibres, less variability in

fibre size and better dispersion of the HA. Furthermore, FTIR spectral data confirmed the presence of HA particulates in fabricated composites.

Finally, MLO-A5 cell viability was highest for scaffolds fabricated with 70/30 DMF/THF solvent across most time points for both types of PU, whilst cell viabilities for MLO-A5 cells, were highest on both Z9-nHA and Z3-nHA scaffolds. Z3-nHA scaffolds also had the highest viability with hES-MP cells and produced the highest deposition of collagen across all time points. Calcium deposition was supported in all scaffolds. Therefore, a range of scaffolds which have the potential to support bone matrix formation for bone tissue engineering have been developed. These scaffolds provide a variety of material properties which can be tailored depending on the stage of cell differentiation and final application.

7.1.1 Future Work on the Non-Aligned Scaffolds

Although this electrospinning protocol has been optimised for fabricating non-aligned PU scaffolds for bone tissue engineering applications, it has subsequently been adopted by another biomaterial research group for the development of pelvic floor constructs (Hillary et al., 2015, 2016; Roman et al., 2016). The excellent tunable mechanical and biological properties of polyurethane, make it an ideal scaffold choice for numerous tissue engineering applications. It may therefore be possible to examine if other cell types can be cultured on these PU scaffolds. Although only bone cells were explored in this study, it may be interesting to investigate how these scaffolds could support stem cells to differentiate into other pathways. This could allow the scaffolds to be used in creating tissue engineered constructs for skin, muscle, cartilage and nerve reconstructions.

It may also be possible to improve cellular penetration by creating scaffolds with an increased porosity, more uniform fibre diameters and an even fibre morphology. Hexamethyldisilazane (HMDS) is a popular solvent for electrospinning due to its high electrical conductivity. Using HMDS to dissolve PU could be explored for creating such scaffolds. HMDS has been used extensively in the literature for creating uniform electrospun scaffolds from polymers such as PCL, Gelatin, PLGA, cellulose, chitosan,

amongst others, and could uncover interesting scaffold features for polyurethane (Jia et al., 2013; Adam et al., 2014). A project to explore the ability of using HMDS and PU from the ZnA1 series, could also investigate whether modifying electrospinning conditions such as the tip to collector distance, flow rate, speed of rotating drum and polymer concentration could create scaffolds with exceptional physical and biological properties.

Aside from attempts to increase the amount of HA in composite PU-HA scaffolds, it may also be beneficial to explore the effect of using substituted HA in these scaffolds. Although the HA used in this study had a similar crystallographic structure to bone, it lacks the various cationic and anionic substitutions found in human bone. It will therefore be interesting to investigate the ability of various substituted HA particles in fabricated scaffolds to support a higher deposition of calcified matrix. Substituting ions such as potassium, sodium, strontium, magnesium, zinc, fluorine, chlorine or silicon into the HA lattice has been reported to promote cell proliferation, improve bioactivity and bone function, stimulate bone cell activity and collagen synthesis, and also enhance osteoblastic differentiation (Hing et al., 2006; Best et al., 2008).

7.2   Aligned Fibre Scaffolds

The aligned electrospun scaffolds created as part of this project had an interesting fibre morphology. Fibres of Z3-PU assembled very closely together to form thick aligned bundles, which were large enough to be seen with the naked eye. Including HA particles in PU solutions had an effect on electrospun fibre morphology. Although mHA particles distorted fibre alignment and increased fibre diameters, nHA composites had a more uniform fibre morphology, and showed good porosity and an interconnected porous network.

Raman spectroscopy confirmed the presence of HA in both micro and nano-composites, whilst FTIR spectroscopy compared aligned and non-aligned electrospun scaffolds, and identified vibrations in the $\nu3$ phosphate peak as the main distinction between these scaffolds.

Similar to non-aligned scaffolds, the inclusion of both types of HA particles reinforced the mechanical properties of Z3-PU, when tested in both transverse and parallel orientations. Z3-mHA scaffolds had the highest mechanical properties in the transverse orientation, whilst Z3-nHA had the highest mechanical properties in the parallel orientation. Although the Young's Modulus of Z3-PU in the parallel orientation was about 7 times that of its transverse testing result, it had the weakest mechanical behaviour.

Cell viability of both MLO-A5 and hES-MP cells were generally higher on aligned scaffolds than on scaffolds in the non-aligned group. However, compared to non-aligned fibre Z3-nHA, Z3-PU had the highest viability across all time points within the aligned group for both MLO-A5 and hES-MP cells. Histological images of the scaffolds also highlighted an increased cellular penetration and extracellular matrix production on PU-only scaffolds with aligned fibres.

Xylenol orange staining showed that Z3-mHA scaffolds supported a higher percentage of mineral area coverage compared to Z3-PU, as mineralized nodules in Z3-mHA penetrated almost the entire length of the scaffold compared to Z3-PU, which only had a partial deposition and about 50% depth converge. Moreover, SEM images of cells on the scaffolds also showed a higher amount of calcified matrix production on Z3-mHA than on Z3-PU.

Finally, SHG imaging identified that collagen deposition was originally guided by the alignment of the scaffold fibres but changed orientation with an increase in the depth of extracellular matrix deposition. There were higher amounts of collagen deposition on the Z3-PU scaffolds, however, composite scaffolds showed higher collagen intensities compared to PU-only scaffolds, with D21 collagen deposition on Z3-nHA scaffolds being the brightest and most intense across the entire period.

7.2.1 Future Work on the Aligned Scaffolds

These aligned scaffolds were created by increasing the rotational speed of the cylindrical drum. However, other methods that combine using an auxiliary electrode and an electrical

field (Bornat, 1987), using a thin wheel with sharp edge (Theron et al., 2001), placing a rectangular frame structure under the spinning jet (Huang et al., 2003), have also been used to create aligned fibres. It may therefore be good to consider creating aligned PU-based scaffolds with some of these methods and compare the physical and mechanical properties of such scaffolds with those created as part of this project. Also, the fibre-like structure of carbon nanotubes make them particularly attractive for use as reinforcement in aligned electrospun composites (Han et al., 2009; Meng et al., 2010; Sirivisoot and Harrison, 2011; Mi et al., 2015). The nanosized nature of these particles allow their composite scaffolds to posses exceptional mechanical properties. It would therefore be interesting to explore if replacing HA with carbon nanotubes would lead to scaffolds with a more aligned fibre morphology and improved mechanical properties. However, it may still be interesting to increase the amount of HA in composite scaffolds or attempt to introduce the bundling effect seen in PU-only scaffolds into the HA composites. This would allow an opportunity to explore if a higher amount of HA could compete with the bundling effect of the PU scaffolds in cell viability data, and also identify which of the two is a better method for increasing cell viability, bundling effect or HA particles.

Moreover, SEM images of MLO-A5 cells on the aligned scaffolds showed that the cells were overly confluent and had secreted copious amounts of extracellular matrix. However, since hES-MPs as well as non-aligned scaffolds were not also analysed in this way, it would be interesting to know if these cells/scaffolds would show a similar pattern. This would also serve as an opportunity to further compare the two cell types/scaffolds. Also, since SEM images of MLO-A5 cells showed a higher amount of calcified matrix production in Z3-mHA than on Z3-PU, it would be good to further undertake TEM analysis of these cells on the scaffolds to investigate the nature of the mineral deposits. This would present an opportunity to attain a better understanding of the mechanisms of cell attachment and the influence of fibre morphology in guiding matrix deposition. It could also be used to investigate and understand how errors in collagen deposition could lead to diseases such as osteogenesis imperfecta.

Similarly, its would be good to also use hES-MPs and non-aligned scaffolds for SHG

experiments similar to those undertaken as part of this project. This would strengthen the conclusions of the experiments, and afford an opportunity to further confirm if the interesting changes in orientation observed were influenced by cell type or resulted from specific scaffold morphology. Furthermore, its would be better to counter stain the SHG scaffolds with DAPI to identify where the cells are located. This would allow an opportunity to also investigate if the change in collagen alignment was caused by more cells proliferating at the top of the scaffold. This may have caused the changes in direction as new matrix deposited and aligned itself in respect to the preceding matrix. Moreover, it would also be interesting to explore how these experiments could be used to test the drivers of collagen orientation such as disrupting actin, blocking collagen from cross-linking amongst others (Gerecht et al., 2007; Murshid et al., 2007; Clarke, 2008).

7.3 Foam Scaffolds

Although freeze drying was the initial fabrication technique to be explored for this project, the very large and irregularly shaped nature of its pore structures made it impossible for these scaffolds to be biologically characterized. However, mechanical analysis of these scaffolds showed a clear distinction between the mechanical properties of Z9A1 and Z3A1 polymers.

The layer-by-layer technique developed as part of this study addressed initial challenges encountered with fabricating PU foams with sugar particles. LbL-PL scaffolds made from all three types of PU in the ZnA1 series had a highly porous 3D structure and were significantly thicker than the electrospun scaffolds. As observed with non-aligned and aligned electrospun scaffolds, including HA particles in composite scaffolds reinforced the mechanical properties of LbL-PL scaffolds. 3:1 nHA composites had the highest Young's Modulus and yield strength in this group. Young's Modulus of LbL-PU at 0.32 MPa was significantly lower than the 0.63 and 0.67 MPa of 3:1 PU+mHA and 3:1 PU+nHA composites, respectively. However, there was no significant difference between the mechanical properties of 3:1 mHA composites and 2:1 mHA composites that had a

higher amount of mHA particles.

μ-CT imaging of these LbL-PL scaffolds also confirmed that with a porosity of 89.4%, plain-PU scaffolds were about 6% more porous than both 3:1 and 2:1 PU+mHA scaffolds, but only 3% more porous than 3:1 PU+nHA scaffolds. This high porosity in plain-PU scaffolds enhanced *in vitro* cell viability, as LbL-PL nHA composites did not show an improved alamar blue cell viability over their PU-only counterparts. However, a subcutaneous *in vivo* implantation showed that nano-sized HA particles stimulated more fibroblastic activity and tissue ingrowth than mHA particles, whilst a cortical defect *in vivo* characterization confirmed that nano-HA particles stimulated more osteoblastic activity and accelerated early bone formation in nHA composites by D7.

Compared to the LbL-PL technique, a novel physical mixing fabrication protocol created as part of this project shortened fabrication time by about 90% and was used to mass produce reproducible PL scaffolds in a shorter period of time. PM-PU scaffolds had the largest pore sizes within the group, whilst PU+nHA scaffolds the fewest pores and the smallest pore sizes. Interestingly, these PM-PL scaffolds had a contrasting mechanical profile to previous fabricated scaffolds. PM-PU had the highest mechanical properties in this group and the inclusion of neither nano, micro nor combined micro and nano-HA particles enhanced their mechanical properties. The Young's modulus and yield strength of PM-PU around 0.55 & 0.041 MPa, respectively, was surprisingly similar to that of LbL-PU+nHA scaffolds at 0.68 & 0.040 MPa.

Similar to LbL-PL scaffolds, PM-PU-only scaffolds had the highest cell viability for all time-points. This was significantly higher than the viability of composite scaffolds with micro, nano and combined HA particles. Collagenous matrix deposition increased over the 56 day period in all scaffold types, however, this increase was more pronounced in PU-only scaffolds compared to their PU+mHA counterparts. Finally, mimicking push-out and pull-out tests by inserting test titanium screws into the cylindrical centres of LbL-PL and PM-PL scaffolds, showed that inserting the screws during cell seeding is a better method than inserting them after a D28 culture period.

PU-based scaffolds that serve as a novel biomimetic *in vitro* 3D bone model for

testing of small orthopaedic implants have been developed. In addition to providing an alternative approach to the use of animals for scientific experiments, the developed model could afford orthopaedic and dental implant manufacturers an opportunity to test their conceptual designs at a reduced cost and provide data that can only be currently obtained from expensive *in vivo* experiments. Furthermore, data from such bone-like matrix experiments can also be used to validate other bone forming tissue engineered products. The developed construct could provide academic research laboratories and industrial bioengineering firms a cost effective approach for testing new designs and translational products. This would go a long way to developing cheaper and faster regenerative solutions that address current clinical and healthcare challenges, and ultimately contribute to delivering a better quality of life to suffering patients.

7.3.1 Future Work on the Foam Scaffolds

Unfortunately, the bioactivity of all fabricated scaffolds was not analyzed *in vitro*. The ability of biomaterials to develop an HA surface in Stimulated Body Fluid (SBF) is an indicative of its chemical reactivity. This also correlates with the materials ability to bond to bone *in vitro*. Although such bonding was observed in the *in vivo* studies carried out as part of this project, it would be instructive to undertake *in vitro* bioactivity studies to further characterize the scaffolds. This can be done by immersing the material in the physiologically similar solution (SBF) and analysing the material surface and the composition of the surrounding solution, for a precipitation of amorphous Ca/Ph ions or an increase in the deposition of Ca/Ph ions in solution.

Incorporating biomolecules in the foam scaffolds may improve the biological performance of these scaffolds, and enhance the deposition of a higher amount of calcified matrix. This could improve the current tissue engineered construct and further promote its use as a 3D alternative for *in vitro* testing of small orthopaedic implants. Exploring ways to incorporate and deliver biomolecules such as Transforming growth factor-Beta, bone morphogenetic proteins, fibroblast growth factor,vascular endothelial growth factor and insulin-like growth factors have been reported to be integral to in the regulation

of new bone formation, bone tissue regeneration and extracellular matrix formation, by recruiting and differentiating osteoprogenitor cells into osteoblasts.

Also, bone is a dynamic tissue and hence constantly remodelling with the combined action of bone forming osteoblasts and bone resorbing osteoclasts. Although osteoblasts produce disorganized or woven bone matrix composed predominately of type-1 collagen which mineralises with HA crystals to form bone, it is the action of the osteoclasts that resorb woven bone during bone remodelling, and inefficiencies in the process could lead to irregular bone formation. Therefore an important and challenging step will be to incorporate osteoclasts into the tissue engineered bone. It would also be interesting to explore how the current model could be optimized for studying bone pathologies and testing new drug therapies, as well as exploring its use as a model for understanding infection and exploring antibacterial surfaces.

Moreover, the current design could benefit from a much longer period of culture in a controlled bioreactor environment. This would prevent necrosis and ensure all the cells receive an adequate supply of nutrients as well as the removal of debris. It may also provide a dynamic environment that can be used to explore the influence of mechanical conditioning on the engineered construct (Vetsch et al., 2015). Increasing evidence suggests that mechanical forces, which are known to be important modulators of cell physiology, could possibly improve or accelerate the rate of bone tissue formation *in vitro*. Exploring mechanical conditioning effects in these scaffolds may therefore advance the current design.

Finally, in order to test the full scale potential of the engineered constructs to act as a medium for testing small implants, an extensive study to investigate several different types of implants, different culture periods, different experimental set-ups need to be undertaken. Such studies could make use of actual push out and pull out tests similar to those experienced by explanted *in vivo* samples. These implant push out and pull out tests are established assessment tools used in investigating the shear strength of a bone-implant interface. Such tests are commonly applied in testing the effect of implant materials, surface texture, porosity, cross-sectional geometry and surface composition

resulting from bone ingrowth or bone apposition to the implant surface (An and Draughn, 2000). In a typical test, a load is applied to the implant via a device connected to the crosshead of the materials testing machine and a force-displacement curve is recorded until the test is terminated with failure of the bone-implant interface (Berzins and Summer, 2000).

Bibliography

Adam, J. et al. (2014). Electrospun hybrid fibers with substantial filler contents formed through kinetically arrested phase separation in liquid jet. *RSC Advances*, 4(53):27683–27686.

Adhikari, R., Gunatillake, P. A., Griffiths, I., Tatai, L., Wickramaratna, M., Houshyar, S., Moore, T., Mayadunne, R. T. M., Field, J., McGee, M., and Carbone, T. (2008). Biodegradable injectable polyurethanes: Synthesis and evaluation for orthopaedic applications. *Biomaterials*, 29(28):3762–3770.

Agarwal, S., Wendorff, J. H., and Greiner, A. (2008). Use of electrospinning technique for biomedical applications. *Polymer*, 49(26):5603–5621.

Ahmed, S. A., Gogal, R. M., and Walsh, J. E. (1994). A new rapid and simple non-radioactive assay to monitor and determine the proliferation of lymphocytes: an alternative to [3 h] thymidine incorporation assay. *Journal of immunological methods*, 170(2):211–224.

Albright F, S. P. R. A. (1941). Postmenopausal osteoporosis: Its clinical features. *Journal of the American Medical Association*, 116(22):2465–2474.

Altman, G., Horan, R., Martin, I., Farhadi, J., Stark, P., Volloch, V., Vunjak-Novakovic, G., Richmond, J., and Kaplan, D. L. (2002). Cell differentiation by mechanical stress. *Faseb Journal*, 16(2):270–272.

Alvarez-Lloret, P., Rodriguez-Navarro, A., Romanek, C. S., Gaines, K., and Congdon, J. (2006). Quantitative analysis of bone mineral using ftir. *Macla*, 6:45–47.

An, Y. H. and Draughn, R. A. (2000). *Mechanical testing of bone and the bone-implant interface*. CRC PressI Llc.

BIBLIOGRAPHY

Andriano, K. P., Tabata, Y., Ikada, Y., and Heller, J. (1999). In vitro and in vivo comparison of bulk and surface hydrolysis in absorbable polymer scaffolds for tissue engineering. *Journal of Biomedical Materials Research*, 48(5):602–612.

Anee, T. K., Ashok, M., Palanichamy, M., and Narayana Kalkura, S. (2003). A novel technique to synthesize hydroxyapatite at low temperature. *Materials Chemistry and Physics*, 80(3):725–730.

Anselme, K., Broux, O., Noel, B., Bouxin, B., Bascoulergue, G., Dudermel, A.-F., Bianchi, F., Jeanfils, J., and Hardouin, P. (2002). In vitro control of human bone marrow stromal cells for bone tissue engineering. *Tissue engineering*, 8(6):941–953.

Armentano, I., Dottori, M., Fortunati, E., Mattioli, S., and Kenny, J. M. (2010). Biodegradable polymer matrix nanocomposites for tissue engineering: A review. *Polymer Degradation and Stability*, 95(11):2126–2146.

Arokoski, J., Arokoski, M., Jurvelin, J., Helminen, H., Niemitukia, L., and Kröger, H. (2002). Increased bone mineral content and bone size in the femoral neck of men with hip osteoarthritis. *Annals of the rheumatic diseases*, 61(2):145–150.

Asefnejad, A., Behnamghader, A., Khorasani, T. M., and Farsadzadeh, B. (2011). Polyurethane/fluor-hydroxyapatite nanocomposite scaffolds for bone tissue engineering. part I: Morphological, physical, and mechanical characterization. *International Journal of Nanomedicine*, 6(1):93–100.

Athanasiou, K. A., Niederauer, G. G., and Agrawal, C. M. (1996). Sterilization, toxicity, biocompatibility and clinical applications of polylactic acid/polyglycolic acid copolymers. *Biomaterials*, 17(2):93–102.

Attawia, M. A., Herbert, K. M., and Laurencin, C. T. (1995). Osteoblast-like cell adherance and migration through three-dimensional porous polymer matrices. *Biochemical and biophysical research communications*, 213(2):639–644.

Babensee, J. E., McIntire, L. V., and Mikos, A. G. (2000). Growth factor delivery for tissue engineering. *Pharmaceutical research*, 17(5):497–504.

Baker, B. M., Gee, A. O., Metter, R. B., Nathan, A. S., Marklein, R. A., Burdick, J. A., and Mauck, R. L. (2008). The potential to improve cell infiltration in

composite fiber-aligned electrospun scaffolds by the selective removal of sacrificial fibers. *Biomaterials*, 29(15):2348–2358.

Baker-LePain, J. C. and Lane, N. E. (2012). Role of bone architecture and anatomy in osteoarthritis. *Bone*, 51(2):197–203.

Bakker, A. D. and Klein-Nulend, J. (2012). *Osteoblast isolation from murine calvaria and long bones*, pages 19–29. Springer.

Bancroft, G. N., Sikavitsas, V. I., and Mikos, A. G. (2003). Technical note: Design of a flow perfusion bioreactor system for bone tissue-engineering applications. *Tissue engineering*, 9(3):549–554.

Banwart, J. C., Asher, M. A., and Hassanein, R. S. (1995). Iliac Crest Bone Graft Harvest Donor Site Morbidity: A Statistical Evaluation. *Spine*, 20(9):1055–1060.

Barlow, D. G. B. D. o. H., editor (1994). *Report of the Advisory Group on Osteoporosis*. Report of the Advisory Group on Osteoporosis.

Bashur, C. A., Shaffer, R. D., Dahlgren, L. A., Guelcher, S. A., and Goldstein, A. S. (2009). Effect of fiber diameter and alignment of electrospun polyurethane meshes on mesenchymal progenitor cells. *Tissue Engineering Part A*, 15(9):2435–2445.

Batson, O. V. (1921). The differential staining of bone. i. the staining of preserved specimens. *The Anatomical Record*, 22(3):159–164.

Baxter, M. A., Wynn, R. F., Jowitt, S. N., Wraith, J., Fairbairn, L. J., and Bellantuono, I. (2004). Study of telomere length reveals rapid aging of human marrow stromal cells following in vitro expansion. *Stem cells*, 22(5):675–682.

Beresford, J. N., Graves, S. E., and Smoothy, C. A. (1993). Formation of mineralized nodules by bone derived cells in vitro: a model of bone formation? *American journal of medical genetics*, 45(2):163–178.

Bergmeister, H., Schreiber, C., Grasl, C., Walter, I., Plasenzotti, R., Stoiber, M., Bernhard, D., and Schima, H. (2013). Healing characteristics of electrospun polyurethane grafts with various porosities. *Acta Biomaterialia*, 9(4):6032–6040.

Bernas, T. and Dobrucki, J. (2002). Mitochondrial and nonmitochondrial reduction of mtt: Interaction of mtt with tmre, jc-1, and nao mitochondrial fluorescent probes.

BIBLIOGRAPHY

Cytometry, 47(4):236–242.

Berridge, M. V. and Tan, A. S. (1993). Characterization of the cellular reduction of 3-(4, 5-dimethylthiazol-2-yl)-2, 5-diphenyltetrazolium bromide (mtt): subcellular localization, substrate dependence, and involvement of mitochondrial electron transport in mtt reduction. *Archives of biochemistry and biophysics*, 303(2):474–482.

Bertoldi, S., Farè, S., Denegri, M., Rossi, D., Haugen, H. J., Parolini, O., and Tanzi, M. C. (2010). Ability of polyurethane foams to support placenta-derived cell adhesion and osteogenic differentiation: Preliminary results. *Journal of Materials Science: Materials in Medicine*, 21(3):1005–1011.

Berzins, A. and Summer, D. R. (2000). Implant pushout and pullout tests. *Mechanical testing of bone and the bone-implant interface*, pages 463–467.

Best, S., Porter, A., Thian, E., and Huang, J. (2008). Bioceramics: past, present and for the future. *Journal of the European Ceramic Society*, 28(7):1319–1327.

Bianco, A., Di Federico, E., Moscatelli, I., Camaioni, A., Armentano, I., Campagnolo, L., Dottori, M., Kenny, J. M., Siracusa, G., and Gusmano, G. (2009). Electrospun poly(ϵ-caprolactone)/Ca-deficient hydroxyapatite nanohybrids: Microstructure, mechanical properties and cell response by murine embryonic stem cells. *Materials Science and Engineering: C*, 29(6):2063–2071.

BJD (2013). Key Facts and Figures - The Bone and Joint Decade. http://bjdonline.org/?page_id=1574. Date Accessed: 03/04/2013.

Black, L. and Berenbaum, M. (1964). Factors affecting the dye exclusion test for cell viability. *Experimental cell research*, 35(1):9–13.

Blond, D., Walshe, W., Young, K., Blighe, F. M., Khan, U., Almecija, D., Carpenter, L., McCauley, J., Blau, W. J., and Coleman, J. N. (2008). Strong, tough, electrospun polymer–nanotube composite membranes with extremely low density. *Advanced Functional Materials*, 18(17):2618–2624.

Bobovich, Y. S. (1988). Classical size effects in the Raman scattering spectra of highly dispersed particles. Experimental studies (review). *Journal of Applied Spectroscopy*, 49(3):869–888.

Boccaccini, A. R. and Maquet, V. (2003). Bioresorbable and bioactive polymer/Bioglass® composites with tailored pore structure for tissue engineering applications. *Composites Science and Technology*, 63(16):2417–2429.

Boccaccini, A. R., Roelher, J. A., Hench, L. L., Maquet, V., and Jerome, R. (2008). *A Composites Approach to Tissue Engineering*, pages 805–816. John Wiley & Sons, Inc.

Bohner, M. (2001). Physical and chemical aspects of calcium phosphates used in spinal surgery. *European Spine Journal*, 10:S114–S121.

Boissard, C. I. R., Bourban, P.-E., Tami, A. E., Alini, M., and Eglin, D. (2009). Nanohydroxyapatite/poly (ester urethane) scaffold for bone tissue engineering. *Acta biomaterialia*, 5(9):3316–3327.

Bonab, M. M., Alimoghaddam, K., Talebian, F., Ghaffari, S. H., Ghavamzadeh, A., and Nikbin, B. (2006). Aging of mesenchymal stem cell in vitro. *BMC cell biology*, 7(1):14.

Bonewald, L. F. and Johnson, M. L. (2008). Osteocytes, mechanosensing and wnt signaling. *Bone*, 42(4):606–615.

Bonfield, W. (1971). Mechanisms of deformation and fracture in bone. *Composites*, 2(3):173–175.

Bonfield, W. (1988a). Composites for bone replacement. *Journal of Biomedical Engineering*, 10(6):522–526.

Bonfield, W. (1988b). Hydroxyapatite-Reinforced Polyethylene as an Analogous Material for Bone Replacementa. *Annals of the New York Academy of Sciences*, 523(1):173–177.

Bonucci, E. (2000). Basic composition and structure of bone. *Mechanical testing of bone and the bone-implant interface. CRC Press, Boca Raton*, pages 3–21.

Bonzani, I. C., Adhikari, R., Houshyar, S., Mayadunne, R., Gunatillake, P., and Stevens, M. M. (2007). Synthesis of two-component injectable polyurethanes for bone tissue engineering. *Biomaterials*, 28(3):423–433.

Bornat, A. (1987). Production of electrostatically spun products. US Patent 4,689,186.

Bose, S., Roy, M., and Bandyopadhyay, A. (2012). Recent advances in bone tissue engineering scaffolds. *Trends in Biotechnology*.

Boskey, A. L. (2001). Bone mineralization. *Bone Biomechanics, ed*, 3:5.1—-5.34.

BIBLIOGRAPHY

Boskey, A. L. (2005). The organic and inorganic matrices. *Bone Tissue Engineering*, pages 91–123.

Bostrom, R. and Mikos, A. (1997). Tissue engineering of bone. *Synthetic biodegradable polymer scaffolds*, 1:215–234.

Boutin, P. (1972). Total arthroplasty of the hip by fritted aluminum prosthesis. Experimental study and 1st clinical applications. *Revue de chirurgie orthopedique et reparatrice de l'appareil moteur*, 58(3):229–246.

Bredbenner, T. L., Eliason, T. D., Potter, R. S., Mason, R. L., Havill, L. M., and Nicolella, D. P. (2010). Statistical shape modeling describes variation in tibia and femur surface geometry between control and incidence groups from the osteoarthritis initiative database. *Journal of biomechanics*, 43(9):1780–1786.

Brunski, J. B. (1992). Biomechanical factors affecting the bone-dental implant interface. *Clinical materials*, 10(3):153–201.

Brydone, A., Meek, D., and Maclaine, S. (2010). Bone grafting, orthopaedic biomaterials, and the clinical need for bone engineering. volume 224, pages 1329–1343. SAGE Publications.

Buckwalter, J. and Mankin, H. (1997). Articular cartilage: degeneration and osteoarthritis, repair, regeneration, and transplantation. *Instructional course lectures*, 47:487–504.

Burg, K. J. L., Porter, S., and Kellam, J. F. (2000). Biomaterial developments for bone tissue engineering. *Biomaterials*, 21(23):2347–2359.

Burgeson, R. E. and Nimni, M. E. (1992). Collagen types. Molecular structure and tissue distribution. *Clinical orthopaedics and related research*, (282):250.

Burr, D. B. and Martin, R. B. (2005). Errors in bone remodeling: toward a unified theory of metabolic bone disease. *American Journal of Anatomy*, 186(2):186–216.

Bye, F. J., Bissoli, J., Black, L., Bullock, A. J., Puwanun, S., Moharamzadeh, K., Reilly, G. C., Ryan, A. J., and MacNeil, S. (2013). Development of bilayer and trilayer nanofibrous/microfibrous scaffolds for regenerative medicine. *Biomaterials Science*, 1(9):942–951.

Campagnola, P. J., Clark, H. A., Mohler, W. A., Lewis, A., and Loew, L. M. (2001). Second-harmonic imaging microscopy of living cells. *Journal of biomedical optics*, 6(3):277–286.

Campagnola, P. J. and Loew, L. M. (2003). Second-harmonic imaging microscopy for visualizing biomolecular arrays in cells, tissues and organisms. *Nature biotechnology*, 21(11):1356–1360.

Cao, J., Chen, N., Chen, Y., and Luo, X. (2010). Synthesis of a novel biodegradable polyurethane with phosphatidylcholines. *International journal of molecular sciences*, 11(4):1870–1877.

Cao, W. and Hench, L. L. (1996). Bioactive materials. *Ceramics International*, 22(6):493–507.

Cao, X. and Chen, D. (2005). The BMP signaling and in vivo bone formation. *Gene*, 357(1):1.

Carlberg, B., Axell, M. Z., Nannmark, U., Liu, J., and Kuhn, H. G. (2009). Electrospun polyurethane scaffolds for proliferation and neuronal differentiation of human embryonic stem cells. *Biomedical Materials*, 4(4):45004.

Carter, D. R. and Spengler, D. M. (1978). Mechanical Properties and Composition of Cortical Bone. *Clinical orthopaedics and related research*, 135:192–217.

CDC (1991). Consensus development conference: Prophylaxis and treatment of osteoporosis. *Osteoporosis International*, 1(2):114–117.

Chapman, T. M. (1989). Models for polyurethane hydrolysis under moderately acidic conditions: A comparative study of hydrolysis rates of urethanes, ureas, and amides. *Journal of Polymer Science Part A: Polymer Chemistry*, 27(6):1993–2005.

Charnley, J. (1960). ANCHORAGE OF THE FEMORAL HEAD PROSTHESIS TO THE SHAFT OF THE FEMUR. *Journal of Bone & Joint Surgery, British Volume*, 42-B(1):28–30.

Chaudhry, A. A., Haque, S., Kellici, S., Boldrin, P., Rehman, I., Khalid, F. A., and Darr, J. A. (2006). Instant nano-hydroxyapatite: a continuous and rapid hydrothermal synthesis. *Chemical communications*, (21):2286–2288.

BIBLIOGRAPHY

Chen, P. Y., Stokes, A. G., and McKittrick, J. (2009). Comparison of the structure and mechanical properties of bovine femur bone and antler of the North American elk (Cervus elaphus canadensis). *Acta biomaterialia*, 5(2):693–706.

Chen, X., Nadiarynkh, O., Plotnikov, S., and Campagnola, P. J. (2012). Second harmonic generation microscopy for quantitative analysis of collagen fibrillar structure. *Nature protocols*, 7(4):654–669.

Chen, Y.-C., Sosnoski, D. M., and Mastro, A. M. (2010). Breast cancer metastasis to the bone: mechanisms of bone loss. *Breast cancer research*, 12(6):1.

Choi, K., Kuhn, J. L., Ciarelli, M. J., and Goldstein, S. A. (1990). The elastic moduli of human subchondral, trabecular, and cortical bone tissue and the size-dependency of cortical bone modulus. *Journal of biomechanics*, 23(11):1103–1113.

Ciardelli, G., Rechichi, A., Sartori, S., DAcunto, M., Caporale, A., Peggion, E., Vozzi, G., and Giusti, P. (2006). Bioactive polyurethanes in clinical applications. *Polymers for advanced technologies*, 17(9-10):786–789.

Ciccone, W. J., Motz, C., Bentley, C., and Tasto, J. P. (2001). Bioabsorbable implants in orthopaedics: new developments and clinical applications. *Journal of the American Academy of Orthopaedic Surgeons*, 9(5):280–288.

Clarke, B. (2008). Normal bone anatomy and physiology. *Clinical journal of the American Society of Nephrology*, 3(Supplement 3):S131–S139.

Clarke, D., Puppi, D., Detta, N., Ferrer, M. C. C., Crawford, A., Reilly, G., and Chiellini, F. (2008). Electrospun polyurethane scaffolds for mechanical stimulation of cells in bone tissue engineering. *Tissue Engineering Part A*, 14(5):846.

Clover, J. and Gowen, M. (1994). Are mg-63 and hos te85 human osteosarcoma cell lines representative models of the osteoblastic phenotype? *Bone*, 15(6):585–591.

Colina, M., La Corte, R., De Leonardis, F., and Trotta, F. (2008). Paget's disease of bone: a review. *Rheumatology International*, 28(11):1069—-+.

Compston, J. E. and of London, R. C. o. P. (1996). *Osteoporosis: New Perspectives on Causes, Prevention and Treatment.* Royal College of Physicians.

Cory, A. H., Owen, T. C., Barltrop, J. A., and Cory, J. G. (1991). Use of an

aqueous soluble tetrazolium/formazan assay for cell growth assays in culture. *Cancer communications*, 3(7):207–212.

Coury, A. J., Slaikeu, P. C., Cahalan, P. T., Stokes, K. B., and Hobot, C. M. (1988). Factors and interactions affecting the performance of polyurethane elastomers in medical devices. *Journal of biomaterials applications*, 3(2):130–179.

Croft, P., Coggon, D., Cruddas, M., and Cooper, C. (1992). Osteoarthritis of the hip: an occupational disease in farmers. *BMJ: British Medical Journal*, 304(6837):1269.

Croteau, S., Rauch, F., Silvestri, A., and Hamdy, R. C. (1999). Bone morphogenetic proteins in orthopedics: From basic science to clinical practice. *Orthopedics*, 22(7):686–695.

Curzon, M. E. and Cutress, T. W. (1983). *Trace elements and dental disease*, volume 9. J. Wright/Psg Inc.

Dallas, S. L., Veno, P. A., Rosser, J. L., Barragan-Adjemian, C., Rowe, D. W., Kalajzic, I., and Bonewald, L. F. (2009). Time lapse imaging techniques for comparison of mineralization dynamics in primary murine osteoblasts and the late osteoblast/early osteocyte-like cell line mlo-a5. *Cells Tissues Organs*, 189(1-4):6–11.

DDL (2013). Orthopeadic Implant Test Standards.

De Fries, R. and Mitsuhashi, M. (1995). Quantification of mitogen induced human lymphocyte proliferation: Comparison of alamarbluetm assay to 3h-thymidine incorporation assay. *Journal of clinical laboratory analysis*, 9(2):89–95.

de l'Europe, C. (1986). *European Convention for the protection of vertebrate animals used for experimental and other scientific purposes/Convention européenne sur la protection des animaux vertébrés utilisés à des fins expérimentales ou à d'autres fins scientifiques:[Strasbourg, 18. III. 1986]*. Conseil de l'Europe Section des publications.

De Mulder, E., Hannink, G., Verdonschot, N., and Buma, P. (2013). Effect of polyurethane scaffold architecture on ingrowth speed and collagen orientation in a subcutaneous rat pocket model. *Biomedical Materials*, 8(2):025004.

de Peppo, G. M., Sladkova, M., Sjövall, P., Palmquist, A., Oudina, K., Hyllner, J., Thomsen, P., Petite, H., and Karlsson, C. (2012). Human embryonic stem cell-derived

mesodermal progenitors display substantially increased tissue formation compared to human mesenchymal stem cells under dynamic culture conditions in a packed bed/column bioreactor. *Tissue Engineering Part A*, 19(1-2):175–187.

de Peppo, G. M., Svensson, S., Lennerås, M., Synnergren, J., Stenberg, J., Strehl, R., Hyllner, J., Thomsen, P., and Karlsson, C. (2010). Human embryonic mesodermal progenitors highly resemble human mesenchymal stem cells and display high potential for tissue engineering applications. *Tissue Engineering Part A*, 16(7):2161–2182.

Deitzel, J. M., Kleinmeyer, J. D., Hirvonen, J. K., and Beck Tan, N. C. (2001). Controlled deposition of electrospun poly (ethylene oxide) fibers. *Polymer*, 42(19):8163–8170.

Delaine-Smith, R. M. (2013). Mechanical and physical guidance of osteogenic differentiation and matrix production.

Delaine-Smith, R. M., Green, N. H., Matcher, S. J., MacNeil, S., and Reilly, G. C. (2014). Monitoring Fibrous Scaffold Guidance of Three-Dimensional Collagen Organisation Using Minimally-Invasive Second Harmonic Generation. *PloS one*, 9(2):e89761.

Delaine-Smith, R. M., MacNeil, S., and Reilly, G. C. (2012). Matrix production and collagen structure are enhanced in two types of osteogenic progenitor cells by a simple fluid shear stress stimulus. *European Cells and Materials*, 24.

Demir, M. M., Soyal, D., U?nlu?, C., Kus, M., and O?zc?elik, S. (2009). Controlling spontaneous emission of cdse nanoparticles dispersed in electrospun fibers of polycarbonate urethane. *The Journal of Physical Chemistry C*, 113(26):11273–11278.

Demir, M. M., Yilgor, I., Yilgor, E., and Erman, B. (2002). Electrospinning of polyurethane fibers. *Polymer*, 43(11):3303–3309.

Dillon, J. P., Waring-Green, V. J., Taylor, A. M., Wilson, P. J. M., Birch, M., Gartland, A., and Gallagher, J. A. (2012). *Primary human osteoblast cultures*, pages 3–18. Springer.

Dimitrova, M., Ivanova, D., Karamancheva, I., Milev, A., and Dobrev, I. (2009). Application of ftir-spectroscopy for diagnosis of breast cancer tumors. *Journal of the University of Chemical Technology and Metallurgy*, 44(3):297–300.

Doll, B. and Koch, H. (2004). BONE REMODELING. *Bone Tissue Engineering*, page 27.

Doshi, J. and Reneker, D. H. (1995). Electrospinning process and applications of electrospun fibers. *Journal of electrostatics*, 35(2):151–160.

Du, J., Zuo, Y., Zou, Q., Sun, B., Zhou, M., Li, L., Man, Y., and Li, Y. (2014). Preparation and in vitro evaluation of polyurethane composite scaffolds based on glycerol esterified castor oil and hydroxyapatite. *Materials Research Innovations*, 18(3):160–168.

Ducheyne, P., Healy, K., Hutmacher, D. E., Grainger, D. W., and Kirkpatrick, C. J. (2011). *Comprehensive Biomaterials: Online Version*. Elsevier.

Dunn, A. S., Campbell, P. G., and Marra, K. G. (2001). The influence of polymer blend composition on the degradation of polymer/hydroxyapatite biomaterials. *Journal of Materials Science: Materials in Medicine*, 12(8):673–677.

Edmondson, R., Broglie, J. J., Adcock, A. F., and Yang, L. (2014). Three-dimensional cell culture systems and their applications in drug discovery and cell-based biosensors. *Assay and drug development technologies*, 12(4):207–218.

El-Ghannam, A. (2005). Bone reconstruction: from bioceramics to tissue engineering. *Expert Review of Medical Devices*, 2(1):87–101.

European-Commission (2013). Legislation for the protection of animals used for scientific purposes. http://ec.europa.eu/environment/chemicals/lab_animals/legislation_en.htm. Date Accessed: 04/04/2013.

Faulstich, H., Trischmann, H., and Mayer, D. (1983). Preparation of tetramethylrhodaminyl-phalloidin and uptake of the toxin into short-term cultured hepatocytes by endocytosis. *Experimental cell research*, 144(1):73–82.

F.D.A. (2013). Draft guidance for industry and food and drug administration staff use of international standard iso-10993, "biological evaluation of medical devices part 1: Evaluation and testing". http://www.fda.gov/downloads/MedicalDevices/DeviceRegulationandGuidance/GuidanceDocument Date Accessed: 31-05-2013.

Feldman, D., Marcus, R., Nelson, D., and Rosen, C. J. (2007). *Osteoporosis*. Elsevier

BIBLIOGRAPHY

Science.

Fields, R. and Lancaster, M. (1993). Dual-attribute continuous monitoring of cell proliferation/cytotoxicity. *American biotechnology laboratory*, 11(4):48.

Fowler, B., Moreno, E., and Brown, W. (1966). Infra-red spectra of hydroxyapatite, octacalcium phosphate and pyrolysed octacalcium phosphate. *Archives of oral biology*, 11(5):477–492.

Freshney, R. I. (2005). Culture of animal cells, a manual of basic technique. 5 ed.

Frost, H. (1966). Bone dynamics in metabolic bone disease. *The Journal of Bone & Joint Surgery*, 48(6):1192–1203.

Ganguly, A., Nail, S. L., and Alexeenko, A. A. (2012). Rarefied gas dynamics aspects of pharmaceutical freeze-drying. *Vacuum*, 86(11):1739–1747.

Ganz, R., Parvizi, J., Beck, M., Leunig, M., Nötzli, H., and Siebenrock, K. A. (2003). Femoroacetabular impingement: a cause for osteoarthritis of the hip. *Clinical orthopaedics and related research*, 417:112–120.

Garg, K. and Bowlin, G. L. (2011). Electrospinning jets and nanofibrous structures. *Biomicrofluidics*, 5(1):013403.

Gelber, A. C., Hochberg, M. C., Mead, L. A., Wang, N.-Y., Wigley, F. M., and Klag, M. J. (2000). Joint injury in young adults and risk for subsequent knee and hip osteoarthritis. *Annals of internal medicine*, 133(5):321–328.

Gerecht, S., Bettinger, C. J., Zhang, Z., Borenstein, J. T., Vunjak-Novakovic, G., and Langer, R. (2007). The effect of actin disrupting agents on contact guidance of human embryonic stem cells. *Biomaterials*, 28(28):4068–4077.

Giannoudis, P. V., Dinopoulos, H., and Tsiridis, E. (2005). Bone substitutes: an update. *Injury*, 36(3):S20–S27.

Ginebra, M. P., Traykova, T., and Planell, J. A. (2006). Calcium phosphate cements as bone drug delivery systems: A review. *Journal of Controlled Release*, 113(2):102–110.

Gingras, M., Bergeron, J., Déry, J., Durham, H. D., and Berthod, F. (2003). In vitro development of a tissue-engineered model of peripheral nerve regeneration to study neurite growth. *The FASEB journal*, 17(14):2124–2126.

Giraud-Guille, M.-M. (1988). Twisted plywood architecture of collagen fibrils in human compact bone osteons. *Calcified tissue international*, 42(3):167–180.

Gleiter, H. (2000). Nanostructured materials: basic concepts and microstructure. *Acta materialia*, 48(1):1–29.

Gloeckner, H., Jonuleit, T., and Lemke, H.-D. (2001). Monitoring of cell viability and cell growth in a hollow-fiber bioreactor by use of the dye alamar blue. *Journal of immunological methods*, 252(1):131–138.

Gogolewski, S. (2001). Nonmetallic materials for bone substitutes. *European Cells and Materials*, 1(2):54–55.

Gogolewski, S. (2007). Structure-property relations and cytotoxicity of isosorbide-based biodegradable polyurethane scaffolds for tissue repair and regeneration. *JBiomed Mater Res*, 85A:456–465.

Gogolewski, S. and Gorna, K. (2007). Biodegradable polyurethane cancellous bone graft substitutes in the treatment of iliac crest defects. *Journal of Biomedical Materials Research Part A*, 80(1):94–101.

Gorna, K. and Gogolewski, S. (2003). Preparation, degradation, and calcification of biodegradable polyurethane foams for bone graft substitutes. *Journal of Biomedical Materials Research Part A*, 67A(3):813–827.

Gorna, K., Polowinski, S., and Gogolewski, S. (2002). Synthesis and characterization of biodegradable poly (ϵcaprolactone urethane) s. I. Effect of the polyol molecular weight, catalyst, and chain extender on the molecular and physical characteristics. *Journal of Polymer Science Part A: Polymer Chemistry*, 40(1):156–170.

Gorna K., G. S. (2006). Biodegradable porous polyurethane scaffolds for tissue repair and regeneration. *J. Biomed. Mater. Res.*, 79A(1):128–138.

Gorrasi, G., Vittoria, V., Murariu, M., Ferreira, A. D. S., Alexandre, M., and Dubois, P. (2008). Effect of filler content and size on transport properties of water vapor in PLA/calcium sulfate composites. *Biomacromolecules*, 9(3):984–990.

Goulet, J. A., Senunas, L. E., DeSilva, G. L., and Greenfield, M. L. V. H. (1997). Autogenous Iliac Crest Bone Graft: Complications and Functional Assessment. *Clinical*

orthopaedics and related research, 339:76–81.

Grad, S., Kupcsik, L., Gorna, K., Gogolewski, S., and Alini, M. (2003). The use of biodegradable polyurethane scaffolds for cartilage tissue engineering: potential and limitations. *Biomaterials*, 24(28):5163–5171.

Grassino, S. B. (2000). How a polymer gets dissolved. Online Source: http://pslc.ws/macrog/property/solpol/ps3.htm Accessed:23.03.2016.

Gregory, C. A., Gunn, W. G., Peister, A., and Prockop, D. J. (2004). An alizarin red-based assay of mineralization by adherent cells in culture: comparison with cetylpyridinium chloride extraction. *Analytical biochemistry*, 329(1):77–84.

Gregory, J. S., Waarsing, J. H., Day, J., Pols, H. A., Reijman, M., Weinans, H., and Aspden, R. M. (2007). Early identification of radiographic osteoarthritis of the hip using an active shape model to quantify changes in bone morphometric features: can hip shape tell us anything about the progression of osteoarthritis? *Arthritis & Rheumatism*, 56(11):3634–3643.

Greiner, A. and Wendorff, J. H. (2007). Electrospinning: a fascinating method for the preparation of ultrathin fibers. *Angewandte Chemie International Edition*, 46(30):5670–5703.

Griesser, H. J. (1991). Degradation of polyurethanes in biomedical applications a review. *Polymer degradation and stability*, 33(3):329–354.

Guarino, V. and Ambrosio, L. (2008). The synergic effect of polylactide fiber and calcium phosphate particle reinforcement in poly epsilon-caprolactone-based composite scaffolds. *Acta Biomaterialia*, 4(6):1778–1787.

Guelcher, S. A. (2008). Biodegradable polyurethanes: Synthesis and applications in regenerative medicine. *Tissue Engineering - Part B: Reviews*, 14(1):3–17.

Guelcher, S. A., Patel, V., Gallagher, K., Connolly, S., Didier, J. E., Doctor, J., and Hollinger, J. O. (2004). Synthesis of polyurethane foam scaffolds for bone tissue engineering. pages 6261–6263.

Gunatillake, P. A., Martin, D. J., Meijs, G. F., McCarthy, S. J., and Adhikari, R. (2003). Designing biostable polyurethane elastomers for biomedical implants. *Australian*

journal of chemistry, 56(6):545–557.

Gupta, T. K., Singh, B. P., Dhakate, S. R., Singh, V. N., and Mathur, R. B. (2013). Improved nanoindentation and microwave shielding properties of modified mwcnt reinforced polyurethane composites. *Journal of Materials Chemistry A*, 1(32):9138–9149.

Hale, L., Ma, Y., and Santerre, R. (2000). Semi-quantitative fluorescence analysis of calcein binding as a measurement of in vitro mineralization. *Calcified Tissue International*, 67(1):80–84.

Han, M., Giese, G., and Bille, J. (2005). Second harmonic generation imaging of collagen fibrils in cornea and sclera. *Optics Express*, 13(15):5791–5797.

Han, Z., Kong, H., Meng, J., Wang, C., Xie, S., and Xu, H. (2009). Electrospun aligned nanofibrous scaffold of carbon nanotubes-polyurethane composite for endothelial cells. *Journal of nanoscience and nanotechnology*, 9(2):1400–1402.

Harris, W. H. (1986). Etiology of osteoarthritis of the hip. *Clinical orthopaedics and related research*, 213:20–33.

Harrison, C. A., Heaton, M. J., Layton, C. M., and Mac Neil, S. (2006). Use of an in vitro model of tissue-engineered human skin to study keratinocyte attachment and migration in the process of reepithelialization. *Wound repair and regeneration*, 14(2):203–209.

Haugh, M. G., Murphy, C. M., and O'Brien, F. J. (2009). Novel freeze-drying methods to produce a range of collagen–glycosaminoglycan scaffolds with tailored mean pore sizes. *Tissue Engineering Part C: Methods*, 16(5):887–894.

Haycock, J. W. (2011). 3d cell culture: a review of current approaches and techniques. In *3D Cell Culture*, pages 1–15. Springer.

He, X., Xiao, Q., Lu, C., Wang, Y., Zhang, X., Zhao, J., Zhang, W., Zhang, X., and Deng, Y. (2014). Uniaxially aligned electrospun all-cellulose nanocomposite nanofibers reinforced with cellulose nanocrystals: scaffold for tissue engineering. *Biomacromolecules*, 15(2):618–627.

Health and Safety (2006). The health and safety executive - back pain statistics 2006. http://www.hse.gov.uk/. Date Accessed: 15/07/2015.

BIBLIOGRAPHY

Health and Safety (2011). The health and safety executive annual statistics report 2010/11. http://www.hse.gov.uk/statistics/overall/hssh1011.pdf. Date Accessed: 15/07/2015.

Heidemann, W., Jeschkeit, S., Ruffieux, K., Fischer, J. H., Wagner, M., Krüger, G., Wintermantel, E., and Gerlach, K. L. (2001). Degradation of poly (D, L) lactide implants with or without addition of calciumphosphates in vivo. *Biomaterials*, 22(17):2371–2381.

Heijkants, R., Van Tienen, T. G., De Groot, J. H., Pennings, A. J., Buma, P., Veth, R. P. H., and Schouten, A. J. (2006). Preparation of a polyurethane scaffold for tissue engineering made by a combination of salt leaching and freeze-drying of dioxane. *Journal of materials science*, 41(8):2423–2428.

Helfrich, M. H. and Ralston, S. H. (2003). *Bone research protocols*, volume 80. Springer.

Hench, L. L. (1980). Biomaterials. *Science*, 208(4446):826–831.

Hench, L. L. (1991). BIOCERAMICS - FROM CONCEPT TO CLINIC. *Journal of the American Ceramic Society*, 74(7):1487–1510.

Hench, L. L. (1998). Biomaterials: a forecast for the future. *Biomaterials*, 19(16):1419–1423.

Hench, L. L. and Polak, J. M. (2002). Third-generation biomedical materials. *Science*, 295(5557):1014–1017.

Hench, L. L., Splinter, R. J., Allen, W. C., and Greenlee, T. K. (1971). Bonding mechanisms at the interface of ceramic prosthetic materials. *Journal of Biomedical Materials Research*, 5(6):117–141.

Herø, H. k., Wie, H., Jø rgensen, R. B., and Ruyter, I. (1994). Hydroxyapatite coatings on Ti produced by hot isostatic pressing. *Journal of Biomedical Materials Research*, 28(3):343–348.

Hill, C. M., An, Y. H., Kang, Q. K., Hartsock, L. A., Gogolewski, S., and Gorna, K. (2007). Osteogenesis of Osteoblast Seeded Polyurethane-Hydroxyapatite Scaffolds in Nude Mice. In *Macromolecular Symposia*, volume 253, pages 94–97. Wiley Online Library.

Hillary, C., Roman, S., Bullock, A., Chapple, C., and MacNeil, S. (2015). Response of scaffold materials designed for treatment of stress urinary incontinence (sui) and pelvic organ prolapse (pop) to distension. In *NEUROUROLOGY AND URODYNAMICS*, volume 34, pages S291–S292. WILEY-BLACKWELL 111 RIVER ST, HOBOKEN 07030-5774, NJ USA.

Hillary, C. J., Roman, S., Bullock, A. J., Green, N. H., Chapple, C. R., and MacNeil, S. (2016). Developing repair materials for stress urinary incontinence to withstand dynamic distension. *PloS one*, 11(3):e0149971.

Hillsley, M. V. and Frangos, J. A. (1994). Review: Bone tissue engineering: The role of interstitial fluid flow. *Biotechnology and Bioengineering*, 43(7):573–581.

Hing, K. A., Best, S. M., and Bonfield, W. (1999). Characterization of porous hydroxyapatite. *Journal of Materials Science: Materials in Medicine*, 10(3):135–145.

Hing, K. A., Revell, P. A., Smith, N., and Buckland, T. (2006). Effect of silicon level on rate, quality and progression of bone healing within silicate-substituted porous hydroxyapatite scaffolds. *Biomaterials*, 27(29):5014–5026.

Ho, A., Wagner, W., and Franke, W. (2008). Heterogeneity of mesenchymal stromal cell preparations. *Cytotherapy*, 10(4):320–330.

Ho, S. T. and Hutmacher, D. W. (2006). A comparison of micro ct with other techniques used in the characterization of scaffolds. *Biomaterials*, 27(8):1362–1376.

Hofmann, S., Hagenmüller, H., Koch, A. M., Müller, R., Vunjak-Novakovic, G., Kaplan, D. L., Merkle, H. P., and Meinel, L. (2007). Control of in vitro tissue-engineered bone-like structures using human mesenchymal stem cells and porous silk scaffolds. *Biomaterials*, 28(6):1152–1162.

Holen, I., Nutter, F., Wilkinson, J., Evans, C., Avgoustou, P., and Ottewell, P. D. (2015). Human breast cancer bone metastasis in vitro and in vivo: a novel 3d model system for studies of tumour cell-bone cell interactions. *Clinical & experimental metastasis*, 32(7):689–702.

Hollinger, J. O. (1983). Preliminary -Report on the Osteogenic potential of a biodegrada2ble co-polymer of PLA and PGA . *Journal of Biomedical Materials*

BIBLIOGRAPHY

Research, 17(1):71–82.

Hollinger, J. O. (2005). *Bone Tissue Engineering*. CRC Press.

Hollinger, J. O., Brekke, J., Gruskin, E., and Lee, D. (1996). Role of bone substitutes. *Clinical orthopaedics and related research*, 324:55–65.

Hollinger, J. O. and Schmitz, J. P. (1997). Macrophysiologic roles of a delivery system for vulnerary factors needed for bone regeneration. *Bioartificial Organs: Science, Medicine, and Technology*, 831:427–437.

Hollinger, J. O., Winn, S., and Bonadio, J. (2000). Options for tissue engineering to address challenges of the aging skeleton. *Tissue engineering*, 6(4):341–350.

Holtrop, M. E. (1967). The potencies of the epiphyseal cartilage in endochondral ossification. *Proceedings of the Koninklijke Nederlandse Akademie van Wetenschappen. Series C. Biological and medical sciences*, 70(1):21.

Holy, C. E., Dang, S. M., Davies, J. E., and Shoichet, M. S. (1999). In vitro degradation of a novel poly(lactide-co-glycolide) 75/25 foam. *Biomaterials*, 20(13):1177–1185.

Home-Office (2014). Annual statistics of scientific procedures on living animals great britain 2013. http://www.understandinganimalresearch.org.uk/files/1214/1207/5255/home-office-animal-statistics Date Accessed: 14.05.15.

Hsu, W. K. and Wang, J. C. (2008). The use of bone morphogenetic protein in spine fusion. *The Spine Journal*, 8(3):419–425.

Huang, C., Ouyang, Y., Niu, H., He, N., Ke, Q., Jin, X., Li, D., Fang, J., Liu, W., Fan, C., et al. (2015). Nerve guidance conduits from aligned nanofibers: improvement of nerve regeneration through longitudinal nanogrooves on a fiber surface. *ACS applied materials & interfaces*, 7(13):7189–7196.

Huang, Y.-S., Kuo, C.-C., Shu, Y.-C., Jang, S.-C., Tsen, W.-C., Chuang, F.-S., and Chen, C.-C. (2014). Highly aligned and single-layered hollow fibrous membranes prepared from polyurethane and silica blends through a two-fluid coaxial electrospun process. *Macromolecular Chemistry and Physics*, 215(9):879–887.

Huang, Z. M., Zhang, Y. Z., Kotaki, M., and Ramakrishna, S. (2003). A review

on polymer nanofibers by electrospinning and their applications in nanocomposites. *Composites Science and Technology*, 63(15):2223–2253.

Huiskes, R., Weinans, H., and Van Rietbergen, B. (1992). The relationship between stress shielding and bone resorption around total hip stems and the effects of flexible materials. *Clinical orthopaedics and related research*, 274:124–134.

Hutmacher, D. W. (2000). Scaffolds in tissue engineering bone and cartilage. *Biomaterials*, 21(24):2529–2543.

Imam Khasim, H., Henning, S., Michler, G., and Brand, J. (2010). Development of nanocomposite scaffolds for bone tissue engineering. In *Macromolecular symposia*, volume 294, pages 144–152. Wiley Online Library.

Jabbar, S., Twentyman, P., and Watson, J. (1989). The mtt assay underestimates the growth inhibitory effects of interferons. *British journal of cancer*, 60(4):523.

Janik, H. and Marzec, M. (2015). A review: Fabrication of porous polyurethane scaffolds. *Materials Science and Engineering: C*, 48:586–591.

Janik, H., Pałys, B., and Petrovic, Z. S. (2003). Multiphase-separated polyurethanes studied by micro-raman spectroscopy. *Macromolecular rapid communications*, 24(3):265–268.

Jansen, J. A., Vehof, J. W. M., Ruhe, P. Q., Kroeze-Deutman, H., Kuboki, Y., Takita, H., Hedberg, E. L., and Mikos, A. G. (2005). Growth factor-loaded scaffolds for bone engineering. *Journal of Controlled Release*, 101(1):127–136.

Jarcho, M., Kay, J. F., Gumaer, K. I., Doremus, R. H., and Drobeck, H. P. (1977). Tissue, cellular and subcellular events at a bone-ceramic hydroxylapatite interface. *Journal of bioengineering*, 1(2):79.

Jasmund, I. and Bader, A. (2002). *Bioreactor developments for tissue engineering applications by the example of the bioartificial liver*, pages 99–109. Springer.

Jeon, K. C., Kim, B. S., Do Kim, Y., Suk, M.-J., and Oh, S.-T. (2015). Porous mo–30wt.% w alloys synthesized from camphene/moo 3–wo 3 slurry by freeze drying and sintering process. *International Journal of Refractory Metals and Hard Materials*.

Jia, L., Prabhakaran, M. P., Qin, X., Kai, D., and Ramakrishna, S. (2013).

BIBLIOGRAPHY

Biocompatibility evaluation of protein-incorporated electrospun polyurethane-based scaffolds with smooth muscle cells for vascular tissue engineering. *Journal of Materials Science*, 48(15):5113–5124.

Jones, A. C., Arns, C. H., Sheppard, A. P., Hutmacher, D. W., Milthorpe, B. K., and Knackstedt, M. A. (2007). Assessment of bone ingrowth into porous biomaterials using micro-ct. *Biomaterials*, 28(15):2491–2504.

Junqueira, L., Bignolas, G., and Brentani, R. (1979). A simple and sensitive method for the quantitative estimation of collagen. *Analytical biochemistry*, 94(1):96–99.

Kalita, S. J. and Verma, S. (2010). Nanocrystalline hydroxyapatite bioceramic using microwave radiation: Synthesis and characterization. *Materials Science and Engineering: C*, 30(2):295–303.

Kanis, J. A., Melton, L. J., Christiansen, C., Johnston, C. C., and Khaltaev, N. (1994). PERSPECTIVE - THE DIAGNOSIS OF OSTEOPOROSIS. *Journal of Bone and Mineral Research*, 9(8):1137–1141.

Kaplan, S. J., Hayes, W. C., Stone, J. L., and Beaupré, G. S. (1985). Tensile strength of bovine trabecular bone. *Journal of biomechanics*, 18(9):723–727.

Karlsson, C., Emanuelsson, K., Wessberg, F., Kajic, K., Axell, M. Z., Eriksson, P. S., Lindahl, A., Hyllner, J., and Strehl, R. (2009). Human embryonic stem cell-derived mesenchymal progenitors—potential in regenerative medicine. *Stem cell research*, 3(1):39–50.

Kasaj, A., Willershausen, B., Reichert, C., Gortan-Kasaj, A., Zafiropoulos, G.-G., and Schmidt, M. (2008). Human periodontal fibroblast response to a nanostructured hydroxyapatite bone replacement graft in vitro. *Archives of oral biology*, 53(7):683–689.

Kato, Y., Boskey, A., Spevak, L., Dallas, M., Hori, M., and Bonewald, L. (2001). Establishment of an osteoid preosteocyte-like cell mlo-a5 that spontaneously mineralizes in culture. *Journal of Bone and Mineral Research*, 16(9):1622–1633.

Kavlock, K. D., Pechar, T. W., Hollinger, J. O., Guelcher, S. A., and Goldstein, A. S. (2007). Synthesis and characterization of segmented poly(esterurethane urea) elastomers for bone tissue engineering. *Acta Biomaterialia*, 3(4):475–484.

Keaveny, T. M., Morgan, E. F., Niebur, G. L., and Yeh, O. C. (2001). Biomechanics of trabecular bone. *Annual review of biomedical engineering*, 3(1):307–333.

Keaveny, T. M., Wachtel, E. F., Ford, C. M., and Hayes, W. C. (1994). Differences between the tensile and compressive strengths of bovine tibial trabecular bone depend on modulus. *Journal of Biomechanics*, 27(9):1137–1146.

Khan, A. S., Ahmed, Z., Edirisinghe, M. J., Wong, F. S. L., and Rehman, I. U. (2008). Preparation and characterization of a novel bioactive restorative composite based on covalently coupled polyurethane-nanohydroxyapatite fibres. *Acta Biomaterialia*, 4(5):1275–1287.

Khil, M. S., Cha, D. I., Kim, H. Y., Kim, I. S., and Bhattarai, N. (2003). Electrospun nanofibrous polyurethane membrane as wound dressing. *Journal of Biomedical Materials Research Part B-Applied Biomaterials*, 67B(2):675–679.

Kieswetter, K., Schwartz, Z., Dean, D. D., and Boyan, B. D. (1996). The role of implant surface characteristics in the healing of bone. *Critical Reviews in Oral Biology & Medicine*, 7(4):329–345.

Klawitter, J. J. and Hulbert, S. F. (1971). Application of porous ceramics for the attachment of load bearing internal orthopedic applications. *Journal of Biomedical Materials Research*, 5(6):161–229.

Klein, C., Wolke, J. G. C., Blieck Hogervorst, D., and De Groot, K. (1994). Calcium phosphate plasma sprayed coatings and their stability: An in vivo study. *Journal of Biomedical Materials Research*, 28(8):909–917.

Knott, L. and Bailey, A. J. (1998). Collagen cross-links in mineralizing tissues: a review of their chemistry, function, and clinical relevance. *Bone*, 22(3):181.

Koh, A., Carpenter, A. W., Slomberg, D. L., and Schoenfisch, M. H. (2013). Nitric oxide-releasing silica nanoparticle-doped polyurethane electrospun fibers. *ACS applied materials & interfaces*, 5(16):7956–7964.

Kokubo, T., Miyaji, F., Kim, H.-M., and Nakamura, T. (1996). Spontaneous Formation of Bonelike Apatite Layer on Chemically Treated Titanium Metals. *Journal of the American Ceramic Society*, 79(4):1127–1129.

BIBLIOGRAPHY

Kolk, A., Handschel, J., Drescher, W., Rothamel, D., Kloss, F., Blessmann, M., Heiland, M., Wolff, K.-D., and Smeets, R. (2012). Current trends and future perspectives of bone substitute materials–From space holders to innovative biomaterials. *Journal of Cranio-Maxillofacial Surgery.*

Kordyum, V. (2001). Bioethics-its past, present and future. first nat. congr. *Bioethics (September 17-20, 2001, Kyiv): Abstracts. Kyiv*, pages 6–7.

Kucinska-Lipka, J., Gubanska, I., and Janik, H. (2013). Gelatin-Modified Polyurethanes for Soft Tissue Scaffold. *Scientific World Journal.*

Kupcsik, L. (2011). Estimation of cell number based on metabolic activity: the mtt reduction assay. In *Mammalian Cell Viability*, pages 13–19. Springer.

Kurien, T., Pearson, R., and Scammell, B. (2013). Bone graft substitutes currently available in orthopaedic practice the evidence for their use. *Bone & Joint Journal*, 95(5):583–597.

Kuwahara, N. (1963). On the polymer–solvent interaction in polymer solutions. *Journal of Polymer Science Part A: General Papers*, 1(7):2395–2406.

Langer, R. and Vacanti, J. (1993). Tissue engineering. *Science*, 260(5110):920–6.

Laszlo, A. (2004). Postmenopausal osteoporosis. *Orvosi Hetilap*, 145(1):3–13.

Laurencin, C. T., Ambrosio, A. M. A., Borden, M. D., and Cooper Jr, J. A. (1999). Tissue engineering: orthopedic applications. *Annual review of biomedical engineering*, 1(1):19–46.

Lee, C. H., Shin, H. J., Cho, I. H., Kang, Y.-M., Kim, I. A., Park, K.-D., and Shin, J.-W. (2005). Nanofiber alignment and direction of mechanical strain affect the ecm production of human acl fibroblast. *Biomaterials*, 26(11):1261–1270.

Lee, D., Assoku, E., and Doyle, V. (1998). A specific quantitative assay for collagen synthesis by cells seeded in collagen-based biomaterials using sirius red f3b precipitation. *Journal of Materials Science: Materials in Medicine*, 9(1):47–51.

Lee, J. B., Jeong, S. I., Bae, M. S., Yang, D. H., Heo, D. N., Kim, C. H., Alsberg, E., and Kwon, I. K. (2011). Highly porous electrospun nanofibers enhanced by ultrasonication for improved cellular infiltration. *Tissue Engineering Part A*, 17(21-22):2695–2702.

Lee, T. C. and Taylor, D. (1999). Bone remodelling: Should we cry wolff? *Irish journal of medical science*, 168(2):102–105.

Leong, M. F., Chan, W. Y., Chian, K. S., Rasheed, M. Z., and Anderson, J. M. (2010). Fabrication and in vitro and in vivo cell infiltration study of a bilayered cryogenic electrospun poly(D,L-lactide) scaffold. *Journal of Biomedical Materials Research Part A*, 94A(4):1141–1149.

Leslie, S. A. and Mitchell, J. C. (2007). Removing gold coating from sem samples. *palaeontology*, 50(6):1459–1461.

Leventon, W. (2008). Putting Implants to the Test. An MD&DI May 2008 Column- http://www.mddionline.com/article/putting-implants-test. Date Accessed: 31-05-2013.

Lewiecki, E. M. and Silverman, S. L. (2006). Redefining osteoporosis treatment: who to treat and how long to treat. *Arquivos Brasileiros de Endocrinologia & Metabologia*, 50(4):694–704.

Li, Z., Yubao, L., Aiping, Y., Xuelin, P., Xuejiang, W., and Xiang, Z. (2005). Preparation and in vitro investigation of chitosan/nano-hydroxyapatite composite used as bone substitute materials. *Journal of Materials Science: Materials in Medicine*, 16(3):213–219.

Lim, G. K., Wang, J., Ng, S. C., Chew, C. H., and Gan, L. M. (1997). Processing of hydroxyapatite via microemulsion and emulsion routes. *Biomaterials*, 18(21):1433–1439.

Lim, S. H., Liu, X. Y., Song, H., Yarema, K. J., and Mao, H.-Q. (2010). The effect of nanofiber-guided cell alignment on the preferential differentiation of neural stem cells. *Biomaterials*, 31(34):9031–9039.

Lin-Vien, D., Colthup, N. B., Fateley, W. G., and Grasselli, J. G. (1991). *The handbook of infrared and Raman characteristic frequencies of organic molecules*. Elsevier.

Linkhart, T. A., Mohan, S., and Baylink, D. J. (1996). Growth factors for bone growth and repair: IGF, TGFβ and BMP. *Bone*, 19(1):S1—-S12.

Liu, C., Abedian, R., Meister, R., Haasper, C., Hurschler, C., Krettek, C., von

BIBLIOGRAPHY

Lewinski, G., and Jagodzinski, M. (2012). Influence of perfusion and compression on the proliferation and differentiation of bone mesenchymal stromal cells seeded on polyurethane scaffolds. *Biomaterials*, 33(4):1052–1064.

Loh, Q. L. and Choong, C. (2013). Three-dimensional scaffolds for tissue engineering applications: role of porosity and pore size. *Tissue Engineering Part B: Reviews*, 19(6):485–502.

Lokesh, A. and Dhillon, M. (2006). Bioabsorbable implants in orthopaedics. *Indian Journal of Orthopaedics*, 40(4):205–209.

Lu, T., Li, Y., and Chen, T. (2013). Techniques for fabrication and construction of three-dimensional scaffolds for tissue engineering. *International journal of nanomedicine*, 8:337.

Lundvall, H. (1905). Weiteres über demonstration embryonaler skelette. *Anatomischer Anzeiger*, 27:520–523.

Luo, G., Teh, K. S., Liu, Y., Zang, X., Wen, Z., and Lin, L. (2015). Direct-write, self-aligned electrospinning on paper for controllable fabrication of three-dimensional structures. *ACS applied materials & interfaces*, 7(50):27765–27770.

Lv, Q. and Feng, Q. (2006). Preparation of 3-d regenerated fibroin scaffolds with freeze drying method and freeze drying/foaming technique. *Journal of Materials Science: Materials in Medicine*, 17(12):1349–1356.

Lyman, D. J. (1960). Polyurethanes. I. The solution polymerization of diisocyanates with ethylene glycol. *Journal of Polymer Science*, 45(145):49–59.

Ma, P. X. (2004). Scaffolds for tissue fabrication. *Materials today*, 7(5):30–40.

MacNeil, S. (2007). Progress and opportunities for tissue-engineered skin. *Nature*, 445(7130):874–880.

Mahadevan-Jansen, A. and Richards-Kortum, R. R. (1996). Raman spectroscopy for the detection of cancers and precancers. *Journal of Biomedical Optics*, 1(1):31–70.

Mahfuz, H., Rangari, V. K., Islam, M. S., and Jeelani, S. (2004). Fabrication, synthesis and mechanical characterization of nanoparticles infused polyurethane foams. *Composites Part A: Applied Science and Manufacturing*, 35(4):453–460.

Malkusch, W., Rehn, B., and Bruch, J. (1995). Advantages of sirius red staining for quantitative morphometric collagen measurements in lungs. *Experimental lung research*, 21(1):67–77.

Maniadakis, N. and Gray, A. (2000). The economic burden of back pain in the uk. *Pain*, 84(1):95–103.

Maquet, V., Boccaccini, A. R., Pravata, L., Notingher, I., and Jerome, R. (2004). Porous poly (α-hydroxyacid)/Bioglass® composite scaffolds for bone tissue engineering. I: preparation and in vitro characterisation. *Biomaterials*, 25(18):4185–4194.

Marchant, R., Zhao, Q., Anderson, J., and Hiltner, A. (1987). Degradation of a poly (ether urethane urea) elastomer: infra-red and xps studies. *Polymer*, 28(12):2032–2039.

Marchant, R. E., Miller, K. M., and Anderson, J. M. (1984). In vivo biocompatibility studies. V. In vivo leukocyte interactions with biomer. *Journal of Biomedical Materials Research*, 18(9):1169–1190.

Marotta, M. and Martino, G. (1985). Sensitive spectrophotometric method for the quantitative estimation of collagen. *Analytical biochemistry*, 150(1):86–90.

Marra, K. G., Szem, J. W., Kumta, P. N., DiMilla, P. A., and Weiss, L. E. (1999). In vitro analysis of biodegradable polymer blend/hydroxyapatite composites for bone tissue engineering. *Journal of Biomedical Materials Research*, 47(3):324–335.

Martin, I., Miot, S., Barbero, A., Jakob, M., and Wendt, D. (2007). Osteochondral tissue engineering. *Journal of Biomechanics*, 40(4):750 – 765.

Martin, I., Wendt, D., and Heberer, M. (2004). The role of bioreactors in tissue engineering. *Trends in Biotechnology*, 22(2):80–86.

Martin, T. P. (1996). Shells of atoms. *Physics Reports*, 273(4):199–241.

Martinez-Valencia, A. B., la Torre, G., Torres-Sanchez, R., Tellez-Jurado, L., and Esparza-Ponce, H. E. (2011). Production of polyurethane/nano-hydroxyapatite hybrid materials and microstructural characterization. *Int. J. Phys. Sci*, 6(11):2731–2743.

Martini, L., Fini, M., Giavaresi, G., and Giardino, R. (2001). Sheep model in orthopedic research: a literature review. *Comparative medicine*, 51(4):292–299.

Mauney, J. R., Jaquiéry, C., Volloch, V., Heberer, M., Martin, I., and Kaplan, D. L.

BIBLIOGRAPHY

(2005). In vitro and in vivo evaluation of differentially demineralized cancellous bone scaffolds combined with human bone marrow stromal cells for tissue engineering. *Biomaterials*, 26(16):3173.

Mayer, M. H. and Hollinger, J. O. (1995). Biodegradable bone fixation devices. *Biomedical applications of synthetic biodegradable polymers*, pages 173–195.

McClure, M. J., Wolfe, P. S., Simpson, D. G., Sell, S. A., and Bowlin, G. L. (2012). The use of air-flow impedance to control fiber deposition patterns during electrospinning. *Biomaterials*, 33(3):771–779.

McKoy, B. E., An, Y. H., and Friedman, R. J. (2000). Factors affecting the strength of the bone-implant interface. *Mechanical testing of bone and the bone-implant interface*, pages 439–462.

McLeod, M. J. (1980). Differential staining of cartilage and bone in whole mouse fetuses by alcian blue and alizarin red s. *Teratology*, 22(3):299–301.

McMahon, R. E., Qu, X., Jimenez-Vergara, A. C., Bashur, C. A., Guelcher, S. A., Goldstein, A. S., and Hahn, M. S. (2011). Hydrogel–Electrospun Mesh Composites for Coronary Artery Bypass Grafts. *Tissue Engineering Part C: Methods*, 17(4):451–461.

Meinel, L., Karageorgiou, V., Hofmann, S., Fajardo, R., Snyder, B., Li, C., Zichner, L., Langer, R., Vunjak-Novakovic, G., and Kaplan, D. L. (2004). Engineering bone-like tissue in vitro using human bone marrow stem cells and silk scaffolds. *Journal of Biomedical Materials Research Part A*, 71(1):25–34.

Meng, J., Han, Z., Kong, H., Qi, X., Wang, C., Xie, S., and Xu, H. (2010). Electrospun aligned nanofibrous composite of mwcnt/polyurethane to enhance vascular endothelium cells proliferation and function. *Journal of Biomedical Materials Research Part A*, 95(1):312–320.

Merz, W. A. and Schenk, R. K. (1970). A quantitative histological study on bone formation in human cancellous bone. *Cells Tissues Organs*, 76(1):1–15.

Mi, H.-Y., Palumbo, S., Jing, X., Turng, L.-S., Li, W.-J., and Peng, X.-F. (2014). Thermoplastic polyurethane/hydroxyapatite electrospun scaffolds for bone tissue engineering: Effects of polymer properties and particle size. *Journal of Biomedical*

Materials Research Part B: Applied Biomaterials, pages n/a—-n/a.

Mi, H.-Y., Salick, M. R., Jing, X., Crone, W. C., Peng, X.-F., and Turng, L.-S. (2015). Electrospinning of unidirectionally and orthogonally aligned thermoplastic polyurethane nanofibers: Fiber orientation and cell migration. *Journal of Biomedical Materials Research Part A*, 103(2):593–603.

Miller, L. M. (2002). Infrared microsperctroscopy and imaging. *Retrieved in October.*

Miller-Chou, B. A. and Koenig, J. L. (2003). A review of polymer dissolution. *Progress in Polymer Science*, 28(8):1223–1270.

Milleret, V., Simona, B., Neuenschwander, P., and Hall, H. (2011). Tuning electrospinning parameters for production of 3D-fiber-fleeces with increased porosity for soft tissue engineering applications. *Eur Cell Mater*, 21:286–303.

Mo, C., Yuan, Z., Zhang, L., and Xie, C. (1993). Infrared absorption spectra of nano-alumina. *Nanostructured Materials*, 2(1):47–54.

Mondrinos, M. J., Koutzaki, S., Lelkes, P. I., and Finck, C. M. (2007). A tissue-engineered model of fetal distal lung tissue. *American journal of physiology-lung cellular and molecular physiology*, 293(3):L639–L650.

Moore, K. L. and Dalley, A. F. (1999). *Clinically oriented anatomy*. Lippincott Williams & Wilkins.

Mosmann, T. (1983). Rapid colorimetric assay for cellular growth and survival: application to proliferation and cytotoxicity assays. *Journal of immunological methods*, 65(1):55–63.

Muggli, D. S., Burkoth, A. K., Keyser, S. A., Lee, H. R., and Anseth, K. S. (1998). Reaction behavior of biodegradable, photo-cross-linkable polyanhydrides. *Macromolecules*, 31(13):4120–4125.

Murphy, C. M., Haugh, M. G., and O'Brien, F. J. (2010). The effect of mean pore size on cell attachment, proliferation and migration in collagen–glycosaminoglycan scaffolds for bone tissue engineering. *Biomaterials*, 31(3):461–466.

Murshid, S. A., Kamioka, H., Ishihara, Y., Ando, R., Sugawara, Y., and Takano-Yamamoto, T. (2007). Actin and microtubule cytoskeletons of the processes

BIBLIOGRAPHY

of 3d-cultured mc3t3-e1 cells and osteocytes. *Journal of bone and mineral metabolism*, 25(3):151–158.

Nandi, S., Roy, S., Mukherjee, P., Kundu, B., De, D., and Basu, D. (2010). Orthopaedic applications of bone graft & graft substitutes: a review.

Navarro, M., Ginebra, M. P., Planell, J. A., Barrias, C. C., and Barbosa, M. A. (2005). In vitro degradation behavior of a novel bioresorbable composite material based on PLA and a soluble CaP glass. *Acta biomaterialia*, 1(4):411–420.

Navarro, M., Michiardi, A., Castano, O., and Planell, J. A. (2008). Biomaterials in orthopaedics. *Journal of the Royal Society Interface*, 5(27):1137–1158.

NHS (2012). Paget's disease. NHS Choices - http://www.nhs.uk/Conditions/Pagets-disease/P... Go to this Web page. Date Accessed : 03.04.2013.

Nirmala, R., Kang, H.-S., El-Newehy, M. H., Navamathavan, R., Park, H.-M., and Kim, H. Y. (2011). Human Osteoblast Cytotoxicity Study of Electrospun Polyurethane/Calcium Chloride Ultrafine Nanofibers. *Journal of Nanoscience and Nanotechnology*, 11(6):4749–4756.

NJR (2012). National Joint Registry for England and Wales, 9th Annual Report. National Joint Registery - http://www.njrcentre.org.uk/NjrCentre/Portals/0/Documents/England/Reports/9th_annual_repo 9th Annual Report 2012.pdf. Date Accessed: 20.01.2013.

NJR (2014). National joint registry 11th annual report. http://www.njrreports.org.uk/hips-all-procedures-activity. Date Accessed: 21.07.15.

O'Brien, J., Wilson, I., Orton, T., and Pognan, F. (2000a). Investigation of the alamar blue (resazurin) fluorescent dye for the assessment of mammalian cell cytotoxicity. *European Journal of Biochemistry*, 267(17):5421–5426.

O'Brien, J., Wilson, I., Orton, T., and Pognan, F. (2000b). Investigation of the alamar blue (resazurin) fluorescent dye for the assessment of mammalian cell cytotoxicity. *European Journal of Biochemistry*, 267(17):5421–5426.

Oonishi, H., Kushitani, S., Iwaki, H., Saka, K., Ono, H., Tamura, A., Sugihara, T.,

Hench, L. L., Wilson, J., and Tsuji, E. (1995). Comparative bone formation in several kinds of bioceramic granules. *Bioceramics*, 8:137–144.

Oprea, S. (2005). Effect of solvent interactions on the properties of polyurethane films. *High Performance Polymers*, 17(2):163–173.

Pangman et al. (1958). Compound prosthesis device. US Patent 2,842,775.

Pangman, W. J. (1968). Compound prosthesis. US Patent 3,366,975.

Papadimitropoulos, A., Scherberich, A., Guven, S., Theilgaard, N., Crooijmans, H., Santini, F., Scheffler, K., Zallone, A., and Martin, I. (2011). A 3d in vitro bone organ model using human progenitor cells. *Eur Cell Mater*, 21:445–58.

Parirokh, M., Mirsoltani, B., Raoof, M., Tabrizchi, H., and Haghdoost, A. (2011). Comparative study of subcutaneous tissue responses to a novel root-end filling material and white and grey mineral trioxide aggregate. *International endodontic journal*, 44(4):283–289.

Parliament, T. E. and Union, T. C. O. T. E. (2010). Directive 2010/63/eu of the european parliament and of the council of 22 september 2010 on the protection of animals used for scientific purposes. http://eur-lex.europa.eu/LexUriServ/LexUriServ.do?uri=OJ:L:2010:276:0033:0079:en:PDF. Date Accessed: 18/01/2016.

Paschalis, E., DiCarlo, E., Betts, F., Sherman, P., Mendelsohn, R., and Boskey, A. (1996). Ftir microspectroscopic analysis of human osteonal bone. *Calcified tissue international*, 59(6):480–487.

Patel, N., Best, S. M., Bonfield, W., Gibson, I. R., Hing, K. A., Damien, E., and Revell, P. A. (2002). A comparative study on the in vivo behavior of hydroxyapatite and silicon substituted hydroxyapatite granules. *Journal of Materials Science: Materials in Medicine*, 13(12):1199–1206.

Paul, H., Reginato, A. J., and Ralph Schumacher, H. (1983). Alizarin red s staining as a screening test to detect calcium compounds in synovial fluid. *Arthritis & Rheumatism*, 26(2):191–200.

Pautke, C., SCHIEKER, M., TISCHER, T., KOLK, A., NETH, P., MUTSCHLER, W.,

BIBLIOGRAPHY

and MILZ, S. (2004). Characterization of osteosarcoma cell lines mg-63, saos-2 and u-2 os in comparison to human osteoblasts. *Anticancer research*, 24(6):3743–3748.

Pautke, C., Vogt, S., Tischer, T., Wexel, G., Deppe, H., Milz, S., Schieker, M., and Kolk, A. (2005). Polychrome labeling of bone with seven different fluorochromes: enhancing fluorochrome discrimination by spectral image analysis. *Bone*, 37(4):441–445.

Pearce, A. I., Richards, R. G., Milz, S., Schneider, E., and Pearce, S. G. (2007). Animal models for implant biomaterial research in bone: a review. *Eur Cell Mater*, 13(1):1–10.

Pedicini, A. and Farris, R. J. (2003). Mechanical behavior of electrospun polyurethane. *Polymer*, 44(22):6857–6862.

Pelker, R. R., Friedlaender, G. E., and Markham, T. C. (1983). Biomechanical Properties of Bone Allografts. *Clinical orthopaedics and related research*, 174:54–57.

Pendegrass, C., El-Husseiny, M., and Blunn, G. (2012). The development of fibronectin-functionalised hydroxyapatite coatings to improve dermal fibroblast attachment in vitro. *J Bone Joint Surg Br*, 94(4):564–569.

Penel, G., Leroy, G., Rey, C., and Bres, E. (1998). Microraman spectral study of the po4 and co3 vibrational modes in synthetic and biological apatites. *Calcified Tissue International*, 63(6):475–481.

Pereira, M. M., Jones, J. R., and Hench, L. L. (2005). Bioactive glass and hybrid scaffolds prepared by sol–gel method for bone tissue engineering. *Advances in applied ceramics*, 104(1):35–42.

PETA (2015). More than $16 billion in taxpayer money wasted annually on animal testing. People for the Ethical Treatment of Animals - http://www.peta.org/features/16-billion-taxpayer-money-wasted-annually-animal-testing/. Date Accessed: 14.07. 2015.

Petite, H., Viateau, V., Bensaid, W., Meunier, A., de Pollak, C., Bourguignon, M., Oudina, K., Sedel, L., and Guillemin, G. (2000). Tissue-engineered bone regeneration. *Nature biotechnology*, 18(9):959–963.

Pfeifer, M. and Pollahne, W. (2011). Diagnostic of Paget's disease by X-rays. *Osteologie*, 20(2):128–133.

Pittenger, M. F., Mackay, A. M., Beck, S. C., Jaiswal, R. K., Douglas, R., Mosca, J. D., Moorman, M. A., Simonetti, D. W., Craig, S., and Marshak, D. R. (1999). Multilineage potential of adult human mesenchymal stem cells. *science*, 284(5411):143–147.

Popescu, L., Piticescu, R., Antonelli, A., Rusti, C., Carboni, E., Sfara, C., Magnani, M., Badilita, V., Vasile, E., Trusca, R., et al. (2013). Recent advances in synthesis, characterization of hydroxyapatite/polyurethane composites and study of their biocompatible properties. *Journal of Materials Science: Materials in Medicine*, 24(11):2491–2503.

Porter, A. E., Patel, N., Skepper, J. N., Best, S. M., and Bonfield, W. (2004). Effect of sintered silicate-substituted hydroxyapatite on remodelling processes at the bone–implant interface. *Biomaterials*, 25(16):3303–3314.

Powell, C. A., Smiley, B. L., Mills, J., and Vandenburgh, H. H. (2002). Mechanical stimulation improves tissue-engineered human skeletal muscle. *American Journal of Physiology-Cell Physiology*, 283(5):C1557—-C1565.

Puchtler, H., Meloan, S. N., and Terry, M. S. (1969). On the history and mechanism of alizarin and alizarin red s stains for calcium. *Journal of Histochemistry & Cytochemistry*, 17(2):110–124.

Radin, E. L. and Rose, R. M. (1986). Role of subchondral bone in the initiation and progression of cartilage damage. *Clinical orthopaedics and related research*, 213:34–40.

Raghavan, P., Lim, D.-H., Ahn, J.-H., Nah, C., Sherrington, D. C., Ryu, H.-S., and Ahn, H.-J. (2012). Electrospun polymer nanofibers: The booming cutting edge technology. *Reactive & Functional Polymers*, 72(12):915–930.

Rahn, B. A. and Perren, S. M. (1971). Xylenol orange, a fluorochrome useful in polychrome sequential labeling of calcifying tissues. *Biotechnic & Histochemistry*, 46(3):125–129.

Ralston, S. H. (2009). Bone structure and metabolism. *Medicine*, 37(9):469–474.

Rao, R. R., Roopa, H. N., and Kannan, T. S. (1997). Solid state synthesis and thermal stability of HAP and HAP – β-TCP composite ceramic powders. *Journal of Materials Science: Materials in Medicine*, 8(8):511–518.

BIBLIOGRAPHY

Ratner, B. D., Gladhill, K. W., and Horbett, T. A. (1988). Analysis of in vitro enzymatic and oxidative degradation of polyurethanes. *Journal of Biomedical Materials Research*, 22(6):509–527.

Rehman, I. and Bonfield, W. (1997). Characterization of hydroxyapatite and carbonated apatite by photo acoustic FTIR spectroscopy. *Journal of Materials Science: Materials in Medicine*, 8(1):1–4.

Rehman, I., Smith, R., Hench, L., and Bonfield, W. (1995). Structural evaluation of human and sheep bone and comparison with synthetic hydroxyapatite by ft-raman spectroscopy. *Journal of biomedical materials research*, 29(10):1287–1294.

Reilly, D. T., Burstein, A. H., and Frankel, V. H. (1974). The elastic modulus for bone. *Journal of Biomechanics*, 7(3):271–275.

Reneker, D. H. and Chun, I. (1996). Nanometre diameter fibres of polymer, produced by electrospinning. *Nanotechnology*, 7(3):216–223.

Rezwan, K., Chen, Q. Z., Blaker, J. J., and Boccaccini, A. R. (2006). Biodegradable and bioactive porous polymer/inorganic composite scaffolds for bone tissue engineering. *Biomaterials*, 27(18):3413–3431.

Rho, J.-Y., Kuhn-Spearing, L., and Zioupos, P. (1998). Mechanical properties and the hierarchical structure of bone. *Medical Engineering & Physics*, 20(2):92–102.

Riboldi, S., Sadr, N., Pigini, L., Neuenschwander, P., Simonet, M., Mognol, P., Sampaolesi, M., Cossu, G., and Mantero, S. (2008). Skeletal myogenesis on highly orientated microfibrous polyesterurethane scaffolds. *Journal of Biomedical Materials Research Part A*, 84(4):1094–1101.

Risbud, M. V. and Sittinger, M. (2002). Tissue engineering: advances in in vitro cartilage generation. *TRENDS in Biotechnology*, 20(8):351–356.

Rokkanen, P. U., Böstman, O., Hirvensalo, E., Mäkelä, E. A., Partio, E. K., Pätiälä, H., Vainionpää, S., Kimmo, V., and Törmälä, P. (2000). Bioabsorbable fixation in orthopaedic surgery and traumatology. *Biomaterials*, 21(24):2607–2613.

Roman, S., Urbánková, I., Callewaert, G., Lesage, F., Hillary, C., Osman, N. I., Chapple, C. R., Deprest, J., and MacNeil, S. (2016). Evaluating alternative materials for the

treatment of stress urinary incontinence and pelvic organ prolapse: a comparison of the in vivo response to meshes implanted in rabbits. *The Journal of urology.*

Rosser, J. and Bonewald, L. F. (2012). *Studying osteocyte function using the cell lines MLO-Y4 and MLO-A5*, pages 67–81. Springer.

Rottmar, M., Richter, M., Mäder, X., Grieder, K., Nuss, K., Karol, A., von Rechenberg, B., Zimmermann, E., Buser, S., Dobmann, A., et al. (2016). In vitro investigations of a novel wound dressing concept based on biodegradable polyurethane. *Science and Technology of Advanced Materials.*

Ruoslahti, E. (1991). Integrins. *Journal of Clinical Investigation*, 87(1):1.

Russell, J. L. and Block, J. E. (1999). Clinical utility of demineralized bone matrix for osseous defects, arthrodesis, and reconstruction: impact of processing techniques and study methodology. *Orthopedics*, 22(5):524.

Sachlos, E. and Czernuszka, J. T. (2003). Making tissue engineering scaffolds work: Review on the application of solid freeform fabrication technology to the production of tissue engineering scaffolds. *European Cells & Materials*, 5(January-June Cited July 25, 2003):29–40.

Sarig, S. and Kahana, F. (2002). Rapid formation of nanocrystalline apatite. *Journal of Crystal Growth*, 237–239, Part 1(0):55–59.

Scharla, S. (2011). Paget's disease of bone - clinical symptoms and changes in biochemical markers. *Osteologie*, 20(2):109–113.

Schliephake, H., Zghoul, N., Jäger, V., van Griensven, M., Zeichen, J., Gelinsky, M., and Wülfing, T. (2009). Effect of seeding technique and scaffold material on bone formation in tissue-engineered constructs. *Journal of Biomedical Materials Research Part A*, 90A(2):429–437.

Schollen.Cs and Stewart, F. D. (1973). Thermoplastic polyurethane hydrolysis stability. *Angewandte Makromolekulare Chemie*, 29-3:413–430.

Schreader, K. J., Bayer, I. S., Milner, D. J., Loth, E., and Jasiuk, I. (2013). A polyurethane-based nanocomposite biocompatible bone adhesive. *Journal of Applied Polymer Science*, 127(6):4974–4982.

BIBLIOGRAPHY

Scudiero, D. A., Shoemaker, R. H., Paull, K. D., Monks, A., Tierney, S., Nofziger, T. H., Currens, M. J., Seniff, D., and Boyd, M. R. (1988). Evaluation of a soluble tetrazolium/formazan assay for cell growth and drug sensitivity in culture using human and other tumor cell lines. *Cancer Research*, 48(17):4827–4833.

Seitz, S., Priemel, M., von Domarus, C., Beil, F. T., Barvencik, F., Amling, M., and Rueger, J. M. (2008). The Second Most Common Bone Disease: A Review on Paget's Disease of Bone. *European Journal of Trauma and Emergency Surgery*, 34(6):549–553.

Sell, S. A., Wolfe, P. S., Garg, K., McCool, J. M., Rodriguez, I. A., and Bowlin, G. L. (2010). The use of natural polymers in tissue engineering: a focus on electrospun extracellular matrix analogues. *Polymers*, 2(4):522–553.

Shawon, J. and Sung, C. (2004). Electrospinning of polycarbonate nanofibers with solvent mixtures thf and dmf. *Journal of materials science*, 39(14):4605–4613.

Shea, L. D., Wang, D., Franceschi, R. T., and Mooney, D. J. (2000). Engineered bone development from a pre-osteoblast cell line on three-dimensional scaffolds. *Tissue engineering*, 6(6):605–617.

Shearer, H., Ellis, M. J., Perera, S. P., and Chaudhuri, J. B. (2006). Effects of common sterilization methods on the structure and properties of poly (d, l lactic-co-glycolic acid) scaffolds. *Tissue engineering*, 12(10):2717–2727.

Sheikh, F. A., Kanjwal, M. A., Saran, S., Chung, W.-J., and Kim, H. (2011). Polyurethane nanofibers containing copper nanoparticles as future materials. *Applied Surface Science*, 257(7):3020–3026.

Shin, S.-H., Purevdorj, O., Castano, O., Planell, J. A., and Kim, H.-W. (2012). A short review: recent advances in electrospinning for bone tissue regeneration. *Journal of tissue engineering*, 3(1):2041731412443530.

Sirivisoot, S. and Harrison, B. S. (2011). Skeletal myotube formation enhanced by electrospun polyurethane carbon nanotube scaffolds. *Int. J. Nanomedicine*, 6:2483–2497.

Sittichockechaiwut, A., Scutt, A. M., Ryan, A. J., Bonewald, L. F., and Reilly, G. C. (2009). Use of rapidly mineralising osteoblasts and short periods of mechanical loading

to accelerate matrix maturation in 3D scaffolds. *Bone*, 44(5):822–829.

Sittichokechaiwut, A., Edwards, J. H., Scutt, A. M., and Reilly, G. C. (2010). Short bouts of mechanical loading are as effective as dexamethasone at inducing matrix production by human bone marrow mesenchymal stem cell. *Eur Cell Mater*, 20:45–57.

Spaans, C. J., De Groot, J. H., Belgraver, V. W., and Pennings, A. J. (1998). A new biomedical polyurethane with a high modulus based on 1,4-butanediisocyanate and epsilon-caprolactone. *Journal of Materials Science-Materials in Medicine*, 9(12):675–678.

Stoddart, M. J. (2011). Cell viability assays: introduction. In *Mammalian Cell Viability*, pages 1–6. Springer.

Stolzing, A., Jones, E., McGonagle, D., and Scutt, A. (2008). Age-related changes in human bone marrow-derived mesenchymal stem cells: consequences for cell therapies. *Mechanisms of ageing and development*, 129(3):163–173.

Strober, W. (2001). Trypan blue exclusion test of cell viability. *Current protocols in immunology*, pages A–3B.

Subramanian, A., Krishnan, U. M., and Sethuraman, S. (2011). Fabrication of uniaxially aligned 3d electrospun scaffolds for neural regeneration. *Biomedical Materials*, 6(2):025004.

Subramanian, B., Rudym, D., Cannizzaro, C., Perrone, R., Zhou, J., and Kaplan, D. L. (2010). Tissue-engineered three-dimensional in vitro models for normal and diseased kidney. *Tissue Engineering Part A*, 16(9):2821–2831.

Suuronen, E. J., Nakamura, M., Watsky, M. A., Stys, P. K., Müller, L. J., Munger, R., Shinozaki, N., and Griffith, M. (2004). Innervated human corneal equivalents as in vitro models for nerve-target cell interactions. *The FASEB journal*, 18(1):170–172.

Sweat, F., Puchtler, H., and Rosenthal, S. I. (1964). Sirius red f3ba as a stain for connective tissue. *Archives of pathology*, 78:69–72.

Szycher, M. (1988). Biostability of polyurethane elastomers: a critical review. *Journal of biomaterials applications*, 3(2):297–402.

Taboas, J., Maddox, R., Krebsbach, P., and Hollister, S. (2003). Indirect solid free form

fabrication of local and global porous, biomimetic and composite 3d polymer-ceramic scaffolds. *Biomaterials*, 24(1):181–194.

Tada, H., Shiho, O., Kuroshima, K.-i., Koyama, M., and Tsukamoto, K. (1986). An improved colorimetric assay for interleukin 2. *Journal of immunological methods*, 93(2):157–165.

Takahashi, Y., Yamamoto, M., and Tabata, Y. (2005). Osteogenic differentiation of mesenchymal stem cells in biodegradable sponges composed of gelatin and β-tricalcium phosphate. *Biomaterials*, 26(17):3587–3596.

Tang, C., Chen, P., and Liu, H. (2008). Cocontinuous cellulose acetate/polyurethane composite nanofiber fabricated through electrospinning. *Polymer Engineering & Science*, 48(7):1296–1303.

Taylor, M. J. and Hunt, C. J. (1981). Dual staining of corneal endothelium with trypan blue and alizarin red s: importance of ph for the dye-lake reaction. *British Journal of Ophthalmology*, 65(12):815–819.

Tetteh, G., Khan, A., Delaine-Smith, R., Reilly, G., and Rehman, I. (2014). Electrospun polyurethane/hydroxyapatite bioactive scaffolds for bone tissue engineering: The role of solvent and hydroxyapatite particles. *journal of the mechanical behavior of biomedical materials*, 39:95–110.

Theron, A., Zussman, E., and Yarin, A. (2001). Electrostatic field-assisted alignment of electrospun nanofibres. *Nanotechnology*, 12(3):384.

Thian, E. S., Huang, J., Best, S. M., Barber, Z. H., Brooks, R. A., Rushton, N., and Bonfield, W. (2006). The response of osteoblasts to nanocrystalline silicon-substituted hydroxyapatite thin films. *Biomaterials*, 27(13):2692–2698.

Tibbitt, M. W. and Anseth, K. S. (2009). Hydrogels as extracellular matrix mimics for 3d cell culture. *Biotechnology and bioengineering*, 103(4):655–663.

Tjong, S. C. (2006). Structural and mechanical properties of polymer nanocomposites. *Materials Science and Engineering: R: Reports*, 53(3):73–197.

TNC (2001). Introduction to Fourier Transform Infrared Spectrometry. Thermo Nicolet Corporation - http://mmrc.caltech.edu/FTIR/FTIRintro.pdf.

Tommila, M., Jokilammi, A., Terho, P., Wilson, T., Penttinen, R., and Ekholm, E. (2009). Hydroxyapatite coating of cellulose sponges attracts bone-marrow-derived stem cells in rat subcutaneous tissue. *Journal of The Royal Society Interface*, 6(39):873–880.

Tortelli, F. and Cancedda, R. (2009). Three-dimensional cultures of osteogenic and chondrogenic cells: a tissue engineering approach to mimic bone and cartilage in vitro. *Eur Cell Mater*, 17:1–14.

Tsui, Y. K. and Gogolewski, S. (2009). Microporous biodegradable polyurethane membranes for tissue engineering. *Journal of Materials Science: Materials in Medicine*, 20(8):1729–1741.

Ulery, B. D., Nair, L. S., and Laurencin, C. T. (2011). Biomedical Applications of Biodegradable Polymers. *Journal of Polymer Science Part B-Polymer Physics*, 49(12):832–864.

Ulrich, H. (1983). Urethane polymers. *Kirk-Othmer Encyclopedia of Chemical Technology*, 23:576–608.

Unsworth, B. R. and Lelkes, P. I. (1998). Growing tissues in microgravity. *Nature Medicine*, 4(8):901–907.

ur Rehman, I., Movasaghi, Z., and Rehman, S. (2012). *Vibrational spectroscopy for tissue analysis*. CRC Press.

Urist, M. R., Silverman, B. F., Buring, K., Dubuc, F. L., and Rosenberg, J. M. (1967). The bone induction principle. *Clinical orthopaedics and related research*, 53:243–283.

van Gaalen, S. M., Kruyt, M. C., Geuze, R. E., de Bruijn, J. D., Alblas, J., and Dhert, W. J. (2010). Use of fluorochrome labels in in vivo bone tissue engineering research. *Tissue engineering Part B: Reviews*, 16(2):209–217.

Van Heest, A. and Swiontkowski, M. (1999). Bone-graft substitutes. *The Lancet*, 353:S28–S29.

Vetsch, J. R., Müller, R., and Hofmann, S. (2015). The evolution of simulation techniques for dynamic bone tissue engineering in bioreactors. *Journal of tissue engineering and regenerative medicine*, 9(8):903–917.

Vingård, E., Alfredsson, L., Goldie, I., and Hogstedt, C. (1993). Sports and osteoarthrosis

of the hip an epidemiologic study. *The American journal of sports medicine*, 21(2):195–200.

Vos, T., Flaxman, A. D., Naghavi, M., Lozano, R., Michaud, C., and Others (2012). Years lived with disability (YLDs) for 1160 sequelae of 289 diseases and injuries 1990?2010: a systematic analysis for the Global Burden of Disease Study 2010. *The Lancet*, 380(9859):2163–2196.

Vunjak-Novakovic, G., Freed, L. E., Biron, R. J., and Langer, R. (1996). Effects of mixing on the composition and morphology of tissue-engineered cartilage. *AIChE Journal*, 42(3):850–860.

Wallin, R. F. (1998). A Practical Guide to ISO 10993-6: Implants Effects. http://www.mddionline.com/article/practical-guide-iso-10993-6-implant-effects.

Wang, J. C., Alanay, A., Mark, D., Kanim, L. E., Campbell, P. A., Dawson, E. G., and Lieberman, J. R. (2007). A comparison of commercially available demineralized bone matrix for spinal fusion. *European Spine Journal*, 16(8):1233–1240.

Wang, Y.-H., Liu, Y., Maye, P., and Rowe, D. W. (2006). Examination of mineralized nodule formation in living osteoblastic cultures using fluorescent dyes. *Biotechnology progress*, 22(6):1697–1701.

Wannatong, L., Sirivat, A., and Supaphol, P. (2004). Effects of solvents on electrospun polymeric fibers: preliminary study on polystyrene. *Polymer International*, 53(11):1851–1859.

Wassersug, R. J. (1976). A procedure for differential staining of cartilage and bone in whole formalin-fixed vertebrates. *Biotechnic & Histochemistry*, 51(2):131–134.

Webster, T. J., Schadler, L. S., Siegel, R. W., and Bizios, R. (2001). Mechanisms of enhanced osteoblast adhesion on nanophase alumina involve vitronectin. *Tissue engineering*, 7(3):291–301.

Weibel, E. R. and Elias, H. (1967). Quantitative methods in morphology [proceedings].

Wen, J., Somorjai, G., Lim, F., and Ward, R. (1997). XPS Study of Surface Composition of a Segmented Polyurethane Block Copolymer Modified by PDMS End Groups and Its Blends with Phenoxy. *Macromolecules*, 30(23):7206–7213.

WHO (2005). Transplantation. World Health Organization - http://www.who.int/transplantation/xeno/en/. Date Accessed: 03/04/2013.

Wilkinson, D. (2012). Paget's Disease, The Simple Facts. Paget's Association - http://www.paget.org.uk/simplefacts.pdf. Date Accessed: 03/04/13.

Wirpsza, Z. (1993). *Polyurethanes: chemistry, technology, and applications.* Ellis Horwood.

Woodard, J. R., Hilldore, A. J., Lan, S. K., Park, C. J., Morgan, A. W., Eurell, J. A. C., Clark, S. G., Wheeler, M. B., Jamison, R. D., and Wagoner Johnson, A. J. (2007). The mechanical properties and osteoconductivity of hydroxyapatite bone scaffolds with multi-scale porosity. *Biomaterials*, 28(1):45–54.

Wozney, J. M., Rosen, V., Byrne, M., Celeste, A. J., Moutsatsos, I., and Wang, E. A. (1990). Growth factors influencing bone development. *Journal of cell science. Supplement*, 13:149–156.

Woźniak, P., Bil, M., Ryszkowska, J., Wychowański, P., Wróbel, E., Ratajska, A., Hoser, G., Przybylski, J., Kurzydłowski, K. J., and Lewandowska-Szumieł, M. (2010). Candidate bone-tissue-engineered product based on human-bone-derived cells and polyurethane scaffold. *Acta biomaterialia*, 6(7):2484–2493.

Xie, J., MacEwan, M. R., Ray, W. Z., Liu, W., Siewe, D. Y., and Xia, Y. (2010). Radially aligned, electrospun nanofibers as dural substitutes for wound closure and tissue regeneration applications. *ACS nano*, 4(9):5027–5036.

Xu, C., Inai, R., Kotaki, M., and Ramakrishna, S. (2004). Aligned biodegradable nanofibrous structure: a potential scaffold for blood vessel engineering. *Biomaterials*, 25(5):877–886.

Yaltirik, M., Ozbas, H., Bilgic, B., and Issever, H. (2004). Reactions of connective tissue to mineral trioxide aggregate and amalgam. *Journal of Endodontics*, 30(2):95–99.

Yang, W., Both, S. K., Zuo, Y., Birgani, Z. T., Habibovic, P., Li, Y., Jansen, J. A., and Yang, F. (2015). Biological evaluation of porous aliphatic polyurethane/hydroxyapatite composite scaffolds for bone tissue engineering. *Journal of Biomedical Materials Research Part A*, 103(7):2251–2259.

BIBLIOGRAPHY

Yao, J., Bastiaansen, C. W., and Peijs, T. (2014). High strength and high modulus electrospun nanofibers. *Fibers*, 2(2):158–186.

Yeganegi, M., Kandel, R. A., and Santerre, J. P. (2010). Characterization of a biodegradable electrospun polyurethane nanofiber scaffold: Mechanical properties and cytotoxicity. *Acta Biomaterialia*, 6(10):3847–3855.

Yin, Z., Chen, X., Chen, J. L., Shen, W. L., Nguyen, T. M. H., Gao, L., and Ouyang, H. W. (2010). The regulation of tendon stem cell differentiation by the alignment of nanofibers. *Biomaterials*, 31(8):2163–2175.

Yoshii, T., Dumas, J. E., Okawa, A., Spengler, D. M., and Guelcher, S. A. (2012). Synthesis, characterization of calcium phosphates/polyurethane composites for weight bearing implants. *Journal of Biomedical Materials Research Part B: Applied Biomaterials*.

Zanetta, M., Quirici, N., Demarosi, F., Tanzi, M. C., Rimondini, L., and Farè, S. (2009). Ability of polyurethane foams to support cell proliferation and the differentiation of MSCs into osteoblasts. *Acta biomaterialia*, 5(4):1126–1136.

Zanoni, M., Piccinini, F., Arienti, C., Zamagni, A., Santi, S., Polico, R., Bevilacqua, A., and Tesei, A. (2016). 3d tumor spheroid models for in vitro therapeutic screening: a systematic approach to enhance the biological relevance of data obtained. *Scientific reports*, 6.

Zdrahala, R. J. and Zdrahala, I. J. (1999). Biomedical applications of polyurethanes: a review of past promises, present realities, and a vibrant future. *Journal of biomaterials applications*, 14(1):67–90.

Zhang, J., Doll, B. A., Beckman, E. J., and Hollinger, J. O. (2003). A biodegradable polyurethane-ascorbic acid scaffold for bone tissue engineering. *Journal of Biomedical Materials Research - Part A*, 67(2):389–400.

Zhang, J. Y., Beckman, E. J., Piesco, N. P., and Agarwal, S. (2000). A new peptide-based urethane polymer: synthesis, biodegradation, and potential to support cell growth in vitro. *Biomaterials*, 21(12):1247–1258.

Zhang, K., Wang, H., Huang, C., Su, Y., Mo, X., and Ikada, Y. (2010). Fabrication of

silk fibroin blended p (lla-cl) nanofibrous scaffolds for tissue engineering. *Journal of Biomedical Materials Research Part A*, 93(3):984–993.

Zhang, S., Gelain, F., and Zhao, X. (2005). Designer self-assembling peptide nanofiber scaffolds for 3d tissue cell cultures. In *Seminars in cancer biology*, volume 15, pages 413–420. Elsevier.

Zhao, J., Xiao, S., Lu, X., Wang, J., and Weng, J. (2006). A study on improving mechanical properties of porous HA tissue engineering scaffolds by hot isostatic pressing. *Biomedical Materials*, 1(4):188.

Zhao, L., Weir, M. D., and Xu, H. H. (2010). An injectable calcium phosphate-alginate hydrogel-umbilical cord mesenchymal stem cell paste for bone tissue engineering. *Biomaterials*, 31(25):6502–6510.

Zhong, S., Teo, W. E., Zhu, X., Beuerman, R. W., Ramakrishna, S., and Yung, L. Y. L. (2006). An aligned nanofibrous collagen scaffold by electrospinning and its effects on in vitro fibroblast culture. *Journal of Biomedical Materials Research Part A*, 79(3):456–463.

Zhu, W., Holmes, B., Glazer, R. I., and Zhang, L. G. (2016). 3d printed nanocomposite matrix for the study of breast cancer bone metastasis. *Nanomedicine: Nanotechnology, Biology and Medicine*, 12(1):69–79.

Zong, X., Kim, K., Fang, D., Ran, S., Hsiao, B. S., and Chu, B. (2002). Structure and process relationship of electrospun bioabsorbable nanofiber membranes. *Polymer*, 43(16):4403–4412.

Available online at www.sciencedirect.com

ScienceDirect

www.elsevier.com/locate/jmbbm

Research Paper

Electrospun polyurethane/hydroxyapatite bioactive Scaffolds for bone tissue engineering: The role of solvent and hydroxyapatite particles ☆

G. Tetteh, A.S. Khan[1], R.M. Delaine-Smith[2,3], G.C. Reilly*, I.U. Rehman

Kroto Research Institute, Department of Materials Science and Engineering, University of Sheffield, Sheffield S3 7HQ, UK

ARTICLE INFO

ABSTRACT

Polyurethane (PU) is a promising polymer to support bone–matrix producing cells due to its durability and mechanical resistance. In this study two types of medical grade poly-ether urethanes Z3A1 and Z9A1 and PU-Hydroxyapatite (PU–HA) composites were investigated for their ability to act as a scaffold for tissue engineered bone. PU dissolved in varying concentrations of dimethylformamide (DMF) and tetrahydrofuran (THF) solvents were electrospun to attain scaffolds with randomly orientated non-woven fibres.

Bioactive polymeric composite scaffolds were created using 15 wt% Z3A1 in a 70/30 DMF/THF PU solution and incorporating micro- or nano-sized HA particles in a ratio of 3:1 respectively, whilst a 25 wt% Z9A1 PU solution was doped in ratio of 5:1. Chemical properties of the resulting composites were evaluated by FTIR and physical properties by SEM. Tensile mechanical testing was carried out on all electrospun scaffolds. MLO-A5 osteoblastic mouse cells and human embryonic mesenchymal progenitor cells, hES-MPs were seeded on the scaffolds to test their biocompatibility and ability to support mineralised matrix production over a 28 day culture period. Cell viability was assayed by MTT and calcium and collagen deposition by Sirius red and alizarin red respectively.

SEM images of both electrospun PU scaffolds and PU–HA composite scaffolds showed differences in fibre morphology with changes in solvent combinations and size of HA particles. Inclusion of THF eliminated the presence of beads in fibres that were present in scaffolds fabricated with 100% DMF solvent, and resulted in fibres with a more uniform morphology and thicker diameters. Mechanical testing demonstrated that the Young's Modulus and yield strength was lower at higher THF concentrations. Inclusion of both sizes of HA particles in PU–HA solutions reinforced the scaffolds leading to higher mechanical properties, whilst FTIR characterisation confirmed the presence of HA in all composite scaffolds.

Although all scaffolds supported proliferation of both cell types and deposition of calcified matrix, PU–HA composite fibres containing nano-HA enabled the highest cell viability and collagen deposition. These scaffolds have the potential to support bone matrix formation for bone tissue engineering.

1. Introduction

Bone tissue engineering aims at improving musculoskeletal health by providing a living bone graft substitute to fill and aid in the repair of bone defects caused by trauma, disease, or congenital malformations or to augment bone stock around an implant site. While small bone defects heal spontaneously, critical size defects do not heal during a lifetime (Gogolewski and Gorna, 2007). Bone tissue engineering involves the use of materials to either induce formation of bone from the surrounding tissue or to act as a carrier or template for implanted bone cells. Bone regeneration requires four components: a morphogenetic signal, responsive host cells, a suitable carrier to serve as scaffolding for the growth of host cells and a viable and well vascularised host bed (Croteau et al., 1999; Burg et al., 2000). The scaffold provides a three dimensional porous structure that facilitates cell attachment, growth and matrix deposition.

Orthopaedic implant materials were initially selected for structural restoration based on their biomechanical properties (termed 'first generation implants'). Later bone implant materials were engineered to be bioactive or bioresorbable to enhance tissue growth ('second generation'), a development which coincided with the development of tissue engineering scaffolds as cell supports for multiple tissue types. Currently, bone implant materials are designed to induce bone formation (Bose et al., 2012) and many bone graft substitute materials are also used as experimental scaffolds to support cells for bone tissue engineering.

An ideal scaffold should possess a suitable surface chemistry that supports cell attachment, proliferation, migration and growth. Additionally, it should serve as a biocompatible template for osteoprogenitor cell growth and aid in the differentiation of mesenchymal stem cells into osteoblasts, as well as supporting the production, organisation and maintenance of an extracellular matrix (Gogolewski, 2007; Gorna and Gogolewski, 2003). In addition to being biocompatible, scaffolds are required to be composed of highly interconnected macro and micro-porous networks to facilitate cell migration and nutrient distribution.

Several polymers of both natural and synthetic origin can be used for bone tissue engineering; however polyurethanes are of particular interest due to the flexibility associated with their versatile chemistry (Guelcher, 2008). This makes it possible to customise scaffolds in order to attain desirable chemical, physical and mechanical properties such as durability, elasticity and fatigue resistance, by altering the choice and quantity of the starting materials (Zdrahala and Zdrahala, 1999). Biocompatible and biodegradable polyurethanes have been investigated as scaffolds for tissue

engineering applications for almost thirty years (Guelcher et al., 2004), and also as heart valves, stents, intra-aortic balloons and pacing lead insulators, amongst others (Grad et al., 2003).

The microphase separation between the hard and soft segments enables polyurethane to withstand physical stresses and therefore it possesses desirable mechanical properties useful for dynamic bone tissue engineering (Wen et al., 1997). For example, we have demonstrated that cyclic mechanical conditioning of osteoprogenitor cells in a PU scaffold upregulates bone formation (Sittichockechaiwut et al., 2009; Sittichockechaiwut et al., 2010; Delaine-Smith and Reilly, 2011). PU has several advantages as a scaffold for cells that will be subjected to mechanical conditioning, as its high yield strain and fatigue life enable it to undergo repeated cycles of mechanical strain, without changing its mechanical properties. Additionally, the use of elastomeric scaffolds as alternatives to bone grafts, prevents generation of shear forces at the interface between native bone and the substitute; thus enhancing intimate contact with bone and enabling the proliferation of osteogenic cells and bone regeneration (Gorna and Gogolewski, 2003).

Composite scaffolds range from stable to degradable, and most of those used in tissue engineering/regenerative medicine are biodegradable polymers reinforced with ceramic particles. Bonfield first proposed the concept of polymer–ceramic combination materials, mimicking the ductile and brittle properties of the collagen and mineral components of bone respectively, in 1988, which was later commercialised with the trade name, HAPEX™ (Bonfield, 1988a, 1988b). Mechanically, polymers are noted for their extensive deformation and high toughness whilst ceramics, such as hydroxyapatites (HA), are noted for their high compressive strength but brittle failure. Combining polyurethane with hydroxyapatite has been shown by a number of researchers to improve the mechanical properties of the resulting composite, as long as a strong interfacial bond strength is established between the ceramic phase and the polymer matrix (Attawia et al., 1995; Boccaccini and Maquet, 2003; Bonzani et al., 2007; Martinez-Valencia et al., 2011).

Previous research has been undertaken on the synthesis of PU with varying additives such as ascorbic acid (Zhang et al., 2003) HA (Gorna and Gogolewski, 2003), and β-tri-calcium phosphate (Adhikari et al., 2008; Yoshii et al., 2012). Others have investigated fabrication techniques for PU scaffolds including Thermally Induced Phase Separation (TIPS) (Tsui and Gogolewski, 2009) and Solvent Casting/Particulate Leaching (Gorna and Gogolewski, 2006; Heijkants et al., 2006; Kucinska-Lipka et al., 2013; Boissard et al., 2009). However, to date little work has been undertaken on electrospinning of

polyurethane composites for bone tissue engineering applications.

Electrospinning is an efficient, simple and relatively easy polymer fabrication technique that produces nano and micro diameter polymer fibres, with the advantage that it can be performed with different polymers in both solution and melt states. Such thin fibres provide high surface area to volume ratios, high porosity, flexibility in surface functionalities, superior mechanical performance and membrane technology (Demir et al., 2002). In the field of biomaterials and tissue engineering, electrospinning has been utilised for producing scaffolds that mimic the morphological characteristics and biological function of the natural extracellular matrix, by providing an optimal template for cell attachment, proliferation and growth (Carlberg et al., 2009; Huang et al., 2003). Several different polymers such as polyurethanes, poly(ε -caprolactone), poly(lactic acid), poly(glycolic acid) and their co-polymers have been successfully spun for musculoskeletal, nerve, skin, vascular and drug delivery applications (Bashur et al., 2009; Clarke et al., 2008; Nirmala et al., 2011). Electrospinning may be an ideal technique for bone tissue engineering where repair of a thin defect is required, for example a cleft palate repair (Bye et al., 2013), or electrospun sheets may be layered or rolled for larger defects (McMahon et al., 2011).

Demir et al. (2002) studied the effect of electrical field, temperature and conductivity on electrospun polyurethane–urea fibres and reported that the morphology of electrospun fibres is strongly correlated with viscosity, equivalent concentration and temperature. In their study, they reported that solution temperature, a key parameter that affects fibre morphology and spinning ability was essential to spin polymer concentrations beyond 12.8 wt%. Khan et al. (2008) and Mi et al. (2014) electrospun polyurethane composites with micro and nano sized hydroxyapatite for dental and bone tissue engineering applications, respectively. In their studies, Khan et al. developed a novel composite material by chemically binding the HA particles to the diisocyanate component of the polyurethane backbone through solvent polymerisation, whilst Mi et al. studied the effect of polymer properties and particle size on electrospun PU–HA scaffold and reported reduced tensile properties with the inclusion of micro HA

(mHA) and nano HA (nHA) particles, although the reduction was more significant with the inclusion of mHA.

The aim of this study was to identify polyurethane solutions that would create consistent microfibrous mats without beads and irregularities at room temperature and to examine the effect of incorporating HA particles into these scaffolds. Our hypothesis was that HA would reinforce the mechanical properties of polymers and improve the bioactive properties compared to polymer-only scaffolds. Our long-term aim is to create a range of scaffolds supportive of bone cell and matrix growth that can withstand mechanical conditioning *in vitro* and mechanical loading *in vivo*. In this study, we investigated the effect of dimethylformamide (DMF) and tetrahydrofuran (THF) solvent combinations on the fibre morphology and mechanical properties of electrospun thermoplastic polyether-urethane polymers Z3A1 and Z9A1. We also investigated the effect of including nano and micro size HA particles on fibre morphology, mechanical properties, biocompatibility, extracellular and calcified matrix production over a 28 day period using MLO-A5 osteoblastic mouse cells and human embryonic mesenchymal progenitor cells (hES-MPs).

2. Materials and methods

2.1. Polyurethane (PU) solutions

Two aromatic medical grade polyether–urethanes Z3A1 (Mn—143,566 Mw—272,857) and Z9A1 (Mn—100K$_D$ Mw—197K$_D$), composed of 4,4′-diphenylmethane diisocyanate, polyether diol, and 1,4 Butane diol were obtained from Biomer Technology, UK and dissolved in dimethylformamide (DMF) and Tetrahydrofuran (THF) solvents (Sigma Aldrich, UK). 15 wt% Z3A1 pellets or 27% Z9A1 pellets were dissolved in 100% DMF, 70/30 DMF/THF (v/v) or 50/50 (v/v) DMF/THF. These solutions will be denoted as Z3-100, Z3-70, Z3-50, Z9-100, Z9-70, and Z9-50 respectively (Table 1).

2.2. PU–HA composite solutions

For composite scaffolds, 15 wt% Z3A1 in 70/30 DMF/THF (Z3-PU) PU solutions were doped with either sintered micro HA ($<5\,\mu$m, Captal® S, Plasma Biotal, UK) or nano-sized HA

Table 1 – Parameters used in preparing electrospun scaffolds.						
Name	PU (wt%)	HA (wt%)	Volumetric ratio of DMF (%)	Volumetric ratio of THF (%)	Spin speed (rpm)	Diameter of rotating drum (cm)
Z9-100	27	0	100	0	150	6
Z9-70	27	0	70	30	150	6
Z9-50	27	0	50	50	150	6
Z3-100	15	0	100	0	150	6
Z3-70	15	0	70	30	150	6
Z3-50	15	0	50	50	150	6
Z9-PU	25	0	70	30	150	6
Z9-mHA	25	5	70	30	150	6
Z9-nHA	25	5	70	30	150	6
Z3-PU	15	0	70	30	300	8
Z3-mHA	15	5	70	30	300	8
Z3-nHA	15	5	70	30	300	8

(<200 nm, Sigma Aldrich, UK) particles in a ratio of 3:1, PU: HA and will be denoted Z3-mHA or Z3-nHA, respectively (Table 1). For Z9A1 composites, 25 wt% Z9A1 in 70/30 DMF/ THF (Z9-PU) was doped with HA particles in a ratio of 5:1 PU: HA and denoted as Z9-mHA and Z9-nHA. Note that this concentration of PU in the Z9A1 (no HA) group is lower than that used in the non-composite formulations described above, This is because the 27 wt% PU solutions were too viscous to enable adequate distribution of HA particles. In all preparations, solutions were stirred with magnetic beads on the UC151 ceramic plate stirrer at rotation speed of 500 rpm for 24 h at room temperature.

2.3. Electrospinning

Solutions were placed into four 5 ml syringes with 20 gauge luer stub adaptors and electrospun at a voltage of +16.5 kV, a flow rate of 3 ml/h and a tip to collector distance of 20 cm, at room temperature. A mat of randomly orientated polymeric fibres was collected on a sheet of aluminium foil wrapped around a grounded metallic mandrel, rotating at rate of 150 rpm for all scaffolds with the exception of Z3-PU, Z3-mHA and Z3-nHA which were electrospun at a rotation speed of 300 rpm. After electrospinning, the aluminium foil was removed and dried in a vacuum oven at a negative pressure of 1020 mbar for 12 h to evaporate any remaining solvent.

2.4. Scanning electron microscopy (SEM)

SEM was used to examine morphological and topographical details of electrospun scaffolds. Prior to imaging, samples were mounted onto aluminium stubs using double-sided carbon adhesive tabs (12 mm) (Agar Scientific, UK) and sputter-coated with gold powder. Coated scaffolds were imaged with secondary electrons at an accelerating voltage of 20 kV, a spot size of 3.0 and a magnification of 1250×.

2.5. Mechanical testing

The mechanical properties of fabricated scaffolds were analysed in tension on a materials testing machine (ElectroForce 3200, Bose, USA). Rectangular samples with average dimensions of 5 mm × 20 mm were measured with vernier callipers, mounted between two grips to give a guage length of 6 mm and subjected to tensile strain at a rate of 1 Hz up to 100% strain. Deformation was measured by the movement of the cross-head and load measured using a 22 N load cell, the resulting load/deformation curves were converted into stress/ strain curves by dividing by the sample bulk cross-sectional area. Young's modulus was calculated as change in stress divided by change in strain in the linear portion of the curve, yield was defined as the point at which the load deformation curve deviated from the straight line and yield strength was defined as the stress at yield.

2.6. Fourier transform infrared spectroscopy (FTIR)

Chemical structural characterisation of the composites was carried out using a Fourier Transform Infrared spectrometer (FTIR) (Thermo Fisher Scientific Inc., USA) equipped with a Photo-Acoustic (PAS) sampling cell, which allows analysis of neat samples without the need for sample preparation. The PAS cell was purged with helium gas. All spectra were recorded at 4 cm^{-1} resolution, accumulating over a total of 256 scans. The spectral data was acquired and processed using the OMNIC7.4™ software.

2.7. Cell culture

All reagents were obtained from Sigma-Aldrich (UK) unless otherwise stated. Prior to cell culture, electrospun scaffolds were cut with the Epilog Mini 40 W Laser cutter (Epiloglaser, USA) with vector settings at a speed of 80% and a laser power of 6% into disks with a diameter of 1.6 cm and sterilised with 0.1% peracetic acid for 3 h at room temperature. The scaffolds were washed with PBS. Using stainless steel rings, MLO-A5 at passage 33 and hES-MP cells at passage 3 were seeded at 1.0×10^5 cells per scaffold and incubated at 37 °C in a humidified environment with 5% CO_2. The rings were removed after 24 h and Dulbeccos Modified Eagles Medium (DMEM) (Biosera, UK), supplemented with 10% foetal calf serum (FCS), 1% L-glutamine (L-G), 1% penicillin and streptomycin (P/S), 0.25% fungizone (F), 50 μg/ml ascorbic acid-2-phosphate and 5 mM βGP added to the scaffolds; media was changed every 2 days during the 28-day culture period. Media used for hES-MP cells was also supplemented with 100 nM of dexamethosone to stimulate osteoblastic differentiation.

2.8. MTT cell viability

MTT (3-(4, 5-dimethylthiazol-2-yl)-2, 5-diphenyltetrazolium bromide) colorimetric assay was used to investigate cell viability 1, 4, 7, 14, 21 and 28 days after seeding. For each assay, cell-seeded scaffolds were rinsed with PBS and MTT solution at 0.5 mg/ml was added to each well and incubated for a period of 40 min. The yellow MTT dye was reduced by the mitochondrial reductase enzyme in living cells to purple formazan after the incubation period; the formazan was destained with 2 ml of 0.125% acidified isopropanol and its absorbance read with the spectrophotometer at 562 nm reference 630 nm.

2.9. DAPI and phalloidin staining

Four days after cell seeding, Z3-70 and Z9-70 scaffolds seeded with MLO- A5 cells were stained with DAPI (4′, 6-diamidino-2-phenylindole dihydrochloride) nuclear stain and phalloidin fluorescent conjugate cytoskeleton stains to visualise cell attachment and cell morphology. The cells on the scaffolds were fixed with 3.7% formaldehyde for 20 min, washed with PBS and permeablized with 1% Triton X-100 in PBS. The scaffolds were then washed with PBS, 1% Bovine Serum Albumin (BSA) was added as a blocking agent and then 1% Phallodin was added. Scaffolds were then washed with PBS and stained with 0.1 μg/ml of DAPI. Finally, scaffolds were washed with PBS and visualised with a fluorescent image analyser (AXON Instruments ImageXpress 5000A, USA).

2.10. Collagen staining

Sirius red which binds to collagen was used to detect collagen at days 14, 21 and 28. The Sirius red (Direct red dye from Sigma-Aldrich, UK) solution was prepared by dissolving 1 mg/ml in saturated picric acid. Cell-seeded scaffolds were washed with PBS and fixed with 3.7% formaldehyde for 20 min, then washed with distilled water. 1 mg/ml Sirius red solution was added to each well and samples were agitated on a platform rocker at 30 rpm. After 18 h excess Sirius red solution was removed and the scaffolds washed with distilled water. Samples were allowed to air dry for 30 min and photographic images taken for qualitative analysis. For quantitative analysis, 0.2 M of NaOH and methanol at 1:1 was used to destain Sirius red on a platform rocker at 30 rpm for 24 h; the absorbance of the eluate was read with the spectrophotometer at 490 nm.

2.11. Calcium staining

Alizarin red (AR) staining was used to detect extracellular calcium deposition on days 14, 21 and 28 of culture. 1% w/v of alizarin Red S (Sigma-Aldrich, UK) powder in distilled water was used to stain MLO-A5 and hES-MPs seeded scaffolds for two hours under dynamic rocking at 30 rpm. Prior to staining, scaffolds were washed and fixed with 3.7% formaldehyde as per the procedure described for collagen staining. Excess AR solution was removed after staining and samples washed 3 times with distilled water. For quantitative analysis, 5% v/v perchloric acid in distilled water was used to destain AR on a platform rocker at 30 rpm for 24 h. The absorbance of the eluate was read with the spectrophotometer at 405 nm.

2.12. Histology

Histological samples were taken as complete transverse-sections across the centre of electrospun scaffolds. Samples were fixed with 3.7% formaldehyde, soaked in 1% sucrose solution and embedded in OCT^{TM} compound media prior to sectioning. Samples were cryo-sectioned at 15 μm and stained with Haematoxylin and Eosin. Stained sections were imaged with a light microscope with 20 × objective.

2.13. Statistical analysis

All data are reported as mean ± standard deviation. Comparison of sample means of fibre diameter and mechanical analysis was performed by one-way analysis of variance using GraphPad Prism 6 software, whilst MTT cell viability, calcium and collagen absorbance data were analysed by two-ways repeated measures analysis of variance. Differences between two groups were defined as statistically significant if $p \leq 0.05$ as determined by the Tukey's multiple comparisons post hoc test.

3. Results and discussion

Bone, the major load bearing tissue of the human body is subjected to varying degrees of loading and unloading on a daily basis. Hence, designing a scaffold for bone tissue engineering requires a material that is mechanically compatible, that should be able to undergo varying degrees of deformation without rupturing. Polyurethane remains a popular choice amongst polymers for its advantageous properties of biocompatibility, biodegradability, mechanical flexibility and versatile chemistry allowing it to be tailor-made for specific applications.

3.1. PU scaffolds

Microphase segregation, a key characteristic of thermoplastic polyurethane elastomers occurs as a result of the thermodynamic incompatibility of the hard and soft segments of PU and is known to play a key role in the mechanical properties of PU. Factors known to affect the degree of separation include segment polarity, hydrogen bonding responsible for hard/soft segment interaction, overall sample constitution and molecular weight. Thermoplastic elastomers with different molecular weights Z9A1 and Z3A1 but identical chemical structures and composed of 4,4′-diphenylmethane diisocyanate, polyether diol, and 1,4 butane diol were dissolved in graded concentrations of DMF and THF to study the effect of solvent combination on electrospun fibre morphology and mechanical properties. DMF and THF are popular solvents used in dissolving and synthesising polyurethane (Khil et al., 2003; Tsui and Gogolewski, 2009). These solvents differ in polarity, evaporation rate, and conductivities, which are key parameters that affect electrospinning and microphase segregation.

Scaffolds fabricated from solution containing 100% DMF had more nano-diameter fibres and beads than other solvent combinations of DMF and THF for both types of PU (Fig. 1). Reducing the amount of DMF, by replacing with THF eliminated the presence of beads and resulted in fibres with a more uniform morphology for Z9A1 scaffolds, and a combination of nano and micro fibres for Z3A1 scaffolds. For both types of PU, scaffolds made from solutions containing 50% THF solvent had fibres with significantly larger diameters to those fabricated from 100% DMF and 70/30 DMF/THF combinations. We cannot directly compare the effects of molecular weight (Z3A1 versus Z9A1) in this study as spinning parameters were also slightly different between these two sets of scaffolds. However in general, Z3A1 dissolved faster and more uniformly than Z9A1 prior to electrospinning, presented with a more uniform viscosity and was easier to fabricate. Armentano et al. (2010) reported that the solvent choice used in fabricating polymer films influences several scaffold properties, including the heterogeneity of the surface structure, reorientation or mobility of the surface crystal segment, as well as swelling and deformation. In our study, differences in electrospun morphology which resulted from changing the amount of DMF contained in solution is supported by the work of Oprea, (2005) who studied the effect of N-methyl-2-pyrrolidone (NMP), DMF, toluene and ethyl acetate on the properties of polymer films, and reported differences in morphology and mechanical properties of films fabricated from solutions containing NMP and DMF solvents. They suggested that NMP was a better solvent than DMF for developing polyurethane films. Wannatong et al., (2004) also studied the effect of five different solvents on electrsospun polystyrene (PS) and reported that DMF was the best solvent for preparing beadless PS scaffolds. This is in contrast to what was observed in our study, but these different results could be due
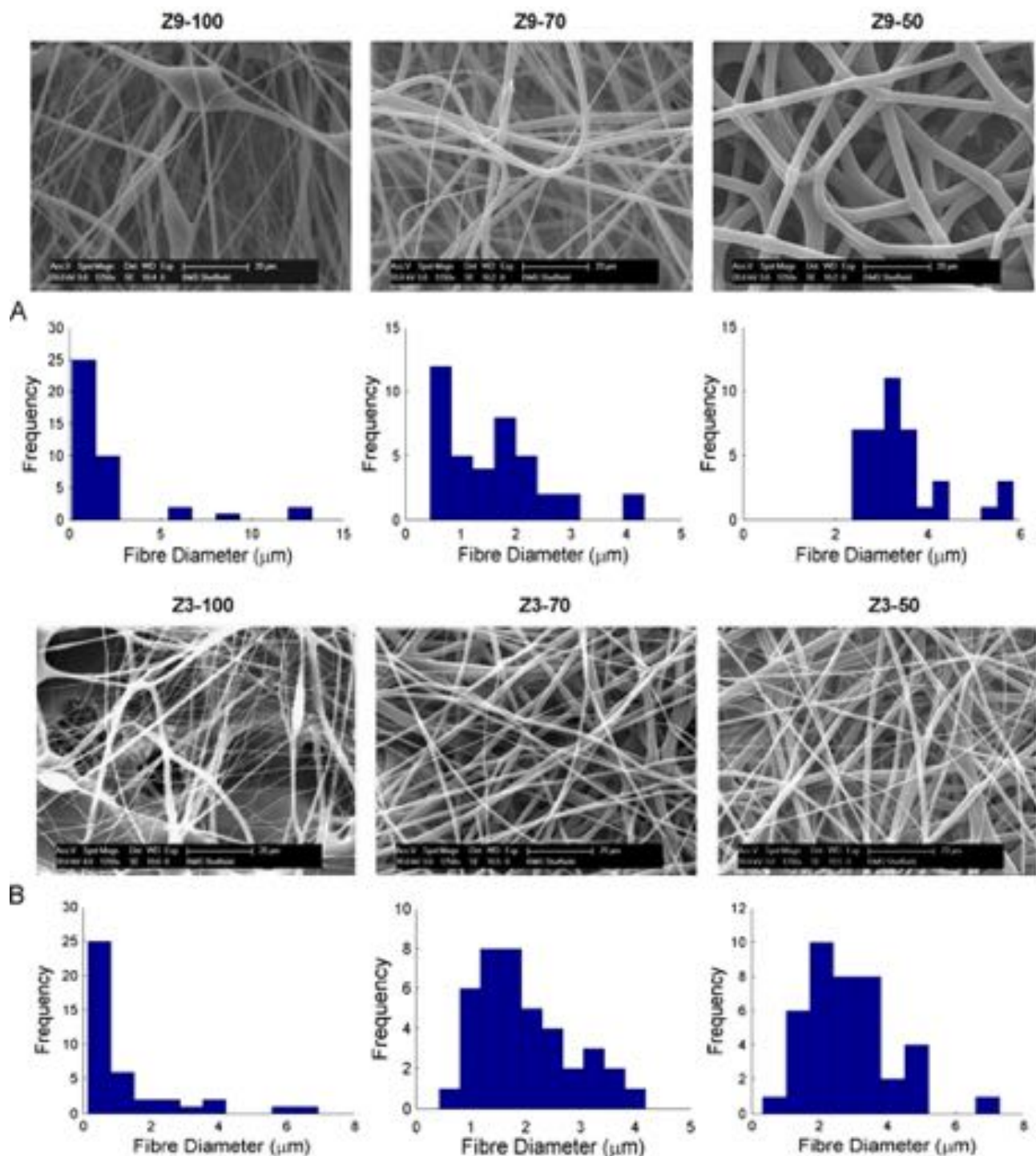
Fig. 1 – SEM images of electrospun (A) Z9A1 and (B) Z3A1 scaffolds synthesised with different combinations of DMF & THF (scale bar=20 μm), and (below) a histogram of the fibre diamter (n=40).

to differences in concentration of solutions, molecular weights and polymer choice, as PU and PS have different chemical and physical properties.

3.2.   PU–HA composites

Mimicking the ductile properties of collagen and the strength of the mineralised phase of bone with PU and HA particles combined in micro or nano composites has been proposed for bone substitute materials for a number of reasons. The elastomeric nature of PU serves as a matrix, reinforced by the HA particles. Nano HA and micro HA differ in several ways including surface area and the degree of crystallinity which both affect overall sample constitution. By including both particle types in separate solutions, we were able to assess the effect

of particle size on fibre morphology and mechanical properties.

Note that the PU scaffolds without HA for this set of experiments were spun from a 70/30 solution of DMF/THF because this enabled the best fibre morphology (without beads), however the processing conditions for Z9-PU and Z3-PU are slightly different from those used in the Z9-70 and Z3-70 groups (Table 1) so these are not expected to have identical morphological and mechanical properties.

Electrospun 25 wt% Z9A1 and 15 wt% Z3A1 dissolved in 70/30 DMF/THF solvents showed relatively uniform fibre diameter distributions. However, the inclusion of mHA and nHA particles resulted in changes to fibre morphology. For both types of PU, nHA particles with a higher surface area and smaller particle size, blended well with PU and resulted in more uniform fibres compared to composite scaffolds containing mHA particles, which presented with a beaded morphology and generally reduced fibre diameters (Fig. 2) but with some particularly large
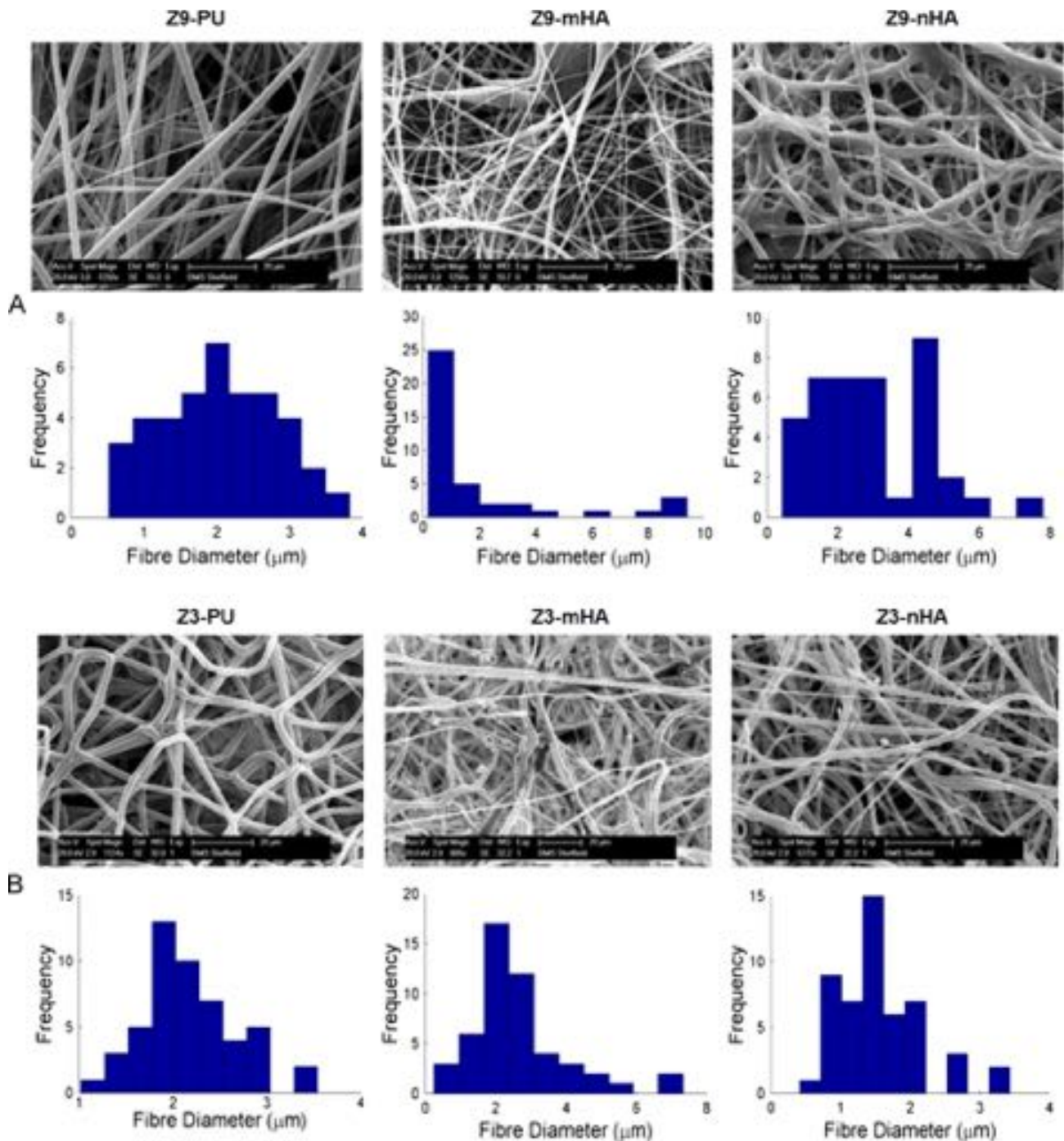
Fig. 2 – SEM images of electrospun (A) Z9A1 and (B) Z3A1 PU (left column), mHA (middle column) and nHA (right column) composite scaffolds (scale bar=20 μm), and (below) a histogram of the fibre diamter (n=40). Note that the axes for each histogram are to different scales reflecting the varibility in fibre size between scaffold compositions and the histogram for Z9-mHA excludes a single 35 μm fibre which is included in the mean values presented in Table 3.

fibres. It is likely that the particularly large fibres contain large chunks of mHA leading to a bimodal distribution of fibre size and large standard deviation (Table 2). There was a single extremely large fibre of 35 μm in the field of view examined which was not included in the frequency plot (Fig. 2A) as it would have made it difficult to visualise the rest of the data but this is included in the fibre average diameter data (Table 2).

Reduction in fibre diameter with the inclusion of mHA particles to create composites was also observed by Nirmala et al. (2011) who electrospun nanofibrous polyurethane with micro Calcium Chloride particles and by Mi et al. (2014) who suggested that that mHA particles may have stretched the polymer jets while the fibres were being deposited. The effect of more fibres at a lower diameter and a few fibres at a much larger diameter caused by the inclusion of mHA is much less marked when the Z3A1 polymer is used, this may be explained by smaller molecular weight and polymer chain length of Z3A1 compared to Z9A1 and lower viscosity.

It has been reported that the higher surface area of nHA compared to mHA enables better bonding between the nano-sized HA particles and PU enabling greater reinforcement of the polymer matrix and ultimately, enhancing mechanical and functional properties of nanocomposites compared to conventional microcomposites (Armentano et al., 2010). This probably explains why the nHA fibres are much more consistent in their size and morphology as the particles would be better distributed within, and bound to, their polymer matrix.

3.3. FTIR characterisation

The polar nature of PU and HA makes FTIR characterisation, which elicits differences in dipole moments, an ideal characterisation technique for analysing the chemical composition of composite scaffolds. The FTIR spectrum of polyurethane is presented in Fig. 3A, and the combined spectra of PU–HA composites are presented in Fig. 3B and C

For PU, the peak at 3325 cm^{-1} is attributed to the stretching v(N–H). The peak at 3121 cm^{-1} was the overtone of 1533 cm^{-1} and 3039 cm^{-1} attributed to the v(C–H) in benzene ring. The peaks at 2940, 2857 and 2795 cm^{-1} were CH$_2$ peaks of the polyether. The peak at 2940 cm^{-1} was the asymmetric stretching peak of CH$_2$ and the peak at 2857 cm^{-1} was the symmetric stretching of CH$_2$. The carbonyl absorption region was observed in between 1730 and 1700 cm^{-1}, the carbonyl

absorption band classified into two peaks. The peak due to bonded C=O stretching was at 1701 cm^{-1} and the free C=O stretching appeared at 1730 cm^{-1}. The peak at 1597 cm^{-1} was assigned to v(C=C) in the benzene ring and 1533 cm^{-1} was the amide II δ (N–H)+v(C=N). 1478 cm^{-1} was the weak CH$_2$ peak and the 1413 cm^{-1} attributed to the strong v(C–C) in benzene ring. The peak at 1310 cm^{-1} was assigned to amide III δ(N–H)+v(C=N), β(C–H) peak and δ(N–H)+v(C=N) appeared at 1225 cm^{-1}. The region between 1103 and 916 cm^{-1} was the v(CH$_2$–O–CH$_2$) of ether peak and 1018 cm^{-1} was the weak β(C–H) in benzene ring. The peak at 817 cm^{-1} was the γ(C–H) from butane diol. These observations were similar to those reported by Khan et al. (2008) in their study of polyurethane composites for dental restoration applications.

Fig. 3B shows the combined spectra of Z3-PU, Z3-mHA and Z3-nHA at common scale, with emphasis on the hydroxyl, carbonyl, phosphate and bending phosphate groups whilst Fig. 3C shows the combined spectra in greater detail for a wave number region of 1800−450 cm^{-1}. The characteristic peak of stretching O–H was observed at 3570 cm^{-1} (Rehman and Bonfield, 1997). The bands at 1060, 961, 603 and 571 cm^{-1} were assigned to vibration of the phosphate group, PO$_4$. The peak at 1078 cm^{-1} was the triply degenerated vibration v_3, and 961 cm^{-1} was the non-degenerated symmetric stretching mode v_1, of the P–O bond of the phosphate group. The peaks at 603 and 571 cm^{-1} were assigned to a triple degenerated bending mode v_4, of the O–P–O bond. The peak at 633 cm^{-1} was due to the phosphate v_4 bending. The stretching O–H and P–O (stretching and bending) peaks were not present in the polyurethane spectrum. After mixing the micro and nano hydroxyapatite in polyurethane, the appearance of characteristic peaks of HA were observed and it was noted from the shifting and appearance of new peaks in the region of 1100–916 cm^{-1} that nano-HA with a higher surface area and more crystalline structure was mixed better than micro-HA and affected the shifting of peaks v_3 P–O from 1078 cm^{-1} for Z3-mHA to 1060 cm^{-1} for Z3-nHA. It has been mentioned in the literature that the width and intensity of peaks in FTIR spectrum have explicit dependence on the particle size. As particle size increases, the width of the peak decreases and intensity increases. The restoring force of nano particles created by surface polarisation charge is responsible for the frequency difference. The difference in the frequency of vibrational modes is attributed to dipolar interactions,

Electrospun Scaffolds	Fibre diameter (μm)	Thickness (mm)	Young's modulus (MPa)	Yield strength (MPa)
Z9-100	2.06±3.09[c]	0.27±0.02	60.09±10.1[b,c]	2.13±0.55[c]
Z9-70	1.54±0.96[c]	0.29±0.06	25.89±4.54[a]	1.73±0.79
Z9-50	3.47±0.89[a,b]	0.36±0.04	30.11±0.78[a]	1.27±0.29[a]
Z3-100	1.25±1.56[b,c]	0.06±0.01	18.54±2.31[b,c]	1.56±0.34[b,c]
Z3-70	1.93±0.85[a,c]	0.18±0.03	7.61±0.76[ac]	0.71±0.03[a]
Z3-50	2.82±1.29[a,b]	0.10±0.01	3.38±1.25[a,b]	0.50±0.04[a]

Table 2 – Morphological and mechanical properties of Z9A1 and Z3A1 scaffolds with different solvent combinations (mean±S.D., n=40 for fibre measurements and 6 for all other measurements).

[a] Significantly different from scaffolds made from 100% DMF, at $p \leq 0.05$.
[b] Significantly different from scaffolds made from 70/30 DMF/THF, at $p \leq 0.05$.
[c] Significantly different from scaffolds made from 50/50 DMF/THF, at $p \leq 0.05$.

Table 3 – Morphological and mechanical properties of Z9A1 and Z3A1 scaffolds with different types of HA, (mean±S.D., $n=40$ for fibre measurements and 6 for all other measurements).

Electrospun Scaffolds	Fibre diameter (μm)	Thickness (mm)	Young's modulus (MPa)	Yield strength (MPa)
Z9-PU	2.01±0.80	0.36±0.01	9.56± 3.03[b]	0.61±0.18[b]
Z9-mHA	2.86±6.01	0.30±0.01	88.69±20.20[a,c]	3.02±0.80[a,c]
Z9-nHA	2.95±1.60	0.42±0.02	10.21±2.99[b]	0.79±0.16[b]
Z3-PU	2.18±0.51[c]	0.43±0.09	2.42±0.21[b,c]	0.29±0.04[b,c]
Z3-mHA	2.61±1.45[c]	0.31±0.01	4.77±0.29[a,c]	0.46±0.03[a]
Z3-nHA	1.56±0.63[a,b]	0.09±0.01	3.09±0.30[a,b]	0.52±0.09[c]

[a] Significantly different from PU scaffolds, at $p \leq 0.05$.
[b] Significantly different from scaffolds made with mHA, at $p \leq 0.05$.
[c] Significantly different from scaffolds made with nHA, at $p \leq 0.05$.
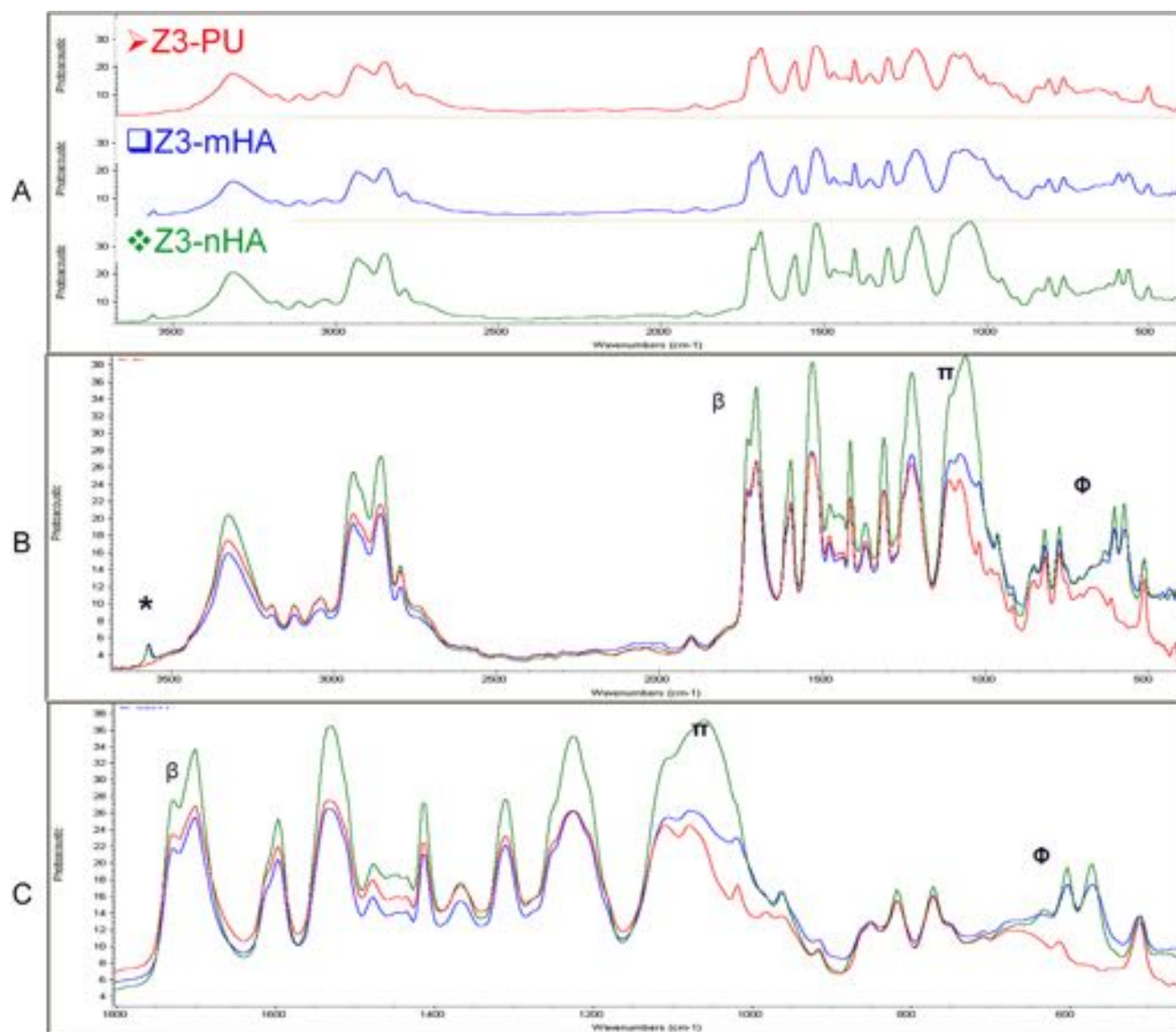

Fig. 3 – FTIR spectra of Z3A1 composites (A) stacked FTIR spectra of Electrospun Z3-PU, Z3-mHA and Z3-nHA. (B) Combined FTIR spectra of Z3-PU, Z3-mHA and Z3-nHA at Common Scale with Hydroxyl, Carbonyl, Phosphate and bending Phosphate groups highlighted as $*$, β, π and Φ, respectively. (C) Combined spectra of Z3-PU, Z3-mHA and Z3-nHA at common scale for a wavenumber region of $1800-450\ \mathrm{cm}^{-1}$.

interfacial effects, surface amorphousness, surface free energy etc. (Mo et al., 1993; Martin, 1996; Bobovich, 1988).

3.4. Mechanical analysis of PU scaffolds

In general, Z9A1 scaffolds were stronger than Z3A1 scaffolds and presented with higher mechanical properties for all combinations of DMF and THF solvents. With identical chemical structures, differences in the mechanical properties of Z9A1 and Z3A1 probably resulted from the differences in molecular weights, which would have affected the interaction between the hard and soft segments, causing differences in the microphase segregation.

Decreasing the proportion of DMF in the solvent reduced Young's Modulus and strength of Z9A1 and Z3A1 scaffolds. Z9-100 (100% DMF) showed a brittle stress-strain profile with plastic deformation occurring at 30% strain (Fig. 4A). Z9-100 also had the highest Young's Modulus and yield strength, significantly higher than those of Z9-50 for both properties, however, only Young's Modulus was significantly higher than that of Z9-70 scaffolds (Table 2).

A similar pattern was observed with the Z3 groups (Fig. 4B). Values of Young's Modulus for Z3-100, Z3-70 and Z3-50 were significantly reduced with less DMF in the electrospinning solvent (Table 1). For both polymers these differences in mechanical properties are likely to be the result of differences in fibre morphology (Fig. 1) which in turn may have resulted from differences in the solvent properties of DMF and THF. Beads present in scaffolds fabricated with 100% DMF solvent (Fig. 1) probably created short regions of

large fibre cross-sectional area, which would have caused there to be a greater amount of material relative to void space within the sample, which would in turn create an overall stronger scaffold but with a reduced ability to undergo strain.

3.5. Mechanical analysis of PU–HA composites

Mechanical properties of composites are controlled by several micro-structural factors such as the properties of the matrix, the properties and distribution of fillers, interfacial bonding strength, and processing methods. The interface strength between PU and HA particles greatly affects the effectiveness of load transfer from the polymer matrix to micro and nanocomposites. For composite scaffolds, inclusion of HA particles improved the tensile properties of both Z9A1 and Z3A1 scaffolds, Young's Modulus and yield strength of composite scaffolds were significantly higher than those of plain PU scaffolds, for both Z9A1 and Z3A1. SEM images of electrospun composites (Fig. 2) show that nHA, with its smaller size and higher surface area, properly integrated with the PU fibres compared to mHA which can be seen sticking out of the fibres and creating lumps and beads. Better mixing of nHA particles with PU as compared to mHA particles was also confirmed with FTIR for Z3-composites. We therefore expected that the nano-composites would be stiffer and stronger than the micro-composites However, for Z9A1, both yield strength and Young's Modulus of mHA scaffolds were significantly higher than those of Z9-nHA scaffolds. Interestingly, the yield strength of Z3-nHA scaffolds was higher than that of Z3-mHA, although not statistically
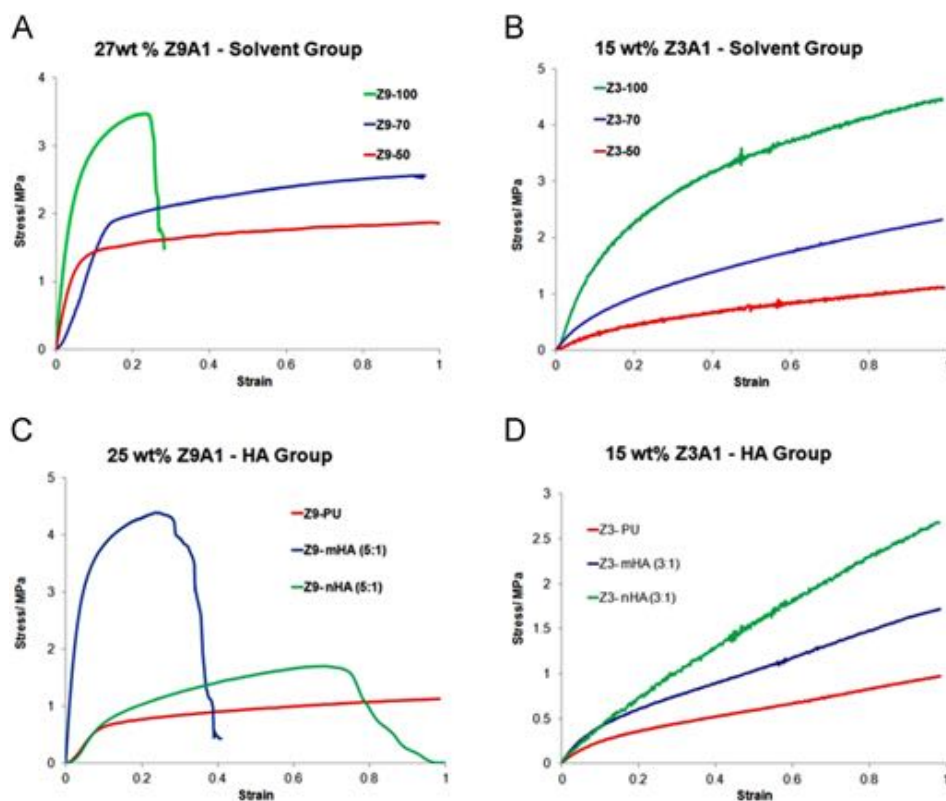

Fig. 4 – Example stress/strain curves of fabricated scaffolds, (A) effect of solvent combination on Z9A1 scaffolds, (B) effect of solvent combination on Z3A1 scaffolds, (C) effect of HA particles on Z9A1 scaffolds, (D) effect of HA particles on Z3A1 scaffolds.

significant. These differences in behaviour between Z9A1 and Z3A1 composite scaffolds could have resulted from the difference in the PU:HA ratio between Z9A1 (5:1) and Z3A1 (3:1) and the molecular weight of the polymers. Z9A1 is of higher molecular weight and produces scaffolds that are high in Young's modulus and strength but more brittle, the addition of HA further increases the brittleness of the electrospun scaffold. In contrast, Z3 is of lower molecular weight and more flexible and the addition of HA, albeit at a higher concentration that for Z9, has a smaller effect on the properties of the electrospun scaffold. Molecular weight and concentration and size of HA would all have resulted in differences in interactions between solvents, macromolecular chains of the polymer and the HA particles. These difference in interactions have been reported to affect microphase separation between the hard and soft segment of PU, hence ultimately affecting its mechanical properties (Oprea, 2005).

3.6.   Cell viability on PU Scaffolds

The MLO-A5 mouse cell line has characteristics of a post-osteoblast and pre-osteocyte cell type, and rapidly mineralises in sheets rather than nodules. These cells have been used to extensively study the osteoblast to osteocyte differentiation process, bone mineralisation and the effects of mechanical loading on biomineralization (Sittichockechaiwut et al., 2009,

Rosser and Bonewald, 2012). MLO-A5 cells were seeded on Z9A1 and Z3A1 PU scaffolds fabricated from solutions containing varying combinations of DMF/THF solvents.

In general, cells were viable on all scaffolds during the 14 day culture period. Cells had similar viability on all Z9A1 on day 1, indicating that, there were no differences in the cell's ability to attach to scaffolds. Viability increased steadily from day 1 to day 4 with similar values on Z9-100 and Z9-70 scaffolds between day 4 and day 7. On day 14 of culture, there was no significant difference between MTT absorbance on Z9-70 and Z9-100, however, cell viability on Z9-50 scaffolds was significantly lower than that of Z9-100 and Z9-70 ($p \leq 0.05$) (Fig. 5A). This could have been the result of morphological differences in fibre diameter, as Z9-50 fibre diameters were significantly larger than Z9-70 and Z9-100 scaffolds.

For Z3A1 scaffolds, there was a steady increase in cell viability on all Z3-100, Z3-70 and Z3-50 scaffolds during the culture period (Fig. 5B). There was however, no significant difference between all groups of scaffolds, except that Z3-50 supported lower cell viability on day 4 ($p \leq 0.05$). The ability of electrospun scaffolds to mimic the natural three-dimensional environment of the *in vivo* extracellular matrix whilst providing structural support with high surface to volume ratio makes excellent structures for tissue engineering applications. It has been reported that cells assume a more spindle-shaped morphology with increasing fibre diameters and rather orient parallel to fibres with aligned meshes (Bashur et al., 2009,
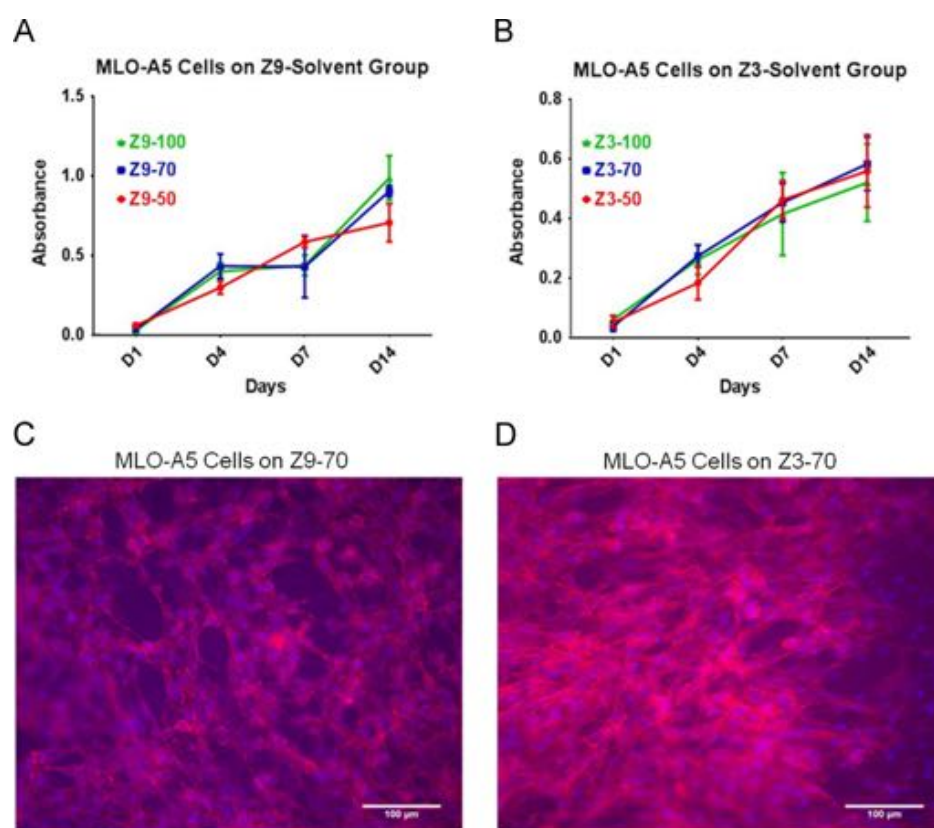

Fig. 5 – MTT absorbance for MLO-A5 cells seeded on (A) Z9A1 PU scaffolds, (B) Z3A1 PU scaffolds (mean ± S.D. $n=6$) for statistical analysis see text. (C) and (D) Fluorescent micrographs of DAPI (blue=nucleus) and phalloidin (red=actin) staining of MLO-A5 Cells on Z9-70 (C) and Z3-70 (D) scaffolds on day 4, scale bar at 100 μm. (For interpretation of the references to colour in this figure legend, the reader is referred to the web version of this article.)

Delaine-Smith et al., 2014). DAPI (nucleus) and Phalloidin (actin cytoskeleton) staining over a seven day period confirmed the MTT data indicating increasing numbers of cells attached to the scaffolds over time (data not shown). Fig. 5 shows representative micrographs of cell attachment on day 4 indicating that cells are well spread across the scaffolds with an elongated morphology for Z9-70 (Fig. 5C) and Z3-70 (Fig. 5D) scaffolds.

3.7.   Cell viability on composite scaffolds

Hydroxyapatite ($Ca_{10}(PO_4)_6(OH)_2$), HA is well established as a synthetic material for bone replacement due to its chemical resemblance to the inorganic component of bone and tooth, and has been widely used a biocompatible material in many areas of medicine. HA is known to promote faster bone regeneration and direct bonding to regenerated bone without intermediate connective tissue (Patel et al., 2002).

For composite scaffolds, Z3A1 scaffolds consistently presented with a more uniform combination of nano and micro fibre diameters and were less brittle than Z9A1 composites, therefore Z3A1 was used to examine the effect on cell behaviour of including HA in the scaffold. MLO-A5 cells seeded on Z3-nHA scaffolds had the highest cell viability at all-time points after day 1, being 22% higher by day 28 (Fig. 6A), this implies that cell proliferation rate was higher on these scaffolds as MTT absorbance at day 1 was the same for all groups. This is similar to the effects of nHA observed in previous studies (Rezwan et al., 2006; Bianco et al., 2009; Mi et al., 2014) and probably resulted from the bioactive nature of HA coupled with the higher surface area and crystallinity of nHA particles. A high HA surface area facilitates a strong interaction between the polymer and ceramic phase, and allows protein attachment. For example, it has been reported that initial calcium absorption to nanoceramic surfaces enhanced binding of vitronectin, that subsequently promoted osteoblastic adhesion and proliferation (Webster et al., 2001). It might be expected that mHA would also elicit cell viabilities as high as those attained by the nano-composites but that was not observed for MLO-A5 in this study. This may have been due to the lower porosity that was observed with the inclusion of mHA particles, which could have hindered cell proliferation, migration, and nutrient transfer.

To investigate the ability of these composites to support progenitor cells, hES-MPs, embryonic derived mesenchymal progenitor cells were also seeded on Z3A1 electrospun scaffolds in osteogenic media (Fig. 6B). hES-MPs have been used in several studies as a model cell for bone tissue engineering (Karlsson et al., 2009). In the presence of osteogenic supplements, hES-MP cells have been shown to differentiate towards the osteogenic lineage *in vitro* (Delaine-Smith et al., 2012). Such mesenchymal progenitor cells also may have advantages over autologous bone marrow derived mesenchymal stem cells for clinical tissue engineering as they are readily available in large numbers and would avoid the extraction and expansion steps needed to tissue engineer bone from a patient's own cells.

As shown in Fig. 6B, there was an increase in hES-MP cell viability over all time-points on Z3A1 scaffolds however, in contrast to MLO-A5 cells; there was no significant difference between Z3-nHA, Z3-mHA and Z3-PU scaffolds in their ability to support cell proliferation. There is no obvious reason for this different effect of nHA on cell proliferation of the two types it but may be related to their different stages in the osteogenic differentiation pathways.

3.8.   Collagen and calcium staining and histology

The ultimate test of a scaffold's ability to support bone tissue engineering is its ability to support bone-like extracellular matrix deposition. Collagen and calcified matrix staining using Sirius red and alizarin red, respectively were used to study extracellular matrix production and mineralisation on days 14, 21 and 28 of culture. Collagen production by MLO-A5 cells on Z3 scaffolds was highest for Z3-nHA scaffolds at all-time points (Fig. 7A) with the highest deposition measured on day 28, significantly higher than that produced on Z3-mHA and Z3-PU scaffolds. This is the same scaffold that supported the highest number of viable MLO-A5 cells. A similar pattern was observed with hES-MP cells (Fig. 7B).

Interestingly, calcium production elicited results opposite to those attained for collagen production. Alizarin red absorbance on of cell-seeded Z3–PU scaffolds was higher for both MLO-A5 (Fig. 7C) and hES-MP cells (Fig. 7d) than for HA composite scaffolds (after substraction of the background absorbance). However, unsurprisingly, alizarin red strongly stained the blank
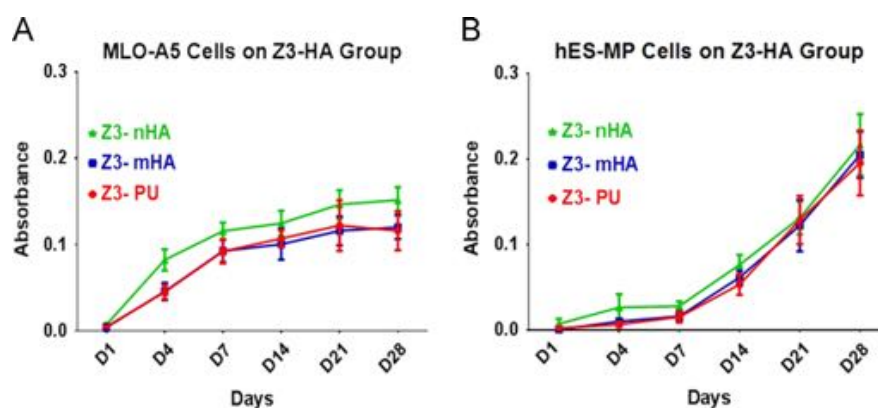

Fig. 6 – MTT absorbance on Z3A1 composite scaffolds (mean ± S.D. $n=6$). (A) MLO-A5 cells on Z3 PU, Z3-mHA and Z3-nHA scaffolds, (B) hES-MP cells on Z3 PU, Z3-mHA and Z3-nHA scaffolds. For statistical analysis see text.
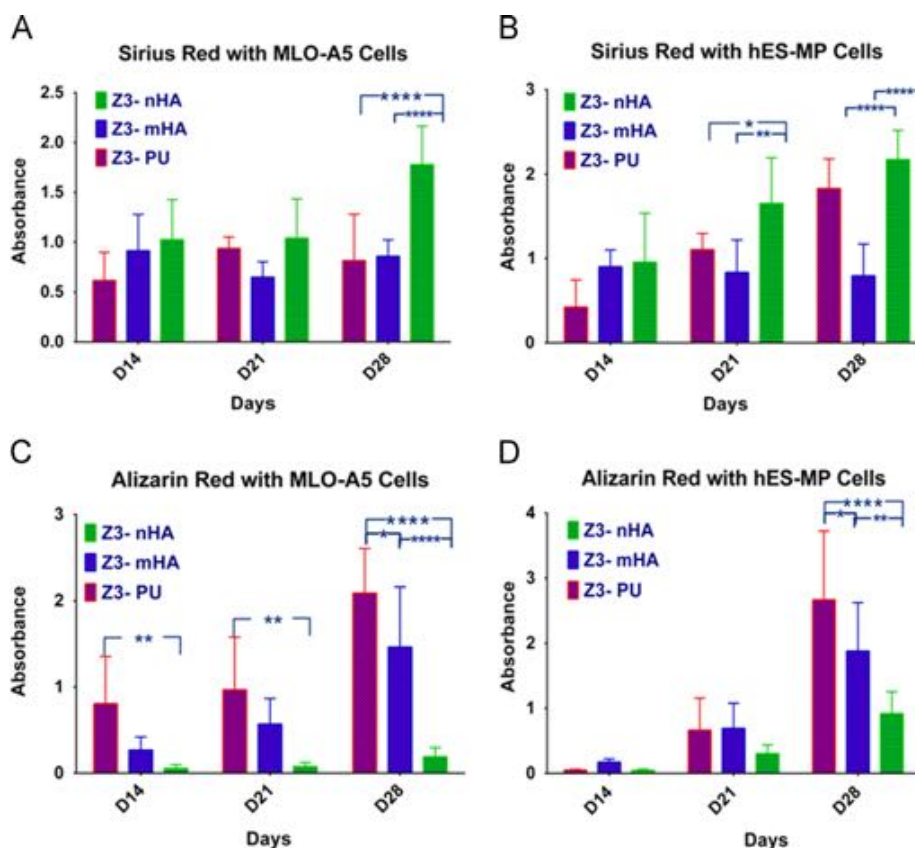
Fig. 7 – Collagen and calcium Staining on Z3-PU, Z3-mHA and Z3-nHA scaffolds on D14, D21 and D28 (mean±S.D. $n=6$). (A) sirius red absorbance of MLO-A5 cells, (B) sirius red absorbance of hES-MP cells, (C) alizarin red absorbance of MLO-A5 cells (D) alizarin red absorbance of hES-MP cells. $*p \leq 0.05$, $** \leq 0.01$, $**** \leq 0.0001$. (For interpretation of the references to colour in this figure legend, the reader is referred to the web version of this article.)

(no cells) control scaffolds that contained HA. As this is a single blank and not the same sample on which cells are seeded, any variability in HA content between scaffold samples would have made it more difficult to distinguish between the scaffold HA and cell-deposited HA. It would be interesting to image mineralisation in the same scaffold over time using a technique such as μCT scanning or Xylenol orange to determine if there was truly less cell deposited calcium in composite scaffolds.

Histological sections were taken to examine how far MLO-A5 and hES-MP cells penetrated into the Z3 PU and composite scaffolds by day 14 of culture, having been seeded at the surface (Fig. 8). In general, MLO-A5 cells were densely distributed on the surface of all scaffolds as compared to hES-MP cells which exhibited thinner coverage in Z3-PU and Z3-mHA scaffolds and were more loosely dispersed throughout the scaffold interior. hES-MPs cells cultured on Z3-nHA scaffolds appeared to penetrate to the greatest depth and were found in more locations compared to all other groups, although no cells were seen at the bottom of the scaffold at this time-point. The lack of cell penetration into the scaffold may have resulted from the low porosity, pore size and interconnectivity of scaffolds associated with the closely packed arrangement of the fibres. It is interesting that hES-MPs appear to penetrate deeper than MLO-A5s, which may be related cell size or differences in attachment and migration cell surface molecules. This observation has also been reported extensively in the literature as a major limitation of

traditional electrospun sheets (Bergmeister et al., 2013; Leong et al., 2010). It would therefore be advantageous to increase the porosity of electrospun scaffolds by opening up spaces between the fibres. Electrospinning with a cryogenic mandrel, controlling fibre deposition with air-flow impedance and electrospinning with porogens, amongst others, have reported to enhance scaffold porosity and cell penetration (McClure et al., 2012). It is also possible to increase porosity by co-spinning polymer solutions with a very fast degrading or water-soluble polymer (Milleret et al., 2011), and using mechanical techniques such as ultrasonication (Lee et al., 2011) and static stretch to force fibres apart and thus facilitate greater cell penetration, nutrient diffusion and transport of metabolic products.

4. Conclusions

Choice of solvents, on their own or in combination, strongly influences the final properties of solution, hence fibre morphology during the electrospinning process. Two types of thermoplastic polyurethane Z9A1 and Z3A1 were electrospun from solutions made with varying combinations of DMF and THF solvents. For both types of PU reducing the amount of DMF contained in the solution, increased fibre diameter, resulting in fibres with a more uniform morphology, and also eliminating the beads which were found in the scaffolds fabricated from 100% DMF solvent.
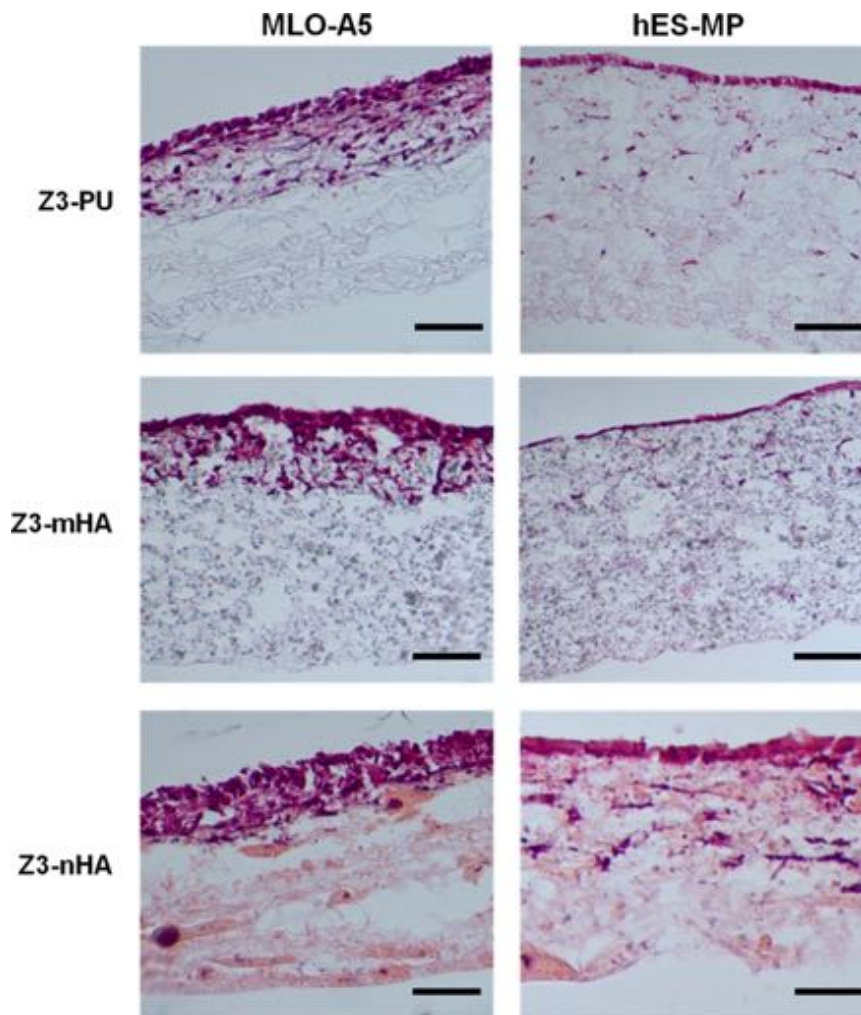
Fig. 8 – H&E staining on Z3-PU, Z3-mHA and Z3-nHA scaffolds on Day 14 of culture for MLO-A5 and hES-MP cells. Scale Bar at 100 μm.

In addition, reducing the DMF solvent content led to lower tensile properties of electrospun scaffolds, whilst incorporation of nano and micro HA particles in both Z9-PU and Z3-PU solutions reinforced the mechanical properties of electrospun composites. Young's Modulus and yield strength values of composites were higher than that of PU scaffolds; these differences were significantly higher with mHA composites compared to nHA composites but nHA composites exhibited smoother fibres, less variability in fibre size and better dispersion of the HA. Furthermore, FTIR spectral data confirmed the presence of HA particulates in fabricated composites.

Finally, MLO-A5 cell viability was highest for scaffolds fabricated with 70/30 DMF/THF solvent across most time points for both types of PU, whilst cell viabilities for both MLO-A5 and hES-MP cells, were highest with Z3-nHA scaffolds which also produced the highest deposition of collagen across all time points. Calcium deposition was supported in all scaffolds. Therefore, we have developed a range of scaffolds which have the potential to support bone matrix formation for bone tissue engineering, providing varying material properties which can be tailored depending on the stage of cell differentiation and final application.

Acknowledgements

REFERENCES

Adhikari, R., Gunatillake, P.A., Griffiths, I., Tatai, L., Wickramaratna, M., Houshyar, S., Moore, T., Mayadunne, R.T. M., Field, J., Mcgee, M., Carbone, T., 2008. Biodegradable injectable polyurethanes: synthesis and evaluation for orthopaedic applications. Biomaterials 29, 3762–3770.

Armentano, I., Dottori, M., Fortunati, E., Mattioli, S., Kenny, J.M., 2010. Biodegradable polymer matrix nanocomposites for tissue engineering: a review. Polym. Degrad. Stabil. 95, 2126–2146.

Attawia, M., Herbert, K., Laurencin, C., 1995. Osteoblast-like cell adherance and migration through three-dimensional porous polymer matrices. Biochem. Biophys. Res. Commun. 213, 639–644.

Bashur, C.A., Shaffer, R.D., Dahlgren, L.A., Guelcher, S.A., Goldstein, A.S., 2009. Effect of fiber diameter and alignment of electrospun polyurethane meshes on mesenchymal progenitor cells. Tissue Eng. Part A 15, 2435–2445.

Bergmeister, H., Schreiber, C., Grasl, C., Walter, I., Plasenzotti, R., Stoiber, M., Bernhard, D., Schima, H., 2013. Healing characteristics of electrospun polyurethane grafts with various porosities. Acta Biomater. 9, 6032–6040.

Bianco, A., Federico, D.I., Moscatelli, E., Camaioni, I., Armentano, A., Campagnolo, I., Dottori, L., Kenny, M., Siracusa, G., J.M., Gusmano, G., 2009. Electrospun poly(ε-caprolactone)/Ca-deficient hydroxyapatite nanohybrids: Microstructure, mechanical properties and cell response by murine embryonic stem cells. Mater. Sci. Eng.: C 29, 2063–2071.

Bobovich, Y.S., 1988. Classical size effects in the Raman scattering spectra of highly dispersed particles. Experimental studies (review). J. Appl. Spectrosc. 49, 869–888.

Boccaccini, A.R., Maquet, V., 2003. Bioresorbable and bioactive polymer/Bioglass® composites with tailored pore structure for tissue engineering applications. Compos. Sci. Technol. 63, 2417–2429.

Boissard, C., Bourban, P.-E., Tami, A., Alini, M., Eglin, D., 2009. Nanohydroxyapatite/poly (ester urethane) scaffold for bone tissue engineering. Acta zBiomater. 5, 3316–3327.

Bonfield, W., 1988a. Composites for bone replacement. J. Biomed. Eng. 10, 522–526.

Bonfield, W., 1988b. Hydroxyapatite-reinforced polyethylene as an analogous material for bone replacementa. Ann. NY Acad. Sci. 523, 173–177.

Bonzani, I.C., Adhikari, R., Houshyar, S., Mayadunne, R., Gunatillake, P., Stevens, M.M., 2007. Synthesis of two-component injectable polyurethanes for bone tissue engineering. Biomaterials 28, 423–433.

Bose, S., Roy, M., Bandyopadhyay, A., 2012. Recent advances in bone tissue engineering scaffolds. Trends Biotechnol. 30 (10), 546–554.

Burg, K.J. L., Porter, S., Kellam, J.F., 2000. Biomaterial developments for bone tissue engineering. Biomaterials 21, 2347–2359.

Bye, F.J., Bissoli, J., Black, L., Bullock, A.J., Puwanun, S., Moharamzadeh, K., Reilly, G.C., Ryan, A.J., Macneil, S., 2013. Development of bilayer and trilayer nanofibrous/microfibrous scaffolds for regenerative medicine. Biomater. Sci. 1, 942–951.

Carlberg, B., Axell, M.Z., Nannmark, U., Liu, J., Kuhn, H.G., 2009. Electrospun polyurethane scaffolds for proliferation and neuronal differentiation of human embryonic stem cells. Biomed. Mater. 4, 045004.

Clarke, D., Puppi, D., Detta, N., Ferrer, M.C. C., Crawford, A., Reilly, G., Chiellini, F., 2008. Electrospun polyurethane scaffolds for mechanical stimulation of cells in bone tissue engineering. Tissue Eng. Part A 14, 846 (pp.).

Croteau, S., Rauch, F., Silvestri, A., Hamdy, R.C., 1999. Bone morphogenetic proteins in orthopedics: From basic science to clinical practice. Orthopedics 22, 686–695.

Delaine-Smith, R., Macneil, S., Reilly, G., 2012. Matrix production and collagen structure are enhanced in two types of osteogenic progenitor cells by a simple fluid shear stress stimulus. Eur. Cells Mater. 24, 162–174.

Delaine-Smith, R.M., Green, N.H., Matcher, S.J., Macneil, S., Reilly, G.C., 2014. Monitoring fibrous scaffold guidance of three-dimensional collagen organisation using minimally-invasive second harmonic generation. PloS One 9, e89761.

Delaine-Smith, R.M., Reilly, G.C., 2011. The effects of mechanical loading on mesenchymal stem cell differentiation and matrix production. Vitam. Horm. 87, 417–480.

Demir, M.M., Yilgor, I., Yilgor, E., Erman, B., 2002. Electrospinning of polyurethane fibres. Polymer 24, 3303–3309.

Gogolewski, S., 2007. Structure-property relations and cytotoxicity of isosorbide-based biodegradable polyurethane scaffolds for tissue repair and regeneration. J. Biomed. Mater. Res. 85A, 456–465.

Gogolewski, S., Gorna, K., 2007. Biodegradable polyurethane cancellous bone graft substitutes in the treatment of iliac crest defects. J. Biomed. Mater. Res. Part A 80, 94–101.

Gorna, K., Gogolewski, S., 2003. Preparation, degradation, and calcification of biodegradable polyurethane foams for bone graft substitutes. J. Biomed. Mater. Res. Part A 67A, 813–827.

Gorna, K., Gogolewski, S., 2006. Biodegradable porous polyurethane scaffolds for tissue repair and regeneration. J. Biomed. Mater. Res. 79A, 128–138.

Grad, S., Kupcsik, L., Gorna, K., Gogolewski, S., Alini, M., 2003. The use of biodegradable polyurethane scaffolds for cartilage tissue engineering: potential and limitations. Biomaterials 24, 5163–5171.

Guelcher, S.A., 2008. Biodegradable polyurethanes: synthesis and applications in regenerative medicine. Tissue Eng. Part B: Rev. 14, 3–17.

Guelcher, S.A., Patel, V., Gallagher, K., Connolly, S., Didier, J.E., Doctor, J., Hollinger, J.O., 2004. Synthesis of polyurethane foam scaffolds for bone tissue engineering, Proc. AIChE, Annual meeting, Austin, Texas, 6261–6263 ISBN 0-8169-0965-2.

Heijkants, R., Van Tienen, T., de Groot, J., Pennings, A., Buma, P., Veth, R., Schouten, A., 2006. Preparation of a polyurethane scaffold for tissue engineering made by a combination of salt leaching and freeze-drying of dioxane. J. Mater. Sci. 41, 2423–2428.

Huang, Z.M., Zhang, Y.Z., Kotaki, M., Ramakrishna, S., 2003. A review on polymer nanofibers by electrospinning and their applications in nanocomposites. Compos. Sci. Technol. 63, 2223–2253.

Karlsson, C., Emanuelsson, K., Wessberg, F., Kajic, K., Axell, M.Z., Eriksson, P.S., Lindahl, A., Hyllner, J., Strehl, R., 2009. Human embryonic stem cell-derived mesenchymal progenitors—potential in regenerative medicine. Stem Cell Res. 3, 39–50.

Khan, A.S., Ahmed, Z., Edirisinghe, M.J., Wong, F.S. L., Rehman, I.U., 2008. Preparation and characterisation of a novel bioactive restorative composite based on covalently coupled polyurethane–nanohydroxyapatite fibres. Acta Biomater. 4, 1275–1287.

Khil, M.S., Cha, D.I., Kim, H.Y., Kim, I.S., Bhattarai, N., 2003. Electrospun nanofibrous polyurethane membrane as wound dressing. J. Biomed. Mater. Res. Part B—Appl. Biomater. 67B, 675–679.

Kucinska-Lipka, J., Gubanska, I., Janik, H., 2013. Gelatin-modified polyurethanes for soft tissue scaffold. Sci. World J. 2013 Article ID 450132, 12 pages, http://dx.doi.org/10.1155/2013/450132.

Lee, J.B., Jeong, S.I., Bae, M.S., Yang, D.H., Heo, D.N., Kim, C.H., Alsberg, E., Kwon, I.K., 2011. Highly porous electrospun nanofibers enhanced by ultrasonication for improved cellular infiltration. Tissue Eng. Part A 17, 2695–2702.

Leong, M.F., Chan, W.Y., Chian, K.S., Rasheed, M.Z., Anderson, J.M., 2010. Fabrication and in vitro and in vivo cell infiltration study of a bilayered cryogenic electrospun poly(D,L-lactide) scaffold. J. Biomed. Mater. Res. Part A 94A, 1141–1149.

Martin, T.P., 1996. Shells of atoms. Phys. Rep. 273, 199–241.

Martinez-Valencia, A., Carbajal-de La Torre, G., Torres-Sanchez, R., Tellez-Jurado, L., Esparza-Ponce, H., 2011. Production of

polyurethane/nano-hydroxyapatite hybrid materials and microstructural characterisation. Int. J. Phys. Sci. 6, 2731–2743.

Mcclure, M.J., Wolfe, P.S., Simpson, D.G., Sell, S.A., Bowlin, G.L., 2012. The use of air-flow impedance to control fiber deposition patterns during electrospinning. Biomaterials 33, 771–779.

Mcmahon, R.E., Qu, X., Jimenez-Vergara, A.C., Bashur, C.A., Guelcher, S.A., Goldstein, A.S., Hahn, M.S., 2011. Hydrogel–electrospun mesh composites for coronary artery bypass grafts. Tissue Eng. Part C: Methods 17, 451–461.

Mi, H.-Y., Palumbo, S., Jing, X., Turng, L.-S., Li, W.-J., Peng, X.-F, 2014. Thermoplastic polyurethane/hydroxyapatite electrospun scaffolds for bone tissue engineering: effects of polymer properties and particle size. J. Biomed. Mater. Res. Part B: Appl. Biomater., http://dx.doi.org/10.1002/jbm.b.33122.

Milleret, V., Simona, B., Neuenschwander, P., Hall, H., 2011. Tuning electrospinning parameters for production of 3D-fiber-fleeces with increased porosity for soft tissue engineering applications. Eur. Cell Mater. 21, 286–303.

Mo, C., Yuan, Z., Zhang, L., Xie, C, 1993. Infrared absorption spectra of nano-alumina. Nanostruct. Mater. 2, 47–54.

Nirmala, R., Kang, H.-S., EL-Newehy, M.H., Navamathavan, R., Park, H.-M., Kim, H.Y., 2011. Human osteoblast cytotoxicity study of electrospun polyurethane/calcium chloride ultrafine nanofibers. J. Nanosci. Nanotechnol. 11, 4749–4756.

Oprea, S., 2005. Effect of solvent interactions on the properties of polyurethane films. High Perform. Polym. 17, 163–173.

Patel, N., Best, S., Bonfield, W., Gibson, I., Hing, K., Damien, E., Revell, P., 2002. A comparative study on the in vivo behavior of hydroxyapatite and silicon substituted hydroxyapatite granules. J. Mater. Sci. Mater. Med. 13, 1199–1206.

Rehman, I., Bonfield, W., 1997. Characterisation of hydroxyapatite and carbonated apatite by photo acoustic FTIR spectroscopy. J. Mater. Sci. Mater. Med. 8, 1–4.

Rezwan, K., Chen, Q.Z., Blaker, J.J., Boccaccini, A.R., 2006. Biodegradable and bioactive porous polymer/inorganic composite scaffolds for bone tissue engineering. Biomaterials 27, 3413–3431.

Rosser, J., Bonewald, L.F., 2012. Studying Osteocyte Function Using the Cell Lines MLO-Y4 and MLO-A5. Bone Research Protocols. Humana Press, Springer, New York, NY.

Sittichockechaiwut, A., Scutt, A.M., Ryan, A.J., Bonewald, L.F., Reilly, G.C., 2009. Use of rapidly mineralising osteoblasts and short periods of mechanical loading to accelerate matrix maturation in 3D scaffolds. Bone 44, 822–829.

Sittichokechaiwut, A., Edwards, J., Scutt, A., Reilly, G., 2010. Short bouts of mechanical loading are as effective as dexamethasone at inducing matrix production by human bone marrow mesenchymal stem cell. Eur. Cell Mater. 20, 45–57.

Tsui, Y.K., Gogolewski, S., 2009. Microporous biodegradable polyurethane membranes for tissue engineering. J. Mater. Sci. Mater. Med. 20, 1729–1741.

Wannatong, L., Sirivat, A., Supaphol, P., 2004. Effects of solvents on electrospun polymeric fibres: preliminary study on polystyrene. Polym. Int. 53, 1851–1859.

Webster, T.J., Schadler, L.S., Siegel, R.W., Bizios, R., 2001. Mechanisms of enhanced osteoblast adhesion on nanophase alumina involve vitronectin. Tissue Eng. 7, 291–301.

Wen, J., Somorjai, G., Lim, F., Ward, R, 1997. XPS study of surface composition of a segmented polyurethane block copolymer modified by PDMS end groups and its blends with phenoxy. Macromolecules 30, 7206–7213.

Yoshii, T., Dumas, J.E., Okawa, A., Spengler, D.M., Guelcher, S.A., 2012. Synthesis, characterisation of calcium phosphates/polyurethane composites for weight-bearing implants. J. Biomed. Mater. Res. Part B: Appl. Biomater. 100B, 32–40.

Zdrahala, R.J., Zdrahala, I.J., 1999. Biomedical applications of polyurethanes: a review of past promises, present realities, and a vibrant future. J. Biomater. Appl. 14, 67–90.

Zhang, J., Doll, B.A., Beckman, E.J., Hollinger, J.O., 2003. A biodegradable polyurethane-ascorbic acid scaffold for bone tissue engineering. J. Biomed. Mater. Res.—Part A 67, 389–400.